JORGE ISAAC PEREN MONTERO

Geometry and ventilation: Evaluation of the leeward sawtooth roof potential in the natural ventilation of buildings

Sao Paulo
2015

JORGE ISAAC PEREN MONTERO

Geometry and ventilation: Evaluation of the leeward sawtooth roof potential in the natural ventilation of buildings

Thesis presented at the Polytechnic School as part of a double-degree agreement between the University of São Paulo (USP) and the Eindhoven University of Technology (TU/e) to obtain the PhD degree in Science.

Concentration Area:
Civil Construction Engineering Department

Supervisor: Prof(a). Dr(a). Brenda Chaves Coelho Leite.
Co-supervisor: Bert Blocken

São Paulo
2015

Catalogação-na-publicação

Perén, Jorge Isaac
Geometry and ventilation: Evaluation of the leeward sawtooth roof potential in the natural ventilation of buildings / J. I. Perén -- São Paulo, 2015.
175 p.

Tese (Doutorado) - Escola Politécnica da Universidade de São Paulo. Departamento de Engenharia de Construção Civil.

1.Dinâmica dos fluidos (simulação computacional) 2.Sheds 3.Ventilação Natural 4.Cobertura de edifícios (otimização) 5.Túneis de vento (experimentos) I.Universidade de São Paulo. Escola Politécnica. Departamento de Engenharia de Construção Civil II.t.

Table of contents

Acknowledgements

To my supervisors for all of their support, pattience, effort and constructive approach that made this research collaboration a very fruitful one. First, my sincere thanks go to dr.ir. Brenda Leite, my supervisor at the University of São Paulo (USP), Brazil. Brenda thank you for starting this PhD journey with me and being supportive and open towards all the possibilities and ideas during this research process. Thank you for relying on me and giving me the opportunity to establish the dual PhD degree process between the University of São Paulo (USP), Brazil and Eindhoven University of Technology (TU/e), the Netherlands. Thank you for all your advice and for taking care and putting an enormous effort during the dual PhD degree agreement process to get it done. Second, I express my special appreciation and thanks to prof.dr.ir. Bert Blocken, my supervisor at TU/e, for giving me the opportunity to be part of his research group and to identify, first by an e-mail and then by a short meeting at 6th floor of Vertigo building, that this collaboration could be successful. It proves his vision and talent to lead PhD candidates to achieve their goals and to maximize their potential. For his friendship and his capacity to diversify his research group with PhD students with different backgrounds who look up to him. He has created a constructive environment within and outside the office. Furthermore, I also want to express my thanks to my co-supervisor dr.ir. Twan van Hooff, for letting the process be an enjoyable moment and for all his valuable comments and support during the production of the ISI journal papers. My thanks also goes to dr.ir. Rubina Ramponi, who supported my research during my first 6 months at TU/e. I am very proud of this research collaboration, which was performed with such talented and efficient researchers and supervisors. Finally, a special thank you to the anonymous reviewers of our ISI journal papers for their valuable insights and recommendations.

To the administrative support of the secretaries at TU/e, the Netherlands and at USP, Brazil. My special thanks to Patrícia Freitas for the invaluable technical support offered since I started my PhD at the Civil Construction Engineering Department of The Polytechnic School of the University of São Paulo, Brazil (POLI-USP). In the same Department, thanks to dr.ir. Cheng Yee and dr.ir. Eduardo Toledo, for their support and advice. Also, to all the professors that inspired me before and during the development of my PhD research project: To my supervisor of my "*Iniciação Científica*" (in English: Scientific Initiation Program for Undergraduate Students) and also supervisor of my master degree prof.dr. Rosana Caram, professor at the Architectural and Urban Planning Institute of the University of São Paulo (IAU-USP; at São Carlos Campus); to prof.dr. Heverson Tamashiro from the Federal University of Technology of Parana, Brazil; to prof. Brian Ford, professor at the Department of Architecture and Built Environment of Nottingham University, the UK; to prof.dr Anesia Barros Frota, from the Architecture and Urban Planning Faculty of the University of São Paulo (FAU-USP); and a special thanks to prof.dr. Fabio Saltara, from the Department of Mechanical Engineering of The Polytechnic School of the University of São Paulo, Brazil (POLI-USP) for his advice in Computational Fluid Dynamics (CFD). Finally, to the main source of inspiration, João Filgueiras Lima "Lelé" (R.I.P) for his never-ending research in building construction and design and especially for his simplicity.

To the Secretary of Education, Science, Research and Technology of Panama (SENACYT) for its partial support to this research. To The Coordination for the Improvement of Higher Level Personnel of Brazil (CAPES), The Polytechnic School of the University of São Paulo, Brazil (USP) and the unit Building Physics and Services of the Department of the Built Environment at Eindhoven University of Technology in the Netherlands for the support. To the Laboratory of Electrical and Fluids Metrology of The Institute of Technical Research of São Paulo, Brazil (IPT) and its Director dr. Gilder Nader, for allowing me to use the atmospheric boundary layer wind tunnel, that help me to developed my PhD research. Within the same laboratory and research group, I am also grateful to ir. Gabriel Borelli, and dr.ir. Paulo Jabardo, for assistance with the wind tunnel pressure coefficient measurements and smoke visualization.

To all my colleagues in both TU/e and USP that helped me during my PhD process. My colleagues at floor 6 of the Vertigo building (VRT), I show my gratitude for the very pleasant environment created around the coffee machine and also outside the workplace during our social activities. For some of them, my thanks for the emotional support demonstrated in different ways (by sharing a drink, a joke or even just a smile). To Rubina for her kind attention and support by e-mail prior and after my arrival in The Netherlands. To Roel for his kindness that he showed me since the first moment I met him at the main entrance of the Vertigo building. To my research group colleagues: Adelya, Alessandro, Allecio, Antonio, Fabio, Feiyu, Hamid, Ivo, Katarina, Okke, Olga, Raffaele, Samy, Thijs, Wendy, Xinrong and Yasin. Special thanks to Hamid for his attention when I was struggling with Gambit and for his comments during the progress meetings. To my colleagues from the other groups Rick, Zara, Basar, Christian, Jacob, Kennedy, Rongling, Timilehin, Yang, Ignacio, Fotis, Raúl, Alberto, Azee, Chris, Guillaume, Pei, Rui, Stepan and Veronica. My especial thank you to Katarina for all of her support. At the University of São Paulo (USP), Brazil, to my colleagues Iara, Luciano, Victor, Carolina, Erica, Fabio, Fabricio and the guys of the aero design team and of the Mechanical Engineering Department Daniel and Felipe, for their input in CFD.

I would like to address a special thanks to Nelson Kon for allow me to use his Photo in the cover of this thesis and also to Rafaela for his kind attention.

To all my friends that helped me to achieve this important goal. In Brazil, my sincere thanks to Chan for his important advice regarding my PhD research application. Also to Tatiana for her valuable input about her experience in The Netherlands. Also thanks to Bruno, Dario, Diogo, Fabiana, Fernando, Pablo, Reginaldo, Ricardo and Carolina. A special acknowledgement to Marcele for her sincere support. In Nottingham, to my friend Yilbert (Lavoe) and Micaela, for all the help and invaluable friendship during the most challenging period. To Peter and Carol for the spiritual support and blessings during the whole journey. In The Netherlands to my flatmates and in particular to Elia for her friendship.

To The Panamaniam Association of São Paulo (APSP) and the former Presidents whom inspired me prior to start my PhD: dr. David Brandford, ir. Aramis Guerra, dr. Ricardo Moreno, dr. Miguel Sing, dr. Moacyr Menendez, and ir. Ricardo Aguilar Bernal, and also to César Aparício and Maria Inez, Abraham

Tudisco, Armando, Melida and Michele Wharton, Gisela and Karina Brandford, Eduardo Rutherford, Edwin Pitre, Jaime Leyton, Thomas Smith, Erica and Ricardo Aguilar and all the APSP family and friend members.

Finally, I would also like to show my enormous gratitude to my family that stood by me in all the difficult moments. To my best friend and mentor, my dad (Jorge) and my mother (Elsa) that supported my big two challenges; the first one, when I left Panama to continue my studies in Brazil and the second one; my whole PhD process. To my sister (Jemily) and my brother-in-law (Ricardo) and my nephews (Carlos and Enrique, my godson).

Resumo

Geometria e ventilação: avaliação do potencial do Shed a sotavento na ventilação natural dos edifícios

O Shed tem aberturas no nível inferior da fachada e aberturas elevadas no nível superior do telhado. Quando a abertura localizada no nível superior capta o vento o Shed é chamado de "Shed Cata-vento" e quando ele é usado para extrair o ar interior do edifício usando a região com pressao negativa é chamado de "Shed a sotavento". Os Sheds permitem a ventilação natural e a entrada da luz natural em maior intensidade e uniformidade que um telhado plano com aberturas laterais. Esta pesquisa foca-se em edifícios com Sheds a sotavento e verifica-se o potencial da sua geometria para aumentar a ventilação vertical cruzada gerada pelo efeito do vento. Emprega-se simulações de Dinâmica dos Fluidos Computacional (CFD) para analisar o fluxo de vento ao redor do edifício e quantificar a ventilação natural por meio das taxas de fluxo de volume e a velocidade do fluxo de ar. Simulações CFD são realizadas utilizando as equações de Navier-Stokes baseadas em médias do número de Reynolds (RANS). Analisa-se a sensibilidade da malha e a validação numérica é realizada com medições em túnel de vento, previamente publicados, usando Velocimetria de Imagem de Partículas (PIV). A validação do modelo de turbulência mostra que o SST K-ω fornece os resultados mais precisos e, a influência do parâmetro "a" para o cálculo da energia cinética turbulenta com um valor de 0,5 resulta na melhor concordância com as medições experimentais. Uma sistemática análise da sensibilidade de diversos parâmetros de Shed a sotavento é levada a cabo usando 3D RANS em combinação com o modelo de turbulência SST k-ω. Os resultados mostram que o ângulo de inclinação do telhado (RIA) tem uma significativa influência na velocidade do ar interior e na taxa de fluxo de volume e a posição vertical da abertura de saída é menos relevante. Quando um ângulo de inclinação de 45° é empregado, a taxa de fluxo de volume é 22% mais elevada do que um telhado plano. A geometria do Shed é fundamental para maximizar a zona de pressão negativa na parte posterior do edifício. Para um ângulo de inclinação de telhado com 27°, a geometria convexa tem taxas de fluxo de volume 13% superiores aos de uma geometria côncava. Os beirais aumentam o fluxo de ventilação em até 24%. Os beirais a barlavento aumentam a taxa de volume de fluxo significativamente (ate 15%) e proporcionam um fluxo de ar interior mais horizontalmente dirigido. Os beirais a sotavento têm uma influência reduzida e a aplicação de ambos (barlavento e sotavento) resulta em um aumento adicional (4%) da taxa de fluxo de volume. Sheds de um e de dois vãos são tambem investigados; as geometrias côncavas resultam em um ligeiro aumento da taxa de fluxo de volume em comparação com Sheds de um vão. A redução da taxa de abertura (A_{inlet} / A_{outlet}; totais) de 1 para 0,5 resulta num aumento da taxa de fluxo de volume de 23-39%, dependendo da geometria do telhado. A geometria interna na abertura de saída é importante no desempenho da ventilação.

Palavras-chave:
Dinâmica dos fluidos (simulação computacional), Sheds, Ventilação natural, Cobertura de edifícios (otimização), Túneis de vento (experimentos).

Summary

Geometry and ventilation: Evaluation of the leeward sawtooth roof potential in the natural ventilation of buildings

Sawtooth roof buildings can contribute to a sustainable and healthy indoor environment as they can allow additional daylight and natural ventilation compared to a standard flat roof. Sawtooth roof buildings have lower level openings in the (windward) facade and also upper-level openings near the roof top in the opposite (leeward) facade. When the upper-level opening captures the wind the sawtooth roof is called "wind catcher" and when it is used to extract indoor air from the building using the underpressure region in the wake of a building it is called a "leeward sawtooth roof". This PhD study focuses on low-rise leeward sawtooth roof buildings. The main goal of the research is to verify the potential of the leeward sawtooth roof geometry to increase the wind-driven upward cross-ventilation. This research employs Computational Fluid Dynamics (CFD) simulations to analyze the wind flow around the building and quantify the natural ventilation by means of the volume flow rates and the airflow patterns (indoor velocity).

CFD simulations are performed using the 3D steady Reynolds-Averaged Navier-Stokes (RANS) equations. The simulations are based on a grid-sensitivity analysis and on validation with previously published wind-tunnel measurements using Particle Image Velocimetry (PIV). The results show that the shear-stress transport (SST) k-ω and the Renormalization-group (RNG) k-ε turbulence models provide the best agreement with the experimental data. Once the numerical model is validated, a sensitive analysis of different building parameters on a single-zone isolated building model is carried out using the 3D steady RANS approach in combination with the SST k-ω turbulence model to provide closure to the governing equations. The following building parameters are systematically tested: (i) roof inclination angle and vertical outlet opening position; (ii) roof geometry; (iii) windward and leeward eaves inclination angle and the combination of both (windward and leeward); and, (iv) a comparison between a single-span and a double-span leeward sawtooth roof with the same and with lower inlet-outlet opening ratio.

In Chapter 1 the relevance, the driving forces of the natural ventilation phenomena, the problem statement and the methodology of the current research are introduced.

Chapter 2 presents the validation study and shows that the SST k-ω turbulence model provides the most accurate results, followed by the RNG k-ε turbulence model. The standard k-ε model, the realizable k-ε model, the standard k-ω model and the Reynolds stress model show larger deviations from the measured velocities. The influence of the parameter "a" for the calculation of the turbulent kinetic energy profiles at the inlet of the computational domain is tested; the results show that a value of 0.5 results in the best agreement with the wind-tunnel measurements. In addition, the impact of the roof inclination angle (RIA) is tested and it is observed that it strongly influences the indoor air velocity and the volume flow rate. The latter increases with a roof inclination angle larger than 18°. When a 45° roof inclination angle is

employed, the volume flow rate is 22% higher than a flat roof and it additionally increases from 22% to 25% when the outlet opening is located near the roof. The vertical outlet opening position is less important as it can just increase the volume flow rate by around 4% and increases or decreases the indoor air velocity by up to 41% and 21%, respectively.

In Chapter 3 five different roof geometries are studied; one straight and four curved roofs. The curved roofs can be subdivided in one concave, one hybrid (convex-concave) and two convex roof geometries. It is observed that the roof geometry is an important design parameter to maximize the size and magnitude of the underpressure zone in the wake of the building and the pressure difference over the building. A roof that directs the external wind flow behind the building upwards will result in a larger underpressure zone and larger underpressures and consequently in higher volume flow rates. For a normal wind incidence angle (0°), from all the roof geometries with a 27° roof inclination angle, the convex roof and the straight roof result in volume flow rates that are up to 13% higher than those of concave roof geometries.

In Chapter 4 the impact of the eaves is explored. It is shown that, in addition to their well-known beneficial effects concerning solar radiation and wind-driven rain, eaves can increase wind-driven cross-ventilation flow by up to 24%. Windward eaves with an inclination angle of 27° result in the highest increase of the volume flow rate (15%) and in a more horizontally directed flow through the occupied zone. On the other hand, leeward eaves appear to have less influence on the ventilation flow than upwind eaves; the maximum increase in volume flow rate is only 5% when eaves with a 90° inclination angle are employed. Application of both a windward eaves and a leeward eaves results in an additional increase (4%) of the volume flow rate in a single-span building.

In Chapter 5 an analysis of single-span and double-span sawtooth roofs is presented. It is shown that the straight and concave double-span leeward sawtooth roof geometries result in a slight increase of the volume flow rate compared to single-span roof geometries with a similar geometry type. However, the convex double-span roof geometry E2x2_OR1 reaches a 12% lower volume flow rate than found for its reference case, the single-span roof geometry E2, which is the result of the narrow internal geometry at the outlet opening. It is also shown that reducing the opening ratio ($A_{inlet}/A_{outlet;total}$) from 1 to 0.5 for the double-span roof geometries results in an increase of the volume flow rate with 23-39%, depending on the roof geometry. For convex double-span cases the building geometry near the outlet-opening plays an important role in the ventilation performance. The internal geometry contraction near the outlet openings generates a resistance to the airflow and reduces the volume flow rate.

Chapter 6 provides a discussion based on the limitations of the presented research and points out recommendations for future research. Chapter 7 summarizes the main conclusions of the current research, whereby it is highlighted that the optimum leeward sawtooth roof building design for increasing cross-ventilation is achieved by the interaction of these four main parameters: (a) roof inclination, (b) roof geometry, (c) eave location and angle, and (d) inlet-outlet opening ratio. In addition, it is pointed out that a single-span with 12 m depth reaches a higher volume flow rate than a single-span with 6 m depth with the same roof geometry type, despite the fact that a lower underpressure is present at the outlet opening.

List of figures

List of tables

Chapter 1

Introduction

1 Introduction

1.1 Relevance

Global mean temperature is rising due to climate change [1] and buildings (new and old buildings) should be adapted to decrease the entrance of solar radiation and to improve natural ventilation to remove the internal heat from the building. In North-Western European countries, such as The Netherlands, temperatures have risen as well [2], facing indoor air temperatures outside the thermal comfort zone in more hours during a year (e.g. [3]). In Latin American countries, such as Brazil, the amount of hours outside the thermal comfort zone will increase as well. Simply applying traditional active electrical cooling systems to improve indoor thermal comfort will increase the energy use in buildings, and will accelerate the depletion of fossil fuels, the emission of greenhouse gasses, and climate change, and should therefore be avoided. A range of passive strategies can be employed in buildings to reduce the indoor air temperature and to increase thermal comfort. For example, solar shading, which will become increasingly important in the future, natural ventilation (i.e. ventilative cooling), thermal storage and a smart use of building materials can prevent the use of energy to actively cooling the interior of buildings to meet the thermal comfort criteria (e.g. [3]). In large parts of Brazil and countries with similar climates (i.e. Tropical rainforest climate (Af), Tropical monsoon climate (Am), Tropical wet and dry or savanna climate (Aw), Mild desert climates (BWh), Hot semi-arid" (BSh), Humid subtropical climate (Cfa, Cwa), Subtropical highland variety (Cwb) and Maritime temperate oceanic (Cfb) according with the Köppen classification [4]) (see Figure 1.1), natural ventilation is one of the most important passive strategies to deal with high temperatures (e.g. [5–8]). Ventilative cooling as a passive cooling technique can both improve the indoor environmental quality in buildings without active cooling systems and decrease the cooling demand when active cooling is present [7,9] and can therefore contribute to a sustainable building environment [8]. The energy consumption related to the operation of heating, ventilation and air-conditioning systems (HVAC) in buildings in Canada, USA, New Zealand and 10 European Countries (Belgium, Denmark, Finland, France, Germany, The Netherlands, Norway, Sweden, Switzerland and UK) is already significant; i.e. it amounts 68% of the total energy use in service and residential buildings [10]. Therefore, a ventilation design in which natural ventilation is applied to reduce the cooling demand of buildings is recommended to reduce the overall energy use of buildings and to reduce the depletion of fossil fuels and the emission of greenhouse gasses.

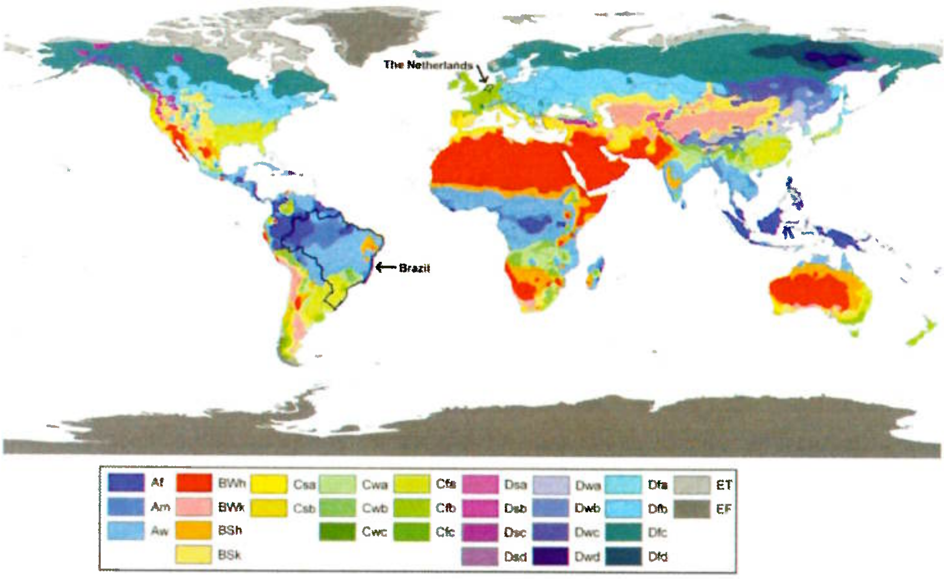

Figure 1.1: World map of Köppen-Geiger climate classification. (modified from [4])

1.2 Natural ventilation

Natural ventilation in buildings can: (1) increase indoor air quality , (2) increase thermal comfort by intensifying the convective heat transfer from the occupants, (3) remove internal heat, and (4) enhance convective heat exchange from the building structure to the indoor air (passive cooling in combination with thermal storage) [7,11,12]. Nevertheless, the fundamental criteria to enhance an efficient ventilation design vary depending on the weather conditions and the type of building (i.e. hospital, restaurant, stadium, school).

1.2.1 Driving forces

Natural ventilation is driven by pressure differences produced by wind and/or buoyancy. Buoyancy forces are significant under very low wind velocities or in absence of wind [13]. The wind flow pattern around buildings, and therefore also the pressure distribution on the building surfaces, is very complex. Important features of the wind flow pattern above and behind the building, as described by Peterka et al. [14] and Cook [15], must be considered in wind-induced ventilation of buildings. For instance, key features that are important are the stagnation point which is located at around ¾ of the windward facade height; the separation point at the front and side edges of the windward facade; the reattachment point that depends – among others – on the roof inclination angle, the building length-depth ratio and the building roof geometry; the "standing vortex" or "horseshoe vortex" generated from the interaction of the wind incidence flow and the geometry of the windward facade (see Figure 1.2).

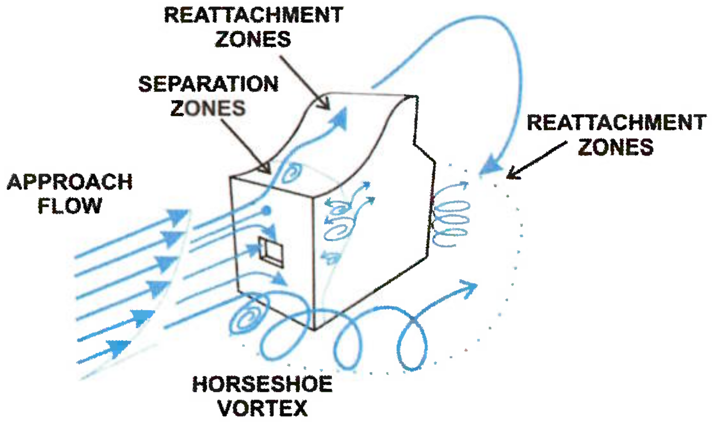

Figure 1.2: Schematic representation of the wind flow around an isolated leeward sawtooth roof building with indication of the horseshoe vortex, the separation and reattachment zones on the roof and the reattachment zone behind the building.

1.2.2 Natural ventilation flow types

One can distinguish between two main types of natural ventilation flow: (1) single-sided ventilation and (2) cross-ventilation (Figure 1.3). The former natural ventilation flow type relies on ventilation openings that are present in only one side of the building enclosure (Figure 1.3a), whereas the latter uses ventilation openings on both sides of a building enclosure, allowing fresh air to enter from one side of the building and to exhaust the polluted air through openings on the opposite side of the enclosure (Figure 1.3b) [11]. Single-sided natural ventilation can be used until a room depth of 2.5H, with H the height of the enclosure (internal height - floor to ceiling), while cross-ventilation can be used for room depths up to 5H [12]. In addition, in general, cross-ventilation is regarded as a more efficient way of providing natural ventilation through an enclosure since the distribution of the wind pressure is more favourable, with positive wind pressures on the windward facade and negative wind pressures on the leeward facade; due to the higher pressure differences in cross-ventilated enclosures higher volume flow rates can be reached than with single-sided natural ventilation [12].

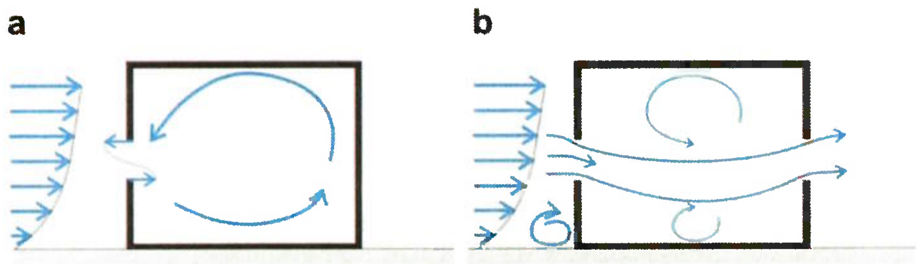

Figure 1.3: Natural ventilation flow types. (a) Single-sided ventilation. (b) Cross-ventilation.

Wind-driven cross-ventilation can be reinforced by buoyancy forces when the exhaust opening is located in the upper part of an enclosure [16]. For instance, a building with a leeward sawtooth roof, as depicted in Figure 1.4a, has the potential to combine the wind-driven flow with buoyancy-driven flow, resulting in an intensified upward cross-ventilation flow. Upward cross-ventilation can help to enhance the exhaust of heat, but also moisture, pollutants and smoke, by the top opening located in the upper part of the enclosure. In addition, upward natural cross-ventilation, when necessary, can be complemented by under-floor ventilation (UFV) (Figure 1.4c).

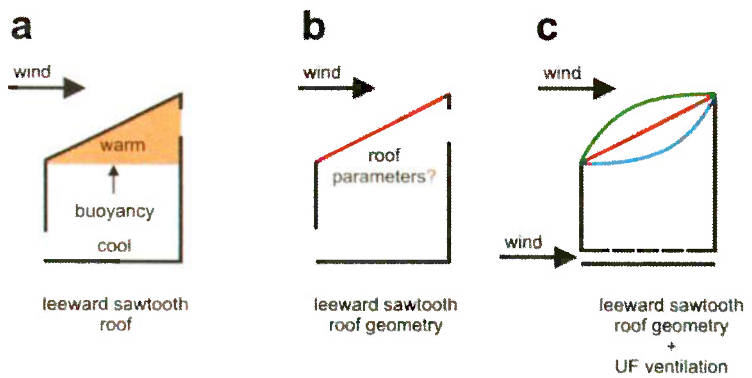

Figure 1.4: Schematic representation of: (a) combination of buoyancy and wind-driven forces in a building with a leeward sawtooth roof; (b) relevance of the roof parameters in leeward sawtooth roof buildings; (c) possible interaction of upward cross-ventilation with under-floor (UF) ventilation.

1.2.3 Natural ventilation modeling

Natural ventilation can be predicted by using analytical models, empirical models, small-scale experimental models, full-scale experimental models, multizone network models, zonal models and Computational Fluid Dynamics (CFD) models [17]. From these methods, CFD has become one of the most popular tools to analyze ventilation performance in buildings [17]. This is the result of the improvements in turbulence modeling and in computational power over the last decades. Furthermore, as opposed to wind tunnel modeling or (semi-) empirical formulae, CFD can provide detailed whole-flow field data under fully controlled conditions and without similarity constraints [18]. Among the CFD modeling approaches, Reynolds-averaged Navier–Stokes simulations (RANS) and large-eddy simulation (LES) are the most commonly used in urban physics in general and in natural ventilation studies in particular. On the one hand, LES is more accurate since it resolves the large scales of the turbulence; i.e. the scales that are larger than the applied filter, which is often equal to the mesh size. On the other hand, although RANS has limitations regarding the prediction of important features of the fully turbulent flow around and inside buildings, it has been successfully applied in a range of previous studies on urban wind flow and natural ventilation. Moreover, due to the computational costs, the increased model complexity of LES and the absence of best practice guidelines for LES simulations, RANS simulations are still most often employed in general, and for parametric studies of natural ventilation and urban wind flow in particular [19]. For CFD simulations using the steady RANS equations or LES validation of the numerical results, using full-scale or reduced-scale measurement results is imperative [20].

Within the CFD modeling approach, one can make a distinction between coupled and decoupled CFD simulation of natural ventilation flow. A coupled approach means that the internal and the external airflows are simultaneously modeled in a single computational domain (e.g. [21–23]). The interaction of outdoor wind flow with the indoor airflow is therefore explicitly included in this approach. The decoupled approach consists of two consecutive simulations; (1) a simulation of the wind flow around a sealed building; (2) a simulation of the flow inside the building, using boundary conditions at the ventilation openings that were obtained in the simulation of the wind flow around the sealed building (mainly pressure).

1.3 Problem statement

1.3.1 Wind-induced cross-ventilation

Wind-induced cross-ventilation is a complex phenomenon in the micro-scale meteorology that can be affected by many environmental and building parameters such as, the atmospheric boundary layer wind flow (ABL), the building height-depth ratio, building length, roof geometry, opening configuration and opening ratio. The flow inside the building is generated by an interaction between the atmospheric boundary layer flow approaching the building and the building itself (with all the building parameters) [24]. A systematic parametric study of the effect of building geometry on wind-induced cross-ventilation is imperative to better understand this interaction.

This thesis focuses on the analysis of wind-driven cross-ventilation flow in isolated generic buildings, with a focus on buildings equipped with leeward sawtooth roofs.

1.3.2 Sawtooth roof

A sawtooth roof, as the name already indicates, has a shape which resembles the teeth of a saw. Figure 1.4 and Figure 1.5 show some examples of sawtooth roof buildings. Normally, the relatively vertical components of the "teeth" are equipped with daylight openings and are orientated to the north to prevent solar radiation from entering the building, whereas the less inclined parts have an opaque construction. Sawtooth roofs are applied because – among others – they can reach more uniform and higher intensity levels of daylights inside buildings [25]. In addition, they can be used to increase the ventilation flow through buildings [26]. The ventilation flow in a building with a sawtooth roof depends, among others, on its orientation with respect to the oncoming wind flow [26]. In the case of a building with a leeward sawtooth roof, the supply openings are located in the bottom part of the windward facade and exhaust openings are present in the top part of the leeward facade, which can enhance the wind-driven natural ventilation since the upward wind-driven cross-ventilation flow can be assisted by buoyancy forces (if present) (see Figure 1.4, Figure 1.5). Although the possible advantages of sawtooth roofs in naturally ventilated buildings are known, the potential of buildings with a leeward sawtooth roof has not yet been extensively explored [27] and this type of roof is still not applied on a large scale. Several studies have been carried out on wind-induced loads on a sawtooth roof [28–30], gable roof [31–33] and arched roof [34]. However, these studies did not focus on the ventilation flow through the building as function of the roof geometry. To the best knowledge of the author, there are only a few studies that studied natural ventilation flows in buildings with asymmetric openings (upward ventilation) and for different roof geometries. Fatnassi et al. [35] investigated the effect of roof openings (windward and leeward) with and without side wall openings on the natural ventilation and indoor climate of a greenhouse with a concave curved multi-span roof [35] and concluded that simultaneous opening of windward and leeward roof vents does not improve the ventilation and the indoor climate. However, the authors did not quantify the isolated impact of the roof geometry on the ventilation. Some studies evaluated the potential of applying sawtooth roofs in schools [36,37], and pointed out that, depending on the wind direction and on the roof configuration, openings in the roof are advantageous for the exchange of indoor air with the outdoor environment. Kindangen et al. [38,39] analyzed the effect of the roof shape on natural ventilation of a building with symmetric opening positions (openings located at the same level) instead of asymmetric openings. Furthermore, the studies by Kindangen et al. [38,39] were not performed for a sawtooth roof building. A review on the effect of ventilation opening configurations on the indoor climate of greenhouses carried out by Bournet et al. [40] pointed out that ventilation rates and velocity patterns inside a naturally ventilated greenhouse are mainly affected by the geometry of the building and by the vent configuration (including size and arrangement of the vent openings).

However, in general, there appears to be a lack of knowledge on the effect of roof geometry on the airflow pattern inside cross-ventilated buildings with asymmetric opening positions. Not many studies have been performed to systematically analyze the impact of building and roof parameters (i.e. roof inclination, roof geometry, eaves, single and double-span) on the cross-ventilation flow. Therefore, the main goal of this research is to evaluate a range of building parameters that might be capable of maximizing the upward cross-ventilation flow in leeward sawtooth roof buildings. Several geometrical parameters of the building (i.e. roof inclination, roof geometry, eaves, number of spans) are evaluated.

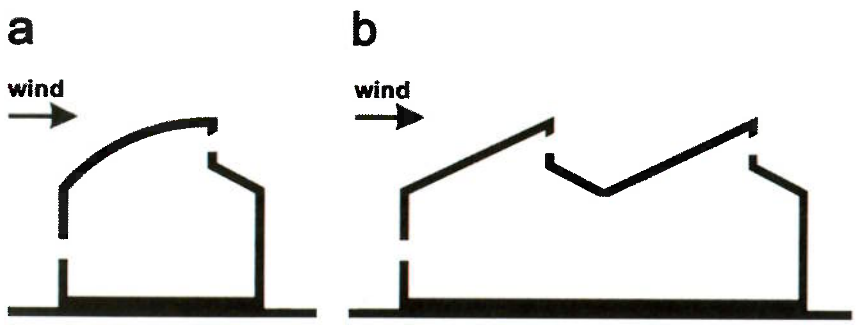

Figure 1.5: Vertical cross-sections of two leeward sawtooth roof geometries. (a) Single-span building with a convex roof geometry. (b) Double-span building with a straight roof geometry.

1.4 Methodology

1.4.1 Building and roof geometries

Two families of geometries were created: one with a horizontal plan area of 3 m x 6 m (W x D) and a height of x 5.7 m (Figure 1.6) and another one with a horizontal plan area of 3 m x 12 m (W x D) and a height of 5.7 m. By elongating the building depth from 6 m to 12 m, the first family of building geometries has an implicit (from lowest to highest location) roof inclination angle of 27° and the second family has an implicit roof inclination angle of 18°. These two families enable a comparison between, for example, single and double-span roofs, since the second family of building geometries has a depth which is equal to two times the depth of the first family of buildings.

A range of roof parameters is studied, among others the roof geometry (Figure 1.6), eaves, roof inclination angle, number of spans. Figure 1.6 distinguishes between the main categories "convex – concave" on the horizontal axis and "curved – straight" on the vertical axis. In addition, the distance from the origin of the axes system is a measure of the roof inclination angle. For all roof parameters under study, their effect on the volume flow rate and on the indoor velocity is investigated.

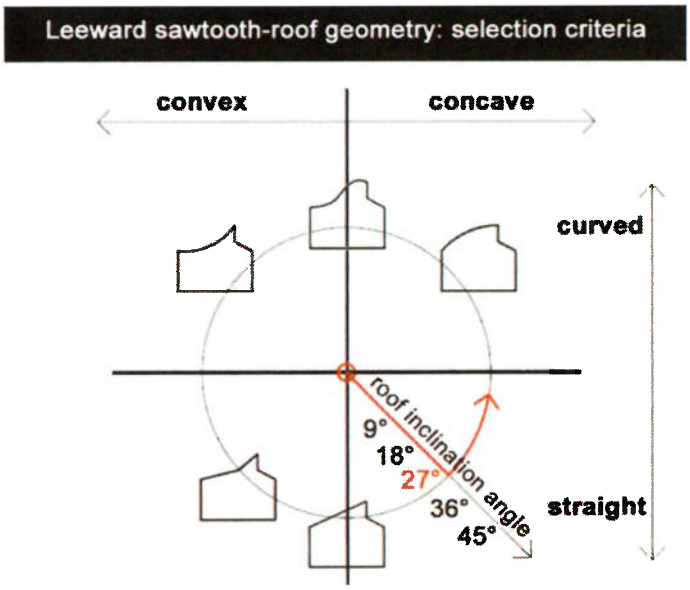

Figure 1.6: Schematic representation of the leeward sawtooth roof geometries evaluated.

1.4.2 Assessment method

For this study, 3D steady RANS Computational Fluid Dynamics (CFD) simulations are performed for a wide range of building and roof geometries. Closure of the governing equations is obtained by using the SST k-ω turbulence model by Menter [41]. The use of CFD for this analysis is required since the performance assessment of the different roof geometries is not only based on the volume flow rates through the windows, but also on the airflow pattern (velocities) inside the building resulting from the upward cross-ventilation flow. In addition, the coupled approach (e.g. [21–23,42]) is employed. The coupled approach enables a detailed analysis of the indoor and outdoor airflow by performing one CFD simulation in which the indoor and outdoor airflow are modeled simultaneously and within the same computational domain [21].

The first phase consisted of an extensive CFD validation study using the PIV measurements of Karava et al. [43], who studied wind-induced cross-ventilation for a generic isolated building model with asymmetric opening positions. The dimensions of the building model are 0.1 x 0.1 x 0.08 m^3 (W x D x H; 1:200 scale), corresponding to full-scale dimensions of 20 x 20 x 16 m^3 (W x D x H). The validation study is conducted for the building model with an inlet opening at the bottom of the windward facade (with the center of the opening at h = 0.02 m) and an outlet opening at the top of the opposite (leeward) facade (with the center of the opening at h = 0.06 m), resulting in an upward-directed cross-ventilation flow.

In the second phase, the validated CFD model was used to assess the influence of the following parameters on the volume flow rate through the building and the velocities inside the building: the roof inclination angle, the roof shape (straight, convex, concave, hybrid; see Figure 1.6), addition of eaves, and the number of spans (single vs. double-span building).

1.5 Thesis outline

This thesis consists of seven Chapters. Chapter 2 until Chapter 5 present numerical studies of the cross-ventilation performance for an isolated leeward sawtooth roof building carried out by the 3D steady RANS equations and the commercial software ANSYS Fluent [44]. Different roof and building parameters were systematically tested and are presented in each chapter. The main topic and the connection between each chapter is as follows:

Chapter 2 is based on the journal paper:

> *Perén JI, van Hooff T, Leite BCC, Blocken B. CFD analysis of cross-ventilation of a generic isolated building with asymmetric opening positions: Impact of roof angle and opening location.* ***Building and Environment*** *2015;85:263–76.*

It presents a review of the literature which indicates that the majority of the studies in natural ventilation focused on flat roofs with symmetric opening positions. A lack of research that analyzes the impact of asymmetric opening positions and roof inclination on natural ventilation potential is evident. Based on Computational Fluid Dynamics (CFD) simulations an analysis is made of the natural ventilation flow in a generic isolated building with different vertical positions of the outlet opening – yielding asymmetric opening positions – and five different roof inclination angles. The computational model is based on a grid-sensitivity analysis and on a detailed validation study using previously published wind-tunnel measurements with Particle Image Velocimetry. In the validation study, the performance of a range of turbulence models is assessed, as well as the influence of approach flow turbulent kinetic energy profile.
Chapter 3 is based on the journal paper:

> *Perén JI, van Hooff T, Ramponi R, Blocken B, Leite BCC. Impact of roof geometry of an isolated leeward sawtooth-roof building on cross-ventilation: Straight, concave, hybrid or convex?* ***Submitted*** *2015.*

In this chapter the impact of five different leeward sawtooth roof geometries is discussed: one straight, one concave, one hybrid (convex-concave) and two convex (being one convex doubled pitched and one convex fully curved). Since Chapter 2 shows that higher volume flow rates are present for higher roof inclination angles, such as 27°, all the roof shape cases evaluated in Chapter 3 have an implicit roof inclination angle of 27° (i.e. the angle measured by drawing a straight line from the windward edge of the roof to the rooftop). The computational grid is based on a grid-sensitivity analysis. A detailed analysis of the flow pattern and pressure distribution around the building is provided for a detailed analysis of the fluid mechanics.

Chapter 4 is based on the journal paper:

> *Perén JI, van Hooff T, Leite BCC, Blocken B. Impact of eaves on cross-ventilation of a generic isolated leeward sawtooth roof building: windward eaves, leeward eaves and eaves inclination.* ***Building and Environment.*** *In press 2015.*

This chapter evaluates the impact of eaves configuration on the cross-ventilation of a generic leeward sawtooth roof building, with a roof geometry equal to the one with the best performance in Chapter 3. An eaves is a roof extension that can protect the indoor environment from direct solar radiation, the exterior facade and the indoor environment from wetting by wind-driven rain, and can be applied to enhance cross-ventilation. Both the type of eaves (windward versus leeward) and the eaves inclination angles are investigated. The eaves length is 1/4 of the building depth and the inclination is varied between 90° to -45° for both the windward and leeward eaves. The best roof geometry obtained in the Chapter 3 is selected as a reference case to evaluate the potential of the eaves to increase the volume flow rate and to lead the airflow through the building. A grid-sensitivity analysis is performed and the computational settings are taken equal to those in the validation study, which is presented in detail in Chapter 2. The ventilation evaluation is based on the volume flow rates and the indoor mean velocities through the occupied zone (i.e. between 0.10 m and 1.70 m height). In addition, the flow patterns around the building are analyzed in detail.

Chapter 5 is based on the journal paper:

> *Perén JI, van Hooff T, Leite BCC, Blocken B. CFD simulations of wind-driven upward cross ventilation and its enhancement in long buildings: Impact of single-span versus double-span leeward sawtooth roof and opening ratio.* ***Submitted*** *2015.*

It compares the ventilation flow in an elongated low-rise building with a (a) single-span, and (b) double-span leeward sawtooth roof. A single-zone leeward sawtooth roof building with dimensions 3.0 x 12.0 x 5.7 m^3 (W x L x H) is selected. First, three single-span leeward sawtooth roof geometries (straight, convex and concave; roof inclination angle = 18°) are analyzed for a normal wind direction. Subsequently, the single-span cases are compared to the double-span cases. The findings presented in Chapter 3 were considered in the current evaluation as is presented in Chapter 5. For instance, the roof geometry types with the lowest and the highest performance were selected and compared for both the single-span and the double-span cases. The computational grid is based on a grid-sensitivity analysis and the computational settings are taken equal to those in the validation study presented in Chapter 2. The ventilation evaluation is based on the volume flow rates and the indoor mean velocities through the occupied zone (i.e. between 0.10 m and 1.70 m height).

Chapter 6 presents a discussion showing the limitations and recommendations for future work. Finally, Chapter 7 summarizes the main conclusions and highlights the relevant parameters of leeward sawtooth roof geometries to increase the natural ventilation flow.

Each Chapter (from 2 to 5) starts with a graph which summarizes the main parameter evaluated which is relevant to the optimization of low-rise leeward sawtooth roof buildings. To explain how all theses Chapters are logically linked, it is important to mention that Chapter 2 shows the numerical validation and the strong dependency of the volume flow rate to roof inclination angle (RIA). The results of Chapter 2 demonstrate that higher inclination angles (RIA > 18°) should be employed. However, for the other evaluations presented in Chapters 3, 4 and 5, the building height is the main constraint established (i.e. from this point a building height of 5.7 m is defined). Other constraints such as height of the inlet and outlet opening, size of the windward facade and so on, are defined as well. Whithin this number of constraints, the building height, the height of the windward facade and the horizontal position of the outlet opening limit the evaluation of roof inclination angles to angles below, or equal to 27°. Therefore, roof inclination angles larger than 27°, e.g. 36° and 45°, are not considered in Chapters 3, 4 and 5.

1.6 References

[1] Pachauri RK, Meyer L. Climate Change 2014: Synthesis Report. Contribution of Working Groups I, II and III to the Fifth Assessment Report of the Intergovernmental Panel on Climate Change. Geneva, Switzerland: IPCC; 2014.

[2] Van den Hurk B, Siegmund P, Tank AK. KNMI'14: Climate Change scenarios for the 21st Century - A Netherlands perspective. Scientific Report WR2014-01. The Netherlands: KNMI, De Bilt; 2014.

[3] Van Hooff T, Blocken B, Hensen JLM, Timmermans HJP. On the predicted effectiveness of climate adaptation measures for residential buildings. Build Environ 2014;82:300–16. doi:10.1016/j.buildenv.2014.08.027.

[4] Köppen W, Geiger R. Klima der Erde (Climate of the Earth) Wall Map 1:16 Mill Klett-Perthes, Gotha 1954.

[5] Rivero R. Arquitectura y clima. Acondicionamiento natural para el hemisferio norte. México D.F.: Universidad Autónoma de México; 1988.

[6] Lamberts R, Dutra L, Ruttkay P. Eficiência energética na arquitetura. São Paulo: 1997.

[7] Allard F, Santamouris M. Natural Ventilation in Buildings: A Design Handbook. Earthscan; 1998.

[8] Etheridge D. Natural Ventilation of Buildings: Theory, Measurement and Design. 1 edition. Chichester, West Sussex: Wiley; 2011.

[9] Santamouris M, Kolokotsa D. Passive cooling dissipation techniques for buildings and other structures: The state of the art. Energy Build 2013;57:74–94. doi:10.1016/j.enbuild.2012.11.002.

[10] Orme M. Estimates of the energy impact of ventilation and associated financial expenditures. Energy Build 2001;33:199–205. doi:10.1016/S0378-7788(00)00082-7.

[11] Liddament M. A guide to energy efficient ventilation. Air Infiltration and Ventilation Centre. Coventry (UK): Oscar Faber; 1996.

[12] Awbi HB. Ventilation of Buildings. 2 edition. London ; New York: Routledge; 2003.

[13] BS 5925 - British Standard. 1991.

[14] Peterka JA, Meroney RN, Kothari KM. Wind flow patterns about buildings. J Wind Eng Ind Aerodyn 1985;21:21–38. doi:10.1016/0167-6105(85)90031-5.

[15] Cook NJ. The Designer's guide to wind loading of building structures. vol. v.1. Butterworths, London, England.: Building Research Establishment, Department of the Environment; 1985.

[16] Hunt GR, Linden PP. The fluid mechanics of natural ventilation—displacement ventilation by buoyancy-driven flows assisted by wind. Build Environ 1999;34:707–20. doi:10.1016/S0360-1323(98)00053-5.

[17] Chen Q. Ventilation performance prediction for buildings: A method overview and recent applications. Build Environ 2009;44:848–58. doi:10.1016/j.buildenv.2008.05.025.

[18] Blocken B, Stathopoulos T, Carmeliet J, Hensen JLM. Application of computational fluid dynamics in building performance simulation for the outdoor environment: An overview. J Build Perform Simul 2011;4:157–84. doi:10.1080/19401493.2010.513740.

[19] Blocken B. Computational Fluid Dynamics for urban physics: Importance, scales, possibilities, limitations and ten tips and tricks towards accurate and reliable simulations. Build Environ n.d. doi:10.1016/j.buildenv.2015.02.015.

[20] Blocken B. 50 years of Computational Wind Engineering: Past, present and future. J Wind Eng Ind Aerodyn 2014;129:69–102. doi:10.1016/j.jweia.2014.03.008.

[21] Van Hooff T, Blocken B. Coupled urban wind flow and indoor natural ventilation modelling on a high-resolution grid: A case study for the Amsterdam Arena stadium. Environ Model Softw 2010;25:51–65. doi:10.1016/j.envsoft.2009.07.008.

[22] Kato S, Murakami S, Mochida A, Akabayashi S, Tominaga Y. Velocity-pressure field of cross ventilation with open windows analyzed by wind tunnel and numerical simulation. J Wind Eng Ind Aerodyn 1992;44:2575–86. doi:10.1016/0167-6105(92)90049-G.

[23] Horan JM, Finn DP. Sensitivity of air change rates in a naturally ventilated atrium space subject to variations in external wind speed and direction. Energy Build 2008;40:1577–85. doi:10.1016/j.enbuild.2008.02.013.

[24] Sandberg M. An Alternative View on the Theory of Cross-Ventilation. Int J Vent 2004;2:409–18.

[25] Robbins CL. Daylighting: design and analysis. Van Nostrand Reinhold Company; 1986.

[26] Gandemer J, Barnaud G. Guide sur la climatisation naturelle de l'habitat em climat tropical humide. Paris, France: CSTB; 1992.

[27] Bittencourt L. Introdução à ventilação natural nas edificações. 2nd ed. Editora da Universidade Federal de Alagoas -EDUFAL; 2006.

[28] Stathopoulos T, Saathoff P. Codification of Wind pressure coefficients for sawtooth roofs. J Wind Eng Ind Aerodyn 1992;43:1727–38. doi:16/0167-6105(92)90584-W.

[29] Cui B. Wind Effects on Monosloped and Sawtooth Roof. Thesis. Clemson University, 2007.

[30] Saathoff P, Stathopoulos, T. Wind loads on buildings with sawtooth roofs. J Struct Eng 1992;108:996–996. doi:10.1061/(ASCE)0733-9445(1993)119:3(996).

[31] Holmes JD. Wind pressures on tropical housing. J Wind Eng Ind Aerodyn 1994;53:105–23. doi:10.1016/0167-6105(94)90021-3.

[32] Pierre LMS, Kopp GA, Surry D, Ho TCE. The UWO contribution to the NIST aerodynamic database for wind loads on low buildings: Part 2. Comparison of data with wind load provisions. J Wind Eng Ind Aerodyn 2005;93:31–59. doi:10.1016/j.jweia.2004.07.007.

[33] Quan Y, Tamura Y, Matsui M. Mean wind pressure coefficients on surfaces of gable-roofed low-rise buildings. Adv Struct Eng 2007;10:259–71. doi:10.1260/136943307781422253.

[34] Holmes JD, Paterson DA. Mean wind pressures on arched-roof buildings by computation. J Wind Eng Ind Aerodyn 1993;50:235–42. doi:10.1016/0167-6105(93)90078-3.

[35] Fatnassi H, Boulard T, Poncet C, Chave M. Optimisation of Greenhouse Insect Screening with Computational Fluid Dynamics. Biosyst Eng 2006;93:301–12. doi:10.1016/j.biosystemseng.2005.11.014.

[36] Cândido C, Bittencourt L, Oliveira J, Fontan J. Avaliação da localização das aberturas de captadores de vento na ventilação natural de edificações escolares, São Paulo: 2004, p. 14.

[37] Bittencourt L, Cândido C, Batista J. A utilização de captadores de vento para aumentar a ventilação natural em espaços de sala de aula, Curitiba - PR - Brasil: 2003, p. 8.

[38] Kindangen J, Krauss G, Depecker P. Effects of Roof Shapes on Wind-Induced Air Motion Inside Buildings. Build Environ 1997;32:1–11.

[39] Kindangen JI. Window and roof configurations for comfort ventilation. Build Res Inf 1997;25:218–25. doi:10.1080/096132197370345.

[40] Bournet P-E, Boulard T. Effect of ventilator configuration on the distributed climate of greenhouses: A review of experimental and CFD studies. Comput Electron Agric 2010;74:195–217. doi:10.1016/j.compag.2010.08.007.

[41] Menter FR. Two-equation eddy-viscosity turbulence models for engineering applications. AIAA J 1994;32:1598–605.

[42] Ramponi R, Blocken B. CFD simulation of cross-ventilation for a generic isolated building: Impact of computational parameters. Build Environ 2012;53:34–48. doi:10.1016/j.buildenv.2012.01.004.
[43] Karava P, Stathopoulos T, Athienitis AK. Airflow assessment in cross-ventilated buildings with operable façade elements. Build Environ 2011;46:266–79. doi:10.1016/j.buildenv.2010.07.022.
[44] ANSYS. Fluent 12 user's guide. Lebanon: Fluent Inc. 2009.

Chapter 2

CFD analysis of cross-ventilation of a generic isolated building with asymmetric opening positions: impact of roof angle and opening location

Published as:

Perén JI, van Hooff T, Leite BCC, Blocken B. CFD analysis of cross-ventilation of a generic isolated building with asymmetric opening positions: Impact of roof angle and opening location. Building and Environment 2015;85:263–76.

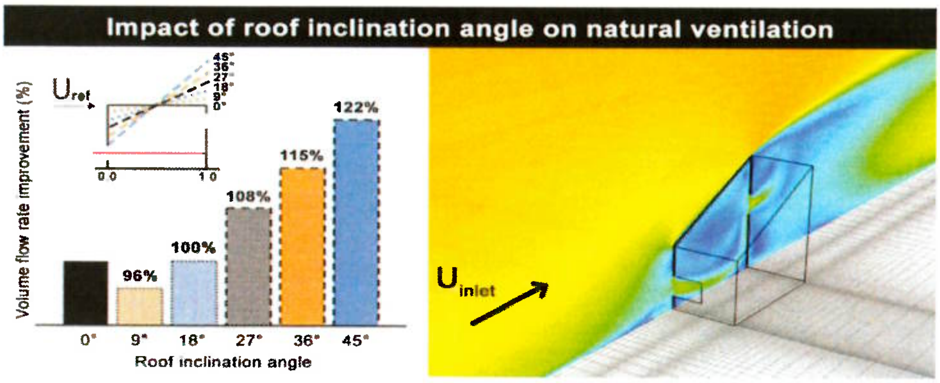

2 CFD analysis of cross-ventilation of a generic isolated building with asymmetric opening positions: impact of roof angle and opening location

Abstract

The position of window openings and roof inclination are important parameters determining the effectiveness of wind-driven cross-ventilation in buildings. Many studies on natural ventilation have been performed in the past, however, a detailed review of the literature indicates that the majority of these studies focused on flat roofs with symmetric opening positions. There is a lack of research that analyses the impact of asymmetric opening positions and roof inclination on natural ventilation potential. This paper presents Computational Fluid Dynamics (CFD) simulations to analyze the natural ventilation flow in a generic isolated building with different vertical positions of the outlet opening – yielding asymmetric opening positions – and five different roof inclination angles. The simulations are performed using the 3D steady Reynolds-Averaged Navier-Stokes (RANS) equations. They are based on a grid-sensitivity analysis and on validation with previously published wind-tunnel measurements using Particle Image Velocimetry. The results show that the shear-stress transport (SST) k-ω and the Renormalization-group (RNG) k-ε turbulence models provide the best agreement with the experimental data. It is also shown that the roof inclination angle has a significant effect on the ventilation flow; the volume flow rate increases by more than 22%. The maximum local indoor air velocity increases considerably when the inclination angle is increased, however, the differences in the average velocity in the occupied zone are only around 7%. The vertical position of the outlet opening has a relatively small impact on the volume flow rate (less than 4%), and a small influence on the average velocity in the occupied zone (< 5%).

Keywords: Computational Fluid Dynamics (CFD); Building geometry; Natural ventilation; Model validation; Urban physics; Building aerodynamics.

2.1 Introduction

A sawtooth roof on buildings can contribute to a sustainable and healthy indoor environment as it can allow additional daylight and natural ventilation compared to a standard flat roof. Sawtooth-roof buildings have lower level openings in the (windward) facade and also upper-level openings near the roof top in the opposite (leeward) facade. Using the upper-level openings located near the roof, the sawtooth roof can achieve more uniform and higher daylight intensity levels than the levels obtained by an opening located in the middle or in the lower part of a facade [1]. When the upper-level opening captures the wind the sawtooth roof is called "wind catcher" and, when it is used to extract indoor air from the building using the underpressure region in the wake of a building it is called a "leeward sawtooth roof" [2]. A sawtooth roof can be employed in different types of buildings, such as schools [3–5], low-rise industrial buildings [6] and hospitals [7]. Although sawtooth roofs have a great potential to increase natural ventilation, especially in hot climates, their design is not well explored and they are still not applied on a large scale [2].

When a sawtooth roof is oriented as leeward sawtooth roof , the wind-driven natural ventilation is improved [8] and it has several advantages compared to a flat roof: (a) it can facilitate upward cross-ventilation (low-level supply and upper-level extraction) using wind and buoyancy as driving forces for the ventilation flow; (b) it can work as part of a hybrid ventilation system, such as displacement ventilation (DV) [9] or under-floor air distribution (UFAD) system, enabling the achievement of thermal comfort in a more energy-efficient way by using wind and buoyancy as driving forces instead of fans as much as possible. The ventilation efficiency of a building with a sawtooth roof depends among others on its orientation with respect to the oncoming wind flow. In addition, the impact of many other building parameters, such as roof height and shape and inlet-outlet opening configuration (size and vertical position), have, to the best knowledge of the authors, not yet been thoroughly investigated.

Several studies have been conducted on wind-induced loads on gable roofs [10–12], arched roofs [13], mono-sloped roofs or shed roofs [14,15], various other roof geometries [16,17] and multi-span roofs such as sawtooth roofs [6,15]. The findings reported in these publications are useful for the understanding of the building aerodynamics and they provide some information on the potential for wind-driven cross-ventilation. In general, wind-driven cross-ventilation studies for low rise-buildings can be organized in four groups: (1) buildings with a flat roof and symmetric opening positions; i.e. inlet and outlet opening at the same height in the windward and leeward building facade; (2) buildings with a flat roof and asymmetric opening positions; (3) buildings with a pitched roof and symmetric opening positions; (4) buildings with a pitched roof and asymmetric opening positions. Many research efforts focused on group (1) (e.g. [18–30]). Within this group, there are studies on the effect of the opening size (wall porosity) [19,21,23,26,27,29], the inlet-outlet opening ratio and location [21,23,25,27,29] and the building aspect ratio [22,28]. Less studies focused on buildings with a flat roof and with asymmetric opening positions located in the facade (group 2); some examples are [23,25-27]. Several studies analyzed the influence of the roof shape but with symmetric opening positions (in terms of height in the facade; group 3) [31–36]. Finally, quite some studies focused on buildings with a pitched roof and asymmetric opening positions (group 4) (e.g. ([37-50]). Within this group however, only one study considered a saw-tooth roof [45].

In addition, there are some related studies on wind towers, wind catchers, venturi-shaped roofs or other constructions on the roof (e.g. [39,51–60]). This review of the literature shows that almost no studies have been conducted on the effect of roof inclination in combination with asymmetric positions of the vertical openings in the building facade.

Therefore, in this paper, the impact of the roof inclination angle and the vertical location of the outlet opening on the mean velocity pattern and volume flow rate for a generic isolated building is analyzed using Computational Fluid Dynamics (CFD). A CFD analysis is required for this study since the performance assessment of the different roof geometries is not only based on the volume flow rates through the windows, but also on the airflow pattern (velocities) inside the building resulting from the cross-ventilation flow. If only the volume flow rates would be of interest one could consider performing CFD simulations of a sealed building, and subsequently using the pressure coefficients and an estimated discharge coefficient to calculate the volume flow rates. It must be noted that the value of the discharge coefficient depends on several factors and is difficult to accurately predict. The Reynolds number, the wind direction, etc. play a role in the determination of the discharge coefficient (e.g. [61]), as well as the presence or absence of "flow contact" in case of cross ventilation through large ventilation openings. When flow contact is present jet momentum is conserved and reaches the leeward opening, resulting in different values of the discharge coefficient for the windward and leeward opening (e.g. [62,63]). In the past 50 years, CFD has developed into a powerful tool for studies in urban physics and building aerodynamics [64], including natural ventilation in buildings, as demonstrated by review and overview papers [30,64–71]. In this paper, the coupled approach (e.g. [29,30,42,47,48,50,63,72]) is employed using the 3D steady Reynolds-Averaged Navier-Stokes (RANS) equations. The coupled approach enables a detailed analysis of the indoor and outdoor airflow by performing one CFD simulation in which the indoor and outdoor airflow are modeled simultaneously and in the same computational domain. The detailed and high-quality Particle Image Velocimetry (PIV) wind-tunnel measurements provided by Karava et al. [27] for a generic isolated building with asymmetric opening positions and a flat roof are used for model validation. First, the PIV measurements are described in Section 2.2. Then, the numerical model for the validation case is presented in Section 2.3 and the validation results in Section 2.4, after which the sensitivity analyses are outlined in Section 2.5. Section 2.6 presents the CFD simulation results for the cases with the different roof inclination angles and the different vertical positions of the outlet opening in the leeward facade. Discussion and conclusions are given in Sections 2.7 and 2.8.

2.2 Wind-tunnel experiment

Karava et al. [27] carried out PIV measurements of wind-induced cross-ventilation for a generic isolated building model with a flat roof and both symmetric and asymmetric opening positions in the open-circuit boundary layer wind tunnel at Concordia University, Montreal, Canada [73]. The wind-tunnel has a test section of 1.8 x 1.8 x 12 m^3 (W x H x L). The building models were made from 2 mm cast transparent polymethyl methacrylate (PMMA) sheet at a scale of 1:200. The models had dimensions 100 x 100 x 80 mm^3 (W x D x H) (reduced-scale) corresponding to full-scale dimensions 20 x 20 x 16 m^3 (W x D x H) (Figure 2.1). The reduced-scale building-model openings had a fixed height of 18 mm (3.6 m full scale) and a variable width, providing a wall porosity (opening area divided by wall area) of 5%, 10% and 20%.

Three opening positions were considered: bottom, middle and top, with the center of the opening at h = 20 mm, 40 mm and 60 mm, respectively. In this paper, the focus is on the building model with the inlet opening at the bottom of the windward facade (center at h = 20 mm) and the outlet opening at the top of the opposite (leeward) facade (center at h = 60 mm) and with a wall porosity of 10%, as shown in Figure 2.1a,b. The PIV measurements were conducted in the vertical center plane, as indicated in Figure 2.1c. The incident mean velocity and turbulence intensity profiles were measured in the empty wind tunnel at the turntable center with a hot-film probe in the test section. Measurement and use of incident profiles rather than approach-flow profiles is important for a reliable validation study [74,75]. The reference mean wind speed U_{ref} = 6.97 m/s and a reference turbulence intensity of 10% were measured at building height (H = z_{ref}). The turbulence intensity was about 17% near ground level (12 mm) and 5% at gradient height (738 mm). The reduced-scale aerodynamic roughness length was z_0 = 0.025 mm corresponding to z_0 = 0.005 m in full scale [27]. For more information related to the wind-tunnel experiments the reader is referred to [27].

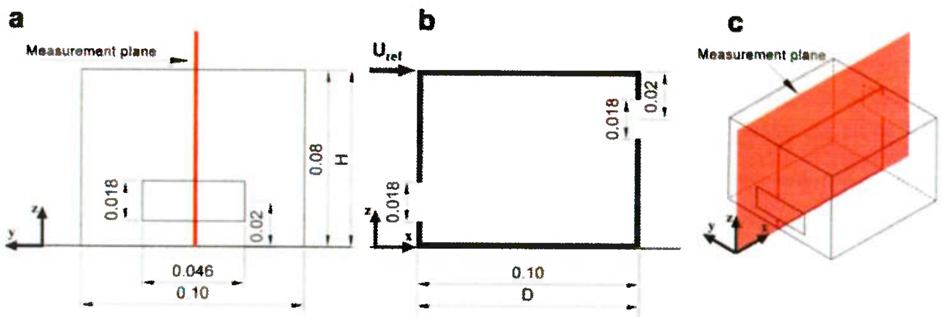

Figure 2.1: (a) Front view of the reduced-scaled building model as studied by Karava et al. [30] with opening size and dimensions (in meters). (b) Vertical cross-section of the reduced-scaled building model with opening size and dimensions (in meters). (c) Perspective indicating the measurement plane.

2.3 CFD simulations: computational settings and parameters

The computational settings and parameters for the reference case are described in this section. These settings and parameters will also be used for the sensitivity analyses (grid resolution, turbulence model, inlet turbulent kinetic energy), which will be presented in Section 2.4.

2.3.1 Computational domain and grid

The computational domain and grid are constructed at reduced scale (1:200) to exactly resemble the wind-tunnel geometry. They adhere to the best practice guidelines by Franke et al. [76] and Tominaga et al. [77], apart from the upstream length, which is reduced to 3 times the height of the building to limit the development of unintended streamwise gradients [78,79]. The dimensions of the domain are 0.9 x 1.54 x 0.48 m^3 (W x D x H) which correspond to 180 x 308 x 96 m^3 in full scale. The computational grid is fully structured and it is created using the surface-grid extrusion technique described by van Hooff and Blocken [47]. This technique allows full control of the size and shape of every grid cell and has been used successfully in previous studies for simple and complex building and urban geometries (e.g. [47,48,59,80-83]). The maximum stretching ratio is 1.2 and the first cell height is 2 mm at the building wall. A grid-sensitivity analysis is performed based on three grids (Figure 2.2c-e); coarse, basic and fine grid, with 421,088 cells, 770,540 cells (reference case), and 1,607,572 cells, respectively. The results of the grid-sensitivity analysis are presented in Section 2.5.1.

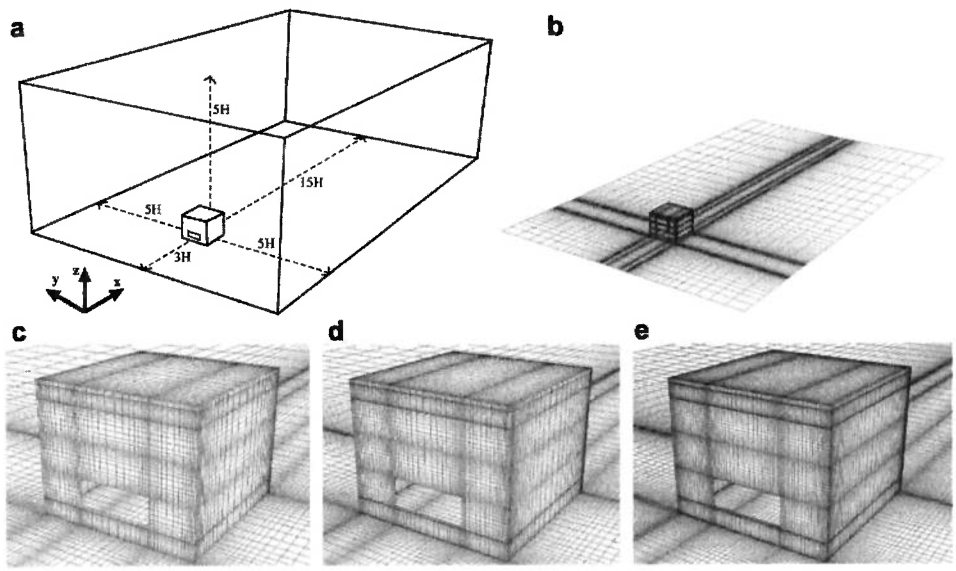

Figure 2.2: (a) Perspective view of the building in its computational domain at model scale. (b) View of the computational grid (building and ground). (c,d,e) Perspective view of grids for the grid-sensitivity analysis: (c) Coarse grid with 421,088 cells; (d) Basic grid with 770,540 cells (reference case); (e) Fine grid with 1,607,572 cells.

2.3.2 **Boundary conditions**

At the inlet of the domain the approach-flow mean wind speed and turbulence profiles are imposed based on the wind-tunnel measurements. The inlet wind-velocity profile is defined according to the logarithmic law (Eq. 1):

$$U(z) = \frac{u^*_{ABL}}{\kappa} \ln\left(\frac{z+z_0}{z_0}\right) \quad (1)$$

where z_0 is the same as in the experiment and where u^*_{ABL} is the ABL friction velocity (= 0.35 m/s) that is determined based on the values of $U_{ref,}$ and z_{ref} from the experiment. Furthermore, κ is the von Karman constant (0.42) and z the height coordinate. The turbulent kinetic energy k is calculated from the mean wind speed and the measured turbulence intensity using Eq. (2):

$$k(z) = a(I_U(z)U(z))^2 \quad (2)$$

In this equation, I_u is the measured streamwise turbulence intensity and "a" is a parameter ranging from 0.5 to 1.5 [31,77]. The sensitivity of the results to the parameter "a" is tested and presented in Section

2.4.3. For the reference case a = 0.5. The turbulence dissipation rate ε is given by Eq. (3) and the specific dissipation rate ω by Eq. (4), where C_μ is an empirical constant taken equal to 0.09.

$$\varepsilon(z) = \frac{u_{ABL}^{*3}}{\kappa(z+z_0)} \quad (3)$$

$$\omega(z) = \frac{\varepsilon(z)}{C_\mu k(z)} \quad (4)$$

At the ground and building surfaces, the standard wall functions by Launder and Spalding [84] are used in conjunction with the sand-grain based roughness modification by Cebeci and Bradshaw [85]. For the ground surfaces, the values of the roughness parameters, i.e. the sand-grain roughness height (k_S = 0.28 mm) and the roughness constant (C_S = 0.874), are determined based on their relationship with the aerodynamic roughness length z_0 derived by Blocken et al. [78] (Eq. 5). For the building surface the value of the sand-grain roughness is zero (k_S = 0).

$$k_S = \frac{9.793 z_0}{C_S} \quad (5)$$

At the outlet plane, zero static pressure is applied and at the top and lateral sides of the domain a symmetry condition is imposed, i.e. zero normal velocity and zero normal gradients of all variables. As recommended by Blocken et al. [78,79], to assess the extent of unintended streamwise gradients (i.e. horizontal inhomogeneity) in the vertical profiles of mean wind speed and turbulent properties, a simulation in an empty computational domain is made using the shear-stress transport (SST) k-ω model [86]. The vertical profiles of U, k and ε at the inlet (inlet profiles) and at the building position (incident profiles) are shown in Figure 2.3, indicating that streamwise gradients are present but limited, especially for the mean wind speed profile.

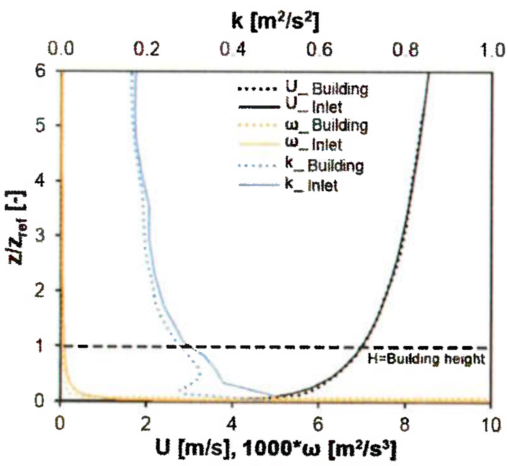

Figure 2.3: Horizontal homogeneity analysis: Profiles of the mean wind speed (U), turbulent kinetic energy (k) and specific dissipation rate (ω) at the inlet (continuous lines) and at the building position

(dotted lines) in the empty domain. The height of the model (Z_{ref}) is 0.08 m. The parameter a = 0.5 is used for the turbulent kinetic energy calculation (reference case).

2.3.3 Solver settings

The commercial CFD code ANSYS Fluent 12 [87] is used to perform the CFD simulations. The 3D steady Reynolds-Averaged Navier-Stokes (RANS) equations are solved in combination with the shear-stress transport (SST) k-ω model. The SIMPLE algorithm is used for pressure-velocity coupling, pressure interpolation is second order and second-order discretization schemes are used for both the convection terms and the viscous terms of the governing equations. Convergence is assumed to be obtained when all the scaled residuals leveled off and reached a minimum of 10^{-6} for x and y momentum, 10^{-5} for z momentum_and 10^{-4} for k, ε and continuity. As also observed by Ramponi and Blocken [29,30], the simulations showed oscillatory convergence. To obtain a reliable steady value of the solution variables, the results are monitored over 10,400 iterations and the variables are calculated by averaging over 400 iterations (10,000-10,400), after the simulation reached a statistically stationary solution.

2.4 CFD simulations: validation

The results from the CFD simulations are compared with the PIV wind-tunnel experiments by Karava et al. [27]. The mean velocity vector field in the vertical center plane by PIV measurements and CFD simulations is shown in Figure 2.4 a and 4b, respectively. The CFD simulations correctly predict the most important flow features such as the standing vortex upstream of the building and the flow pattern inside the building. Figure 2.4c and 4d compare the measured and computed streamwise wind speed ratio U/U_{ref} along a horizontal line going through the middle of the windward opening and along a diagonal line, indicating a good agreement. As pointed out by Ramponi and Blocken [30], the simulations overestimate the mean velocity around the opening, where the PIV measurements cannot provide accurate predictions due to reflections and shading effects [27]. Despite these differences an overall good agreement is observed.

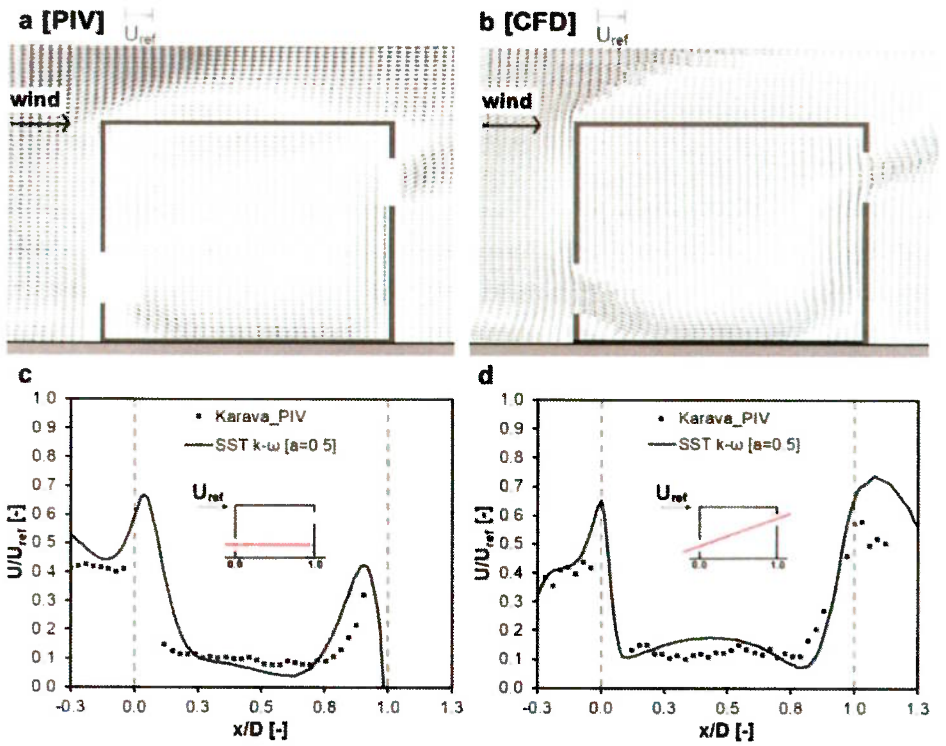

Figure 2.4: (a,b) Comparison of the mean velocity in the vertical center plane obtained from: (a) PIV measurements (processed from [30]); (b) CFD simulations. (c,d) Streamwise wind speed ratio U/U_{ref} along (c) horizontal line and (d) diagonal line.

2.5 CFD simulations: sensitivity analysis for computational parameters

A systematic sensitivity analysis for some of the computational parameters is conducted by varying one single parameter at a time compared to the reference case and comparing the results to those of the reference case. The following parameters are evaluated: (1) resolution of the computational grid (Subsection 2.4.1); (2) turbulence model (Subsection 2.4.2); and (3) inlet values of turbulent kinetic energy (Subsection 2.4.3). Table 2.1 provides an overview of the computational parameters for the sensitivity analysis with indication of the reference case in bold.

Table 2.1: Overview of computational parameters for sensitivity analysis with indication of the reference case in bold.

	Computational grid resolution (Subsection 2.5.1)	Turbulence models (Subsection 2.5.2)	Turbulent kinetic energy (Subsection 2.5.3)
Reference case	**770,540 cells (Average)**	**SST k-ω [84]** Sk-ε [86] Rk-ε [87] RNG k-ε [88,89] Sk-ω [90] RSM [91]	**a = 0.5** a = 1 a = 1.5
	421,088 cells (Coarse)	-	-
	1,607,572 cells (Fine)	-	-

2.5.1 Impact of computational grid resolution

Performing a grid-sensitivity analysis is important to minimize the discretization errors and the computation time. In this study, a grid-sensitivity analysis was performed based on three grids: (1) a coarse grid with 421,088 cells; (2) a basic grid with 770,540 cells (reference case); and (3) a fine grid with 1,607,572 cells. The two additional grids (the coarser and the finer) were constructed by coarsening and refining the average grid with about a factor √2 in each direction. Figure 2.2 shows a perspective view of the three grids. Results of the grid-sensitivity analysis are shown in Figure 2.5, in terms of the streamwise wind speed ratio (U/U_{ref}) along a horizontal line going through the middle of the windward opening (Figure 2.5a) and a diagonal line between the inlet and outlet opening (Figure 2.5b). The results indicate that the basic grid (reference grid) provides nearly grid-independent results. In addition, the difference in the ventilation flow rate through the inlet opening is about 1% between the basic grid and the fine grid, and 7% between the basic and the coarse grid. Therefore, it is concluded that the basic grid is a suitable grid for this study and this grid is used in the remainder of this paper.

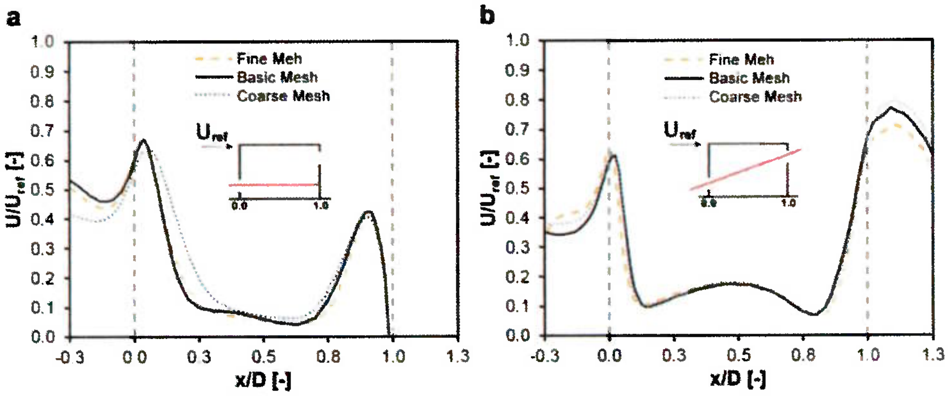

Figure 2.5: Impact of grid resolution. (a) U/U_{ref} along a horizontal centerline. (b) U/U_{ref} along a diagonal line.

2.5.2 Impact of turbulence model

Turbulence model validation is of fundamental importance for the reliability of CFD simulations. 3D steady RANS simulations are carried out in combination with six turbulence models: (1) the standard k-ε model (Sk-ε) [88]; (2) the realizable k-ε model (Rk-ε) [89]; (3) the renormalization group k-ε model (RNG k-ε) [90,91]; (4) the standard k-ω model (Sk-ω) [92]; (5) the shear-stress transport k-ω model (SST k-ω) [86]; and (6) the Reynolds Stress Model (RSM) [93]. The impact of the six different turbulence models on the streamwise wind speed ratio (U/U_{ref}) is illustrated in Figure 2.6. The SST k-ω model (reference case) and the RNG k-ε model clearly provide the best agreement with the PIV measurements. Figure 2.6a shows that the differences between the turbulence models are most pronounced inside the building around $x/D = 0.2 – 0.3$.

In terms of the volume flow rate compared to that by the SST k-ω model (reference case), (= 0.0026 m^3/s), small deviations are observed for the RNG k-ε model (0.22%), the Sk-ε model (-0.05%) and the

Sk-ω model (1.56%), with slightly larger deviations for the Rk-ε model (3.27%) and RSM (3.67%). Clearly, the volume flow rate deviations between the different turbulence models are very small. However, the deviation in indoor air velocity between the RNG k-ε and SST k-ω on the one hand, and the other turbulence models on the other hand, is very large (locally up to 300%). These large local differences can be explained by the different direction of the incoming jet flow. Note that in the majority of the previous studies on cross-ventilation in buildings with asymmetric openings, the Sk-ε turbulence model was used for the CFD simulations [25,37,39–43,45]. In addition, some studies were conducted using the RSM model (e.g. [25,40,43]), the realizable k-ε model (e.g. [25,47,48,50]), and the RNG k-ε model (e.g. [25,37,38]).

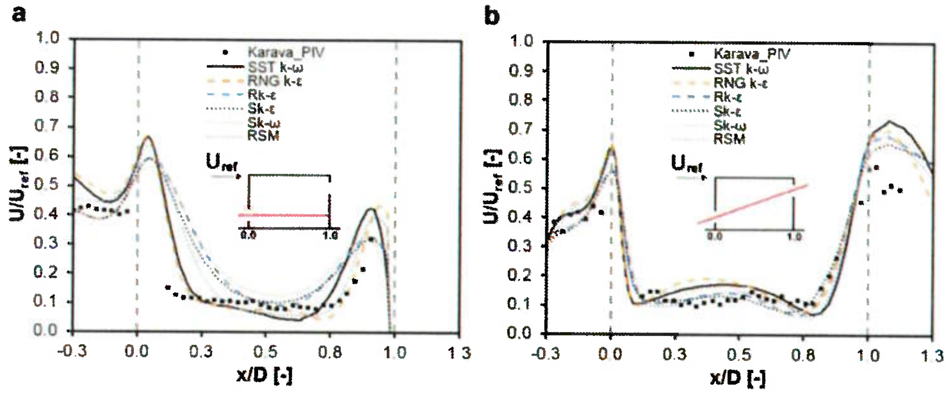

Figure 2.6: Impact of turbulence model Comparison between PIV experiments [30] and CFD with the SST k- ω, RNG k-ε, Realizable k-ε, Standard k-ε, Standard k-ω, and RSM model. (a) U/U_{ref} along a horizontal centerline; (b) U/U_{ref} along a diagonal line.

2.5.3 Impact of inlet turbulent kinetic energy

The values of turbulent kinetic energy (TKE) at the inlet of the domain can have a very large impact on the wind speed ratio inside the building [30]. The TKE profile at the inlet can be estimated from the measured wind velocity and turbulence intensity profiles. However, the turbulence intensity is often not measured is all three directions. If for example – as in this particular case - the only value measured in the wind tunnel is the longitudinal turbulence intensity ($I_u = \sigma_u/U$) this means that for the other components (σ_v and σ_w) assumptions have to be made. These assumptions can yield different values of the parameter a (in Eq. 2), ranging from 0.5 to 1.5. Here, simulations with these three values of a (0.5, 1 and 1.5) are performed and the resulting streamwise wind speed ratios (U/U_{ref}) are shown in Figure 2.7. It can be seen that there is a considerable influence of this value a on the mean velocities inside the building. Figure 2.7a clearly shows that the dimensionless velocity is overestimated inside the building for values of a larger than 0.5. The largest overestimations can be observed between $0 < x/D < 0.4$. They go up to a factor 4 when a = 1 and up to a factor 5 when a = 1.5. When a is taken equal to 1 and 1.5 the predicted volume flow rate is 7.2% and 8.7% higher than with a = 0.5, respectively. It can be concluded that the parameter a = 0.5 provides the best agreement with the experimental results. Although the best practice guidelines by Tominaga et al. [77] suggest using a = 1, and Ramponi and Blocken [30] confirmed that the value a = 1 is the best value for CFD simulations of a building with symmetric openings (inlet and outlet openings at the same height), in this particular study of a building with asymmetric opening positions (inlet and outlet opening at different heights), the most suitable value of the parameter a clearly appears to be 0.5.

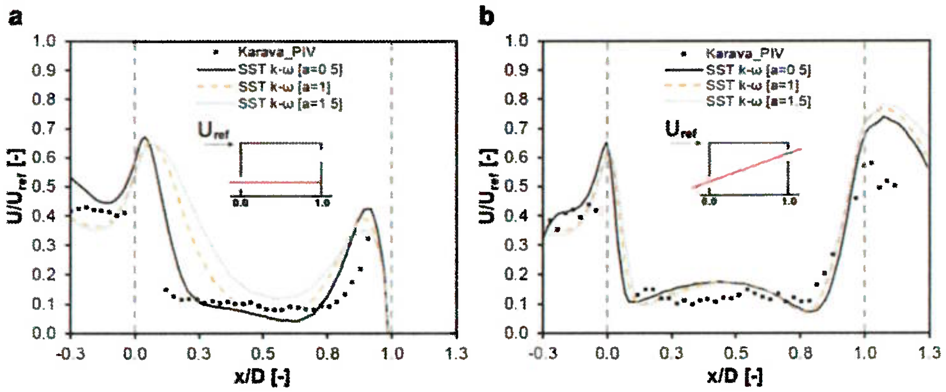

Figure 2.7: Impact of inlet turbulent kinetic energy profile parameter a: (a) U/U_{ref} along a horizontal centerline. (b) U/U_{ref} along a diagonal line.

2.6 CFD simulations: sensitivity analysis for geometrical parameters

The computational parameters and settings presented in the previous section, i.e., the basic grid resolution, the turbulence model (SST k-ω) and the parameter a (0.5), are employed in this section for the sensitivity analyses of roof inclination angle and the vertical location of the outlet opening.

2.6.1 Impact of roof inclination angle

To evaluate the impact of the roof inclination angle (RIA) on the ventilation flow, five roof inclination angles are studied for a normal wind incidence angle (φ = 0°): 9°, 18°, 27°, 36° and 45°. To allow a straightforward comparison that is not influenced by too many factors, the five cases have: (a) the same internal volume (0.0008 m^3 at reduced-scale); b) the same inlet and outlet opening size (consequently, each case has a different facade porosity); and (c) the same inlet and outlet opening location. Figure 2.8 shows the vertical cross-sections and computational grids of the reference case and the five additional cases with different roof inclination angles. Table 2.2 summarizes the cases and parameters. The cases are evaluated based on the volume flow rate and the mean wind speed ratio along a horizontal centerline going through the middle of the windward opening.

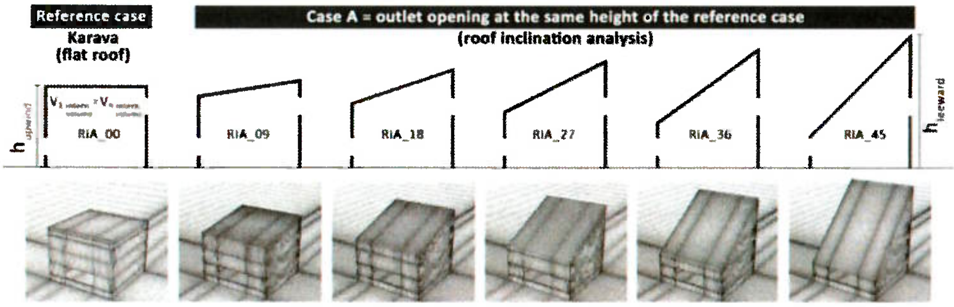

Figure 2.8: Vertical cross-section and computational grid for building geometries iwith different roof inclination angle for the "basic case", i.e. with outlet opening at the same height as in the reference case. All the cases have the same internal volume as the reference case and as a consequence have different heights of the windward (h_{upwind}) and leeward facade ($h_{leeward}$).

Table 2.2: Parameters of the leeward sawtooth roof sensitivity analysis with indication of the reference case.

	Building case name	Roof inclination angle	Outlet opening position case	
			Case A	Case B
			(Section 2.6.1)	(Section 2.6.2)
Ref. case	**RIA_00 (Karava)**	**0°**	**X**	
	RIA_09	9°	X	
	RIA_18	18°	X	
	RIA_27	27°	X	X
	RIA_36	36°	X	
	RIA_45	45°	X	X

Figure 2.9 shows that the volume flow rate increases when increasing the roof inclination angle with more than 18° compared to the reference case. However, the volume flow rate for RIA_09 is only 96% of that of RIA_00. The volume flow rate for RIA_18 is equal to that of RIA_00 (reference case). The volume flow rate for RIA_27 is 8% higher than RIA_00, for RIA_36 the increase is 15%, while for RIA_45 it is 22%.

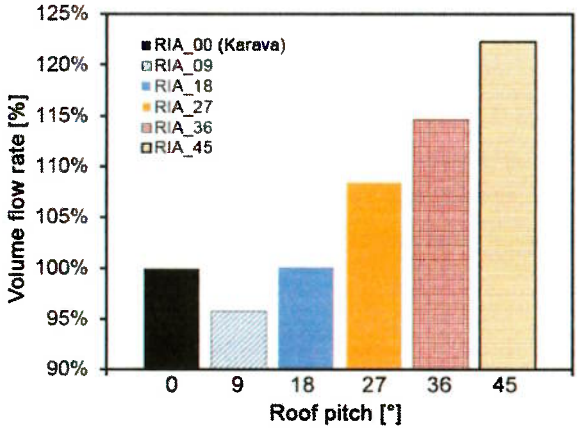

Figure 2.9: Influence of roof inclination angle (RIA) on the volume flow rate.

Figure 2.10a shows that the streamwise wind speed ratio increases along almost the entire horizontal line when the roof inclination angle is increased, except for case RIA_09. Figure 2.10b shows that the indoor mean sctreamwise wind speed ratio along the horizontal line shows very large differences between the roof inclination angles, especially between $0.1 < x/D < 0.8$. Note that although case RIA_09 has a lower volume flow rate than the reference case, the indoor air velocity along the horizontal line is higher in some areas ($0.5 < x/D < 0.7$) than in the case with the flat roof. The streamwise wind speed ratio along the centerline is also locally higher than in the reference case for case RIA_18, despite the fact that the volume flow rate is equal in both cases. However, to provide a more overall judgment of the indoor air velocities, the non-dimensional area-averaged velocity magnitude ($|V|/U_{ref}$) in the occupied zone has been calculated for the vertical center plane. The height of the occupied zone is equal to the top of the windward opening.

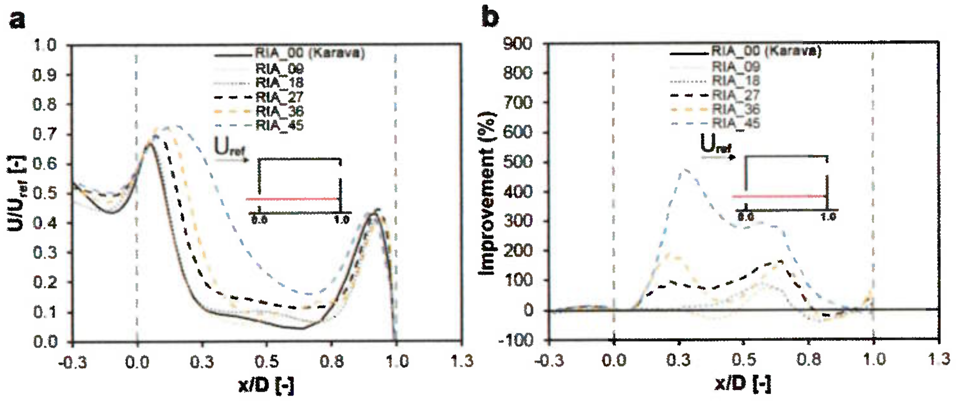

Figure 2.10: Influence of roof inclination angle. (a) U/U_{ref} along a horizontal centerline (b) Percentage increase in wind speed along the same line.

Table 2.3 provides the calculated values for all roof inclination angles. It can be seen that the non-dimensional average velocity magnitude in the occupied zone only shows small differences for the different roof inclination angles; all values are within a range of ± 7%, with the highest average velocity present for RIA_27. If the occupied zone is subdivided into two parts, a lower part (below windward window) and an upper part (from bottom to top of windward window), the effect of roof inclination angle on the jet flow direction through the window can be seen; for lower inclination angles the flow is directed more downwards, resulting in higher average velocities in the lower part of the occupied zone (up to 0.45 for RIA_09), whereas higher average velocities are present in the upper part of the occupied zone for large roof inclination angles, up to 0.34 for RIA_45.

Table 2.3: Non-dimensional area-averaged velocity magnitude ($|V|/U_{ref}$) in the occupied zone in the vertical center plane for the different roof inclination angles.

Building case name	$\|V\|/U_{ref}$ in the occupied zone in the vertical center plane		
	Entire occupied zone	Lower part	Upper part
RIA_00	0.29	0.41	0.22
RIA_09	0.31	0.45	0.23
RIA_18	0.29	0.39	0.22
RIA_27	0.33	0.41	0.28
RIA_36	0.32	0.38	0.29
RIA_45	0.32	0.29	0.34

In order to further analyze the effect of the roof inclination and facade height on the flow pattern around and inside the building in more detail, Figure 2.11 shows contours of the pressure coefficient (C_P) and of the dimensionless velocity magnitude ($|V|/U_{ref}$). The pressure coefficient is calculated as:

$$C_P = \frac{(P - P_0)}{(0.5 \rho U_{ref}{}^2)} \quad (6)$$

where P is the static pressure, P_0 the reference static pressure, ρ = 1.225 kg/m^3 the air density and U_{ref} is the approach-flow wind speed at building height (U_{ref} = 6.97 m/s at z = 0.08 m). It is shown that the overpressure above the inlet opening decreases monotonically when increasing the roof inclination angle, until the overpressures above and below the inlet opening become nearly equal. As a result of this different distribution of the pressure on the windward facade, the direction of the incoming jet flow slightly changes in each case, yielding a more horizontally oriented jet as the roof inclination angle increases. Figure 2.11 shows that the difference in underpressure behind the building between the different cases is higher than the overpressure difference in front of the building. This is an indication that the roof inclination angle is an important geometric parameter to increase wind-driven cross-ventilation.

It can be concluded that the case with a roof inclination angle of 45° results in the best ventilation performance. Nevertheless, it must be noted that this is also the case with the largest building height. Hence, building height could also be a parameter that increases the ventilation flow rate. This is in line with a previous study by Kindangen et al. [34], who found that roof height has a strong influence on the indoor airflow in buildings with wind-driven natural ventilation. However, in the study by Kindangen et al. [34], symmetric opening positions were considered (both openings at the same height).

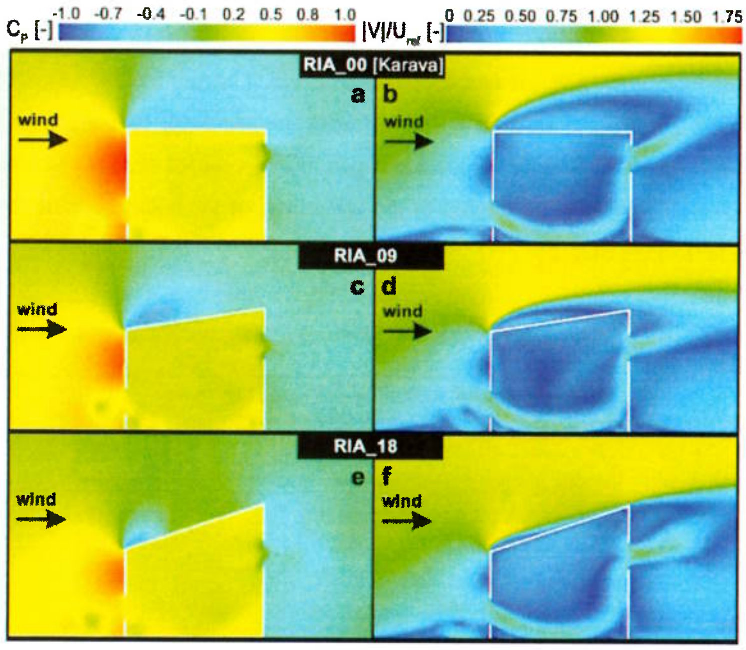

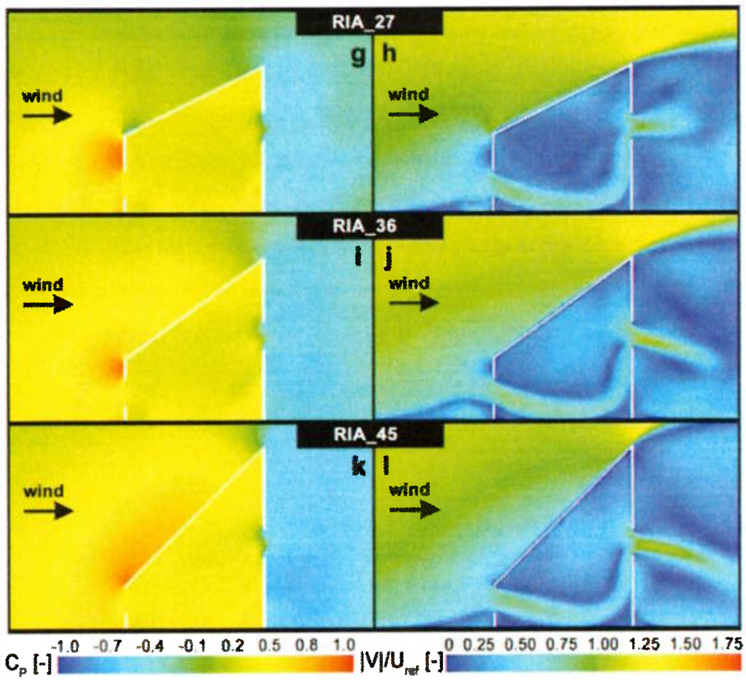

Figure 2.11: (a,c,e,g,i,k) Contours of pressure coefficient C_P in vertical center plane (b,d,f,h,j,l) Contours of non-dimensional velocity magnitude ($|V|/U_{ref}$) in vertical center plane.

2.6.2 Impact of outlet opening position

In order to evaluate the impact of the vertical position of the outlet opening, two additional cases are analyzed, RIA_27_B and RIA_45_B, and they are compared to the previously analyzed cases, RIA_27_A and RIA_45_A (Figure 2.12). For RIA_27_B and RIA_45_B, the distance between the roof and the top of the outlet opening is the same as in the reference case.

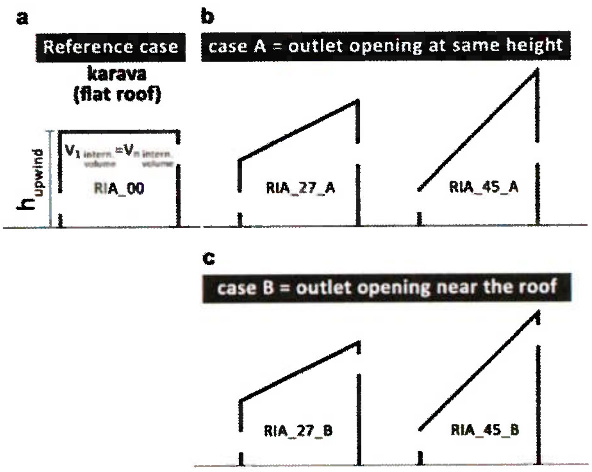

Figure 2.12: Vertical cross-section of the geometries of: (a) case RIA_00 (reference case); (b) A cases with outlet opening at the same height as the reference case: RIA_27_A and RIA_45_A; (c) B cases, with outlet opening near the roof: RIA_27_B and RIA_45_B.

The vertical position of the outlet opening only has a small impact on the volume flow rate. It increases with 4% from RIA_27_A to RIA_27_B and with 2% from RIA_45_A to RIA_45_B. Figure 2.13 shows that also the impact on the mean streamwise wind speed ratio on the horizontal center line is rather small. In addition, Table 2.4 shows the non-dimensional area-averaged velocity magnitude ($|V|/U_{ref}$) in the occupied zone in the vertical center plane for the above mentioned cases. It can be seen that the non-dimensional average velocity magnitudes in the entire occupied zone for the cases RIA_27_B and RIA_45_B are almost equal to the base case with a lower position of the leeward window; the differences between geometry A and B are 4.8% for RIA_27 and 0.4% for RIA_45.

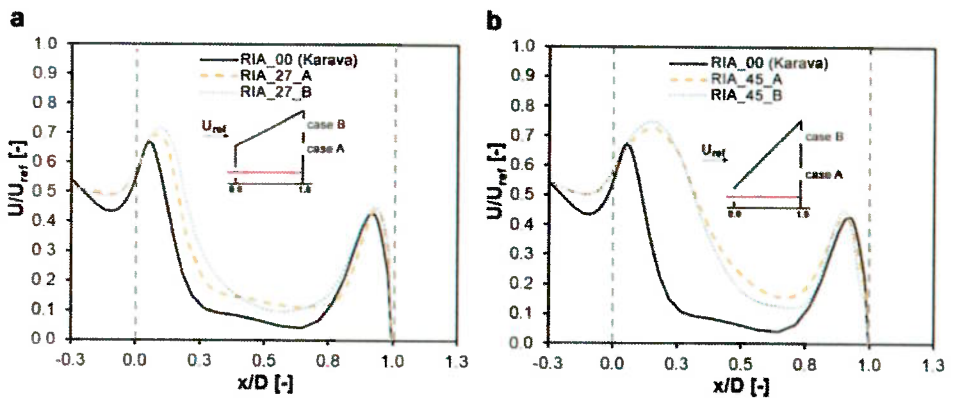

Figure 2.13: Influence of the outlet opening position on the indoor air velocity along a horizontal centerline. (a) RIA_27_B. (b) RIA_45_B.

Table 2.4: Non-dimensional area-averaged velocity magnitude ($|V|/U_{ref}$) in the occupied zone in the vertical center plane for the different leeward window opening locations.

Building case name	$|V|/U_{ref}$ in the occupied zone in the vertical center plane		
	Entire occupied zone	Lower part	Upper part
RIA_27_A	0.33	0.41	0.28
RIA_27_B	0.35	0.42	0.30
RIA_45_A	0.32	0.29	0.34
RIA_45_B	0.32	0.27	0.36

Figure 2.14 shows the pressure coefficient (C_P) and non-dimensional velocity magnitude ($|V|/U_{ref}$) in the vertical center plane for RIA_27_A, RIA_27_B. Figure 2.15 shows the same variables for RIA_45_A and RIA_45_B. There are no significant differences between RIA_27_A and RIA_27_B, and also not between RIA_45_A and RIA_45_B. This finding is in line with the observation of Lo and Novoselac [94], who pointed out that the position of the outlet opening at the leeward facade only has a small impact on the volume flow rate, however, they analyzed a position of the outlet opening that is at the same level as the inlet opening, which is not the case in the current study.

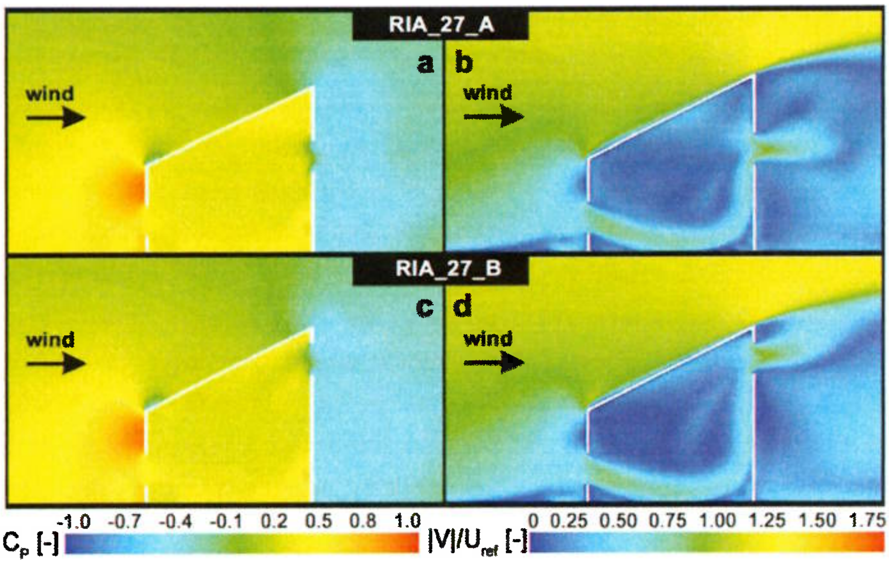

Figure 2.14: Impact of the outlet opening location: (a,b) RIA_27_A and (c,d) RIA_27_B. (a,c) Contours of pressure coefficient C_P in the vertical centerplane. (b,d) Contours of non-dimensional velocity magnitude ($|V|/U_{ref}$) in the vertical centerplane.

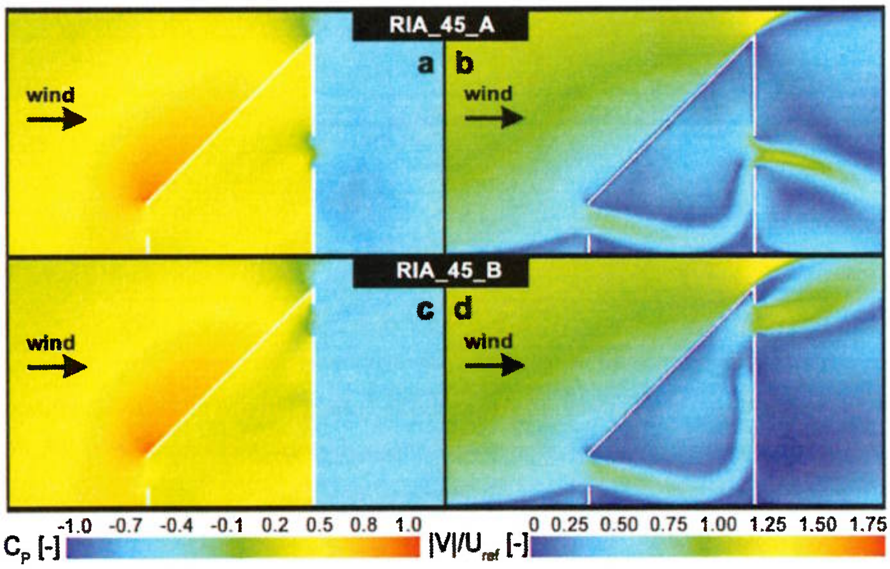

Figure 2.15: Impact of the outlet opening location for (a,b) RIA_45_A and (c,d) RIA_45_B. (a,c) Contours of pressure coefficient C_P in the vertical centerplane. (b,d) Contours of non-dimensional velocity magnitude ($|V|/U_{ref}$) in the vertical centerplane.

2.7 Discussion

2.7.1 Driving pressure differences obtained from sealed building models

In an attempt to further analyze the reason for the large differences in the volume flow rate additional CFD simulations are performed for a sealed building model of RIA_00 and RIA_45. They provide information on the surface pressure coefficients at the locations where the windward and leeward opening would be located. Table 2.5 provides the C_P values for the windward ($C_{P;w}$) and leeward ($C_{P;l}$) opening location, as well as the pressure difference over the building (ΔC_P). The pressure difference (ΔC_P) for RIA_00 is 1.15, whereas it is equal to 1.31 for case RIA_45, which is an increase of 13%. The increase in volume flow rate for case RIA_45 could therefore partly be explained by the larger pressure difference over the building, i.e. a larger ΔC_P. However, Table 2.5 also shows ΔC_P for RIA_45_B, which is equal to 1.24. This value is a bit lower than the ΔC_P = 1.31 for RIA_45_A, and would result in a lower volume flow rate for RIA_45_B when the orifice equation would be applied. However, the coupled simulations in subsection 2.6.2 indicated that the flow rate increased from RIA_45_A to RIA_45_B. This shows that the sealed-building pressure difference is not a good indicator for the actual volume flow rate. This is attributed to two reasons. First, for the different buildings, also the different flow resistance (through the openings and inside the building) will be different. Second, and probably more importantly, the sealed-building pressure difference is not necessarily equal to the actual driving pressure difference in the coupled simulation, especially for larger opening sizes (e.g. [95]). Indeed, in such cases, the sealed-building assumption does not hold (e.g. [63]). In addition, as stated in the introduction, the actual volume flow rate is difficult to obtain from the orifice equation due to the uncertainty in the discharge coefficients (e.g. [61,62,95]).

Table 2.5: Pressure coefficients (C_P) obtained from CFD simulations of a sealed building. Values reported are average C_P values over the window surface.

Building case name	Pressure coefficient C_P [-]		
	$C_{P;w}$ (windward)	$C_{P;l}$ (leeward)	ΔC_P
RIA_00 (Karava)	0.84	-0.31	1.15
RIA_45_A	0.78	-0.53	1.31
RIA_45_B	0.78	-0.46	1.24

2.7.2 Limitations and future research

The two main goals of this study on upward wind-driven cross-ventilation are: (1) to evaluate the impact of the roof inclination angle and (2) to evaluate the impact of the vertical location of the outlet opening, both for a normal wind incidence angle (φ = 0°). Five roof inclination angles are evaluated (9°, 18°, 27°, 36° and 45°) and two of these cases (27° and 45°) are also used to analyze the impact of the vertical location of the outlet opening. It is essential to mention the limitations of the current study, which should be addressed in future research:

- This study considers a simplified single zone building. The impact of other building parameters such as eaves and internal layout must be investigated.
- This study is performed for an isolated building.
- The study focuses on one wind incidence angle (φ = 0°). The ventilation performance could change for other wind incidence angles.
- In this study, the internal volume for all the cases is kept constant, however, as a consequence, each case has a different building height and a different height of the windward facade, and also a different opening area (porosity). The building height and windward facade area could be important factors in the change in volume flow rate with roof inclination angle. Additional research is needed to study the effect of wall area above and below the inlet opening, and to

better understand its effect on the overpressure region around the inlet opening and the consequences for the direction of the incoming flow.

- The simulations in this study are performed for an isothermal situation. Future work will focus on non-isothermal situations to study the effect of temperature gradients inside the building, the balance between wind and buoyancy as driving forces for the ventilation flow, and convective heat transfer inside the building.

2.8 Conclusions

This paper presents a CFD analysis to study the influence of the roof inclination angle and the vertical position of the outlet opening on the wind-driven cross-ventilation flow in a generic isolated low-rise building. CFD is chosen for this study since the different roof geometries are assessed based on both the volume flow rates through the windows, and the airflow pattern (velocities) inside the building. The simulations are based on a grid-sensitivity analysis and on validation using Particle Image Velocimetry (PIV) wind-tunnel measurements. The main conclusions of this paper are:

- The validation study shows that the SST k-ω turbulence model provides the most accurate results, followed by the RNG k-ε turbulence model. The standard k-ε model, the realizable k-ε model, the standard k-ω model and the Reynolds Stress Model show larger deviations from the measured velocities.
- The influence of the parameter "a" for the calculation of the turbulent kinetic energy profiles at the inlet of the computational domain is tested. The results show that a value of 0.5 results in the best agreement with the wind-tunnel measurements.
- The volume flow rate depends on the roof inclination angle. The building with a 45° roof inclination angle (RIA_45) provides better results than all the other cases; the volume flow rate is 22% higher than for the reference case when the outlet opening is located at the same height as in the reference case; and the volume flow rate is 25% higher when the outlet opening is located near the roof.
- The indoor air flow pattern changes with changing roof inclination angle, which also influences the velocities at horizontal lines inside the building. It is shown that the angle under which the jet enters the building through the window changes (becomes more horizontal) with increasing roof inclination angle due to a different pressure distribution on the windward facade of the building. However, the non-dimensional area-averaged velocity magnitude ($|V|/U_{ref}$) in the occupied zone for the vertical center plane only exhibits small changes up to 7%. Larger changes are found when splitting up the occupied zone in a lower and an upper part.
- To improve the volume flow rate in the studied low-rise building the roof inclination angle must be larger than 18°. For smaller roof inclination angles, such as 9°, the volume flow rate is lower than for the same building with a flat roof (reference case). It seems that the windward facade area (height) at lower roof inclination angles (9° and 18°) has a significant impact on the indoor airflow patterns and volume flow rates.
- The vertical position of the outlet opening is less important as it is shown that it can just increase the volume flow rate by around 4% and 2% for case RIA_27_B and RIA_45_B, respectively.

Furthermore, shifting the outlet opening to the top only provides small or no changes in non-dimensional ($|V|/U_{ref}$) average velocities in the occupied zone.

- Simulations for a sealed building for RIA_00 and RIA_45 show that the sealed-building pressure difference (ΔC_P) between the windward and leeward facade cannot be clearly related to the actual volume flow rates with "open" ventilation openings. This is attributed to differences in flow resistance in the different cases but especially to the invalidity of the sealed-body assumption.

2.9 Acknowledgements

This work was supported by The Coordination for the Improvement of Higher Level Personnel (CAPES), Brazil, The Engineering School of the University of São Paulo (USP), Brazil and the unit Building Physics and Services of the Department of the Built Environment at Eindhoven University of Technology in the Netherlands.

Twan van Hooff is currently a postdoctoral fellow of the Research Foundation – Flanders (FWO) and acknowledges its financial support (project FWO 12R9715N).

2.10 References

[1] Robbins CL. Daylighting: design and analysis. Van Nostrand Reinhold Company; 1986.

[2] Bittencourt L. Introdução à ventilação natural nas edificações. EDUFAL; 2006.

[3] Lima L, Bittencourt L, Cândido C, Oliveira J. Ventilação natural em edifícios escolares: avaliação da variação de altura de captadores de vento, São Paulo: 2004.

[4] Cândido C, Bittencourt L, Oliveira J, Fontan J. Avaliação da localização das aberturas de captadores de vento na ventilação natural de edificações escolares, São Paulo: 2004, p. 14.

[5] Bittencourt L, Cândido C, Batista J. A utilização de captadores de vento para aumentar a ventilação natural em espaços de sala de aula, Curitiba - PR - Brasil: 2003, p. 8.

[6] Stathopoulos T, Saathoff P. Codification of wind pressure coefficients for sawtooth roofs. J Wind Eng Ind Aerodyn 1992;43:1727–38. doi:16/0167-6105(92)90584-W.

[7] Perén JI. Ventilação e iluminação naturais na obra de João Filgueiras Lima "Lelé": estudo dos hospitais da rede Sarah Kubitschek Fortaleza e Rio de Janeiro. Universidade de São Paulo, USP-São Carlos, 2006.

[8] Gandemer J, Barnaud G. Ventilation naturelle des habitations sous climat tropical humide: Aproach aerodynamique. Nantes: CSTB; 1989.

[9] Awbi HB. Ventilation Systems: Design and Performance. Routledge; 2007.

[10] Pierre LMS, Kopp GA, Surry D, Ho TCE. The UWO contribution to the NIST aerodynamic database for wind loads on low buildings: Part 2. Comparison of data with wind load provisions. J Wind Eng Ind Aerodyn 2005;93:31–59. doi:10.1016/j.jweia.2004.07.007.

[11] Quan Y, Tamura Y, Matsui M. Mean wind pressure coefficients on surfaces of gable-roofed low-rise buildings. Adv Struct Eng 2007;10:259–71. doi:10.1260/136943307781422253.

[12] Holmes JD. Wind pressures on tropical housing. J Wind Eng Ind Aerodyn 1994;53:105–23. doi:10.1016/0167-6105(94)90021-3.

[13] Holmes JD, Paterson DA. Mean wind pressures on arched-roof buildings by computation. J Wind Eng Ind Aerodyn 1993;50:235–42. doi:10.1016/0167-6105(93)90078-3.

[14] Stathopoulos T, Mohammadian AR. Modelling of wind pressures on monoslope roofs. Eng Struct 1991;13:281–92. doi:16/0141-0296(91)90039-F.

[15] Cui B. Wind effects on monosloped and sawtooth roof. PhD Thesis. Clemson University, 2007.

[16] Stathopoulos T, Wu H. Knowledge-based wind loading for envelope design: beyond building codes. J Wind Eng Ind Aerodyn 1994;53:177–88. doi:10.1016/0167-6105(94)90025-6.

[17] Prasad D, Uliate T, Ahmed MR. Wind loads on low-rise building models with different roof configurations. Int J Fluid Mech Res 2009;36:231–43. doi:10.1615/InterJFluidMechRes.v36.i3.30.

[18] Ohba M, Irie K, Kurabuchi T. Study on airflow characteristics inside and outside a cross-ventilation model, and ventilation flow rates using wind tunnel experiments. J Wind Eng Ind Aerodyn 2001;89:1513–24. doi:10.1016/S0167-6105(01)00130-1.

[19] Karava P, Stathopoulos T, Athienitis AK. Wind driven flow through openings – A review of discharge coefficients. Int J Vent 2004;3:255–66. doi:10.5555/ijov.2004.3.3.255.

[20] Hu C-H, Kurabuchi T, Ohba M. Numerical study of cross-ventilation using two-equation RANS turbulence models. Int J Vent 2005;4:123–32.

[21] Karava P, Stathopoulos T, Athienitis AK. Impact of internal pressure coefficients on wind-driven ventilation analysis. Int J Vent 2006;5:53–66.

[22] Asfour OS, Gadi MB. A comparison between CFD and network models for predicting wind-driven ventilation in buildings. Build Environ 2007;42:4079–85. doi:10.1016/j.buildenv.2006.11.021.

[23] Karava P. Airflow prediction in buildings for natural ventilation design: wind tunnel measurements and simulation. PhD thesis. Department of Building, Civil and Environmental Engineering, Concordia University, 2008.

[24] Hu C-H, Ohba M, Yoshie R. CFD modelling of unsteady cross ventilation flows using LES. J Wind Eng Ind Aerodyn 2008;96:1692–706. doi:10.1016/j.jweia.2008.02.031.

[25] Meroney RN. CFD prediction of airflow in buildings for natural ventilation. Proc. 11th Am. Conf. Wind Eng., San Juan, Puerto Rico: 2009, p. 1–11.

[26] Karava P, Stathopoulos T. Wind-induced internal pressures in buildings with large façade openings. J Eng Mech 2012;138:358–70. doi:10.1061/(ASCE)EM.1943-7889.0000296.

[27] Karava P, Stathopoulos T, Athienitis AK. Airflow assessment in cross-ventilated buildings with operable façade elements. Build Environ 2011;46:266–79. doi:10.1016/j.buildenv.2010.07.022.

[28] Chu C-R, Chiang B-F. Wind-driven cross ventilation in long buildings. Build Environ 2014;80:150–8. doi:10.1016/j.buildenv.2014.05.017.

[29] Ramponi R, Blocken B. CFD simulation of cross-ventilation flow for different isolated building configurations: Validation with wind tunnel measurements and analysis of physical and numerical diffusion effects. J Wind Eng Ind Aerodyn 2012;104–106:408–18. doi:10.1016/j.jweia.2012.02.005.

[30] Ramponi R, Blocken B. CFD simulation of cross-ventilation for a generic isolated building: Impact of computational parameters. Build Environ 2012;53:34–48. doi:10.1016/j.buildenv.2012.01.004.

[31] Karava P, Stathopoulos T, Athienitis AK. Wind-induced natural ventilation analysis. Sol Energy 2007;81:20–30. doi:10.1016/j.solener.2006.06.013.

[32] Kobayashi T, Sandberg M, Kotani H, Claesson L. Experimental investigation and CFD analysis of cross-ventilated flow through single room detached house model. Build Environ 2010;45:2723–34. doi:10.1016/j.buildenv.2010.06.001.

[33] Kindangen J, Krauss G. Investigation of natural ventilation with Computational Fluid Dynamics: A comparison study with wind tunnel results. Archit Sci Rev 1996;39:113–20. doi:10.1080/00038628.1996.9697366.

[34] Kindangen J, Krauss G, Depecker P. Effects of roof shapes on wind-induced air motion inside buildings. Build Environ 1997;32:1–11.

[35] Kindangen JI. Window and roof configurations for comfort ventilation. Build Res Inf 1997;25:218–25. doi:10.1080/096132197370345.

[36] Bartzanas T, Boulard T, Kittas C. Numerical simulation of the airflow and temperature distribution in a tunnel greenhouse equipped with insect-proof screen in the openings. Comput Electron Agric 2002;34:207–21. doi: 10.1016/S0168-1699(01)00188-0.

[37] Mistriotis A, Bot GPA, Picuno P, Scarascia-Mugnozza G. Analysis of the efficiency of greenhouse ventilation using computational fluid dynamics. Agric For Meteorol 1997;85:217–28. doi:10.1016/S0168-1923(96)02400-8.

[38] Mistriotis A, Arcidiacono C, Picuno P, Bot GPA, Scarascia-Mugnozza G. Computational analysis of ventilation in greenhouses at zero- and low-wind-speeds. Agric For Meteorol 1997;88:121–35. doi:10.1016/S0168-1923(97)00045-2.

[39] Bartzanas T, Boulard T, Kittas C. Effect of vent arrangement on windward ventilation of a tunnel greenhouse. Biosyst Eng 2004;88:479–90. doi:10.1016/j.biosystemseng.2003.10.006.

[40] Shklyar A, Arbel A. Numerical model of the three-dimensional isothermal flow patterns and mass fluxes in a pitched-roof greenhouse. J Wind Eng Ind Aerodyn 2004;92:1039–59. doi:10.1016/j.jweia.2004.05.008.

[41] Norton T, Grant J, Fallon R, Sun D-W. Assessing the ventilation effectiveness of naturally ventilated livestock buildings under wind dominated conditions using computational fluid dynamics. Biosyst Eng 2009;103:78–99. doi:10.1016/j.biosystemseng.2009.02.007.

[42] Norton T, Grant J, Fallon R, Sun D-W. Optimising the ventilation configuration of naturally ventilated livestock buildings for improved indoor environmental homogeneity. Build Environ 2010;45:983–95. doi:10.1016/j.buildenv.2009.10.005.

[43] Kobayashi T, Chikamoto T, Osada K. Evaluation of ventilation performance of monitor roof in residential area based on simplified estimation and CFD analysis. Build Environ 2013;63:20–30. doi:10.1016/j.buildenv.2013.01.018.

[44] Gerhardt HJ, Kramer C. Aerodynamic efficiency of smoke ventilators in light streets and shed-type roofs. J Wind Eng Ind Aerodyn 1993;45:341–53. doi:10.1016/0167-6105(93)90105-W.

[45] Fatnassi H, Boulard T, Poncet C, Chave M. Optimisation of greenhouse insect screening with Computational Fluid Dynamics. Biosyst Eng 2006;93:301–12. doi:10.1016/j.biosystemseng.2005.11.014.

[46] Montero JI, Hunt GR, Kamaruddin R, Antón A, Bailey BJ. SE—Structures and environment: Effect of ventilator configuration on wind-driven ventilation in a crop protection structure for the tropics. J Agric Eng Res 2001;80:99–107. doi:10.1006/jaer.2000.0694.

[47] van Hooff T, Blocken B. Coupled urban wind flow and indoor natural ventilation modelling on a high-resolution grid: A case study for the Amsterdam Arena stadium. Environ Model Softw 2010;25:51–65. doi:10.1016/j.envsoft.2009.07.008.

[48] van Hooff T, Blocken B. On the effect of wind direction and urban surroundings on natural ventilation of a large semi-enclosed stadium. Comput Fluids 2010;39:1146–55. doi:10.1016/j.compfluid.2010.02.004.

[49] van Hooff T, Blocken B. Full-scale measurements of indoor environmental conditions and natural ventilation in a large semi-enclosed stadium: Possibilities and limitations for CFD validation. J Wind Eng Ind Aerodyn 2012;104-106:330–41. doi:10.1016/j.jweia.2012.02.009.

[50] van Hooff T, Blocken B. CFD evaluation of natural ventilation of indoor environments by the concentration decay method: CO_2 gas dispersion from a semi-enclosed stadium. Build Environ 2013;61:1–17. doi:10.1016/j.buildenv.2012.11.021.

[51] Cruz-Salas MV, Castillo JA, Huelsz G. Experimental study on natural ventilation of a room with a windward window and different wind exchangers. Energy Build 2014;84:458–65. doi:10.1016/j.enbuild.2014.08.033.

[52] Karakatsanis C, Bahadori MN, Vickery BJ. Evaluation of pressure coefficients and estimation of air flow rates in buildings employing wind towers. Sol Energy 1986;37:363–74. doi:10.1016/0038-092X(86)90132-5.

[53] Horan JM, Finn DP. Sensitivity of air change rates in a naturally ventilated atrium space subject to variations in external wind speed and direction. Energy Build 2008;40:1577–85. doi:10.1016/j.enbuild.2008.02.013.

[54] Asfour OS, Gadi MB. Using CFD to investigate ventilation characteristics of vaults as wind-inducing devices in buildings. Appl Energy 2008;85:1126–40. doi:10.1016/j.apenergy.2007.10.015.

[55] Montazeri H, Azizian R. Experimental study on natural ventilation performance of one-sided wind catcher. Build Environ 2008;43:2193–202. doi:10.1016/j.buildenv.2008.01.005.

[56] Montazeri H, Azizian R. Experimental study on natural ventilation performance of a two-sided wind catcher. Proc Inst Mech Eng Part J Power Energy 2009;223:387–400. doi:10.1243/09576509JPE651.

[57] Montazeri H, Montazeri F, Azizian R, Mostafavi S. Two-sided wind catcher performance evaluation using experimental, numerical and analytical modeling. Renew Energy 2010;35:1424–35. doi:10.1016/j.renene.2009.12.003.

[58] Montazeri H. Experimental and numerical study on natural ventilation performance of various multi-opening wind catchers. Build Environ 2011;46:370–8. doi:10.1016/j.buildenv.2010.07.031.

[59] van Hooff T, Blocken B, Aanen L, Bronsema B. A venturi-shaped roof for wind-induced natural ventilation of buildings: Wind tunnel and CFD evaluation of different design configurations. Build Environ 2011;46:1797–807. doi:16/j.buildenv.2011.02.009.

[60] Blocken B, van Hooff T, Aanen L, Bronsema B. Computational analysis of the performance of a venturi-shaped roof for natural ventilation: venturi-effect versus wind-blocking effect. Comput Fluids 2011;48(1): 202-213.

[61] Chu CR, Chiu Y-H, Chen Y-J, Wang Y-W, Chou C-P. Turbulence effects on the discharge coefficient and mean flow rate of wind-driven cross-ventilation. Build Environ 2009;44:2064-2072.

[62] True JJ, Sandberg M, Heiselberg P, Nielsen PV. Wind driven cross-flow analyzed as a catchment problem and as a pressure driven flow. Int J Vent 2003;1:88–102.

[63] Kato S, Murakami S, Mochida A, Akabayashi S, Tominaga Y. Velocity-pressure field of cross ventilation with open windows analyzed by wind tunnel and numerical simulation. J Wind Eng Ind Aerodyn 1992;44:2575–86. doi:10.1016/0167-6105(92)90049-G.

[64] Blocken B. 50 years of Computational Wind Engineering: Past, present and future. J Wind Eng Ind Aerodyn 2014;129:69–102. doi:10.1016/j.jweia.2014.03.008.

[65] Stathopoulos T. Computational wind engineering: Past achievements and future challenges. J Wind Eng Ind Aerodyn 1997;67–68:509–32. doi:10.1016/S0167-6105(97)00097-4.

[66] Blocken B, Carmeliet J. A review of wind-driven rain research in building science. J Wind Eng Ind Aerodyn 2004;92:1079–130. doi:10.1016/j.jweia.2004.06.003.

[67] Mochida A, Lun IYF. Prediction of wind environment and thermal comfort at pedestrian level in urban area. J Wind Eng Ind Aerodyn 2008;96:1498–527. doi:10.1016/j.jweia.2008.02.033.

[68] Chen Q. Ventilation performance prediction for buildings: A method overview and recent applications. Build Environ 2009;44:848–58. doi:10.1016/j.buildenv.2008.05.025.

[69] Blocken B, Stathopoulos T, Carmeliet J, Hensen JLM. Application of computational fluid dynamics in building performance simulation for the outdoor environment: An overview. J Build Perform Simul 2011;4:157–84. doi:10.1080/19401493.2010.513740.

[70] Moonen P, Defraeye T, Dorer V, Blocken B, Carmeliet J. Urban physics: effect of the microclimate on comfort, health and energy demand. Front Arch Res 2012;1:197–228.

[71] Tominaga Y, Stathopoulos T. CFD simulation of near-field pollutant dispersion in the urban environment: A review of current modeling techniques. Atmos Environ 2013;79:716–30. doi:10.1016/j.atmosenv.2013.07.028.

[72] Jiang Y, Alexander D, Jenkins H, Arthur R, Chen Q. Natural ventilation in buildings: measurement in a wind tunnel and numerical simulation with large-eddy simulation. J Wind Eng Ind Aerodyn 2003;91:331–53. doi:10.1016/S0167-6105(02)00380-X.

[73] Stathopoulos T. Design and fabrication of a wind tunnel for building aerodynamics. J Wind Eng Ind Aerodyn 1984;16:361–76. doi:10.1016/0167-6105(84)90018-7.

[74] Blocken B, Stathopoulos T, Carmeliet J. Wind environmental conditions in passages between two long narrow perpendicular buildings. J Aerosp Eng 2008;21:280–7. doi:10.1061/(ASCE)0893-1321(2008)21:4(280).

[75] Blocken B, Moonen P, Stathopoulos T, Carmeliet J. Numerical study on the existence of the venturi effect in passages between perpendicular buildings. J Eng Mech 2008;134:1021–8. doi:10.1061/(ASCE)0733-9399(2008)134:12(1021).

[76] Franke J, Hellsten A, Schlünzen H, Carissimo B. Best practice guideline for the CFD simulation of flows in the urban environment. Brussels: COST Office 2007.

[77] Tominaga Y, Mochida A, Yoshie R, Kataoka H, Nozu T, Yoshikawa M, et al. AIJ guidelines for practical applications of CFD to pedestrian wind environment around buildings. J Wind Eng Ind Aerodyn 2008;96:1749–61. doi:16/j.jweia.2008.02.058.

[78] Blocken B, Stathopoulos T, Carmeliet J. CFD simulation of the atmospheric boundary layer: wall function problems. Atmos Environ 2007;41:238–52. doi:16/j.atmosenv.2006.08.019.

[79] Blocken B, Carmeliet J, Stathopoulos T. CFD evaluation of wind speed conditions in passages between parallel buildings—effect of wall-function roughness modifications for the atmospheric boundary layer flow. J Wind Eng Ind Aerodyn 2007;95:941–62. doi:10.1016/j.jweia.2007.01.013.

[80] Gousseau P, Blocken B, Stathopoulos T, van Heijst GJF. CFD simulation of near-field pollutant dispersion on a high-resolution grid: A case study by LES and RANS for a building group in downtown Montreal. Atmos Environ 2011;45:428–38. doi:10.1016/j.atmosenv.2010.09.065.

[81] van Hooff T, Blocken B, van Harten M. 3D CFD simulations of wind flow and wind-driven rain shelter in sports stadia: Influence of stadium geometry. Build Environ 2011;46:22–37. doi:10.1016/j.buildenv.2010.06.013.

[82] Blocken B, Janssen WD, van Hooff T. CFD simulation for pedestrian wind comfort and wind safety in urban areas: General decision framework and case study for the Eindhoven University campus. Environ Model Softw 2012;30:15–34. doi:10.1016/j.envsoft.2011.11.009.

[83] Montazeri H, Blocken B, Janssen WD, van Hooff T. CFD evaluation of new second-skin facade concept for wind comfort on building balconies: Case study for the Park Tower in Antwerp. Build Environ 2013;68:179–92. doi:10.1016/j.buildenv.2013.07.004.

[84] Launder BE, Spalding DB. The numerical computation of turbulent flows. Comput Methods Appl Mech Eng 1974;3:269–89. doi:10.1016/0045-7825(74)90029-2.

[85] Cebeci T, Bradshaw P. Momentum transfer in boundary layers. Hemisphere Publishing Corp. New York: 1977.

[86] Menter FR. Two-equation eddy-viscosity turbulence models for engineering applications. AIAA J 1994;32:1598–605.

[87] ANSYS. Fluent 12 user's guide. Lebanon: Fluent Inc. 2009.

[88] Launder BE, Spalding DB. Lectures in mathematical models of turbulence. Academic Press, London, England, 1972.

[89] Shih TH, Liou WW, Shabbir A, Yang Z, Zhu J. A new k-e eddy viscosity model for high Reynolds number turbulent flows. Comput Fluids 1995;24:227–38.

[90] Yakhot V, Orszag SA, Thangam S, Gatski TB, Speziale CG. Development of turbulence models for shear flows by a double expansion technique. Phys Fluids Fluid Dyn 1992;4:1510–20. doi:doi:10.1063/1.858424.

[91] Choudhury D. Introduction to the renormalization group method and turbulence modeling. 1993.

[92] Wilcox DC. Turbulence modeling for CFD. California: DCW Industries, Inc.; 1993.

[93] Launder BE, Reece GJ, Rodi W. Progress in the development of a Reynolds-stress turbulence closure. J Fluid Mech 1975;68:537–66. doi:10.1017/S0022112075001814.

[94] Lo LJ, Novoselac A. Cross ventilation with small openings: Measurements in a multi-zone test building. Build Environ 2012;57:377–86. doi:10.1016/j.buildenv.2012.06.009.

[95] Straw MP. Computation and measurement of wind induced ventilation. PhD thesis. University of Nottingham, UK, 2000.

Chapter 3

Impact of roof geometry of an isolated leeward sawtooth roof building on cross-ventilation: Straight, concave, hybrid or convex?

Published as:

Perén JI, van Hooff T, Ramponi R, Blocken B, Leite BCC. Impact of roof geometry of an isolated leeward sawtooth roof building on cross-ventilation: Straight, concave, hybrid or convex? Submitted.

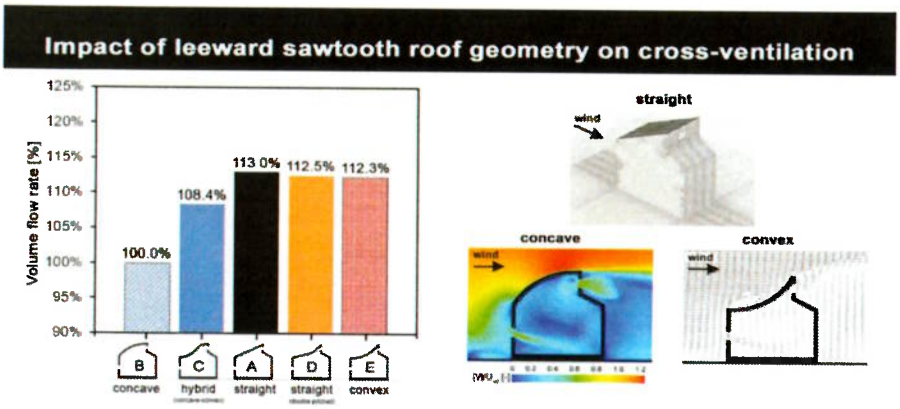

3 Impact of roof geometry of an isolated leeward sawtooth roof building on cross-ventilation: Straight, concave, hybrid or convex?

Abstract

The roof geometry of a leeward sawtooth roof building can have a large influence on the cross-ventilation flow. In this paper, five different leeward sawtooth roof geometries are evaluated using Computational Fluid Dynamics (CFD). The 3D CFD simulations are performed using the steady Reynolds-Averaged Navier-Stokes approach with the SST k-ω turbulence model to provide closure to the governing equations. The computational grid is based on a grid-sensitivity analysis and the computational model is successfully validated using PIV measurements for a generic isolated building from literature. The five different roof geometries that are studied include one straight and four curved roofs. The curved roofs can be subdivided in one concave, one hybrid (convex-concave) and two convex roof geometries. It is shown that a straight or convex roof geometry can maximize the underpressure in the wake of the building, where the outlet opening is located, which results in enhanced wind-driven cross-ventilation flow. Analysis of the results shows that for a normal wind incidence angle (0°) the straight and convex leeward sawtooth roof geometries can result in an increase of the volume flow rate by 13.0%, 12.5% and 12.3% respectively compared to a concave roof geometry. Furthermore, the increase of the indoor air velocity can be as high as 90% in the upper part of the occupied zone (at h = 1.7 m above ground level) for convex versus concave roofs.

Keywords: Computational Fluid Dynamics (CFD); Building geometry; Natural ventilation; Leeward sawtooth roof geometry; Upward cross-ventilation

3.1 Introduction

The application of a sawtooth roof on buildings can contribute to a sustainable and healthy indoor environment as it can allow additional daylight and natural ventilation compared to a standard flat roof. Often, sawtooth roof buildings have openings in the lower part of the facade and upper-level openings near the roof top in the opposite facade. Using the upper-level openings located near the roof, the sawtooth roof can achieve more uniform and higher daylight intensity levels than the levels obtained by an opening located in the middle or in the lower part of a facade (Robbins 1986). The ventilation flow in a building with a sawtooth roof depends – among others – on its orientation to the oncoming wind flow (Gandemer and Barnaud 1989). In a building with a leeward sawtooth roof, with supply openings in the bottom part of the windward facade and exhaust openings in the top part of the leeward facade, the wind-driven natural ventilation can be improved since the upward wind-driven cross-ventilation flow can be assisted by possible buoyancy forces. Although the possible advantages of a leeward sawtooth roof in naturally ventilated buildings are known, the potential of buildings with a leeward sawtooth roof has not yet been extensively explored and this type of roof is still not applied on a large scale (Bittencourt 2006). In the past, several studies have been carried out on wind-induced loads on a sawtooth roof (Saathoff and Stathopoulos 1992, Stathopoulos and Saathoff 1992, Cui 2007), gable roof (Holmes 1994, St. Pierre et al. 2005, Quan et al. 2007) and arched roof (Holmes and Paterson 1993), however, these studies did not focus on the ventilation flow of the building as function of the different roof geometries. To the best knowledge of the authors, only one study by Fatnassi et al. (2006) investigated the impact of the roof shape for buildings with asymmetric opening positions and with respect to building ventilation. In addition, Kindangen et al. (1997a, 1997b) analyzed the effect of the roof shape on natural ventilation of the building, however, all the buildings in these studies had symmetric opening positions (openings located at the same level). Furthermore, these studies were not performed for a sawtooth roof building. In general, there is a lack of knowledge on the effect of roof geometry on the airflow pattern inside cross-ventilated buildings (Kindangen et al. 1997a), which is even more pronounced for buildings with a pitched roof (either a straight or curved geometry) and with asymmetric opening positions (inlet at lower part and outlet near roof level), such as sawtooth roof buildings. A systematic study is required to quantify the effect of a range of roof geometry parameters, e.g. roof inclination, roof shape, roof overhang, roof height, as the indoor airflow is the result of the combined effect of each of these geometrical parameters. A previous paper by the authors showed that a 27° roof inclination angle with the outlet opening near the roof top can increase the volume flow rate through the building with 12% compared to a flat roof (Perén et al. 2015). However, more studies on this topic are needed to increase the understanding of the ventilation flow through these buildings, and to optimize the performance of leeward sawtooth roofs for this purpose.

The current paper analyzes the impact of straight, concave, hybrid (concave-convex) and convex leeward sawtooth roof geometries with a 27° implicit roof inclination angle (i.e. the angle measured by drawing a straight line from the windward edge of the roof to the rooftop) and with asymmetric opening positions. Figure 3.1 shows the five leeward sawtooth roof geometries that are analyzed in this paper. The main objective is to analyze which type of roof geometry can increase the volume flow rate and indoor air velocities, and eventually also the air exchange, ventilation and heat removal effectiveness. In this study, the performance of each roof geometry is evaluated based on the volume flow rate through the building and the mean air velocity ratios in the occupied zone, measured at four different heights: (h = 1.7 m, 1.1 m, 0.6 m and 0.1 m), which are considered as reference for the evaluation of thermal comfort conditions of a seated or standing person, at a steady-state and moderate environment, i.e. where the environmental conditions are close to the thermal comfort standards proposed by ISO 7730/2005 (ISO 2005). Computational Fluid Dynamics (CFD) is employed with the 3D steady Reynolds-Averaged Navier-Stokes (RANS) equations with the SST k-ω turbulence model to provide closure. The simulations are based on grid-sensitivity analysis and on validation with previously published wind-tunnel measurements.

The results presented in this paper are part of a large research project on the enhancement of wind-driven cross-ventilation of residential buildings by adjusting the roof geometry. In this research project, among others, the effect of a range of sawtooth roof geometries (this paper), roof inclination angle [14], the addition of eaves, the size of the building and the roof span on the natural ventilation flow through a single-zone building is studied. For the sake of brevity and to enable a detailed assessment of the flow behavior in and around the building resulting from modification of a certain part of the building and/or roof geometry, this paper will focus on one part of the results obtained in this larger research project, namely the effect of roof geometry.

The building geometry and roof geometries that are analyzed using CFD are presented in Section 3.2. The validation study is addressed in Section 3.3. In Section 3.4 the computational settings are described and the results of the grid-sensitivity analysis and the horizontal homogeneity test are presented. Section 3.5 shows the results of the analysis of the different roof geometries. Section 3.6 (Discussion) and Section 3.7 (Conclusions) conclude this paper.

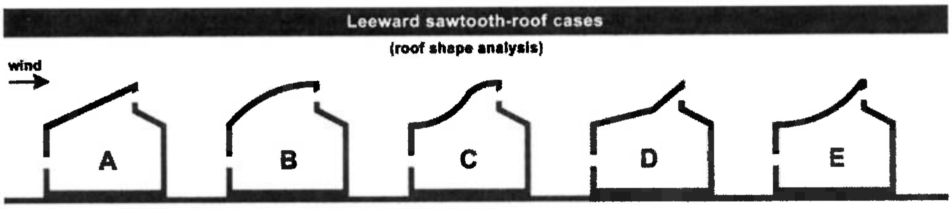

Figure 3.1: Leeward roof shapes analyzed in this paper. The five geometries have the same plan dimensions, the same maximum roof height but different internal volumes.

3.2 Building and roof geometries

Figure 3.1 shows a schematic representation of the five different roof geometries selected for this study. Each geometry is designated by a letter: A, B, C, D and E. Geometry A has a straight roof, whereas geometry B has a concave roof, C a hybrid convex-concave roof and the geometries D and E have convex roofs. Note that we adopt the definitions of "convex" and "concave" as used in the description of mathematical functions, where "a convex function is a continuous function whose value at the midpoint of every interval in its domain does not exceed the arithmetic mean of its values at the ends of the interval" (Wolfram Math World 2014). These five roof geometries have been chosen as fairly representative of the domain of different leeward sawtooth roof buildings, as schematically represented in Figure 3.2. This figure distinguishes between the main categories "convex – concave" on the horizontal axis and "curved – straight" on the vertical axis. In addition, the distance from the origin of the axes system is a measure of the roof inclination angle.

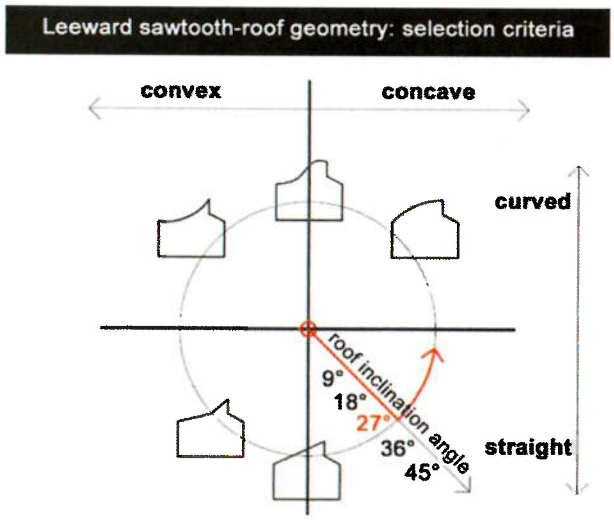

Figure 3.2: Conceptual criteria for the selection of the leeward sawtooth roof geometries

Figure 3.3 shows a front view, a vertical cross-section and a perspective view of the building with geometry A with its main dimensions. Apart from the roof shape, all five geometries have the same: (a) maximum roof height (H = 5.7 m); (b) building depth (D = 6 m); (c) building width (W = 3 m); (d) inlet and outlet opening size (corresponding to 5% windward wall porosity); and, (e) inlet and outlet opening location (the outlet is located at ¾ D). Since all five buildings have different roof shapes, each building has a different internal volume V: $V_A = 54.18$ m^3, $V_B = 60.58$ m^3, $V_C = 53.52$ m^3, $V_D = 50.78$ m^3 and $V_E = 49.91$ m^3. The distance from the ground to the bottom of the inlet and outlet opening is 1.42 m and 4.60 m, respectively.

The roof inclination and the outlet opening position are important factors that influence the volume flow rate and the mean indoor air velocities, as pointed out in a previous paper by the authors (Perén et al. 2015). However, it is important to highlight that in all five geometries, the roof has an implicit roof inclination angle of 27° and the outlet opening is located at exactly the same height near the roof top.

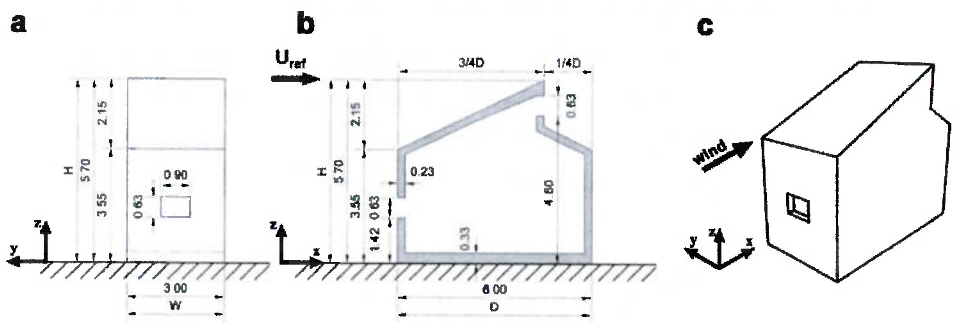

Figure 3.3: Overview of dimensions of geometry A (dimensions in m). (a) Front view (upwind facade) with opening size and dimensions. (b) Vertical cross-section with opening size and dimensions. (c) Perspective view. The other roof geometries (B-E) have the same roof height, facade porosity (inlet-outlet opening size), building depth and width; however, they have diferent roof shapes and consequently diferent internal volumes.

3.3 CFD simulations: validation study

Validation is imperative for CFD simulations in general, and more in particular for CFD simulations based on the 3D steady RANS equations (Franke et al. 2007, Tominaga et al. 2008, Blocken 2014). The CFD model employed in the current study has been validated extensively in a previous publication (Perén et al. 2015). In this section a general overview of the validation study will be provided. The reader is referred to Perén et al. (2015) for more information and an extensive analysis of the sensitivity of the results to a range of computational settings and parameters.

3.3.1 Wind-tunnel measurements

CFD validation is conducted using the PIV measurements of Karava et al. (2011) who studied wind-induced cross-ventilation for a generic isolated building model with asymmetric opening positions. The dimensions of the building model are 0.1 x 0.1 x 0.08 m^3 (W x D x H; 1:200 scale), corresponding to full-scale dimensions of 20 x 20 x 16 m^3 (W x D x H), as shown in Figure 3.4. The openings have a fixed height of 0.018 m (3.6 m full scale) while the width varies to obtain different wall porosities. The validation study is conducted for the building model with an inlet opening at the bottom of the windward facade (with the center of the opening at h = 0.02 m) and an outlet opening at the top of the opposite (leeward) facade (with the center of the opening at h = 0.06 m). The dimensions of the window are 0.046 x 0.018 m^2 (W x H) and the resulting wall porosity is 10%. The reduced-scale aerodynamic roughness length was $z_0 = 0.025$ mm corresponding to 0.005 m in full scale (Karava et al. 2011). The reference mean wind speed at building height (z_{ref}) was $U_{ref} = 6.97$ m/s and the turbulence intensity at building height was 10%. The turbulence intensity was about 17% near ground level (12 mm) and 5% at gradient height (738 mm). The PIV measurements were conducted in the vertical center plane. For more information related to the wind-tunnel experiments the reader is referred to (Karava et al. 2011).

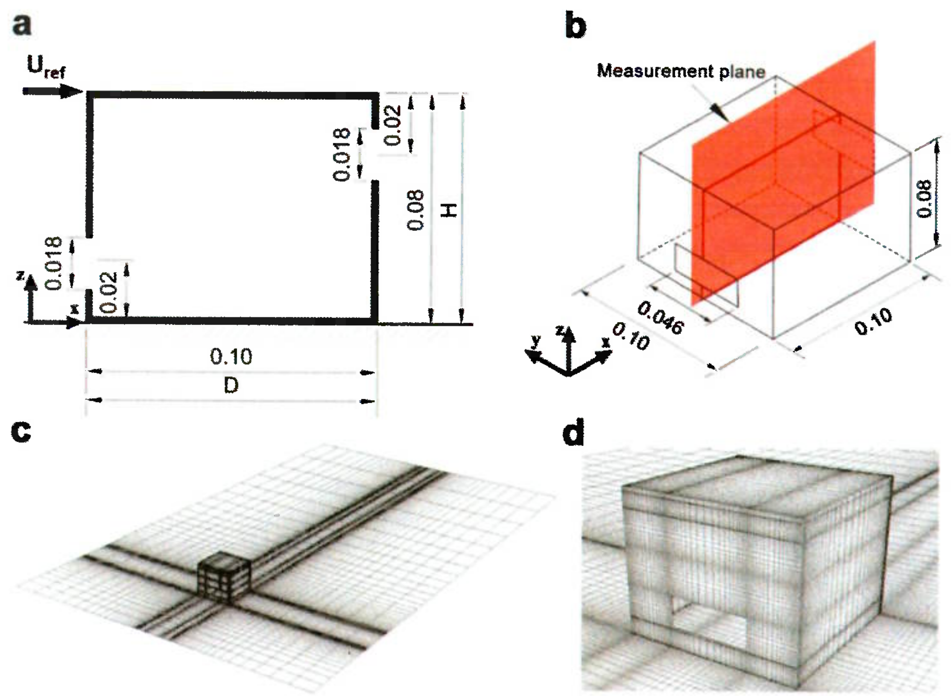

Figure 3.4: (a) Vertical cross-section of the reduced-scaled building model as studied by Karava et al. [17] with opening size and dimensions (in meter). (b) Perspective view indicating the measurement plane with dimensions (in meter). (c) View of the computational grid on the building and ground surfaces. (d) Close-up view of the grid (total number of cells: 770,540).

3.3.2 CFD simulations: computational settings and parameters

The computational model represents the reduced-scale model used in the experiments and follows the best practice guidelines by Franke et al. (2007) and Tominaga et al. (2008). The upstream length of the domain is reduced to 3 times the height of the building to limit the development of unintended streamwise gradients (Blocken et al. 2007a, 2007b, 2015). The dimensions of the domain are 0.9 x 1.54 x 0.48 m^3 (W x D x H). The computational grid is created using the surface-grid extrusion technique by van Hooff and Blocken (2010a) and is shown in Figure 3.4c and Figure 3.4d. The grid resolution resulted from a grid-sensitivity analysis yielding a fully structured hexahedral grid with 770,540 cells. The number of cells per building edge is 27 in the streamwise direction, 43 in the lateral direction and 61 in the vertical direction. The average height of the cells adjacent to the walls is 1 mm and the y^+ values of the cells near the wall inside the building are between 1 and 17. At the inlet of the domain the approach-flow vertical profiles (log-law mean wind speed U, turbulent kinetic energy k and the specific dissipation rate ω) are imposed, based on the incident vertical profiles of mean wind speed U and longitudinal turbulence Intensity I_U as measured in the wind-tunnel experiment. The turbulent kinetic energy k is calculated from the measured wind speed and turbulence intensity as $k = a(UI_U)^2$ where the coefficient "a" is equal to 0.5according to a sensitivity analysis by the authors (Perén et al. 2015), assuming that the turbulent fluctuations in streamwise direction are much larger than those in lateral and vertical direction ($\sigma_u \gg \sigma_v$ and $\sigma_u \gg \sigma_w$).

The commercial CFD code ANSYS Fluent 12 is used to perform the simulations (ANSYS 2009). The 3D steady Reynolds-Averaged Navier-Stokes (RANS) equations are solved in combination with the shear-stress transport (SST) k-ω model (Menter 1994) and automated wall treatment (Ansys 2009). This model is chosen based on previous validation studies of cross-ventilation (Perén et al. 2015, Ramponi and Blocken 2012). For pressure-velocity coupling the SIMPLE algorithm is used, pressure interpolation is second order and second-order discretization schemes are used for both the convection terms and the viscous terms of the governing equations. Convergence is assumed to be obtained when all the scaled residuals leveled off and reached a minimum of 10^{-6} for x, y momentum, 10^{-5} for y momentum and 10^{-4} for k, ε and continuity. As in previous studies of cross-ventilation of single-zone buildings (Perén et al. 2015, Ramponi and Blocken 2012), oscillatory convergence was observed. Oscillatory convergence implies that the scaled residuals do not reach an asymptote but show oscillatory behavior about an asymptotic value. This is caused by the intrinsic discrepancy of forcing an inherently unsteady flow to be predicted with a steady RANS model. It is important to note that this does not mean that the approach is flawed. On the contrary, if acknowledged and treated carefully and appropriately, as part of best practice in CFD (Blocken 2015), results from oscillatory convergence simulations with steady RANS can provide very accurate predictions of mean velocity fields, as shown in (Ramponi and Blocken 2012, Perén et al. 2015). Appropriate treatment refers to identification of the presence of oscillatory convergence and of averaging the results over a sufficient number of iterations. This is required because the results at different iterations actually correspond to different modes of the actual transient flow pattern (Blocken 2015). Note that the local oscillations in the velocities were in general within 10%, where the highest oscillations occurred in areas with low velocities. Therefore, in order to obtain reliable stationary values of the solution variables in the entire flow domain, the results are monitored over 10,400 iterations and the variables are calculated by averaging over 400 iterations (10,000-10,400), after the simulation reached a statistically stationary solution. More information on the presence and effects of oscillatory convergence can be found in (Ramponi and Blocken 2012, Blocken 2015).

3.3.3 CFD validation results: comparison between CFD simulations and wind-tunnel measurements

Figure 3.5a and Figure 3.5b display the mean velocity vector field in the vertical center plane obtained from PIV measurements and CFD simulations, respectively. It is observed that the CFD simulations correctly predict the most important flow features such as the standing vortex upstream of the building and the flow pattern inside the building. Figure 3.5c and Figure 3.5d compare the measured and computed streamwise wind speed ratio U/U_{ref} along a horizontal line going through the middle of the windward opening and along a diagonal line, respectively. It can be concluded that the computational model provides a good agreement with the experimental data. The computational settings and parameters used in this validation study will therefore be used for the evaluation of natural ventilation flow of the buildings with different leeward sawtooth roof geometries, as presented in Section 3.4 (settings and parameters) and Section 3.5 (results).

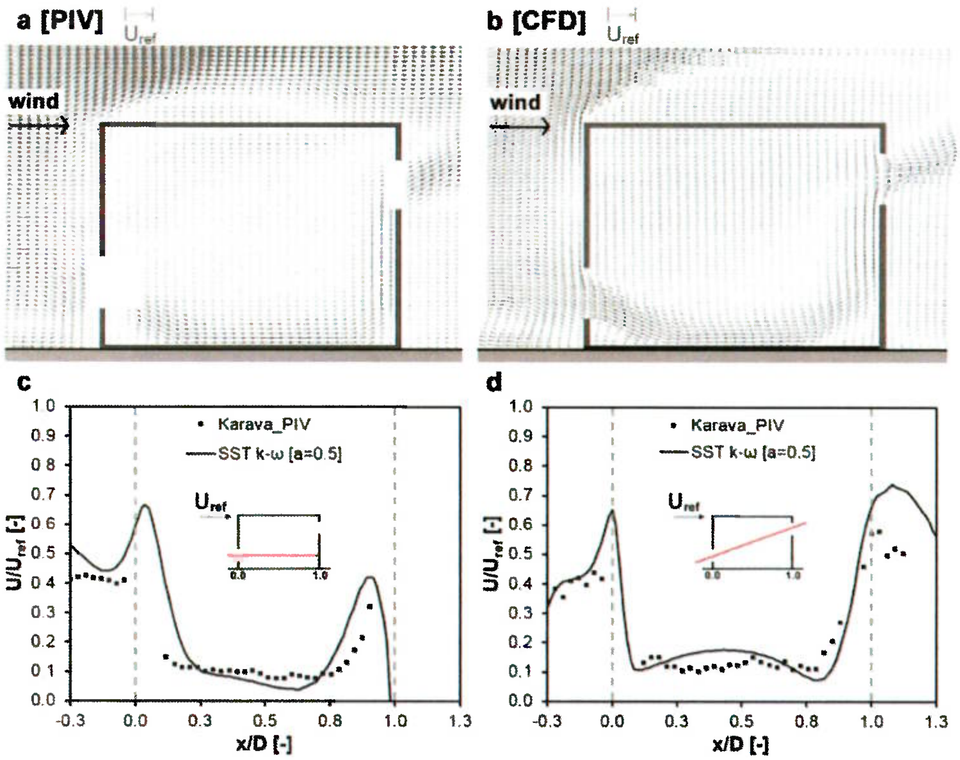

Figure 3.5: (a,b) Comparison of the mean velocity in the vertical center plane obtained from: (a) PIV measurements (processed from [18]); (b) CFD simulation. (c,d) Streamwise wind speed ratio U/U_{ref} from PIV measurements and CFD simulation along: (c) horizontal line; and (d) diagonal line.

3.4 CFD simulations of different roof geometries: computational settings and parameters

3.4.1 Computational geometry, domain and grid

The computational model of the building has dimensions as indicated in Section 3.2 and Figure 3.3. The computational domain is depicted in Figure 3.6a and its dimensions are in accordance to the best practice guidelines by Franke et al. (2007) and Tominaga et al. (2008). To limit the development of unintended streamwise gradients the upstream length of the domain is reduced to 3 times the height of the building (Blocken et al. 2007a, 2007b, Blocken 2015). The dimensions of the domain are 88.35 x 34.20 x 30 m^3 (W x D x H). Note that the simulations presented in this section are performed at full scale, which is in contrast to the validation study presented in Section 3.3, to allow a more easy interpretation of the results. In addition, if thermal effects will be included in future research, full-scale CFD simulations are imperative for dynamic similarity (Reynolds, Grashof and Archimedes numbers). To assess the influence of the scale at which the simulations of the different roof geometries are conducted, one simulation is also performed at reduced scale. The flow pattern and the qualitative results are identical to the results of the full-scale simulation, which can be attributed to the high building Reynolds numbers associated with the flow at both scales; at reduced-scale (1:15) corresponding to a building height similar to the one present in the validation study ($\approx$ 0.10 m), the building Reynolds number equals 94,158, which is much larger than the recommended value of Re > 11,000 by Snyder (1981).

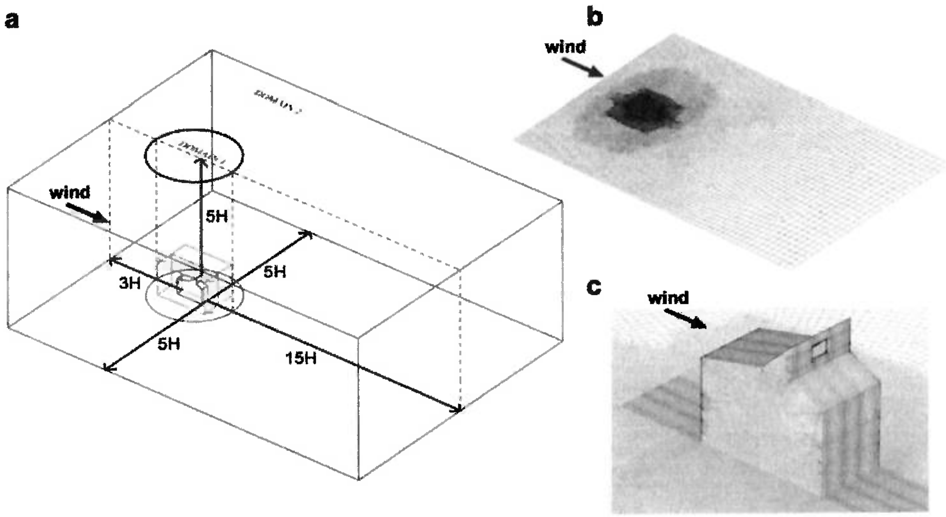

Figure 3.6: (a) Computational domain and (b, c) basic grid for geometry D on building and ground surfaces (total number of cells: 1,961,524).

A non-conformal mesh is used in order to allow future CFD simulations for different wind incidence angles. The computational grid with hexahedral cells is created using the surface-grid extrusion technique by van Hooff and Blocken (2010a) that was also successfully employed in other studies for complex building geometries (e.g. (van Hooff en Blocken 2010b, Gousseau et al. 2011, Blocken et al. 2012, Janssen et al. 2013, Montazeri et al. 2013). The maximum stretching ratio is 1.2. A grid-sensitivity analysis is performed for geometry D based on three grids and the results are presented in Section 3.4.4. Figure 3.7 shows the vertical cross-sections and the computational grids of the five different roof geometries. The number of cells varies slightly for each geometry and ranges from 2.0 to 2.7 million cells.

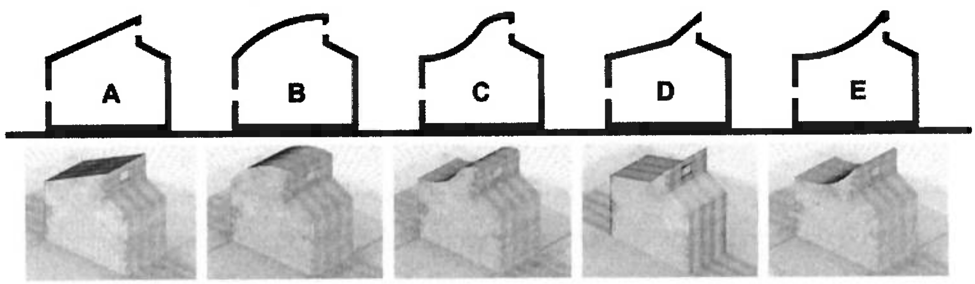

Figure 3.7: Vertical cross-section of leeward sawtooth roof buildings and part of the computational grid on the building and ground surfaces for each of the geometries. The number of cells for each geometry is based on a grid-sensitivity analysis for geometry D (1,961,524 cells) and varies slightly for each geometry.

3.4.2 Boundary conditions

At the inlet of the domain, the approach-flow mean wind speed profile and the profiles of the turbulent kinetic energy (k) and the specific dissipation rate (ω) are imposed. The wind direction is perpendicular to the windward building facade. The inlet wind-velocity profile U(z) is defined according to the logarithmic law (Eq. 1):

$$U(z) = \frac{u^*_{ABL}}{\kappa} \ln\left(\frac{z+z_0}{z_0}\right) \quad (1)$$

with $z_0 = 0.1$ m, u^*_{ABL} is the ABL friction velocity, κ is the von Karman constant (0.42) and z the height coordinate. The value of u^*_{ABL} is determined based on the values of the reference velocity (U_{ref}) at building height (H), which are U_{ref} = 12.48 m/s, H = 5.7 m, yielding a building Reynolds number of 500,000. Note that the aerodynamic roughness length is higher than in the validation study to represent a more realistic wind velocity profile, corresponding to "roughly open country" according to the updated Davenport roughness classification by Wieringa (1992). The turbulent kinetic energy k is calculated from the mean wind speed U(z) and the streamwise turbulence intensity $I_u(z)$ (with a value of 15% at the top of the building model (at z_{ref}) and 45% at ground level) by Eq. (2):

$$k(z) = a(I_U(z)U(z))^2 \quad (2)$$

In this equation "a" is taken equal to 0.5 as in the validation study. The specific dissipation rate ω is given by Eq. (3), where C_μ is an empirical constant (= 0.09), and ε is the turbulence dissipation rate given by Eq. (4).

$$\omega(z) = \frac{\varepsilon(z)}{C_\mu k(z)} \quad (3)$$

$$\varepsilon(z) = \frac{u^{*3}_{ABL}}{\kappa(z+z_0)} \quad (4)$$

The SST k-ω model uses an automated wall treatment (Ansys 2009) for the ground and building surfaces, which automatically switches between low-Reynolds number modelling and standard wall functions (Launder and Spalding 1974) in conjunction with the sand-grain based roughness (k_S) modification defined by Cebeci and Bradshaw (1977) depending on the mesh resolution near the wall. For the ground surfaces, the values of the roughness parameters, i.e. the sand-grain roughness height (k_s = 0.14 m) and the roughness constant (C_s = 7), are determined based on the relationship with the aerodynamic roughness length z_0 derived by Blocken et al. (2007a):

$$k_S = \frac{9.793 z_0}{C_S} \quad (5)$$

For the building surface the value of the sand-grain roughness is zero ($k_S = 0$ m), which corresponds to a smooth wall. This choice was based on previous parametric CFD studies with k_S values of 0 m, 0.01 m and 0.05 m, which showed no notable differences for the ventilation flow rates (van Hooff and Blocken 2010b). At the outlet plane, zero static gauge pressure is applied and at the top and lateral sides of the domain a symmetry condition is imposed, i.e. zero normal velocity and zero normal gradients of all variables. A simulation in an empty computational domain is performed to assess the extent of unintended streamwise gradients (i.e. horizontal inhomogeneity) in the vertical mean-wind speed profile and the turbulence profiles. Figure 3.8 shows the vertical profiles of U, k and ω at the inlet (inlet profiles) and at the location where the building will be positioned (incident profiles). It can be seen that streamwise gradients are absent for the mean wind speed profile. The profiles of k and ω do show some streamwise gradients however, for k up to 60% at building height. This is a large difference. However, this does not compromise the value of this study, for several reasons: (i) First, a similar decay will also occur in reality when an approaching atmospheric boundary layer flow over rough terrain suddenly encounters a much smoother terrain upstream of the building. As such, this decay is a realistic occurrence. (ii) Second, the focus of this study is on the comparison between the performance of difference roof geometries. As such, the comparative evaluation is more important than the absolute values obtained.

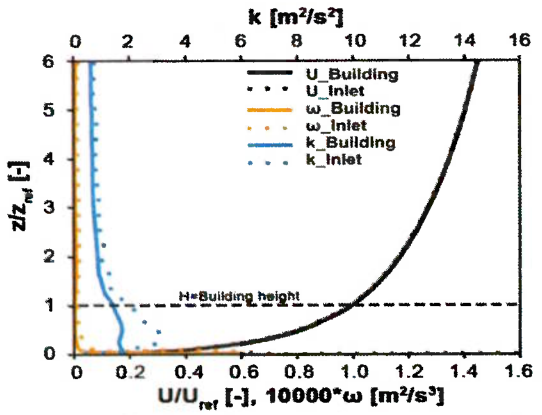

Figure 3.8: Horizontal homogeneity analysis: profiles of mean wind speed (U), turbulent kinetic energy (k) and specific dissipation rate (ω) at the inlet (dashed line) and at the building position (solid line) in an empty domain. The height of the model ($H = z_{ref}$) is 5.7 m.

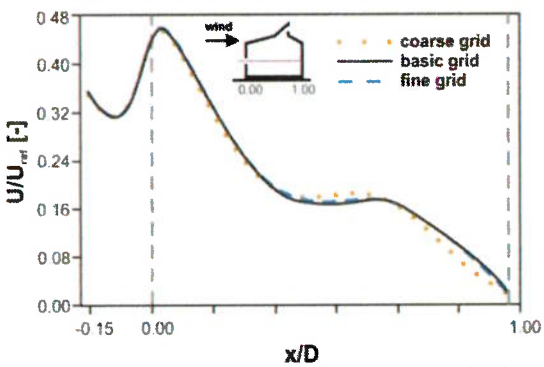

Figure 3.9: Results of grid-sensitivity analysis: impact of the grid resolution on the streamwise wind speed ratio U/U_{ref} along a horizontal line through the middle of the windward opening.

3.4.3 Solver settings

The commercial CFD code ANSYS Fluent 12 (2009) and the 3D steady RANS equations are employed for the analysis of the different roof geometries. Apart from the computational geometry and grid, the computational settings, parameters and the convergence criteria are taken equal to those of the numerical validation study as presented in Section 3.3.2.

3.4.4 Grid-sensitivity analysis

A grid-sensitivity analysis is performed for geometry D based on three grids: (1) a coarse grid with 1,012,336 cells; (2) a basic grid with 1,961,524 cells; and (3) a fine grid with 4,028,476 cells. The two additional grids (basic and the fine grid) are constructed by refining the coarse grid with about a linear factor $2^{1/3}$. Figure 3.9 shows dimensionless velocity magnitude ($|V|/U_{ref}$) at a horizontal line through the middle of the windward opening of the building obtained with the three different grids. It is shown that the basic grid provides nearly grid-independent results. Also in terms of ventilation flow rates there are only very small differences between the three different grids; i.e the volume flow rates are within 1.6% (coarse grid) and 1.1% (basic grid) compared with the finest grid. Therefore, it is concluded that the basic grid is a suitable grid for this study and it is used for the other simulations presented in this paper. The average height of the wall-adjacent cells in this basic grid is 0.07 m and the y^+ values of the cells inside the building are between 1 and 35.

3.5 CFD simulations of different roof geometries: results

The ventilative performance of the five different roof geometries is assessed based on the volume flow rate through the openings and the average dimensionless velocity magnitude ($|V|/U_{ref}$) along four horizontal lines at four different heights (h) from the ground floor; i.e. h = 1.7 m, 1.1 m, 0.6 m, and 0.1 m. In addition, the airflow pattern around and inside the building is analyzed.

3.5.1 Volume flow rate

Figure 3.10a shows the volume flow rate in percentage (%), in which geometry B is taken as the reference case (= 100%) since it has the lowest volume flow rate (= 2.54 m^3/s). The volume flow rate through the inlet opening of the building is obtained by taking the surface integral of the velocity at the inlet opening surface. The building with roof geometry A and the buildings with a convex roof geometry (i.e. D and E) have almost equal volume flow rates, which are respectively 13.0%, 12.5% and 12.3% higher than that of geometry B. The building with a hybrid convex-concave roof geometry (geometry C) has a 8.4% higher volume flow rate than geometry B. Figure 3.10b shows the area-weighted average of the pressure coefficient (C_P) at the outlet opening surface for all five geometries. It can be seen that the roof geometries which result in higher volume flow rates are the geometries with higher underpressure values (i.e. straight roof geometry A with C_P = -0.27; and convex roof geometries D with C_P = -0.29 and E with C_P = -0.29). There is, as expected, a clear relation between the average pressure coefficient and the volume flow rate, as depicted in Figure 3.10.

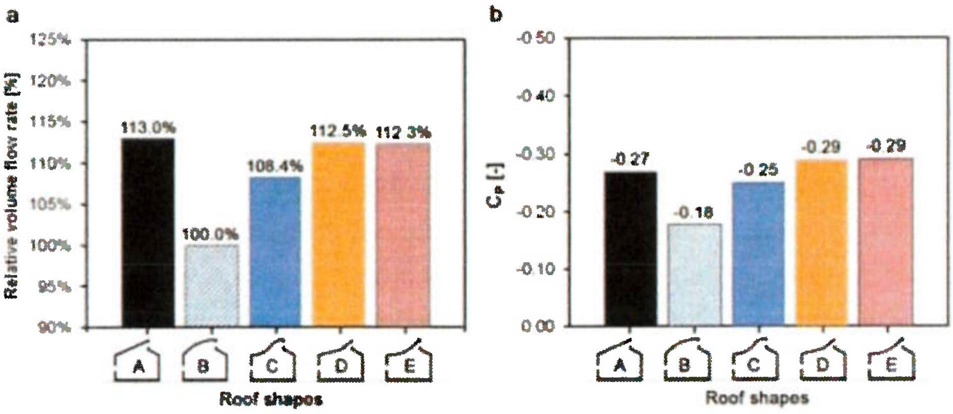

Figure 3.10: Impact of roof geometry on the volume flow rate and the average pressure coefficient at the outlet opening for a normal wind incidence angle. (a) Volume flow rate. The volume flow rate for geometry B is taken as the reference case (= 100%). (b) Pressure coefficient C_P.

3.5.2 Indoor airflow

The impact of the roof shape on the dimensionless velocity magnitude ($|V|/U_{ref}$), along four horizontal lines located at a height h of 1.7 m, 1.1 m, 0.6 m and 0.1 m from the internal floor, as shown in Figure 3.11, is evaluated . The four heights correspond to the positions of the parts of the body (head, chest, legs and feet) of a seated or standing person, which are reference heights for thermal comfort evaluation in an occupied zone of a building (ISO 2005). Figure 3.11b shows that the five different roof geometries result in roughly the same velocity profiles at h = 1.7 m. However, locally, large velocity differences can occur; up to 90% between geometry D and B at x/D = 0.7. At h = 1.1 m, geometries A and D have slightly higher velocities from $0.15 < x < 0.80$. (Figure 3.11c). At h = 0.6 m, geometry E has the highest local velocity from $0.30 < x < 0.70$, but also the lowest from $0.0 < x < 0.3$ and from $0.85 < x < 1.00$ (Figure 3.11d). In general, at h = 1.7 m, 1.1 m and 0.6 m, the concave geometries B and C result in lower indoor air velocities (Figure 3.11b, Figure 3.11c and Figure 3.11d), however, at h = 0.1 m geometries B and C have higher velocities than A, D, and E (Figure 3.11e).

3.5.3 Airflow pattern

In order to further analyze the effect of the roof geometry on the flow pattern around and inside the building, Figure 3.12 shows contours of the pressure coefficient (C_P) and of the dimensionless velocity magnitude ($|V|/U_{ref}$). The pressure coefficient is calculated as:

$$C_P = \frac{(P - P_0)}{(0.5 \rho U_{ref}^{\ 2})} \qquad (5)$$

where P is the static pressure, P_0 the reference static pressure, ρ the density of air (= 1.225 kg/m^3: International Standard Atmosphere (ISA); dry air, θ_a = 15°C, p_0 = 101,325 Pa (ISO 1975) and U_{ref} is the approach-flow wind speed at building height (U_{ref} = 12.48 m/s at z_{ref} = 5.7 m). Figure 3.12h and Figure

3.12j show that the roofs with a convex geometry (D and E) show an increase of the size (height) of the wake behind the building, resulting in lower pressures in the wake region (Figure 3.12g,i) and a larger pressure difference over the building. As a consequence, the convex geometries have a higher volume flow rate through the inlet opening. In geometry B, with a fully curved concave roof shape, the flow stays attached along the entire roof surface. Figure 3.12d and Figure 3.12f show a strong flow acceleration on the roof of the geometries B and C. Under a normal wind incidence angle, a concave roof geometry, such as B, reduces the ventilation potential due to a decrease of the size of the underpressure zone and the magnitude of the underpressure behind the building (wake region), compared to for example geometry E. On the other hand, geometry A and the convex geometries D and E, increase the size and magnitude of the underpressure zone in the wake region (see Figure 3.12a,g,i) and, as a consequence, the volume flow rate is around 13% higher than for geometry B, as shown in Figure 3.10. Note that in addition to geometry B, geometry A also has no, or at least a very limited, flow separation at the windward roof edge (Figure 3.12a,b).

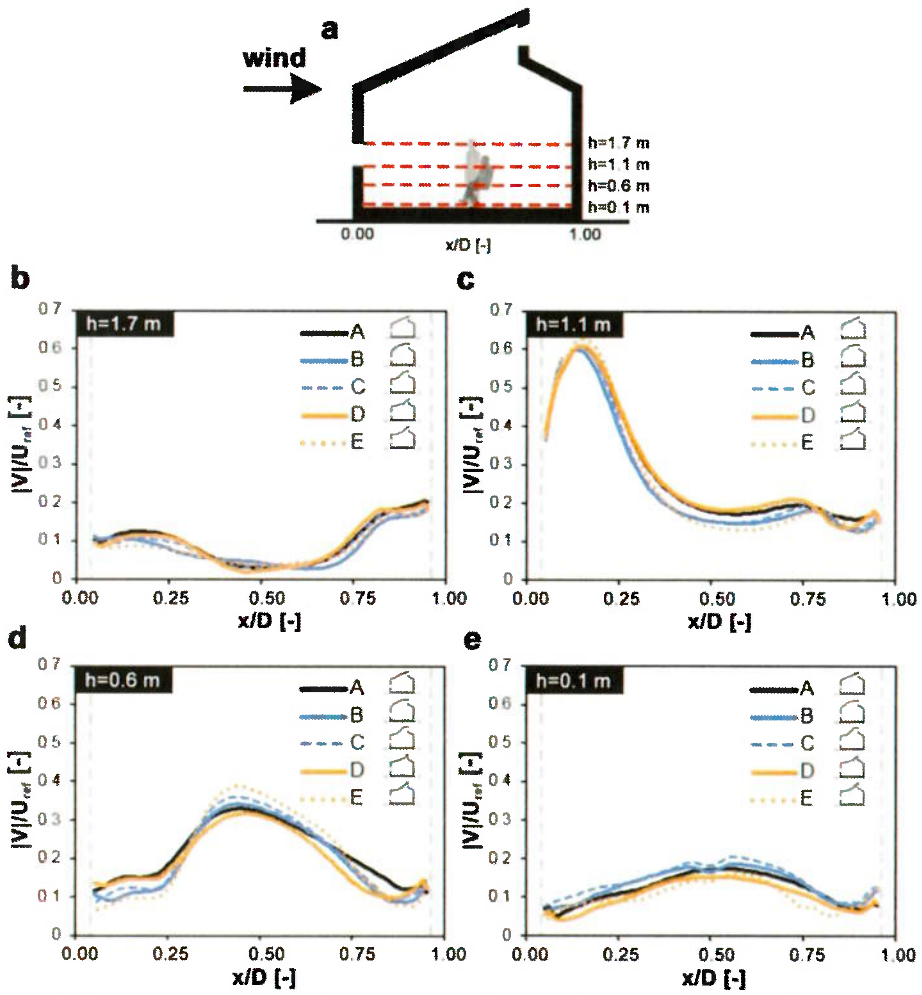

Figure 3.11: Dimensionless velocity magnitude ($|V|/U_{ref}$) along four horizontal lines at a height h above the floor. (a) Location of four lines. (b) h = 1.7 m. (c) h = 1.1 m. (d) h = 0.6 m. (e) h = 0.1 m. The dashed vertical lines indicate the inner surfaces of the walls at the windward and leeward side of the building.

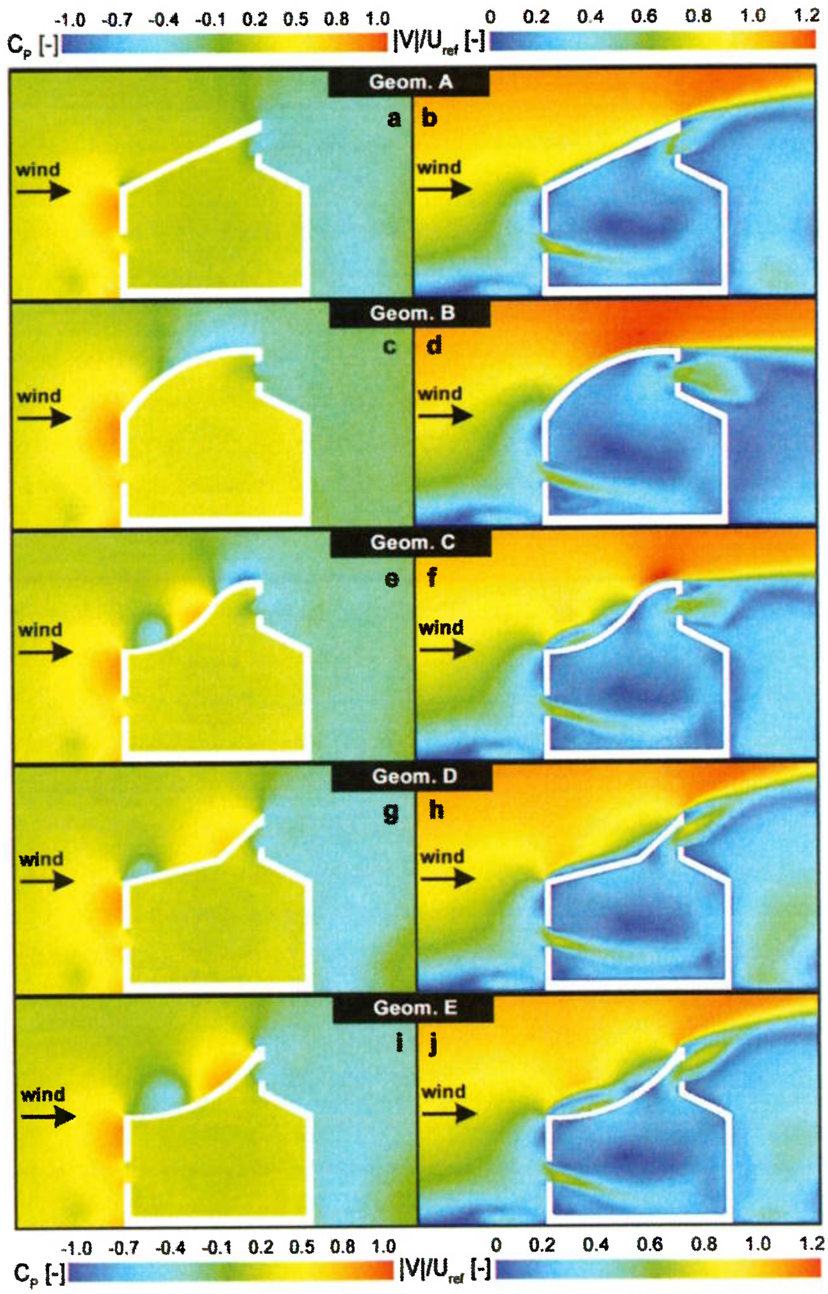

Figure 3.12: Countours of pressure coefficient C_P (a,c,e,g,i) and dimensionless velocity magnitude ($|V|/U_{ref}$) (b,d,f,h,j) in the vertical center plane for the five roof geometry cases.

3.5.4 Comparison between concave (B) and convex (E) roof geometry

The impact of a concave and a convex roof geometry on indoor air velocity is studied in more detail by focusing on geometry B (concave) and geometry E (convex). Figure 3.13 shows the mean velocity vectors in the vertical center plane for both geometries. Figure 3.13a shows that the airflow remains attached to the roof surface of the concave geometry B, and the stagnation point is slightly elevated to the top of the windward facade, compared with the convex geometry E (see also Figure 3.12c). Figure 3.13b shows the separation bubble on the roof for geometry E. The largest differences in the flow pattern around the building can be seen above the roof and in the wake region. As mentioned before, in geometry B the flow remains attached to the roof which results in a horizontally directed flow above the downstream part of the sawtooth roof. The flow above the roof in geometry E is guided upwards by the convex curved roof, resulting in a strong upward flow and a larger wake region. The flow through the outlet opening can be seen as a diagonally directed jet flow, with somewhat larger velocities than in geometry B. As a result, the volume flow rate for geometry E is 12.3% larger than for geometry B.

In addition to the roof geometry, there are two other factors that might have an influence on the ventilation performance of the roof geometries in general, and of roof geometry B and E in particular; (1) the size of the internal volume, and (2) the different geometry above the upper part of the outlet opening, i.e. the small piece of wall above the outlet opening in geometries A, B and C (see Figure 3.1 and dashed circle in Figure 3.13a). The internal volume of geometry B is clearly larger than that of geometry E, which might influence the flow through the building (different internal resistance). Furthermore, in geometry E, the upper part of the outlet opening coincides with the lower part of the roof (= ceiling) (see dashed circle in Figure 3.13b), consequently, there is no 'potential obstruction' to the outgoing flow. In geometry B on the other hand, there is an 'obstruction' above the outlet opening (Figure 3.13a) which might block the flow and influence the volume flow rate through the building. To assess both effects, an additional simulation has been conducted of geometry B-E (see Figure 3.14a), which is a combination of geometry B and E; i.e. external shape of geometry B and internal shape of geometry E. This geometry therefore has the same internal volume as geometry E and does not have the internal obstruction above the outlet opening. Figure 3.14b,d shows the flow through the building for geometry B-E, indicating that the flow indeed does not experience an internal obstruction near the outlet opening for this geometry. This additional simulation shows that the volume flow rate for geometry B-E is only 1.2% higher than the volume flow rate for geometry B. The underpressure near the outlet opening is almost equal as well (Figure 3.12c, Figure 3.14c); the C_P value is -0.18 for geometry B and -0.17 for geometry B-E. Therefore, it can be concluded that in this particular case both factors, i.e. internal volume and vertical obstruction above the outlet opening, based on a combined assessment of both factors, do not significantly affect the results; the higher volume flow rate for geometry E compared to geometry B can almost completely be attributed to the external shape of the roof and its effect on the external wind flow.

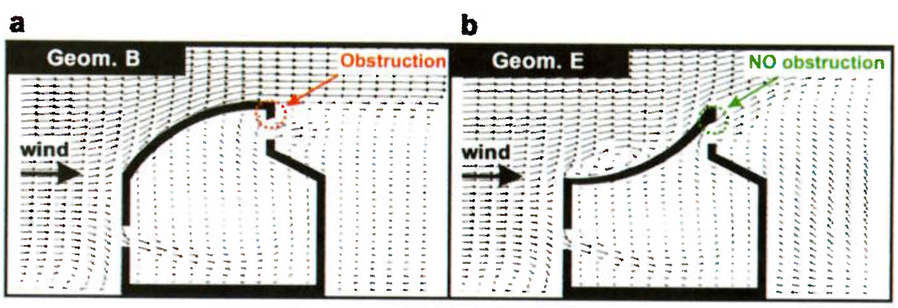

Figure 3.13: Velocity vectors in the vertical center plane. (a) Geometry B. (b) Geometry E.

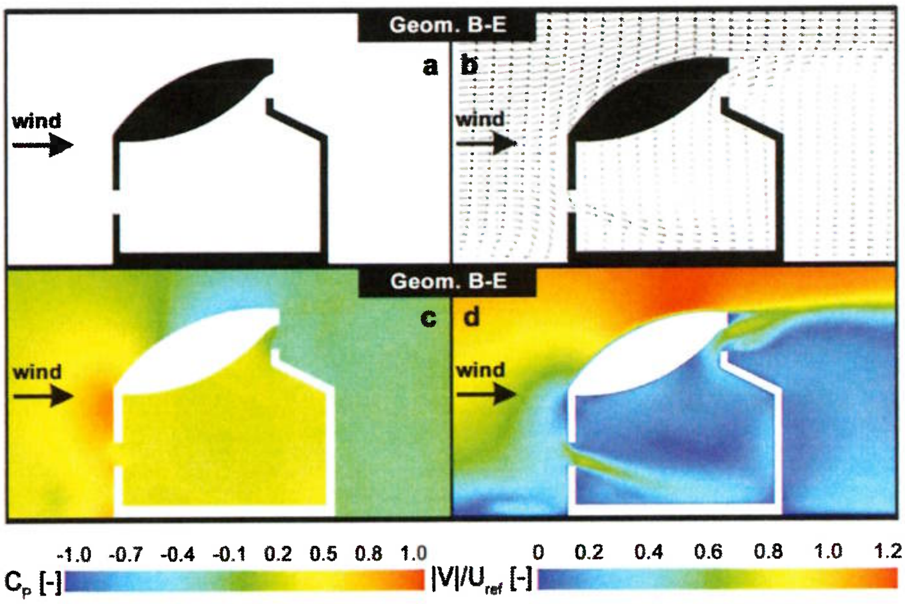

Figure 3.14: (a) Schematic represenation of roof geometry B-E. (b) Velocity vectors in the vertical center plane. (c) Contours of pressure coefficient C_P in the vertical center plane. (d) Contours of dimensionless velocity magnitude ($|V|/U_{ref}$) in the vertical center plane.

Figure 3.15 shows the percentage increase of the indoor velocity magnitude $|V|$ ($(|V|_E-|V|_B)/|V|_B$) for geometry E compared to the wind speed for geometry B, along the four lines defined earlier at h = 1.7 m, 1.1 m, 0.6 m and 0.1 m. This allows a direct comparison between geometry B and E. Figure 3.15a shows that the increase in velocity in geometry E at h = 1.7 m can be as large as 70% between $0.60 < x/D < 0.65$, while the velocities are lower than B from $0.00 < x/D < 0.25$ and from $0.30 < x/D < 0.55$. Figure 3.15b shows that the indoor velocity at h = 1.1 m is increased by up to 18% in geometry E between $0.00 < x/D < 0.40$ and $0.75 < x/D < 0.90$ and decreased between $0.40 < x/D < 0.75$. The indoor air velocity at h = 0.6 m is increased in the middle region (between $0.30 < x/D < 0.85$) (Figure 3.15c). Finally, Figure 3.15d shows that the indoor velocities are higher in geometry B at almost the entire line at h = 0.1 m. Although geometry B has the lowest volume flow rate through the building, it can be seen that the velocities inside the building are higher than for geometry E at several locations. The fact that large differences in indoor air velocities are present between the buildings with different roof geometries, in this case between B and E, is in line with the observations of Kindangen et al. [12], who pointed out that the roof geometry directly affects the indoor airflow pattern in general, and the velocity magnitude in particular. However, the research by Kindangen et al. [12] focused on a position of the outlet opening at the same level as the inlet opening, which is different from the present study.

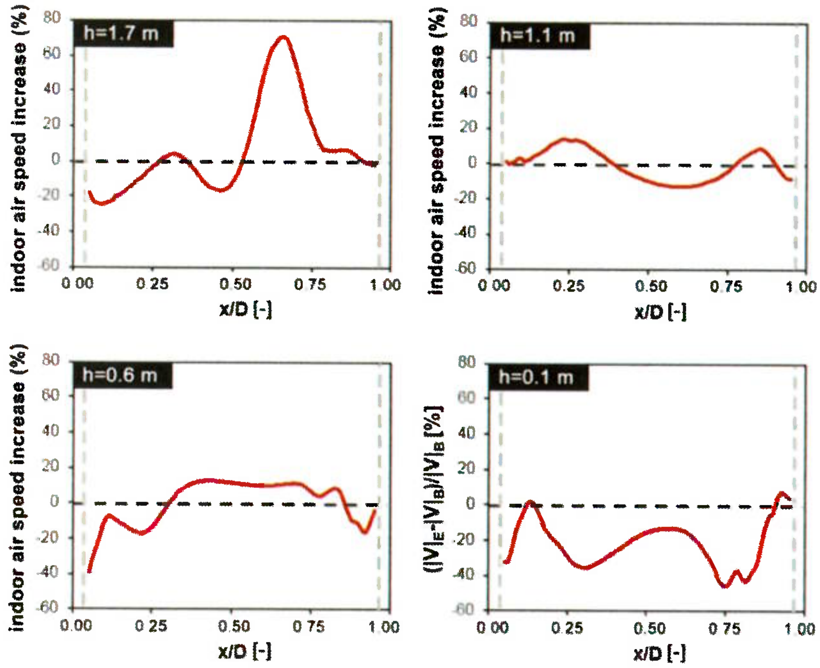

Figure 3.15: Percentage increase of the indoor velocity magnitude |V| $((|V|_E-|V|_B)/|V|_B)$ along four horizontal lines for roof geometry E when compared to geometry B. (a) h = 1.7 m. (b) h = 1.1 m. (c) h = 0.6 m. (d) h = 0.1 m.

3.6 Discussion

The main goal of this paper is evaluate the impact of leeward sawtooth roof geometries on wind-driven cross-ventilation under normal wind incidence angle. Five leeward sawtooth roof geometries are evaluated: a straight roof (A), a concave roof (B), a hybrid convex-concave roof (C) and two convex roofs (D, E). The impact on ventilation performance is analyzed in terms of volume flow rate and indoor air velocities. In order to quantify the impact of the differences in internal volume for the different roof geometries, the concave roof geometry B and the convex roof geometry E are combined to generate the new geometry B-E. Finally, two of the analyzed roof geometries, a concave shape (B) and a convex shape (E), are compared more in detail with respect to the indoor air velocity. It is important to mention the limitations of the current study, which should be addressed in future research:

- This analysis considered a simplified isolated single zone building. The impact of other building parameters such as eaves (overhang) and internal layout should be taken into account in future research.
- The impact of wind incidence angles different than 0° should be considered as well, since this can influence the ventilation performance of the different geometries. For more oblique wind incidence angles it might be necessary to resort to unsteady simulations, such as Large Eddy Simulations (LES) or Detached Eddy Simulation (DES), to accurately predict the volume flow rates through the openings resulting from unsteady flow features (e.g. Jiang and Chen 2001, Wright and Hargreaves 2006).

- Due to the use of steady RANS in this study, only average pressures are obtained, which result in an average volume flow rate. To analyze the effect of pressure fluctuations on the average volume flow rate, future research will include DES or LES simulations from which the calculated volume flow rates will be compared to the results of the steady RANS simulations.
- All geometries analyzed have a different internal volume due to differences in the roof geometry. In order to further evaluate the impact of the internal volume a new building geometry (geometry B-E) was evaluated. This new geometry results from the combination of the external concave shape of geometry B and the internal convex shape of geometry E, yielding a building geometry with the same internal volume as geometry E. The results show a very small impact of the internal volume and the obstruction near the outlet opening on the volume flow rate through the building (1.2% increase). Moreover, it must be noted that it is nearly impossible to keep all geometrical parameters constant when changing the roof geometry.
- Future work can also include an analysis of the performance of a double-span roof with the same roof geometries in addition to the single-span roof as studied in this paper.

3.7 Conclusions

This paper presents the performance of five different roof geometries for an isolated leeward sawtooth roof building, with the aim to optimize the upward cross-ventilation flow. The analysis is performed using 3D steady CFD simulations with the RANS approach and the SST k-ω model. The simulations are based on grid-sensitivity analysis and on validation using Particle Image Velocimetry (PIV) wind-tunnel measurements. The main conclusions of this paper are summarized below:

- The computational model is successfully validated using wind-tunnel measurements from literature.
- The internal airflow and the volume flow rate show a clear dependency on the roof geometry.
- For a normal wind incidence angle (0°), the convex roof geometries (D and E) and the straight roof geometry (A) result in higher volume flow rates than concave (B) and hybrid convex-concave (C) roof geometry. The volume flow rates for geometry A, D and E are about 13% higher than that of geometry B, which shows the lowest performance.
- Analysis of the additional roof geometry (B-E), which consisted of the internal shape of geometry E and the external shape of geometry B showed that the size of the internal volume of the building does not significantly influence the volume flow rate through the building; the volume flow rate is only 1.2% larger for geometry B-E than for geometry B. In addition, this simulation showed that the vertical obstruction above the outlet opening does not affect the results much either.
- The roof geometry is an important design parameter to maximize the size and magnitude of the underpressure zone in the wake of the building and the pressure difference over the building, and consequently the volume flow rate through the building. A roof that directs the external wind flow behind the building upwards will result in a larger underpressure zone and larger magnitude of the underpressure, and consequently in higher volume flow rates.

- The indoor air velocities depend on the roof geometry, although this dependency is less clear. For instance, a comparison of geometry B (lowest volume flow rate) with geometry E (one of the highest volume flow rates) shows that the indoor air velocity in the occupied zone in geometry B is higher than in geometry E at several locations, and the other way around at some other locations. Therefore, it is not easy to draw a firm conclusion on the performance of the different roof geometries with respect to the indoor air velocities.

3.8 Acknowledgements

This work was supported by The Coordination for the Improvement of Higher Level Personnel (CAPES), Brazil, The Polytechnic School of the University of São Paulo (USP), Brazil, The Secretary of Education, Science, Research and Technology of Panama (SENACYT), Panama and the unit Building Physics and Services of the Department of the Built Environment at Eindhoven University of Technology in the Netherlands.

Twan van Hooff is currently a postdoctoral fellow of the Research Foundation – Flanders (FWO) and acknowledges its financial support (project FWO 12R9715N).

3.9 References

[1] Robbins CL. Daylighting: design and analysis. Van Nostrand Reinhold Company; 1986.

[2] Gandemer J, Barnaud G. Ventilation Naturelle des Habitations sous Climat Tropical Humide: Aproach Aerodynamique. Nantes: CSTB; 1989.

[3] Bittencourt L. Introdução à ventilação natural nas edificações. Editora da Universidade Federal de Alagoas - EDUFAL, Maceio, Brasil; 2006.

[4] Saathoff P, Stathopoulos T. Wind loads on buildings with sawtooth roofs . J Struct Eng 1992;118:429-446.

[5] Stathopoulos T, Saathoff P. Codification of Wind pressure coefficients for sawtooth roofs. J Wind Eng Ind Aerodyn 1992;43:1727–38. doi:16/0167-6105(92)90584-W.

[6] Cui B. Wind Effects on Monosloped and Sawtooth Roof. PhD Thesis. Clemson University, 2007.

[7] Holmes JD. Wind pressures on tropical housing. J Wind Eng Ind Aerodyn 1994;53:105–23. doi:10.1016/0167-6105(94)90021-3.

[8] St. Pierre LMS, Kopp GA, Surry D, Ho TCE. The UWO contribution to the NIST aerodynamic database for wind loads on low buildings: Part 2. Comparison of data with wind load provisions. J Wind Eng Ind Aerodyn 2005;93:31–59. doi:10.1016/j.jweia.2004.07.007.

[9] Quan Y, Tamura Y, Matsui M. Mean wind pressure coefficients on surfaces of gable-roofed low-rise buildings. Adv Struct Eng 2007;10:259–71. doi:10.1260/136943307781422253.

[10] Holmes JD, Paterson DA. Mean wind pressures on arched-roof buildings by computation. J Wind Eng Ind Aerodyn 1993;50:235–42. doi:10.1016/0167-6105(93)90078-3.

[11] Fatnassi H, Boulard T, Poncet C, Chave M. Optimisation of Greenhouse Insect Screening with Computational Fluid Dynamics. Biosyst Eng 2006;93:301–12. doi:10.1016/j.biosystemseng.2005.11.014.

[12] Kindangen J, Krauss G, Depecker P. Effects of Roof Shapes on Wind-Induced Air Motion Inside Buildings. Build Environ 1997a;32:1–11.

[13] Kindangen JI. Window and roof configurations for comfort ventilation. Build Res Inf 1997b;25:218–25. doi:10.1080/096132197370345.

[14] Perén JI, van Hooff T, Leite BCC, Blocken B. CFD simulation of cross-ventilation of a generic isolated building with asymmetric opening positions: impact of roof angle and opening location. 85: 263-276.

[15] International Organization for Standardization. Ergonomics of the thermal environment - Analytical determination and interpretation of thermal comfort using calculation of the PMV and PPD indices and local thermal comfort criteria (ISO 7730:2005). European Committee for Standardization, Brussels, Belgium; 2005.

[16] Wolfram MathWorld. http://mathworld.wolfram.com/ConvexFunction.html. Retrieved on 01/12/2014.

[17] Blocken B. 50 years of Computational Wind Engineering: Past, present and future. J Wind Eng Ind Aerodyn 2014;129:69–102. doi:10.1016/j.jweia.2014.03.008.

[18] Karava P, Stathopoulos T, Athienitis AK. Airflow assessment in cross-ventilated buildings with operable façade elements. Build Environ 2011;46:266–79. doi:10.1016/j.buildenv.2010.07.022.

[19] Franke J, Hellsten A, Schlünzen H, Carissimo B. Best practice guideline for the CFD simulation of flows in the urban environment. Brussels: COST Office 2007.

[20] Tominaga Y, Mochida A, Yoshie R, Kataoka H, Nozu T, Yoshikawa M, et al. AIJ guidelines for practical applications of CFD to pedestrian wind environment around buildings. J Wind Eng Ind Aerodyn 2008;96:1749–61. doi:10.1016/j.jweia.2008.02.058.

[21] Blocken B, Stathopoulos T, Carmeliet J. CFD simulation of the atmospheric boundary layer: wall function problems. Atmos Environ 2007a;41:238–52. doi:10.1016/j.atmosenv.2006.08.019

[22] Blocken B, Carmeliet J, Stathopoulos T. CFD evaluation of wind speed conditions in passages between parallel buildings—effect of wall-function roughness modifications for the atmospheric boundary layer flow. J Wind Eng Ind Aerodyn 2007b;95:941–62. doi:10.1016/j.jweia.2007.01.013.

[23] van Hooff T, Blocken B. Coupled urban wind flow and indoor natural ventilation modelling on a high-resolution grid: A case study for the Amsterdam Arena stadium. Environ Model Softw 2010a5);25:51–65. doi:10.1016/j.envsoft.2009.07.008.

[24] ANSYS. Fluent 12 user's guide. Lebanon: Fluent Inc. 2009.

[25] Menter FR. Two-equation eddy-viscosity turbulence models for engineering applications. AIAA J 1994;32:1598–605.

[26] Ramponi R, Blocken B. CFD simulation of cross-ventilation for a generic isolated building: Impact of computational parameters. Build Environ 2012;53:34–48. doi:10.1016/j.buildenv.2012.01.004.

[27] Blocken B. Computational Fluid Dynamics for Urban Physics: Importance, scales, possibilities, limitations and ten tips and tricks towards accurate and reliable simulations. Build Environ 2015; doi:10.1016/j.buildenv.2015.02.015.

[28] Snyder WH. Guideline for fluid modeling of atmospheric diffusion. U.S. Environmental Protection Agency Report No. EPA-600/8-81-009. 1981

[29] van Hooff T, Blocken B. On the effect of wind direction and urban surroundings on natural ventilation of a large semi-enclosed stadium. Comput Fluids 2010;39:1146–55. doi:10.1016/j.compfluid.2010.02.004.

[30] van Hooff T, Blocken B, Aanen L, Bronsema B. A venturi-shaped roof for wind-induced natural ventilation of buildings: Wind tunnel and CFD evaluation of different design configurations. Build Environ 2011;46:1797–807. doi:16/j.buildenv.2011.02.009.

[31] Gousseau P, Blocken B, Stathopoulos T, van Heijst GJF. CFD simulation of near-field pollutant dispersion on a high-resolution grid: A case study by LES and RANS for a building group in downtown Montreal. Atmos Environ 2011;45:428–38. doi:10.1016/j.atmosenv.2010.09.065.

[32] Blocken B, Janssen WD, van Hooff T. CFD simulation for pedestrian wind comfort and wind safety in urban areas: General decision framework and case study for the Eindhoven University campus. Environ Model Softw 2012;30:15–34. doi:10.1016/j.envsoft.2011.11.009.

[33] Janssen WD, Blocken B, van Hooff T. Pedestrian wind comfort around buildings: Comparison of wind comfort criteria based on whole-flow field data for a complex case study. Build Environ 2013;59:547-562.

[34] Montazeri H, Blocken B, Janssen WD, van Hooff T. CFD evaluation of new second-skin facade concept for wind comfort on building balconies: Case study for the Park Tower in Antwerp. Build Environ 2013;68:179–92. doi:10.1016/j.buildenv.2013.07.004.

[35] Wieringa J. Updating the Davenport roughness classification. J Wind Eng Indus Aerodyn 1992;41(1):357-368.

[36] Launder BE, Spalding DB. The numerical computation of turbulent flows. Comput Methods Appl Mech Eng 1974;3:269–89. doi:10.1016/0045-7825(74)90029-2.

[37] Cebeci T, Bradshaw P. Momentum transfer in boundary layers. Hemisphere Publishing Corp. New York: 1977.

[38] International Organization for Standardization. Standard Atmosphere, ISO 2533:1975, 1975.

[39] Jiang Y, Chen Q. Study of natural ventilation in buildings by large eddy simulation. J Wind Eng Ind Aerodyn 2001;89(13):1155-1178.

[40] Wright NG, Hargreaves DM. Unsteady CFD simulations for natural ventilation. Int J Vent 2006;5(1):13-20.

Chapter 4

Impact of eaves on cross-ventilation of a generic isolated leeward sawtooth roof building: windward eaves, leeward eaves and eaves inclination

Published as:

Perén JI, van Hooff T, Leite BCC, Blocken B. Impact of eaves on cross-ventilation of a generic isolated leeward sawtooth-roof building: windward eaves, leeward eaves and eaves inclination angle. Submitted.

Impact of windward and leeward eaves on cross-ventilation

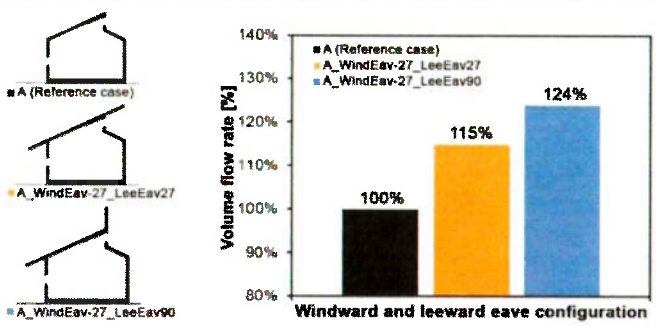

4 Impact of eaves on cross-ventilation of a generic isolated leeward sawtooth roof building: windward eaves, leeward eaves and eaves inclination

Abstract

An eaves is a roof extension that can protect the indoor environment from direct solar radiation, the exterior facade from wetting of by wind-driven rain and can be useful to enhance cross-ventilation. This paper evaluates the impact of eaves configuration on wind-driven cross-ventilation of a generic leeward sawtooth roof building. Both the type of eaves (windward versus leeward) and the eaves inclination angles are investigated. Isothermal Computational Fluid Dynamics (CFD) simulations are performed using the 3D steady Reynolds-Averaged Navier-Stokes (RANS) approach. A grid-sensitivity analysis is performed and validation of the CFD results is conducted based on wind-tunnel measurements with Particle Image Velocimetry from literature. The ventilation evaluation is based on the volume flow rates and the indoor mean velocities. The eaves length is 1/4 of the building depth and the inclination is varied between 90° to -45° for both the windward and leeward eaves. The results show that windward eaves with an inclination of 27° (equal to roof inclination) result in the highest increase of the volume flow rate (15%) compared to the building without eaves. Furthermore, the flow through the occupied zone is more horizontally directed. Leeward eaves have a smaller influence on the ventilation volume flow rate than windward eaves; the maximum increase in volume flow rate is only 6% when a 90° inclination is employed. Application of both (windward and leeward eaves) results in an increase of the volume flow rate of 24%, which is 3% more than the sum of the increases by the two eaves separately.

Keywords: Computational Fluid Dynamics (CFD); Urban physics; Leeward sawtooth-roof geometry; Natural upward cross-ventilation; Eaves configuration; Building envelope optimization.

4.1 Introduction

An eaves is a roof overhang which can be seen as a multi-purpose building component. As an extension of the roof construction, it can protect the building from solar radiation and wind-driven rain. As a result, eaves are commonly used in tropical climates. The solar shading that is provided by eaves can reduce the energy consumption for cooling significantly. Depending on the building, climate and other factors, this reduction can range from 5.3% [1] to higher than 10% [2,3]. In addition to their known effects on solar radiation and wind-driven rain, eaves can be employed to increase cross-ventilation flow (e.g. [4]).

Several studies focused on the effects of eaves (e.g. [5–7]) and parapets (vertical extension on a roof top) (e.g. [8,9]) on wind loads. Other studies evaluated the protection from wind-driven rain (e.g. [10]), snow loads (e.g. [11,12]) and the influence of eaves on convective heat transfer in a roof (e.g. [13]). The majority of the studies focusing on wind loads highlighted the potential of eaves and parapets to reduce the underpressure near the roof edges, where flow separation occurs.

Regarding the potential of eaves to reduce the heat gains due to solar radiation some studies analyzed the shading effects of eaves in for example high-rise residential buildings (e.g. [1]), and school buildings (e.g. [4]) (e.g., [18]). However, to the best of our knowledge, only two studies focused on the impact of eaves on the ventilation flow (e.g. [14,15]). Kindangen [14,15] performed Computational Fluid Dynamics (CFD) simulations and observed that in buildings with symmetric opening locations (inlet and outlet openings located at the same height) the use of eaves can increase the cross-ventilation flow rate. Unfortunately, the cases in these studies combined the effect of the eaves with other parameters such as the roof inclination angle, roof shape, roof height and roof orientation, which makes it difficult to isolate the impact of the eaves on the ventilation flow from the impact of other parameters. Furthermore, these studies only considered the impact of eaves with a 0° inclination (horizontal eaves).

There is a clear lack of research on the impact of the eaves configuration (both eaves at the windward and the leeward side of the building) on wind-driven cross-ventilation. This holds particularly for leeward sawtooth roof buildings. In previous studies by the authors [16,17], the impact of the roof inclination angle [16] and the roof shape [17] on cross-ventilation of leeward sawtooth roof buildings were assessed. The present study builds further on these achievements by reporting a detailed and systematic study on the impact of both windward and leeward eaves on wind-driven upward cross-ventilation of a leeward sawtooth roof building. The study is based on isothermal CFD simulations with the 3D steady Reynolds-Averaged Navier-Stokes (RANS) approach. The performance of each eaves configuration (windward, leeward or the combination of both) is evaluated based on the volume flow rate through the building and the mean air velocity ratios in the occupied zone, measured at four different heights: h = 0.1 m, 0.6 m, 1.1 m and 1.7 m, which are considered as reference for the evaluation of thermal comfort conditions of a seated or standing person, at a steady-state and moderate environment, i.e. where the environmental conditions are close to the thermal comfort standards proposed by ISO 7730/2005 [18]. As mentioned above, the results presented in this paper are part of a large research project on the enhancement of wind-driven cross-ventilation of residential buildings by adjusting the roof geometry. For the sake of brevity and to enable a detailed assessment of the flow behavior in and around the building resulting from the addition of eaves, this paper will only focus on this part of the results obtained in this larger research project.

In the past 50 years, CFD has been increasingly developed and applied as a powerful assessment tool in urban physics and wind engineering [19-23], including natural ventilation in buildings [24-28]. While Large Eddy Simulation (LES) is intrinsically superior to steady RANS simulations, due to the higher computational cost and increased model complexity of LES, a detailed review of the literature [19] shows that RANS simulations still constitute the most frequently used computational approach in urban physics and wind engineering, especially in natural ventilation studies [22,24,26-28].

The paper is structured as follows. The building geometry of the reference case is presented in Section 4.2. Section 4.3 presents a brief overview of the CFD validation study using wind-tunnel experiments from literature. The computational settings and parameters for the current study are presented in Section 4.4. The CFD simulation results of the different eaves configurations are analyzed for a windward eaves and subsequently for a leeward eave, the results of which are outlined in Section 4.5. Section 4.6 shows the effect of the simultaneous application of both a windward eaves and a leeward eave. Discussion and conclusions are given in Sections 4.7 and 4.8, respectively.

4.2 Building geometry: reference case (geometry A)

Figure 4.1 shows the front view (Figure 4.1a) and vertical cross-section (Figure 4.1b) with the building dimensions, and a perspective view (windward and leeward facade) of the leeward sawtooth roof geometry A (Figure 4.1c,d). Leeward sawtooth roof geometry A has a straight upward sloping roof and is selected for this sensitivity analysis as a reference case since it reached the highest volume flow rate compared to other leeward sawtooth roof geometries in a previously published paper by the authors [17]. The building dimensions are 3 x 6 x 5.7 m^3 (W x L x H). Both ventilation openings are 0.9 x 0.63 m^2 (W x H); the bottom of the windward opening is located at z = 1.42 m, whereas the bottom of the leeward opening is located at z = 4.6 m. The distance from the window to the side walls is 1.05 m on both sides. The thickness of the walls is 0.23 m, and the windward facade has a height of 3.55 m.

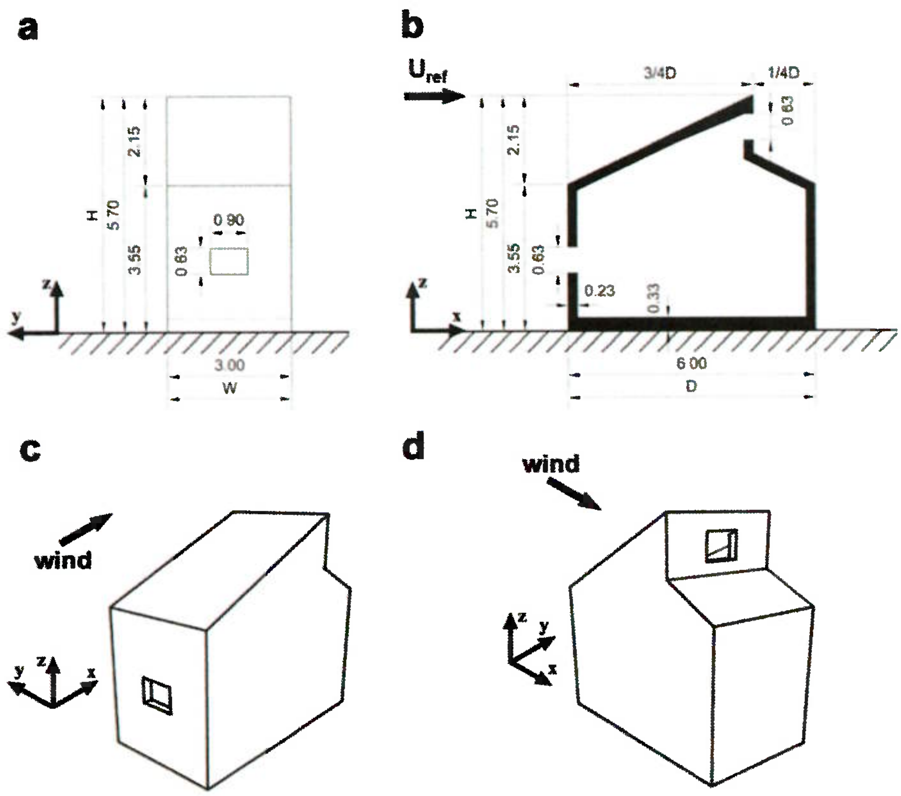

Figure 4.1: Overview of geometry of the reference case (geometry A) (dimensions in meters). (a) Front view (windward facade) with opening size and dimensions. (b) Vertical cross-section with opening size and dimensions. Perspective views: (c) windward facade (d) leeward facade.

4.3 CFD simulations: validation study

When performing CFD simulations based on the 3D steady RANS equations, validation is obligatory to determine the accuracy and reliability of the results. The combination of the computational settings and parameters that will be used in the current study have been validated by the authors in a recent publication [16]. Therefore, only a brief overview of the validation study is provided in this section.

4.3.1 Wind-tunnel experiment

The wind-tunnel measurements by Karava et al. [29] were used for CFD validation. Karava et al. [29] conducted PIV measurements of wind-induced cross-ventilation for a generic isolated building model with symmetric and asymmetric opening positions in the open-circuit atmospheric boundary layer wind tunnel at Concordia University in Montreal, Canada. The dimensions of the 1:200 building model are 0.1 x 0.1 x 0.08 m^3 (W x D x H) at reduced scale (full-scale dimensions: 20 x 20 x 16 m^3 (W x D x H)), as shown in Figure 4.2a and Figure 4.2b. The height of the openings is 0.018 m (3.6 m full scale), and the location and width of the openings were varied. For this validation study, the building model with the inlet opening at the bottom of the windward facade (with the center of the opening at h = 0.02 m), the outlet opening at the top of the opposite (leeward) facade (with the center of the opening at h = 0.06 m), and with a wall porosity of 10%, was used. The choice of these asymmetric opening positions resembles the situation of the reference case (Figure 4.1). The reduced-scale aerodynamic roughness length in the experiments was z_0 = 0.025 mm corresponding to 0.005 m in full scale [30]. A reference mean wind speed U_{ref} = 6.97 m/s and a reference turbulence intensity of 10% were measured at building height (z_{ref} = H). The turbulence intensity was about 17% near ground level (0.012 m) and 5% at gradient height (0.738 m). The PIV measurements were conducted in a horizontal plane at mid-height (h = 0.04 m) and in the vertical plane of symmetry (Figure 4.2b); the latter will be used in this study. For more information related to the wind-tunnel experiments the reader is referred to [29].

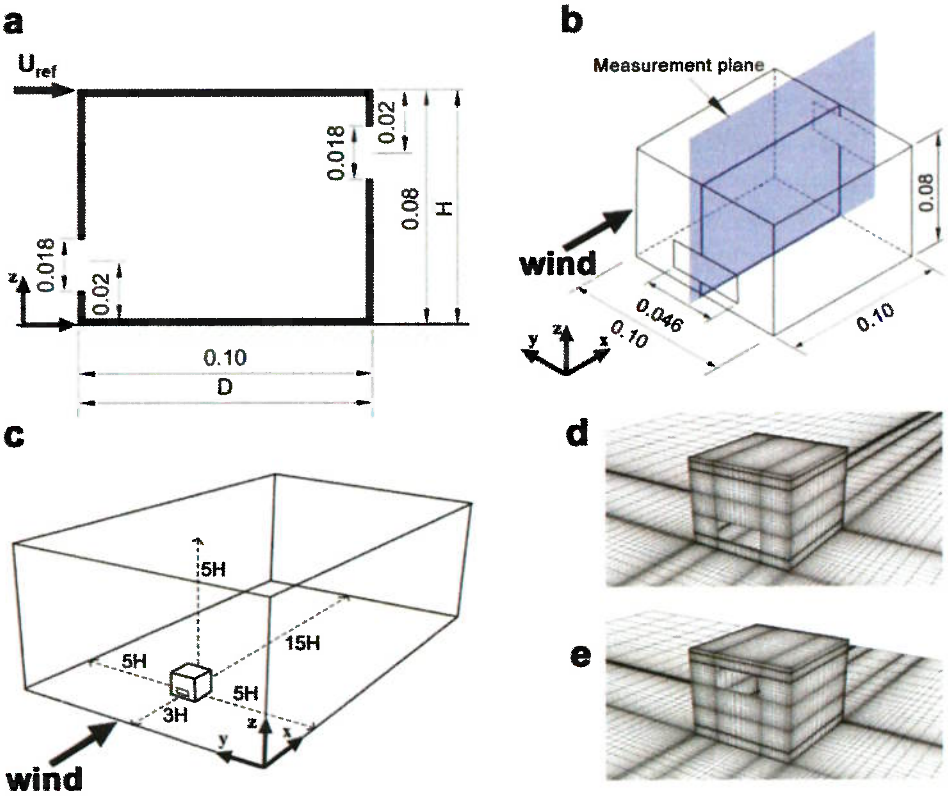

Figure 4.2: (a) Vertical cross-section of the reduced-scaled building model as studied by Karava et al. [29] with opening size and dimensions (in meters). (b) Perspective view indicating the measurement plane with dimensions (in meters). (c) Perspective view of the building in its computational domain. (d,e) Perspective close-up view of the grid (770,540 cells) on the building surface and part of the ground: (d) windward facade; (e) leeward facade.

4.3.2 CFD simulations and validation

The computational domain follows the best practice guidelines by Franke et al. [31] and Tominaga et al. [32], apart from the upstream length, which is reduced to 3 times the height of the building to limit the development of unintended streamwise gradients [33-35]. The dimensions of the domain are 0.9 x 1.54 x 0.48 m^3 (W x D x H) (scale 1:200, equal to the wind-tunnel experiment) (Figure 4.2c). The computational grid is created using the surface-grid extrusion technique by van Hooff and Blocken [27] and is shown in Figure 4.2d and Figure 4.2e (windward and leeward facade view, respectively). The grid resolution resulted from a grid-sensitivity analysis yielding a fully structured hexahedral grid with 770,540 cells. At the inlet of the domain, the vertical approach-flow profiles of mean wind speed U, turbulent kinetic energy k and specific dissipation rate ω are imposed. These are based on the measured incident profiles of mean wind speed U and longitudinal turbulence intensity I_U. More information on the boundary conditions can be found in Ref. [16]. The commercial CFD code ANSYS Fluent 12 is used to perform the simulations [36]. The 3D steady RANS equations are solved in combination with the shear-stress transport k-ω model (SST k-ω) [37]. The SIMPLE algorithm is used for pressure-velocity coupling, pressure interpolation is second order and second-order discretization schemes are used for both the convection terms and the viscous terms of the governing equations.

4.3.3 Validation

Figure 4.3a and Figure 4.3b display the mean velocity vector field in the vertical center plane as obtained by PIV measurements and CFD simulations, respectively. It is observed that the CFD simulations correctly predict the most important flow features such as the standing vortex upstream of the building and specific character of the flow pattern inside the building, with a strong downflow near the inlet opening up to the downstream wall, followed by a strong upflow along this wall, finally leading to an oblique upward flow through the outlet opening. Figure 4.3c and Figure 4.3d compare the measured and computed streamwise wind speed ratio U/U_{ref} along a horizontal line going through the middle of the windward opening and along a diagonal line, showing a good agreement between CFD simulation and PIV experiments.

Although the geometry of the building in the wind-tunnel measurements (Figure 4.2) and that of the reference building in the present study (Figure 4.1) are not identical, there is a sufficient amount of similarity to consider this validation approach applicable for the leeward sawtooth roof reference building: both buildings are isolated, both have only one internal zone, both have two asymmetric openings (lower one in the windward facade and upper one in the leeward) and both are exposed to wind direction perpendicular to the facade with the lower opening. As a result, the salient flow features in the wind-tunnel building will also be present in the reference building.

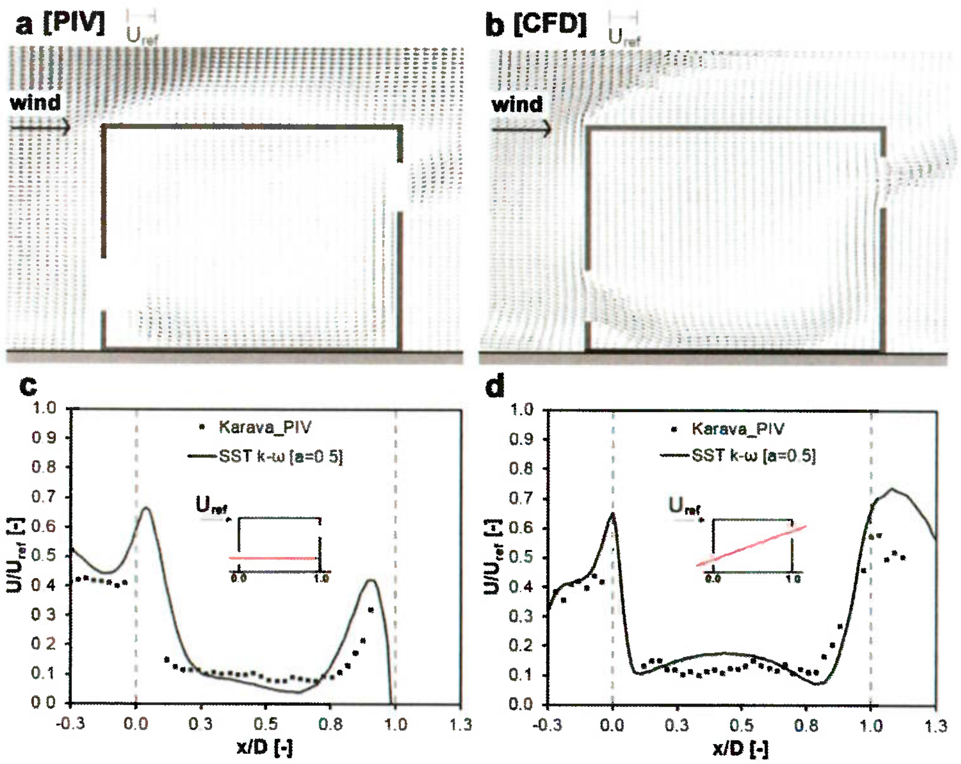

Figure 4.3: (a,b) Comparison of the mean velocity in the vertical center plane obtained from: (a) PIV measurements (processed from [29]; (b) CFD simulations. (c,d) Streamwise wind speed ratio U/U_{ref} from PIV measurements and CFD simulations along: (c) horizontal line; and (d) diagonal line [16].

4.4 CFD simulations of different eaves geometries: computational settings and parameters

In this section the computational model and grid, boundary conditions and solver settings of the CFD model are presented. This CFD model will be employed for the study of the impact of windward and leeward eaves and their inclination angle.

4.4.1 Computational geometry, domain and grid

The geometry of the computational model of the reference case (leeward sawtooth roof geometry A) is as presented in Section 4.2 and Figure 4.1. The computational domain follows the best practice guidelines by Franke et al. [31] and Tominaga et al. [32], apart from the upstream length, which is reduced to 3 times the height of the building to limit the development of unintended streamwise gradients [33-35] (Figure 4.4a). The computational grid is created using the surface-grid extrusion technique by van Hooff and Blocken [27] and is shown in Figure 4.2d and Figure 4.2e. This technique allows full control over the quality (size, shape) of every grid cell was successfully used in previous studies for simple and more complex building geometries (e.g. [16,17,24,27,28,38,39]). Figure 4.4 shows the dimensions of the computational domain, a perspective view of the grid on the building and ground surface and perspective views of the grid on the building surfaces (front and back view) for the reference case building (Geometry A). The grid resolution is based on the grid-sensitivity analysis presented in Perén et al. [17]. The total number of cells is 1,961,524 cells for the reference case, and it varies slightly for each configuration due to the inclusion of the windward and/or leeward eaves, ranging from 1.9 to 2.4 million cells.

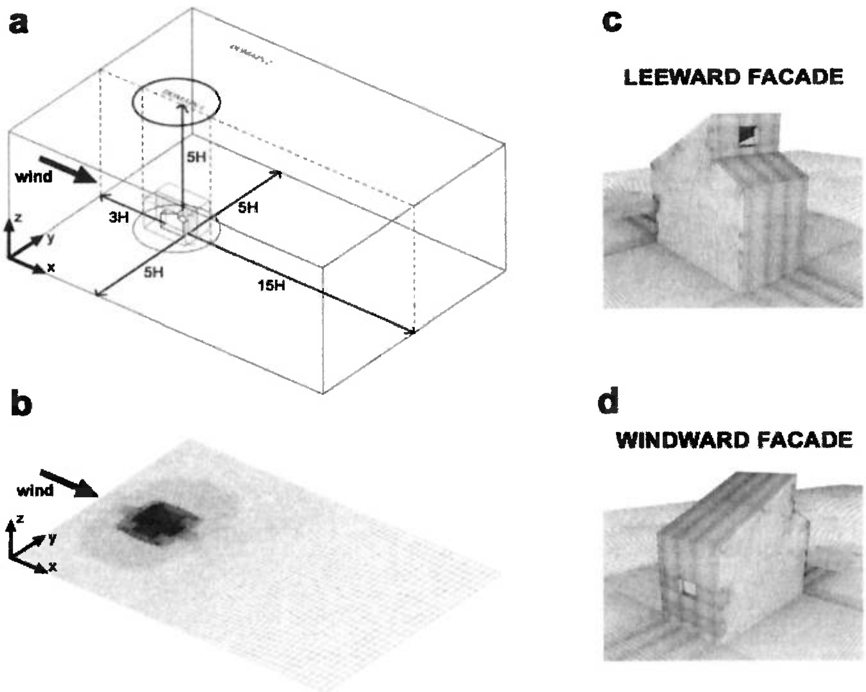

Figure 4.4: (a) Perspective view of the reference case building (geometry A) in its computational domain at model scale. (b,c,d) Perspective view of the grid (geometry A) (total number of cells: 1,961,524 cells);

(b) View of the computational grid on the building surfaces and on the ground surface; (c) View of the leeward facade (outlet opening); (d) View of the windward facade (inlet opening).

4.4.2 Boundary conditions

At the inlet of the domain, vertical profiles of the mean wind speed U, turbulent kinetic energy (k) and specific dissipation rate (ω) are imposed. The wind direction is perpendicular to the windward building facade. The mean wind speed profile is given by the logarithmic law (Eq. 1):

$$U(z) = \frac{u^*_{ABL}}{\kappa} \ln\left(\frac{z+z_0}{z_0}\right) \quad (1)$$

with $z_0 = 0.1$ m, u^*_{ABL} is the atmospheric boundary layer (ABL) friction velocity, κ is the von Karman constant (0.42) and z the height coordinate. The value of u^*_{ABL} is determined based on the values of the reference velocity (U_{ref}) at building height ($z_{ref} = H$), which are $U_{ref} = 12.48$ m/s, and H = 5.7 m, yielding a building Reynolds number of 500,000. To represent a more realistic wind velocity profile, corresponding to "roughly open country" according to the updated Davenport roughness classification by Wieringa [40], the aerodynamic roughness length is higher than in the validation study. The turbulent kinetic energy k is calculated from the mean wind speed U(z) and the streamwise turbulence intensity $I_u(z)$ (with a value of 15% at the top of the building model (at z_{ref}) and 45% at ground level) using Eq. (2):

$$k(z) = a(I_U(z)U(z))^2 \quad (2)$$

In this equation, I_u is the measured streamwise turbulence intensity and "a" is a parameter ranging from 0.5 to 1.5 [24,32]. The value a = 0.5 is used, as in the validation study. The specific dissipation rate ω is given by Eq. (3), where C_μ is an empirical constant taken equal to 0.09, and the turbulence dissipation rate ε is given by Eq. (4).

$$\omega(z) = \frac{\varepsilon(z)}{C_\mu k(z)} \quad (3)$$

$$\varepsilon(z) = \frac{u^{*3}_{ABL}}{\kappa(z+z_0)} \quad (4)$$

At the ground and building surfaces, the standard wall functions by Launder and Spalding [41] are used in conjunction with the sand-grain based roughness (k_s) modification defined by Cebeci and Bradshaw [42]. For the ground surfaces, the values of the roughness parameters, i.e. the sand-grain roughness height (k_s = 0.14 m) and the roughness constant (C_s = 7), are determined by their the relationship with the aerodynamic roughness length z_0 derived by Blocken et al. [33]:

$$k_s = \frac{(9.793 z_0)}{C_s} \quad (5)$$

For the building surface the value of the sand-grain roughness height is zero (k_S = 0 m). At the outlet plane, zero static gauge pressure is applied and at the top and lateral sides of the domain a symmetry condition is imposed, i.e. zero normal velocity and zero normal gradients of all variables.

As recommended by Blocken et al. [33,34], a simulation in an empty computational domain is performed to assess the extent of unintended streamwise gradients (i.e. horizontal inhomogeneity) in the vertical mean wind speed profile and the turbulence profiles. Figure 4.5 shows the profiles of U, k and ω at the inlet (inlet profiles) and at the location where the building will be positioned (incident profiles). It can be seen that streamwise gradients are absent for the mean wind speed profile. The profiles of k and ω do show some streamwise gradients, however, these are relatively limited.

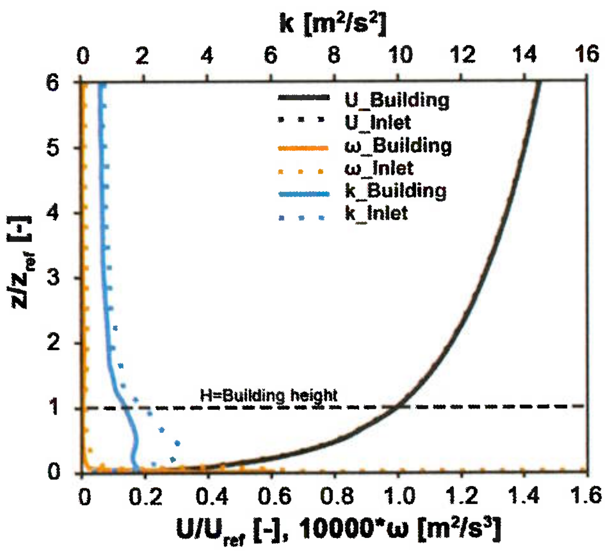

Figure 4.5: Horizontal homogeneity analysis: Profiles of the mean wind speed (U), the turbulent kinetic energy (k) and the specific dissipation rate (ω) at the inlet (dotted line) and at the building position (solid line) in an empty domain. The height of the model (zref = H) is 5.7 m [17].

4.4.3 Solver settings

The commercial CFD code ANSYS Fluent 12 [36] is used to perform the isothermal simulations. The 3D steady RANS equations are solved in combination with the shear-stress transport k-ω model (SST k-ω model) [37]. The SIMPLE algorithm is used for pressure-velocity coupling, pressure interpolation is second order and second-order discretization schemes are used for both the convection terms and the viscous terms of the governing equations. Convergence is assumed to be obtained when all the scaled residuals level off and reach a minimum of 10^{-6} for x, y momentum, 10^{-5} for z momentum and 10^{-4} for k, ε and continuity. As also observed by Ramponi and Blocken [24], the simulations show oscillatory convergence. To obtain a reliable steady value of the solution variables, the results are monitored over

10,400 iterations and the variables are calculated by averaging over 400 iterations (10,000-10,400), after the simulation reached a statistically stationary solution.

4.5 CFD simulations of different eaves geometries: results

The windward and the leeward eaves are added to the reference case, as shown in Figure 4.6. The effect of the windward and leeward eaves on the ventilation, for a normal wind incidence angle ($\varphi = 0°$) are studied independently from each other. The ventilation performance of the eaves cases is assessed based on the volume flow rate through the building and the average non-dimensional velocity magnitude ($|V|/U_{ref}$) along four horizontal lines at four different heights (h) from the ground floor; i.e. h = 0.1 m, 0.6 m, 1.1 m, and 1.7 m. Furthermore, the airflow pattern around and inside the building is analyzed.
The cases are designated as "A", referring to the reference case A, followed by the word "WindEav" or "LeeEav", referring to windward eaves or leeward eaves, respectively. The number following "Eav" is related to the inclination angle of the eaves (-45°, -27°, 0°, 27°, 45°, 90°). The negative or positive sign indicates an eaves rotation downwards or upwards with respect to the horizontal position (Figure 4.6b). All the studied windward and leeward eaves building cases have the same internal volume, the same inlet and outlet opening size, and the same inlet and outlet opening location.

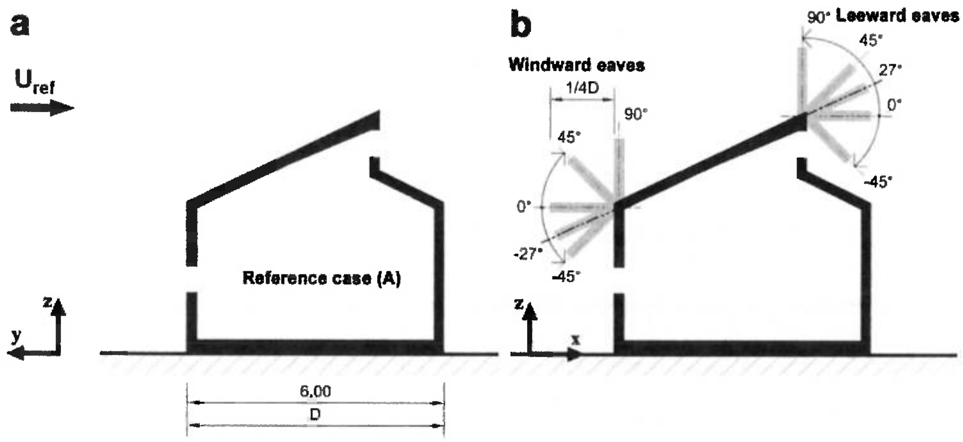

Figure 4.6: (a) Vertical cross-section of the reference case (geometry A). (b) Vertical cross-section with schematic indication of the windward and leeward eaves configuration cases. The length of the eaves is 1/4D.

4.5.1 Impact of windward eaves on ventilation

4.5.1.1 Volume flow rate

Figure 4.7a shows that the windward eaves configuration has a significant impact on the volume flow rate. Windward eaves with inclination angles lower than 0° increase the volume flow rate compared to the reference case. For instance, windward eaves with the same inclination angle as the roof (-27°; A_WindEav-27) increase the volume flow rate by 15%. For case A_WindEav-45 (-45°), this increase is 8%. However, windward eaves with inclination angles higher than 0° decrease the volume flow rate;

windward eaves with an angle of 90° (A_WindEav90) have the worst performance (84%) and windward eaves with an angle of 45° (A_WindEav45) result in a decrease of the volume flow rate to 90% (10% decrease). These results indicate that large parapets located at the lower part of the roof, as is the case for the windward eaves configuration with an angle of 90° (A_WindEav90), should be avoided from a ventilation point of view. Note that eaves with an angle of 0° (A_WindEav0), i.e. horizontal eaves, result in a volume flow rate which is almost equal (99%) to the situation without eaves.

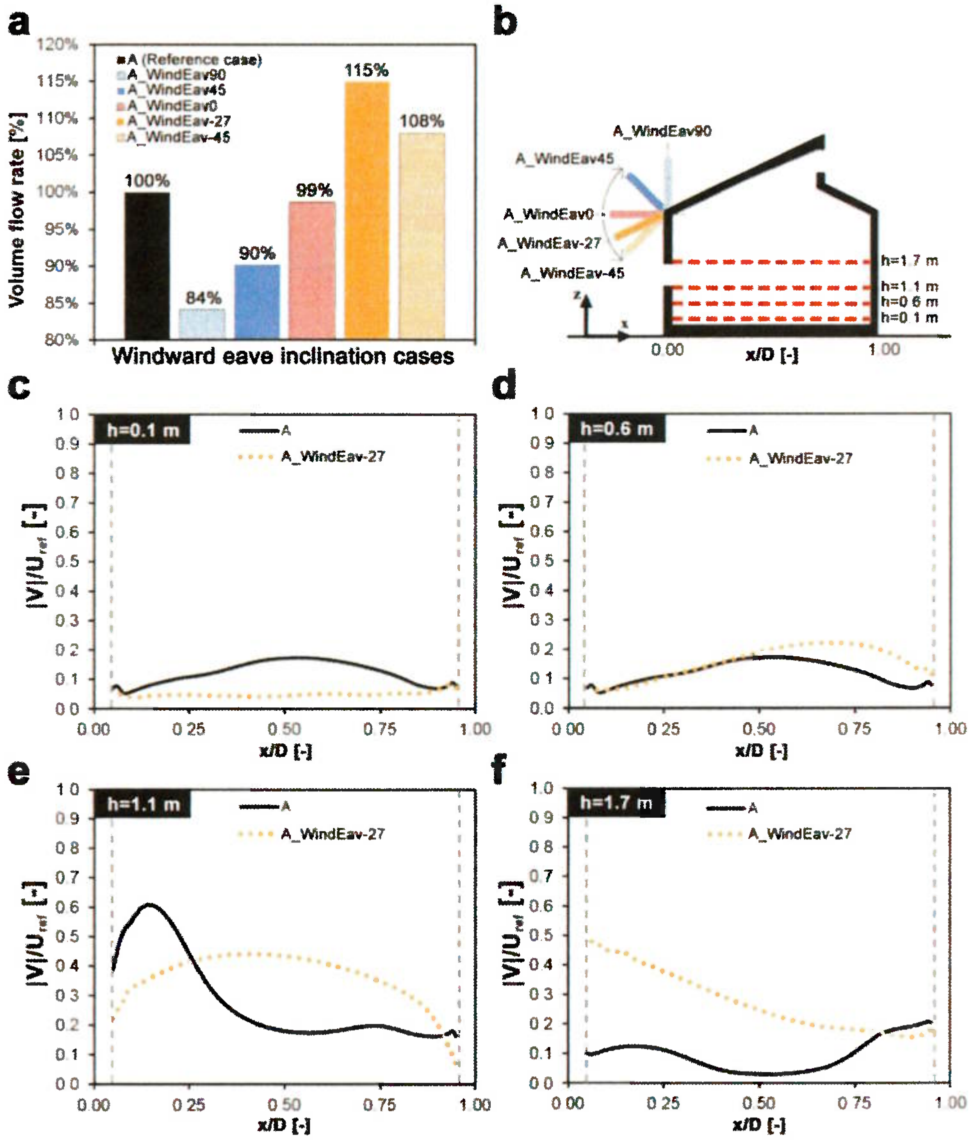

Figure 4.7: (a) Impact of the windward eave inclination angle on the volume flow rate under normal wind incidence angle; (b) Eaves configurations and location of the four horizontal lines. (c-f) Non-dimensional velocity magnitude ($|V|/U_{ref}$) for cases A and A_WindEav-27 along four horizontal lines at a height h above the floor: (c) h = 0.1 m. (d) h = 0.6 m. (e) h = 1.1 m (f) h = 1.7 m. The dashed vertical lines indicate the inner surface of the walls at the windward and leeward side of the building.

4.5.1.2 Air velocity

The impact of windward eaves on the non-dimensional velocity magnitude ($|V|/U_{ref}$) along four horizontal lines, located at a height of h = 0.1 m, 0.6 m, 1.1 m and 1.7 m from the internal floor (see Figure 4.7b), is shown in Figure 4.7c-f, by comparing the case with the highest volume flow rate (A_WindEav-27) with the reference case (A). The non-dimensional velocity magnitude in case A_WindEav-27 is increased in the higher level of the occupancy zone (i.e., at h = 0.6 m, 1.1 m and 1.7 m), in almost the whole internal region. For example, Figure 4.7d shows that the velocity magnitude increases over the last part of the horizontal centerline (from $0.5 < x/D < 1.0$). Figure 4.7e and Figure 4.7f clearly indicate that the indoor mean velocity is higher along the horizontal centerline at h = 1.1 m and at h = 1.7 m in the occupied zone. On the other hand, Figure 4.7c shows that the indoor mean velocity at h = 0.1 m is lower than in the reference case (A).

4.5.1.3 Airflow pattern

To provide a more elaborate analysis of the effect of the eaves configuration on the flow pattern around and inside the building, Figure 4.8 and Figure 4.9 show contours of the pressure coefficient (C_P) and non-dimensional velocity magnitude ($|V|/U_{ref}$) for all cases. The pressure coefficient C_P is calculated as follows:

$$C_P = \frac{(P - P_0)}{(0.5\rho U_{ref}^{\ 2})} \qquad (6)$$

where P is the static pressure, P_0 the reference static pressure, ρ the density of air (= 1.225 kg/m^3: International Standard Atmosphere (ISA); dry air, θ_a = 15°C, p_0 = 101,325 Pa [43]), and U_{ref} is the approach-flow wind speed at building height (U_{ref} = 12.48 m/s at z_{ref} = 5.7 m).

Figure 4.8 shows that windward eaves with inclination angles higher than 0° increase the overpressure in front of the building but that they decrease the (absolute value of the) underpressure behind the building. The net result is the lower airflow rate shown in Figure 4.7a. The static pressure increase in front of the building is caused by the larger blockage of the flow by the building with eaves [34, 44-46]. The decrease of the absolute value of the static pressure behind the building is due to the changed flow separation. Indeed, due to the presence of the eaves, the flow separates at the top of these eaves, and seems to not reattach anymore to the roof, or only near the end of the roof. Figure 4.8 also shows that the direction of the jet entering the building is not significantly influenced by the presence of windward eaves.

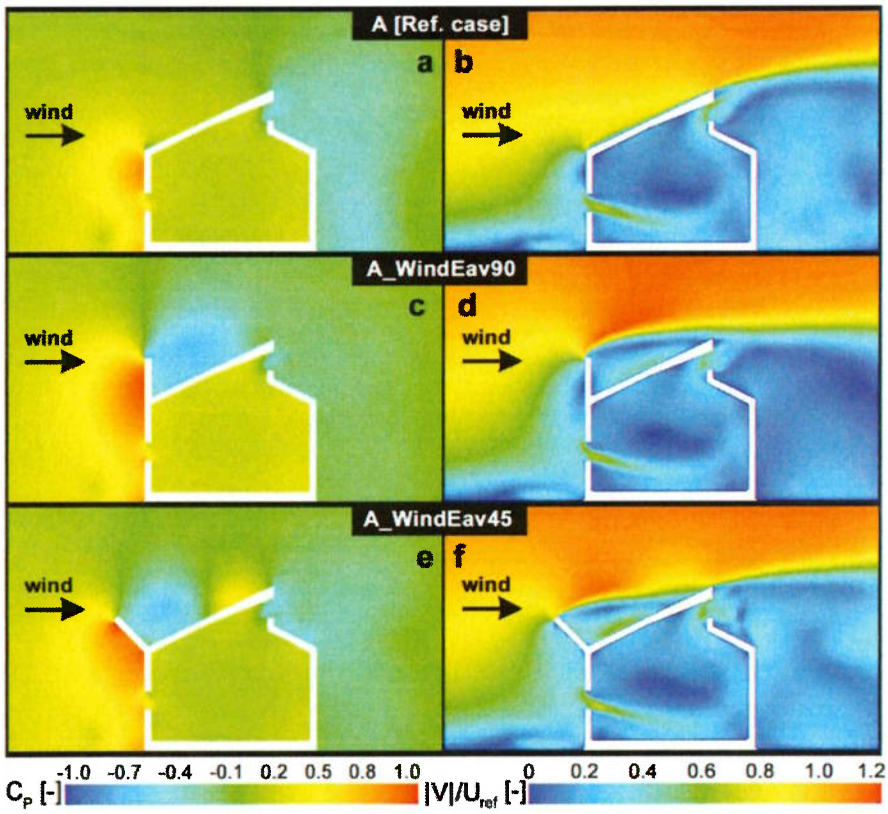

Figure 4.8: Contour plot of the pressure coefficient C_P. (a,c,e) and the non-dimensional velocity magnitude ($|V|/U_{ref}$) (b,d,f) in the vertical center plane for the reference case and for two windward eave geometries: A_WindEav90 and A_WindEav45.

Figure 4.9 shows that windward eaves with inclination angles lower than 0° decrease the overpressure in front of the building, while the (absolute value of the) underpressure behind the building remains approximately the same. The net result is that the magnitude of the pressure difference over the building decreases. At first sight, this should lead to a decrease of the flow rate through the building. However, the simulation results in Figure 4.7a show an increase. The reason for this is the direction of the flow through the inlet opening. Figure 4.9d and Figure 4.9f clearly show that the inlet jet has a more horizontal direction. This leads to a large effective opening area, or, in other words, a larger discharge coefficient. The changed direction of the inlet jet is the direct result of the altered static pressure distribution in front of the building. As can be seen in Figure 4.9c and Figure 4.9e, this distribution is more equal above and below the opening than in Figure 4.8a.

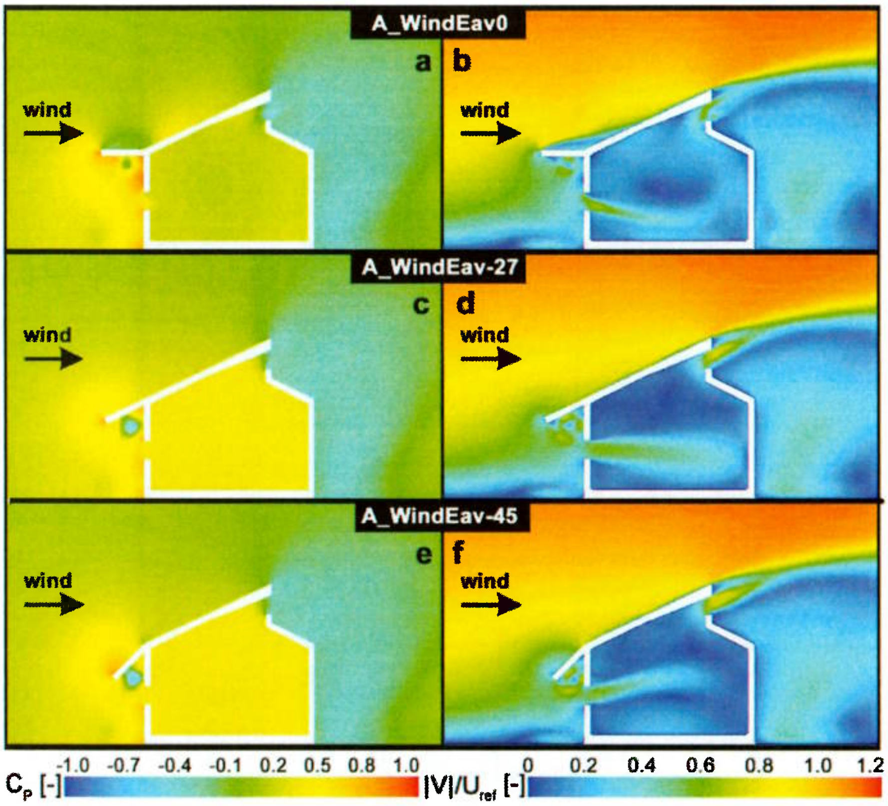

Figure 4.9: Contour plot of the pressure coefficient C_P. (a,c,e) and the non-dimensional velocity magnitude ($|V|/U_{ref}$) (b,d,f) in the vertical center plane for three windward eave geometries: A_WindEav0, A_WindEav-27 and A_WindEav-45.

4.5.2 Impact of leeward eaves on ventilation

4.5.2.1 Volume flow rate

Leeward eaves have a smaller impact on the volume flow rate than windward eaves, as can be seen by comparing Figure 4.7a with Figure 4.10a. Leeward eaves with an inclination angle of 45° (A_LeeEav45) and 90° (A_LeeEav90) result in an increase of the volume flow rate with 5% and 6% compared to the reference case, respectively. However, leeward eaves with an inclination angle of 0° (A_LeeEav0) and -45° (A_LeeEav-45) result in a decrease of the volume flow rate with 8% and 9%, respectively. The leeward eaves with an inclination angle equal to that of the roof (A_LeeEav27) results in a volume flow rate that is equal to that of the reference case. These results show that interferences or blocking objects near the outlet opening in the wake of the building should be avoided. In other words, leeward eaves with angles smaller than the roof angle should not be applied. Moreover, leeward eaves with inclination angles higher than the roof angle (27°) are recommended to increase the volume flow rate.

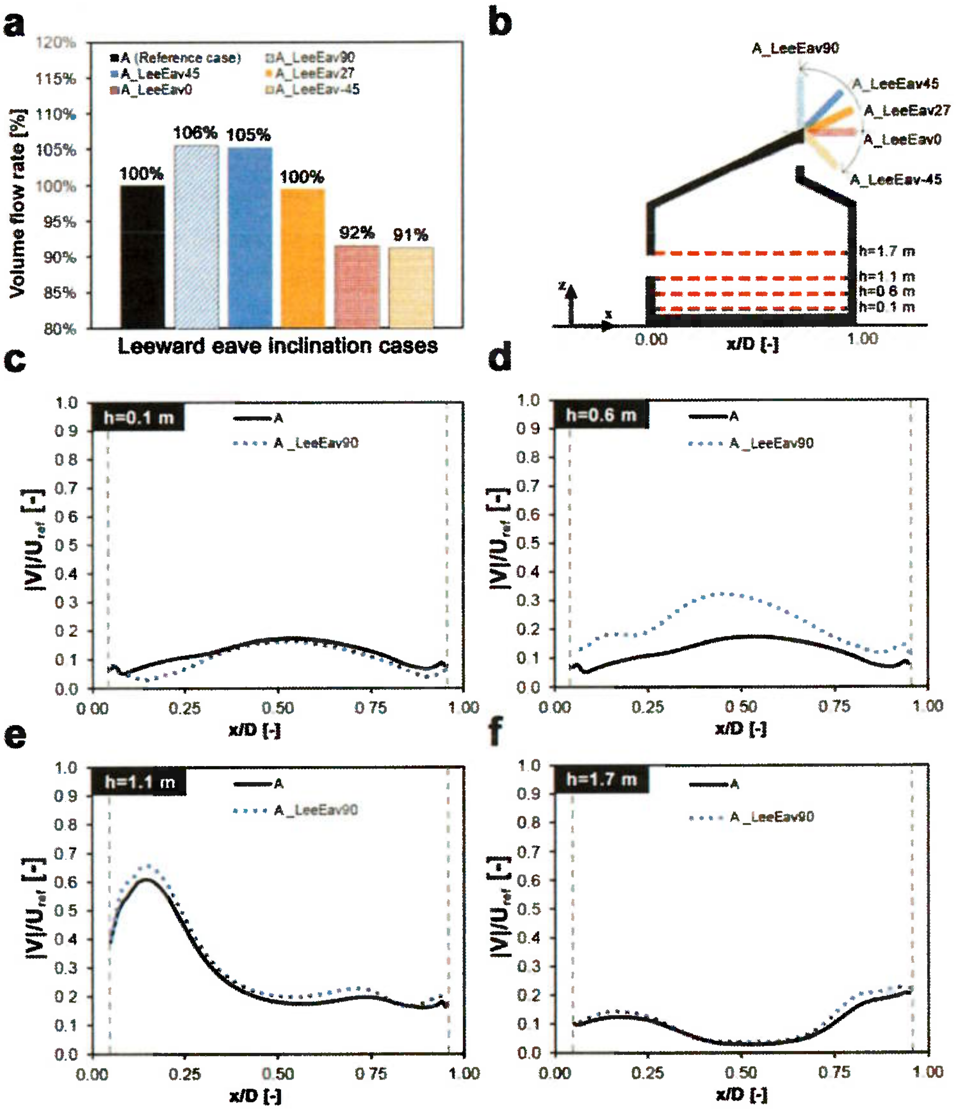

Figure 4.10: (a) Impact of the leeward eave inclination angle on the volume flow rate under normal wind incidence angle; Non-dimensional velocity magnitude ($|V|/U_{ref}$) along four horizontal lines at a height h above the floor. (b) Location of the four lines. (c) h = 0.1 m. (d) h = 0.6 m. (e) h = 1.1 m (f) h = 1.7 m. The dashed vertical lines indicate the inner surface of the walls at the windward and leeward side of the building.

4.5.2.2 Air velocity

Figure 4.10c-f shows a comparison of the non-dimensional velocity magnitude ($|V|/U_{ref}$) inside the building between case A_LeeEav90, which is the case with the highest volume flow rate, and the reference case. It can be seen that the influence of a leeward eaves is smaller than of a windward eaves; however, there is still a clear impact on the mean indoor air velocities. The leeward eaves (A_LeeEav90) increases the indoor velocity mainly in the lower part of the occupied zone (i.e. at h = 0.6 m; Figure 4.10d). Figure 4.10e-f shows that the velocities in the upper part of the enclosure are nearly equal to those in the reference case.

4.5.2.3 Airflow pattern

Figure 4.11and Figure 4.12 show contours of the pressure coefficient (C_P) and non-dimensional velocity magnitude ($|V|/U_{ref}$) for all cases. Figure 4.11 shows that leeward eaves with inclination angles higher than the roof slope have little effect on the overpressure in front of the building but that they increase the (absolute value of the) underpressure behind the building. The net result is the higher airflow rate as shown in Figure 4.10a. The increase of the absolute value of the static pressure behind the building is due to the changed flow separation. Indeed, due to the presence of the eaves, the flow separates at the top of these eaves, and this yields a larger wake with stronger underpressure. Figure 4.11 also shows that the direction of the jet entering the building is not significantly influenced by the presence of these leeward eaves.

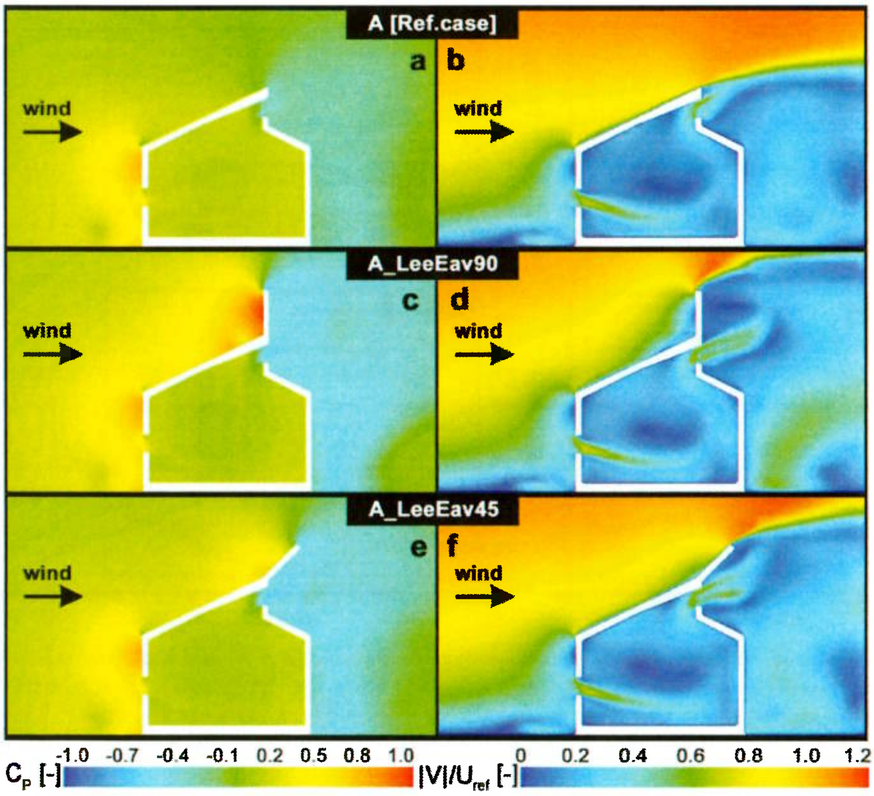

Figure 4.11: Contour plot of the pressure coefficient C_P (a,c,e) and the non-dimensional velocity magnitude ($|V|/U_{ref}$) (b,d,f) in the vertical center plane for the reference case and for two leeward eave geometries: A_LeeEav90 and A_LeeEav45.

Figure 4.12 shows that leeward eaves with inclination angles lower than the roof slope also have little effect on the overpressure in front of the building, but that they decrease the (absolute value of the) underpressure behind the building remains. The net result is the lower airflow rate shown in Figure 4.10a. Figure 4.12 also shows that the direction of the jet entering the building is not significantly influenced by the presence of the leeward eaves.

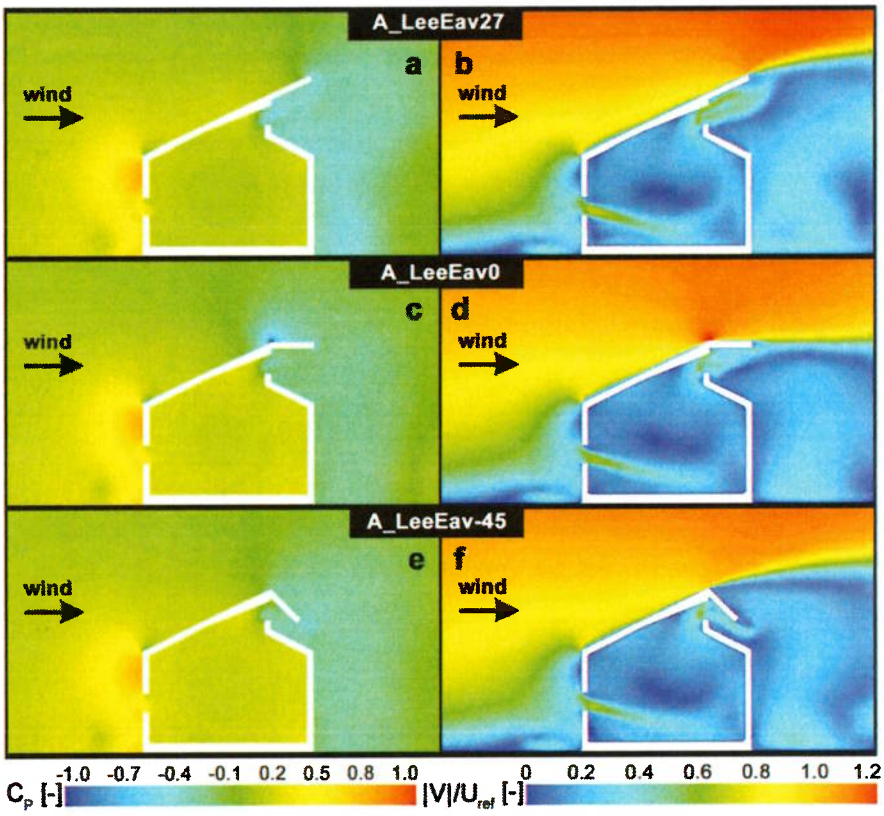

Figure 4.12: Contour plot of the pressure coefficient C_P (a,c,e) and the non-dimensional velocity magnitude ($|V|/U_{ref}$) (b,d,f) in the vertical center plane for tree leeward eave geometries: A_LeeEav27, A_LeeEav0 and A_LeeEav45.

4.6 Combination of windward and leeward eaves

Figure 4.13 shows the volume flow rates for case A (reference case) and for the two cases selected to evaluate the coupled effect of windward and leeward eaves: A_WindEav-27_LeeEav27 and A_WindEav-27_LeeEav90. These two cases combine windward eaves with an inclination angle of -27° (A_WindEav-27), which showed the best performance in Section 4.5.1, with two different leeward eaves configurations: (a) A_LeeEav27 and, (b) A_LeeEav90. The former has the same inclination angle as the roof; i.e. 27°, while the latter is the best leeward eaves configuration, as presented in Section 4.5.2. Note that the aim of this study is to maximize the volume flow rate through a naturally ventilated building. Therefore, possible combinations of other windward and leeward eaves angles have not been analyzed, since the individual performance of other windward and leeward eaves inclination angles is inferior to that of aforementioned angles. Figure 4.13 shows the increase in the volume flow rate obtained by the coupled effect of windward and leeward eaves. From the two cases analyzed, A_WindEav-27_LeeEav90 yields the highest increase, with a 24% higher volume flow rate compared to the reference case (A). It shows that the coupled effect of the windward and the leeward eaves for case A_WindEav-27_LeeEav90 increases the volume flow rate by an additional 3% compared to the sum of the isolated increases; i.e. 15% for A_WindEav-27 and 6% for A_LeeEav90. The A_WindEav-27_LeeEav27 case results in the same increase of the volume flow rate as in the isolated case A_WindEav-27, which can be explained by the fact that the volume flow rate did not increase for A_LeeEav27 (see Section 4.5.2.1).

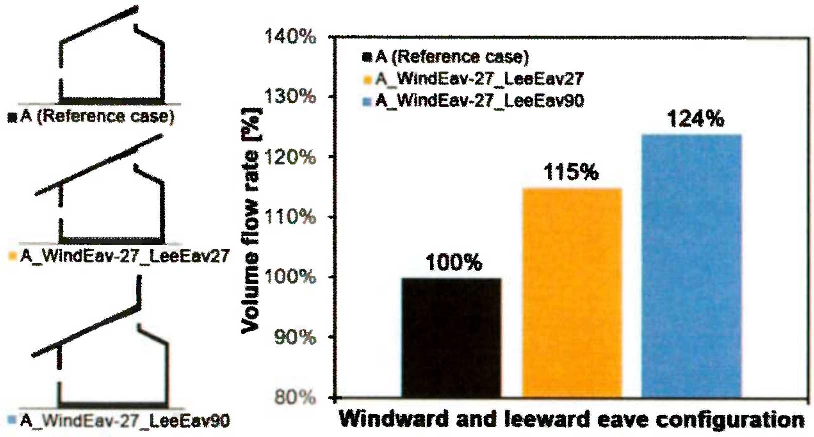

Figure 4.13: Influence of the combination of windward and leeward eaves (A_WindEav-27_LeeEav27 and A_WindEav-27_LeeEav90) on the volume flow rate.

Figure 4.14 displays the pressure coefficient C_P and the non-dimensional velocity magnitude ($|V|/U_{ref}$) inside and around the building for the reference case and the cases A_WindEav-27_LeeEav90 and A_WindEav-27_LeeEav27. Figure 4.14a,c,e shows that the size and magnitude of the underpressure zone are clearly highest for the case A_WindEav-27_LeeEav90. Figure 4.14d and Figure 4.14f again show that for the cases A_WindEav-27_LeeEav27 and A_WindEav-27_LeeEav90 the incoming stream flow follows a more horizontal direction compared to the reference case (Figure 4.14b), contributing to a higher airflow rate.

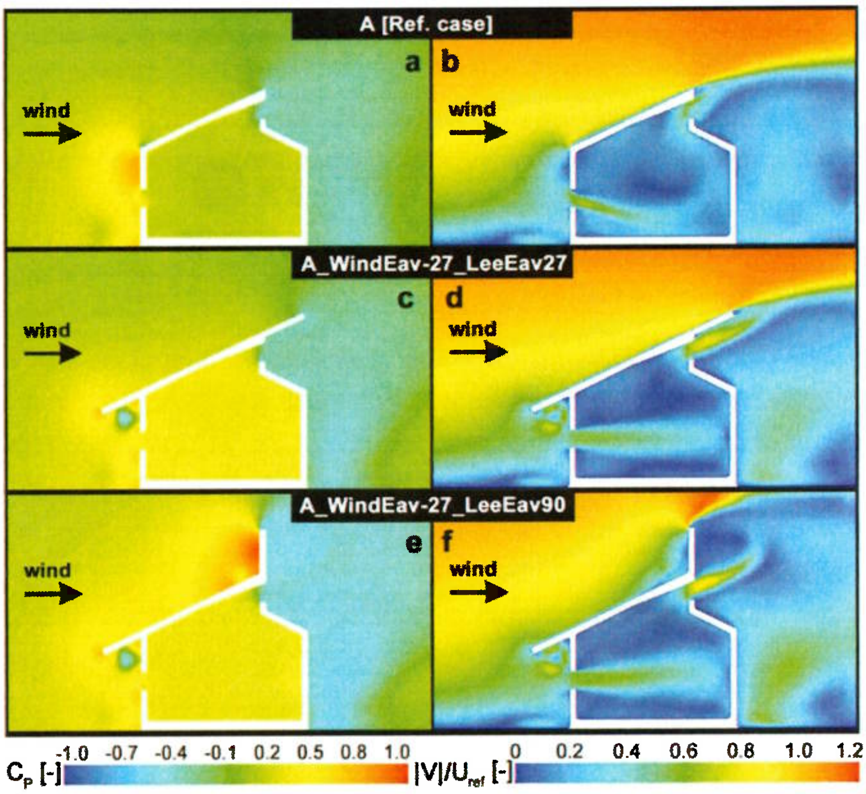

Figure 4.14: Contour plot of the pressure coefficient C_P (a,c,e) and the non-dimensional velocity magnitude ($|V|/U_{ref}$) (b,d,f) in the vertical center plane for the reference case and for A_WindEav-27_LeeEav27 and A_WindEav-27_LeeEav90.

4.7 Discussion

The main goal of this study on upward wind-driven cross-ventilation is to evaluate the impact of the eaves configuration for a normal wind incidence angle (φ = 0°). First, five windward eaves configurations are evaluated, followed by five leeward eaves configurations. Finally, two cases that have both windward and leeward eaves (A_WindEav-27_LeeEav27, A_WindEav-27_LeeEav90) are analyzed to study the combined effect. It is important to mention the limitations of the current study, which should be addressed in future studies:

- Surrounding buildings can have a large influence on the ventilation flow through the building. Therefore, the impact of surrounding buildings needs to be assessed in future work.
- Temperature effects (buoyancy) can alter the flow pattern in and around the building, especially when low wind velocities are present. Future studies can focus on the combined effects of wind and buoyancy on the ventilation flow in the building.
- This study focuses on a normal wind incidence angle (φ = 0°). The impact of wind incidence angles different than 0° should be considered as well, since this can influence the ventilation performance of the different eaves configurations. For more oblique wind incidence angles it might be necessary to resort to unsteady simulations, such as Large Eddy Simulations (LES) or Detached Eddy Simulation (DES), to accurately predict the transient flow features around the

building in general and near the openings in particular, and thus to obtain accurate volume flow rates (e.g. [47,48]).

- Future studies can include other effects of windward and leeward eaves, e.g. the protection of the building interior and exterior from wind-driven rain and solar shading, to provide an integral analysis of the application of eaves to buildings.

4.8 Conclusions

This paper presents numerical simulations to study the impact of windward and leeward eaves on the wind-driven cross-ventilation flow in a generic isolated leeward sawtooth roof building. The study is performed by isothermal CFD simulations with the 3D steady RANS approach and the SST k-ω turbulence model. The computational grid is based on a grid-sensitivity analysis and the computational model is validated using Particle Image Velocimetry (PIV) wind-tunnel measurements from literature. The main conclusions of this paper are:

a) Windward eaves with inclination angles lower than 0° increase the volume flow rate compared to the reference case. The largest increase is obtained when a windward eaves with an inclination angle of -27° (A_WindEav-27) is applied: +15%. On the other hand, windward eaves with inclination angles higher than 0° decrease the volume flow rate with up to 16% for A_WindEav90. A horizontal eaves (0° inclination) results in a volume flow rate which is almost equal to the reference case.
b) The jet flow that enters the building is more horizontally directed when windward eaves are applied with inclination angles lower than 0°. The different direction is the result of an altered distribution of the static pressure above and below the inlet opening. For a given pressure difference between windward and leeward facade, the more horizontal direction leads to a higher volume flow rate.
c) Application of leeward eaves with an inclination angle of 45° (A_LeeEav45) and 90° (A_LeeEav90) results in an increase of the volume flow rate with 5% and 6%, respectively. Leeward eaves with an inclination angle of 0° (A_LeeEav0) and -45° (A_LeeEav-45) result in a decrease of the volume flow rate with 8% and 9%, respectively. A leeward eaves with an inclination angle of 27° results in the same volume flow rate as in the reference case.
d) Interferences or blocking objects near the outlet opening, in the wake of the building, should be avoided. In other words, leeward eaves with angles smaller than the roof angle should not be applied. Moreover, leeward eaves with inclination angles higher than the roof angle (27°) are recommended to increase the volume flow rate.
e) In general, to improve the volume flow rate in the studied low-rise leeward sawtooth roof building, the windward eaves inclination angle must be lower than 0°, such as -27° or -45°, and the inclination of the leeward eaves must be higher than 27°, for instance 45° or 90°. The coupled effect of the eaves (windward and leeward eaves working together) can be larger than the individual effects: applying the best performing windward and leeward eaves simultaneously (i.e. A_WindEav-27_LeeEav90) can increase the volume flow rate with an additional 3% compared to the sum of the two individual effects.

4.9 Acknowledgements

This work was supported by The Coordination for the Improvement of Higher Level Personnel (CAPES), Brazil, The Civil Construction Engineering Department, Polytechnic School of the University of São Paulo (USP), Brazil and the unit Building Physics and Services of the Department of the Built Environment at Eindhoven University of Technology in the Netherlands.

Twan van Hooff is currently a postdoctoral fellow of the Research Foundation – Flanders (FWO) and acknowledges its financial support (project FWO 12R9715N).

4.10 References

[1] Bojić M. Application of overhangs and side fins to high-rise residential buildings in Hong Kong. Civ Eng Environ Syst 2006;23:271–85. doi:10.1080/10286600600888532. 10.

[2] Song WT, Lin G, Wu Z-Y. Computer-supported methodologies to estimate the eave effect on building energy consumption. Proc. 2014 IEEE 18th Int. Conf. Comput. Support. Coop. Work Des. CSCWD, 2014, p. 721–6. doi:10.1109/CSCWD.2014.6846934.

[3] Raeissi S, Taheri M. Optimum overhang dimensions for energy saving. Build Environ 1998;33:293–302.

[4] Chiang WH, Hsu HH, Huang JS. Façade design effect on cross-ventilation in Taiwanese school buildings. J Green Build 2013;8:90–111. doi:10.3992/jgb.8.2.90.

[5] Robertson AP. Effect of eaves detail on wind pressures over an industrial building. J Wind Eng Ind Aerodyn 1991;38:325–33.

[6] Stathopoulos T, Luchian H. Wind-induced forces on eaves of low buildings. J Wind Eng Ind Aerodyn 1994;52:249–61. doi:10.1016/0167-6105(94)90051-5.

[7] Savory E, Dalley S, Toy N. The effects of eaves geometry, model scale and approach flow conditions on portal frame building wind loads. J Wind Eng Ind Aerodyn 1992;43:1665–76. doi:10.1016/0167-6105(92)90576-V.

[8] Stathopoulos T, Baskaran A. Wind pressures on flat roofs with parapets. J Struct Eng ASCE 1987;113:2166–80.

[9] Kopp GA, Surry D, Mans C. Wind effects of parapets on low buildings: Part 1. Basic aerodynamics and local loads. J Wind Eng Ind Aerodyn 2005;93:817–41. doi:10.1016/j.jweia.2005.08.006.

[10] Ishikawa H. Method for estimating rain-wetting patterns over external walls of low-rise buildings in accordance with shapes and sizes of the eaves overhangs. J Struct Constr Eng 2011;76:1069–75. doi:10.3130/aijs.76.1069.

[11] Tsutsumi T, Sato T, Tomabechi T, Chiba T. Experimental studies of snow condition on louvered eaves of building. AIJ J Technol Des 2010;16:59–62. doi:10.3130/aijt.16.59.

[12] Thiis TK, Barfoed P, Delpech P, Gustavsen A, Hofseth V, Uvsløkk S, et al. Penetration of snow into roof constructions—Wind tunnel testing of different eaves cover designs. J Wind Eng Ind Aerodyn 2007;95:1476–85. doi:10.1016/j.jweia.2007.02.017.

[13] Oztop HF, Varol Y, Koca A. Laminar natural convection heat transfer in a shed roof with or without eaves for summer season. Appl Therm Eng 2007;27:2252–65. doi:10.1016/j.applthermaleng.2007.01.018.

[14] Kindangen JI. Window and roof configurations for comfort ventilation. Build Res Inf 1997;25:218–25. doi:10.1080/096132197370345.

[15] Kindangen J, Krauss G, Depecker P. Effects of roof shapes on wind-induced air motion inside buildings. Build Environ 1997;32:1–11.

[16] Perén JI, van Hooff T, Leite BCC, Blocken B. CFD analysis of cross-ventilation of a generic isolated building with asymmetric opening positions: impact of roof angle and opening location. Build Environ 2015;85:263–76. doi:10.1016/j.buildenv.2014.12.007.

[17] Perén JI, Ramponi R, van Hooff T, Blocken B, Leite BCC. Impact of roof geometry of an isolated leeward sawtooth-roof building on cross-ventilation: Straight, concave, hybrid or convex? Submitted 2014.

[18] International Organization for Standardization. Ergonomics of the thermal environment - Analytical determination and interpretation of thermal comfort using calculation of the PMV and PPD indices and local thermal comfort criteria (ISO 7730:2005). European Committee for Standardization, Brussels, Belgium: 2005.

[19] Blocken B. 50 years of Computational Wind Engineering: Past, present and future. J Wind Eng Ind Aerodyn 2014;129:69–102. doi:10.1016/j.jweia.2014.03.008.

[20] Stathopoulos T. Computational wind engineering: Past achievements and future challenges. J Wind Eng Ind Aerodyn 1997;67–68:509–32. doi:10.1016/S0167-6105(97)00097-4.

[21] Mochida A, Lun IYF. Prediction of wind environment and thermal comfort at pedestrian level in urban area. J Wind Eng Ind Aerodyn 2008;96:1498–527. doi:10.1016/j.jweia.2008.02.033.

[22] Chen Q. Ventilation performance prediction for buildings: A method overview and recent applications. Build Environ 2009;44:848–58. doi:10.1016/j.buildenv.2008.05.025.

[23] Blocken B, Stathopoulos T, Carmeliet J, Hensen JLM. Application of computational fluid dynamics in building performance simulation for the outdoor environment: An overview. J Build Perform Simul 2011;4:157–84. doi:10.1080/19401493.2010.513740.

[24] Ramponi R, Blocken B. CFD simulation of cross-ventilation for a generic isolated building: Impact of computational parameters. Build Environ 2012;53:34–48. doi:10.1016/j.buildenv.2012.01.004.

[25] Kato S, Murakami S, Mochida A, Akabayashi S, Tominaga Y. Velocity-pressure field of cross ventilation with open windows analyzed by wind tunnel and numerical simulation. J Wind Eng Ind Aerodyn 1992;44:2575–86. doi:10.1016/0167-6105(92)90049-G.

[26] Horan JM, Finn DP. Sensitivity of air change rates in a naturally ventilated atrium space subject to variations in external wind speed and direction. Energy Build 2008;40:1577–85. doi:10.1016/j.enbuild.2008.02.013.

[27] van Hooff T, Blocken B. Coupled urban wind flow and indoor natural ventilation modelling on a high-resolution grid: A case study for the Amsterdam Arena stadium. Environ Model Softw 2010;25:51–65. doi:10.1016/j.envsoft.2009.07.008.

[28] van Hooff T, Blocken B. On the effect of wind direction and urban surroundings on natural ventilation of a large semi-enclosed stadium. Comput Fluids 2010;39:1146–55. doi:10.1016/j.compfluid.2010.02.004.

[29] Karava P, Stathopoulos T, Athienitis AK. Airflow assessment in cross-ventilated buildings with operable façade elements. Build Environ 2011;46:266–79. doi:10.1016/j.buildenv.2010.07.022.

[30] Karava P. Airflow prediction in buildings for natural ventilation design: wind tunnel measurements and simulation. Department of Building, Civil and Environmental Engineering, Concordia University, 2008.

[31] Franke J, Hellsten A, Schlunzen KH, Carissimo B. Best Practice Guideline for CFD simulation of flows in the urban environment. Bruss COST 2007. doi:10.1504/IJEP.2011.038443.

[32] Tominaga Y, Mochida A, Yoshie R, Kataoka H, Nozu T, Yoshikawa M, et al. AIJ guidelines for practical applications of CFD to pedestrian wind environment around buildings. J Wind Eng Ind Aerodyn 2008;96:1749–61. doi:10.1016/j.jweia.2008.02.058.

[33] Blocken B, Stathopoulos T, Carmeliet J. CFD simulation of the atmospheric boundary layer: wall function problems. Atmos Environ 2007;41:238–52. doi:10.1016/j.atmosenv.2006.08.019.

[34] Blocken B, Carmeliet J, Stathopoulos T. CFD evaluation of wind speed conditions in passages between parallel buildings—effect of wall-function roughness modifications for the atmospheric boundary layer flow. J Wind Eng Ind Aerodyn 2007;95:941–62. doi:10.1016/j.jweia.2007.01.013.

[35] Blocken B. Computational Fluid Dynamics for Urban Physics: Importance, scales, possibilities, limitations and ten tips and tricks towards accurate and reliable simulations. Build Environ 2015. doi:10.1016/j.buildenv.2015.02.015

[36] ANSYS. Fluent 12 user's guide. Lebanon: Fluent Inc. 2009.

[37] Menter FR. Two-equation eddy-viscosity turbulence models for engineering applications. AIAA J 1994;32:1598–605.

[38] van Hooff T, Blocken B, Aanen L, Bronsema B. A venturi-shaped roof for wind-induced natural ventilation of buildings: Wind tunnel and CFD evaluation of different design configurations. Build Environ 2011;46:1797–807. doi:10.1016/j.buildenv.2011.02.009.

[39] Montazeri H, Blocken B, Janssen WD, van Hooff T. CFD evaluation of new second-skin facade concept for wind comfort on building balconies: Case study for the Park Tower in Antwerp. Build Environ 2013;68:179–92. doi:10.1016/j.buildenv.2013.07.004.

[40] Wieringa J. Updating the Davenport roughness classification. J Wind Eng Ind Aerodyn 1992;41:357–68. doi:10.1016/0167-6105(92)90434-C.

[41] Launder BE, Spalding DB. The numerical computation of turbulent flows. Comput Methods Appl Mech Eng 1974;3:269–89. doi:10.1016/0045-7825(74)90029-2.

[42] Cebeci T, Bradshaw P. Momentum transfer in boundary layers. Hemisphere Publishing Corp. New York: 1977.

[43] ISO 2533. International Organization for Standardization. Standard Atmosphere. International Standards Organization; 1975.

[44] Blocken B, Carmeliet J. The influence of the wind-blocking effect by a building on its wind-driven rain exposure. J Wind Eng Ind Aerodyn 2006;94(2): 101-127.

[45] Blocken B, Stathopoulos T, Carmeliet J. Wind environmental conditions in passages between two long narrow perpendicular buildings. J Aerospace Eng - ASCE. 2008;21(4): 280-287.

[46] Blocken B, Moonen P, Stathopoulos T, Carmeliet J. A numerical study on the existence of the Venturi-effect in passages between perpendicular buildings. J Eng Mech - ASCE 2008;134(12): 1021-1028.

[47] Jiang Y, Chen Q. Study of natural ventilation in buildings by large eddy simulation. J Wind Eng Ind Aerodyn 2001;89(13):1155-1178.

[48] Wright NG, Hargreaves DM. Unsteady CFD simulations for natural ventilation. Int J Vent 2006;5(1):13-20.

Chapter 5

CFD simulations of wind-driven upward cross ventilation and its enhancement in long buildings: Impact of single-span versus double-span leeward sawtooth roof and opening ratio

Published as:

Perén JI, van Hooff T, Blocken B, Leite BCC. CFD simulations of wind-driven upward cross-ventilation and its enhancement in long buildings: Impact of single-span versus double-span leeward sawtooth roof and opening ratio. Submitted.

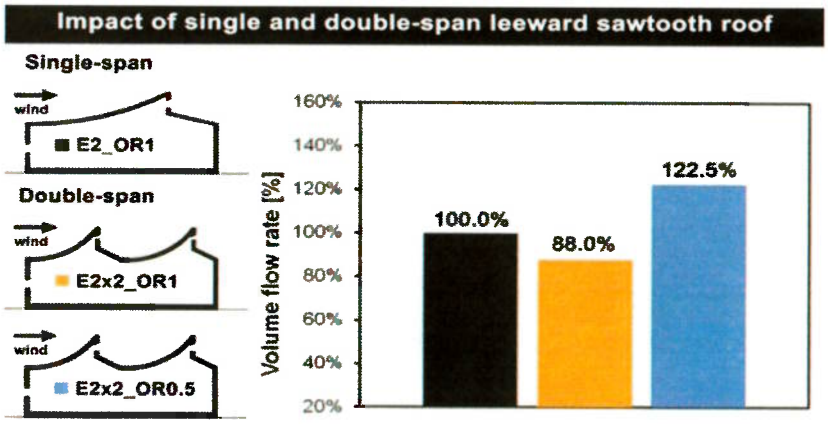

5 CFD simulations of wind-driven upward cross ventilation and its enhancement in long buildings: Impact of single-span versus double-span leeward sawtooth roof and opening ratio

Abstract

A leeward sawtooth roof building has an inlet opening in the lower level of the windward facade and an upper-level outlet opening near the roof top, in the leeward facade. Leeward sawtooth roof buildings can be applied to efficiently ventilate low-rise buildings. Previous studies of the authors showed that the size and magnitude of the underpressure region (wake) behind the building strongly depends on the roof inclination angle and roof geometry. The current study focuses on the ventilation flow in single-zone elongated low-rise buildings with a single-span and a double-span leeward sawtooth roof and different opening ratio. First, three single-span leeward sawtooth roof geometries (straight, convex and concave roof; roof inclination angle = 18°) are analyzed for a normal wind direction. Subsequently, the single-span cases are compared to the double-span cases. The analysis is performed using 3D steady Reynolds-averaged Navier-Stokes Computational Fluid Dynamics (CFD) simulations with the SST k-ω turbulence model. The computational grid is based on a grid-sensitivity analysis and the simulation results are validated based on Particle Image Velocimetry (PIV) measurements from literature. For the single-span cases, a convex roof geometry results in the highest volume flow rate, which is about 8.8% higher than for a concave roof geometry, and 3.5% higher than for a straight roof geometry. A double-span roof performs slightly better than a single-span roof with respect to ventilation flow rates (within 4.2%) in case of a straight or concave roof , but worse in case of a convex roof geometry (-12%). In addition, the internal roof geometry near the outlet opening plays an important role in the ventilation of the building. Finally, the inlet-to-outlet opening ratio has an important effect on the volume flow rates, with significantly higher ventilation flow rates for a lower opening ratio.

Keywords: Computational Fluid Dynamics (CFD), Natural ventilation, Leeward sawtooth roof geometry, Upward cross-ventilation, Double-span leeward sawtooth roof building.

5.1 Introduction

Elongated naturally-ventilated buildings are used in a wide range of applications, such as hospitals, schools, industrial facilities, commercial buildings and even residential buildings in some specific cases. However, in elongated naturally-ventilated buildings, the cross-ventilation efficiency can become critical as the ventilation rate decreases with the building length [1]. Long low-rise buildings with a flat roof require a significant increase of the pressure differences over the building to overcome the higher indoor resistance due to the larger distance between the inlet and outlet opening. However, buildings with side-wall and roof openings can increase the ventilation flow rate [2,3] and can therefore be an option for the ventilation of elongated buildings. For instance, a leeward sawtooth roof building, with inlet openings at the lower part of the windward facade and outlet openings at roof level, might still achieve enough efficient cross-ventilation in elongated buildings. Furthermore, compared to elongated buildings with a flat roof, buildings with a leeward sawtooth roof can achieve more uniform and higher daylight intensity levels due to the openings in the roof construction [4].

Previous studies by the authors on cross-ventilation of a single-span leeward sawtooth roof building showed that the volume flow rate depends on the roof inclination angle [5], the roof geometry [6] and the eaves configuration [7]. Concerning multi-span roof buildings, such as sawtooth roof buildings, previous studies focused on the wind loads [8,9] and others on the ventilation performance of greenhouses [2,3,10–13]. Bournet et al. [13] provided a review on the effect of ventilation opening configuration on the indoor climate of greenhouses and highlighted that the analysis of the response of a greenhouse to outdoor climatic conditions will help to better adjust ventilation management and to develop a more efficient ventilation design. However, so far, guidelines extracted from systematic studies of multi-span buildings are rare.

Therefore, the aim of the current study is to compare the performance of single-span and double-span leeward sawtooth roof configurations and to evaluate the effect of the opening ratio in an elongated long building. The ventilation performance evaluation is based on the volume flow rate through the building and the indoor air velocity in the occupied zone [14], considering that the ventilation rate is not always the best criteria for evaluating the performance of ventilation systems [3] .

Section 5.2 presents the building geometries that are studied. The validation study using Particle Image Velocimetry (PIV) measurements of upward cross-ventilation from literature is presented in Section 5.3, after which the CFD model for the case study is outlined in Section 5.4. The results are presented in Section 5.5. Discussion (Section 5.6) and conclusions (Section 5.7) conclude this paper.

5.2 Building geometries

Figure 5.1 is a schematic representation of the three groups of three different roof geometries selected for this study:

- three single-span cases (Figure 5.1a), with inlet-to-outlet opening ratio ($OR = A_{inlet}/A_{outlet;total} = 1$, with $A_{outlet;total}$ the sum of the two outlet openings areas) (same area for both openings);
- three double-span cases (Figure 5.1b) with the same inlet-to-outlet opening ratio ($OR = 1$). The outlet openings have the same width but only half the height as the inlet opening;
- three cases with the same double-span roof but with a lower opening ratio ($OR = 0.5$) (Figure 5.1c).

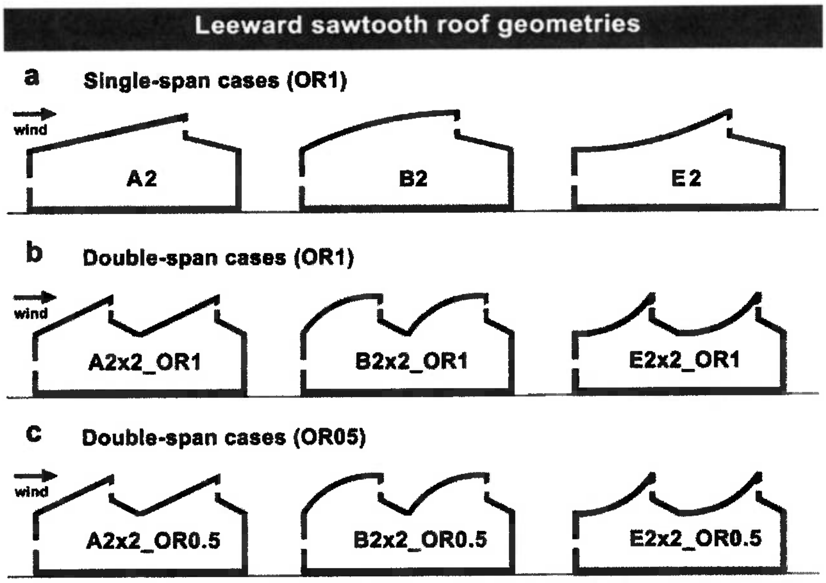

Figure 5.1: Longitudinal cross-section of the leeward sawtooth roof cases analyzed. (a) Single-span leeward sawtooth roof buildings: A2 (straight roof), B2 (concave roof) and E2 (convex roof); (b) double-span cases with opening ratio (OR) equal to those of the single-span cases (OR =1): A2x2_OR1, B2x2_OR1 and E2x2_OR1; (c) double-span cases with lower opening ratio than single-span cases (OR = 0.5): A2x2_OR0.5, B2x2_OR0.5 and E2x2_OR0.5.

The two outlet openings have the same width and the height as the inlet opening; The three different roof geometries are designated by a letter: A, B, and E, to refer to their base cases. These numbers originate from a previous study of the authors [6] focused on cross-ventilation of single-span buildings with a depth of 6 m, as opposed to 12 m in the present study. Geometry A has a straight roof, geometry B has a concave roof, and geometry E has a convex roof. Note that we adopt the definitions of "convex" and "concave" as used in the description of mathematical functions, where "a convex function is a continuous function whose value at the midpoint of every interval in its domain does not exceed the arithmetic mean of its values at the ends of the interval" [15]. For all cases, the number "2" after a letter (i.e., A2, B2, and E2) indicates that the depth of this geometry is two times the depth (D) of its base case in [6]. Since the base case has a horizontal plan area of 3 x 6 m^2 (W x D), the cases studied in this paper have a more elongated horizontal plan area of 3 x 12 m^2 (W x D). The double-span cases have two roofs (double span) and two outlet openings (one in each part of the double-span roof) instead of one and are therefore indicated with "x2" (i.e., A2x2, B2x2 and E2x2). The description "OR" stands for "opening ratio" and the subsequent number provides this ratio, i.e. 1 for the case with inlet opening area equal to the total outlet opening area and 0.5 for the case with total outlet opening area equal to two times the size of the inlet opening area. Note that Karava et al. [16] stated that higher volume flow rates can be achieved when the opening ratio is smaller than 1 ($A_{inlet}/A_{outlet} < 1$). The implicit roof inclination angle, which is the angle of a line from the upwind roof edge till the top roof edge, is 18° for all the single-span cases, and 27° for each span of the double-span cases. Note that the base cases (i.e., A, B, E) previously studied in [6] also have an implicit roof inclination angle of 27°.

Figure 5.2 shows a front view (Figure 5.2a), a vertical cross-section (Figure 5.2b) and a perspective view (Figure 5.2c) of the building with roof geometry E2 with its main dimensions. All studied geometries have the same: (a) maximum roof height (H = 5.7 m); (b) building depth (D = 12 m), (c) building width (W = 3 m); (d) inlet opening size (corresponding to 5% windward wall porosity); and, (e) inlet and outlet opening location (the outlet is located at ¾ D). Since all three buildings have different roof geometries, they all have a different internal volume, which are listed in Table 5.1. The distances from the ground to the bottom of the inlet and outlet opening are 1.42 m and 4.60 m, respectively.

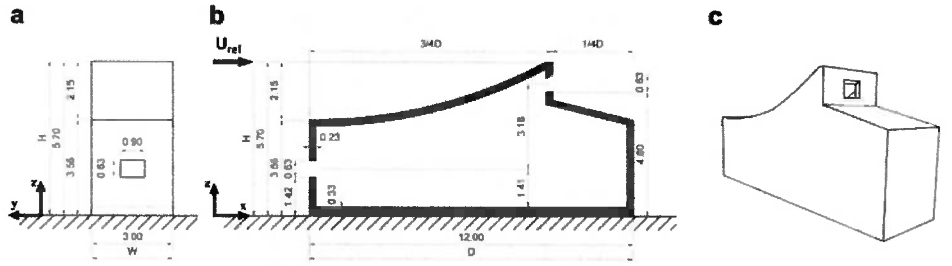

Figure 5.2: Overview of dimensions of case E2 (dimensions in m). (a) Front view (upwind facade) with opening size and dimensions. (b) Vertical cross-section with opening size and dimensions. (c) Perspective view. The other roof geometries (A,B) have the same roof height, facade porosity (inlet-outlet opening size), building depth and width; however, they have different roof geometries and consequently different internal volumes.

Table 5.1: Internal volume (m^3) of the building with different single and double-span roof geometries.

Building case name	Volume (m^3)
Single-span	
A2	118.63
B2	129.63
E2	112.14
Double-span	
A2x2	119.00
B2x2	131.04
E2x2	108.70

5.3 CFD simulations: validation study

Validation is obligatory to determine the accuracy and reliability of the results, when performing CFD simulations based on the 3D steady RANS equations [17–19]. A general overview of the validation study will be provided in this section, a more detailed description of the simulations and an elaborate discussion on the results can be found in another recent publication by the authors [5].

5.3.1 Wind-tunnel experiment

Karava et al. performed reduced-scale PIV wind-tunnel measurements of wind-induced cross-ventilation in a generic isolated building geometry [16]. The measurement results for the asymmetric location (upward cross-ventilation) of the openings are used for model validation. The dimensions of the reduced-scale building model (1:200) are 0.1 x 0.1 x 0.08 m^3 (W x D x H), corresponding to full-scale dimensions of: 20 x 20 x 16 m^3 (W x D x H), as shown in Figure 5.3a and Figure 5.3b. The openings have a fixed height of 0.018 m (3.6 m full scale), and for this validation study, the building model with an inlet opening at the bottom of the windward facade (center of the opening at h = 0.02 m) and an outlet opening at the top of the opposite (leeward) facade (center of the opening at h = 0.06 m) and with a wall porosity of 10% was selected. The reduced-scale aerodynamic roughness length was z_0 = 0.025 mm, which corresponds to 0.005 m in full scale [20]. The reference mean wind speed at building height (z_{ref} = H) was U_{ref} = 6.97 m/s and the reference turbulence intensity at building height was 10%. The turbulence intensity was about 17% near ground level (0.012 m) and 5% at gradient height (0.738 m). For more information related to the wind-tunnel experiments the reader is referred to [16].

5.3.2 CFD simulations: computational settings and parameters

The computational model represents the reduced-scale model used in the experiments and follows the best practice guidelines by Franke et al. [17], Tominaga et al. [18] and Blocken [19]. However, the upstream length of the domain is reduced to 3 times the height of the building to limit the development of unintended streamwise gradients [21,22]. The dimensions of the domain are 0.9 x 1.54 x 0.48 m^3 (W x D x H) at reduced-scale (1:200). The computational grid is created using the surface-grid extrusion technique by van Hooff and Blocken [23] and is shown inFigure 5.3c and Figure 5.3d (vertical cross-section and perspective close-up view). The grid resolution resulted from a grid-sensitivity analysis yielding a fully structured hexahedral grid with 770,540 cells. At the inlet of the domain the vertical approach-flow profiles (log-law mean wind speed U, turbulent kinetic energy k and specific dissipation rate ω) are imposed, based on the measured incident profiles of mean wind speed U and longitudinal turbulence intensity I_U of the experiment. More information on the boundary conditions can be found in Ref. [5]. The commercial CFD code ANSYS Fluent 12 is used to perform the simulations [24]. The 3D steady RANS equations are solved in combination with the shear-stress transport k-ω model (SST k-ω) [25]. The SIMPLE algorithm is used for pressure-velocity coupling, pressure interpolation is second order and second-order discretization schemes are used for both the convection terms and the viscous terms of the governing equations.

5.3.3 CFD validations results: comparison between CFD simulations and wind tunnel-measurements

Figure 5.3e and Figure 5.3f display the mean velocity vector field in the vertical center plane obtained from PIV measurements and CFD simulations, respectively. It is observed that the CFD simulations correctly predict the most important flow features. For example, the standing vortex upstream of the building, and also the specific character of the flow pattern inside the building, which exhibits a strong downward directed flow near the inlet opening followed by a strong upwards directed flow along the downstream wall, which leads to an oblique upward directed flow through the outlet opening. From Figure 5.3e,f, it can be concluded that a good agreement is present between the CFD simulation and the PIV experiments.

It can be noted that the geometry of the building in the wind-tunnel measurements by Karava et al.[16] (Figure 5.3) and that of the single-span and double-span buildings as presented in the current paper

(Figure 5.1) are not identical, but there is a sufficient degree of similarity to consider this validation approach applicable for the leeward sawtooth roof buildings, for the following reasons: (1) both buildings are isolated, (2) both building consist of one internal zone, (3) asymmetric openings are present in both buildings (lower one in the windward and upper one in the leeward facade) and (4) both are exposed to a wind direction normal to the facade with the opening in the lower part of the facade. As a result, the salient flow features in the building studied by Karava et al.[16] are also present in the buildings studied in this paper.

5.4 CFD simulations of single and double-span leeward sawtooth roof geometries: settings and parameters

In this section the computational geometry and grid, boundary conditions and solver settings of the CFD models for the evaluation of the single-span and double-span roofs are presented.

5.4.1 Computational geometry, domain and grid

The computational model of the leeward sawtooth roof geometry E2 has dimensions as indicated in Section 5.2 and Figure 5.2. The computational domain is depicted in Figure 5.4a and is in accordance with the best practice guidelines as published by Franke et al. [17] and Tominaga et al. [18]. As in the validation study, the upstream length of the domain is reduced to 3 times the height of the building to limit horizontal inhomogeneity[21,22] . The surface-grid extrusion technique [23] is applied to construct the computational grid, which allows full control over the quality (size, shape) of every grid cell. The grid resolution is based on the grid-sensitivity analysis presented in Perén et al. [6]. The grid for case E2 is shown in Figure 5.4b-d. The total number of cells is 2,917,152 for case E2 and it varies for each of the cases with different roof geometries, ranging from 2.8 to 3.6 million cells.

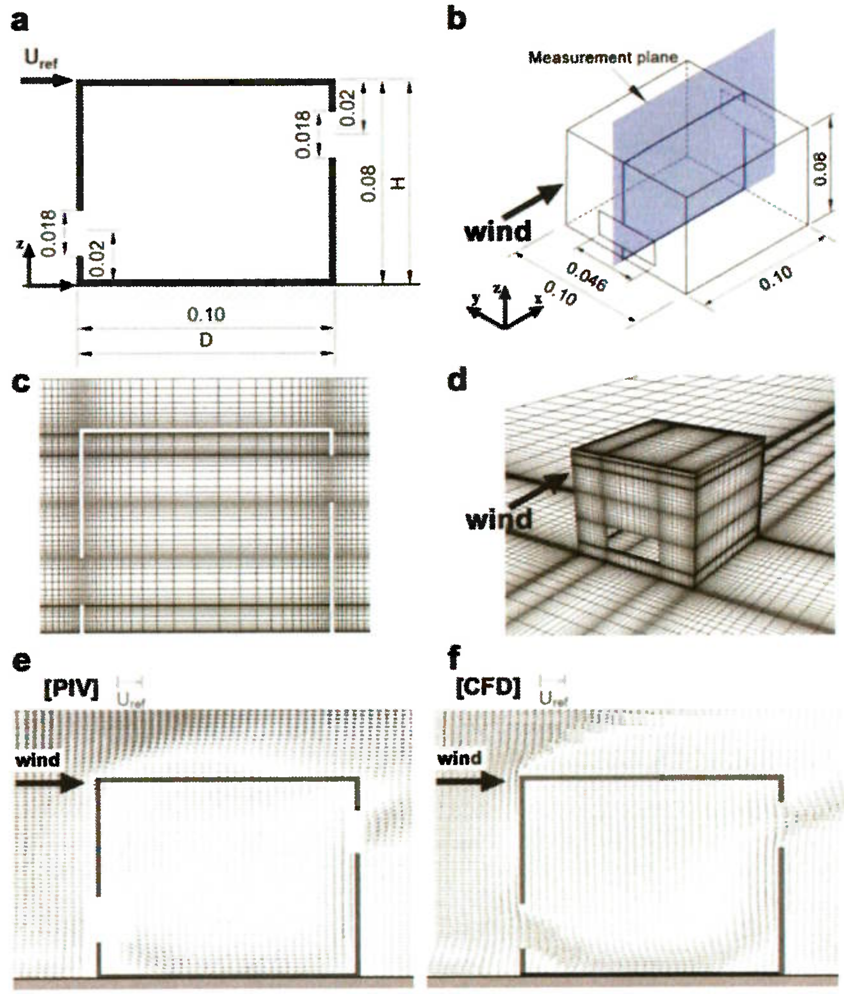

Figure 5.3: (a) Vertical cross-section of the reduced-scaled building model as studied by Karava et al. [16] with opening size and dimensions (in meter). (b) Perspective view indicating the measurement plane with dimensions (in meter). (c) Vertical cross-section of the computational grid (770,540 cells). (d) Perspective close-up view of the grid on the building surface (windward facade) and part of the ground surface. (e,f) Comparison of the mean velocity vector field in the vertical center plane obtained from: (e) PIV measurements (processed from [16]); (f) CFD simulations [5].

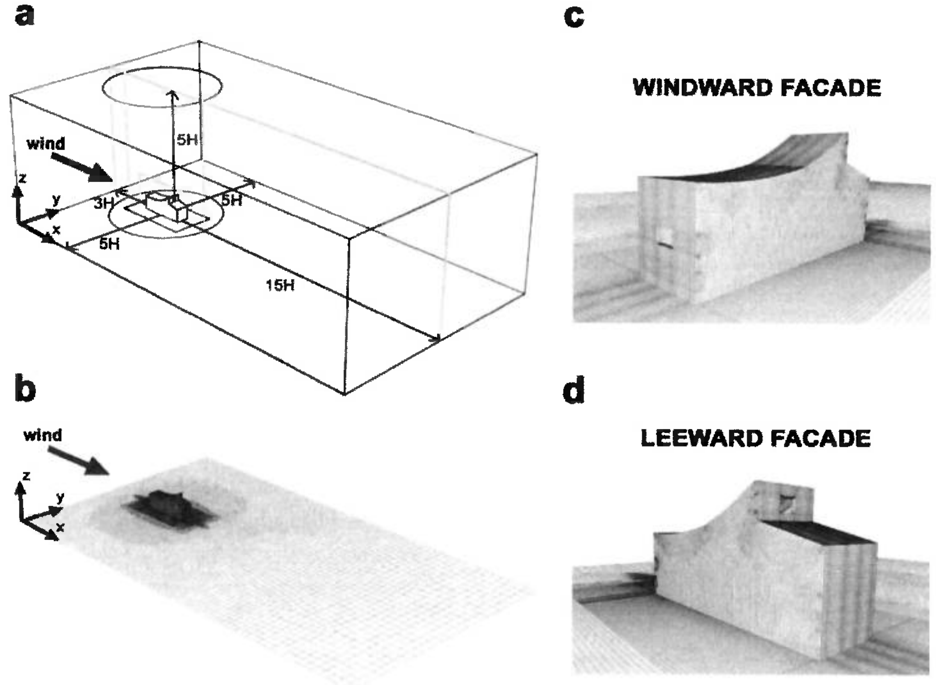

Figure 5.4: (a) Perspective view of building case E2 in its computational domain.(b-d) Perspective view of the computational grid for building case E2 (total number of cells: 2,917,152). (b) View of the computational grid on the building surfaces and on the ground surface. (c) Close-up view of the windward facade (inlet opening). (d) Close-up view of the leeward facade (outlet opening).

5.4.2 **Boundary conditions**

At the inlet of the domain the vertical approach-flow profiles of the mean wind speed U, turbulent kinetic energy (k) and specific dissipation rate (ω) are imposed. The wind direction is perpendicular to the windward building facade. The inlet mean wind-velocity profile U(z) is defined according to the logarithmic law (Eq. 1):

$$U(z) = \frac{u^*_{ABL}}{\kappa} \ln\left(\frac{z + z_0}{z_0}\right) \qquad (1)$$

with $z_0 = 0.1$ m, u^*_{ABL} the atmospheric boundary layer (ABL) friction velocity, κ the von Karman constant (0.42) and z the height coordinate. The value of u^*_{ABL} is determined based on the values of the reference velocity ($U_{ref} = 12.48$ m/s) at building height ($z_{ref} = H = 5.7$ m), yielding a building Reynolds number of 500,000. The aerodynamic roughness length is set higher than the one used in the validation study, to impose a more realistic wind velocity profile, corresponding to "roughly open country"[26]. The turbulent kinetic energy k is calculated from the mean wind speed U(z) and the streamwise turbulence intensity $I_u(z)$, with a value of 15% at the top of the building model (at $z_{ref} = H$) and 45% at ground level, using Eq. (2):

$$k(z) = a(I_U(z)U(z))^2 \quad (2)$$

with I_u the measured streamwise turbulence intensity and "a" a parameter ranging from 0.5 to 1.5 [18,27]. In the current work the value a = 0.5 is used as in the validation study and in previous studies by the authors [5-7], assuming that the turbulent fluctuations in streamwise direction are much larger than those in lateral and vertical direction ($\sigma_u \gg \sigma_v$ and $\sigma_u \gg \sigma_w$). The specific dissipation rate ω is given by Eq. (3), where C_μ is an empirical constant taken equal to 0.09, and the turbulence dissipation rate ε is given by Eq. (4).

$$\omega(z) = \frac{\varepsilon(z)}{C_\mu k(z)} \quad (3)$$

$$\varepsilon(z) = \frac{u^{*3}_{ABL}}{\kappa(z + z_0)} \quad (4)$$

At the ground and building surfaces, the standard wall functions by Launder and Spalding [28] are used in conjunction with the sand-grain based roughness (k_s) modification defined by Cebeci and Bradshaw [29]. For the ground surfaces, the values of the roughness parameters, i.e. the sand-grain roughness height (k_s = 0.14 m) and the roughness constant (C_s = 7), are determined based on the relationship with the aerodynamic roughness length z_0 derived by Blocken et al. [21]:

$$k_S = \frac{9.793 z_0}{C_S} \quad (5)$$

The sand-grain roughness height is zero (k_S = 0 m) for the building surfaces (smooth walls). At the outlet plane, zero static gauge pressure is applied and at the top and lateral sides of the domain zero normal velocities and zero normal gradients of all variables are imposed.

5.4.3 Solver settings

The CFD simulations are performed using the commercial CFD code ANSYS Fluent 12 [24]. The 3D steady RANS equations are solved in combination with the SST k-ω turbulence model by Menter [25]. Pressure-velocity coupling is taken care of by the SIMPLE algorithm, pressure interpolation is second order and second-order discretization schemes are used for both the convection terms and the viscous terms of the governing equations. Convergence is assumed to be obtained when all the scaled residuals level off and reach a minimum of 10^{-6} for x, y momentum, 10^{-5} for y momentum and 10^{-4} for k, ε and continuity. As also observed by Ramponi and Blocken [27], the simulations show oscillatory convergence. To obtain a reliable steady value of the solution variables, the results values are monitored over 10,400 iterations and the variables are calculated by averaging over 400 iterations (10,000-10,400), after the simulation reached a statistically stationary solution. More information on how to deal with oscillatory convergence can be found in[19].

5.5 CFD simulations of single and double-span roof geometries: results

Section 5.5.1 presents the performance of the single-span leeward sawtooth roof geometries (OR = 1). Subsequently, Section 5.5.2 presents the results of the two cases of three double-span roof geometries (OR = 1 and OR = 0.5). The ventilation performance of all leeward sawtooth roof geometries (single-span and double-span) is assessed based on the volume flow rate through the building. In addition, the airflow pattern around and inside the building is analyzed for all cases. Finally, for the cases with a convex roof geometry (E), the average non-dimensional velocity magnitude ($|V|/U_{ref}$) along four horizontal lines at four different heights (h) from the ground floor; i.e. h = 0.1 m, 0.6 m, 1.1 m, and 1.7 m, is presented.

5.5.1 Single-span leeward sawtooth roof geometries

Figure 5.5a shows the volume flow rates in percentage (%) for the single-span leeward sawtooth roof geometries, in which the convex roof geometry E2 reaches the highest volume flow rate (= 3.04 m^3/s) and is taken as the reference case (= 100%). The building with straight roof geometry (A2) and concave roof geometry (B2) respectively reach values of 96.5% and 91.2% of the volume flow rate compared to the case E2. These results are consistent with previous results for similar buildings but with length L = 6 m [6]. In addition, Figure 5.5b shows the area-averaged pressure coefficient C_P at the outlet opening. The pressure coefficient is calculated as:

$$C_P = \frac{(P - P_0)}{(0.5\rho U_{ref}{}^2)} \qquad (5)$$

where P is the static pressure, P_0 the reference static pressure, ρ the density of air (= 1.225 kg/m^3: International Standard Atmosphere (ISA); dry air, θ_a = 15°C, p_0 = 101,325 Pa [30]) and U_{ref} is the approach-flow wind speed at building height (U_{ref} = 12.48 m/s at z_{ref} = 5.7 m). It can be seen that the value of C_P is highest for geometry E2, which indeed results in the highest volume flow rate through the building. Also this is consistent with the results from the previous study on less elongated buildings [6].

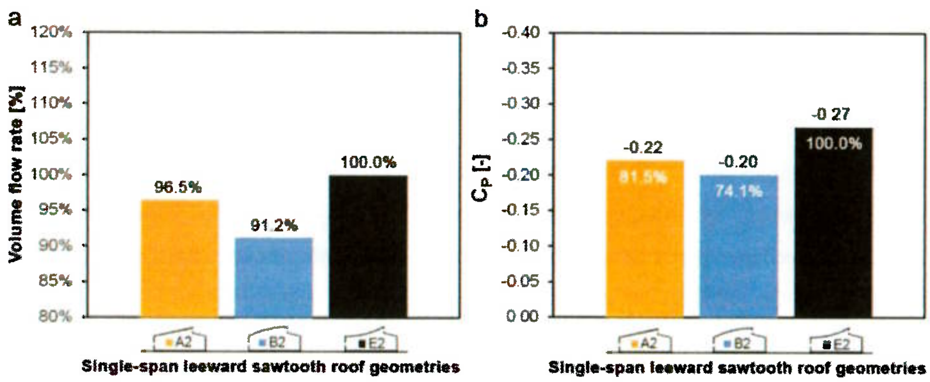

Figure 5.5: Impact of roof geometry for single-span cases. (a) Volume flow rate through the building. (b) Area-averaged pressure coefficient (C_P) at the outlet opening surface under normal wind incidence angle.

In order to better analyze the effect of the roof geometry on the flow pattern around and inside the building, contours of the pressure coefficient (C_P) and of the non-dimensional velocity magnitude ($|V|/U_{ref}$) are shown in Figure 5.6. The figures show that the pressure distribution upstream of the windward facade is almost identical for all three cases. However, they also show that the convex roof geometry E2 increases the size (height) and magnitude of the underpressure behind the building (wake region), resulting in a higher absolute value of the area-averaged C_P value at the outlet opening (C_P = -0.27), compared to geometry B2 (Figure 5.6c: C_P = -0.20) and geometry A2 (Figure 5.6a: C_P = -0.22). The average internal pressure coefficients C_P for the three single-span cases are for geometry A2: C_P = 0.170; for geometry B2: C_P = 0.215; and for geometry E2: C_P = 0.185. Note that geometry B2, in contrast to geometry A2 and E2, has no flow separation at the windward roof edge (Figure 5.6d) and the shear layer downstream of the roof end follows a downward direction. As a consequence of the lower underpressure and the specific flow pattern over the roof, the volume flow rate of the concave roof geometry B2 is 8.8% lower than that of the convex roof geometry E2, as previously shown in Figure 5.5. This is in line with the findings of the authors for a single-span roof with a depth of 6 m [6], which highlighted that convex roof geometries reach higher volume flow rates than concave roof geometries. Note that the geometries in the present study have an inclination angle of 18°, which is lower than in the previous study, where it was 27°.

5.5.2 Double-span leeward sawtooth roof geometries

The performance of double-span leeward sawtooth roof geometries is analyzed systematically by comparison with the corresponding single-span cases (i.e., straight, concave and convex). For all geometries, the corresponding single-span roof geometry is selected as the reference case.

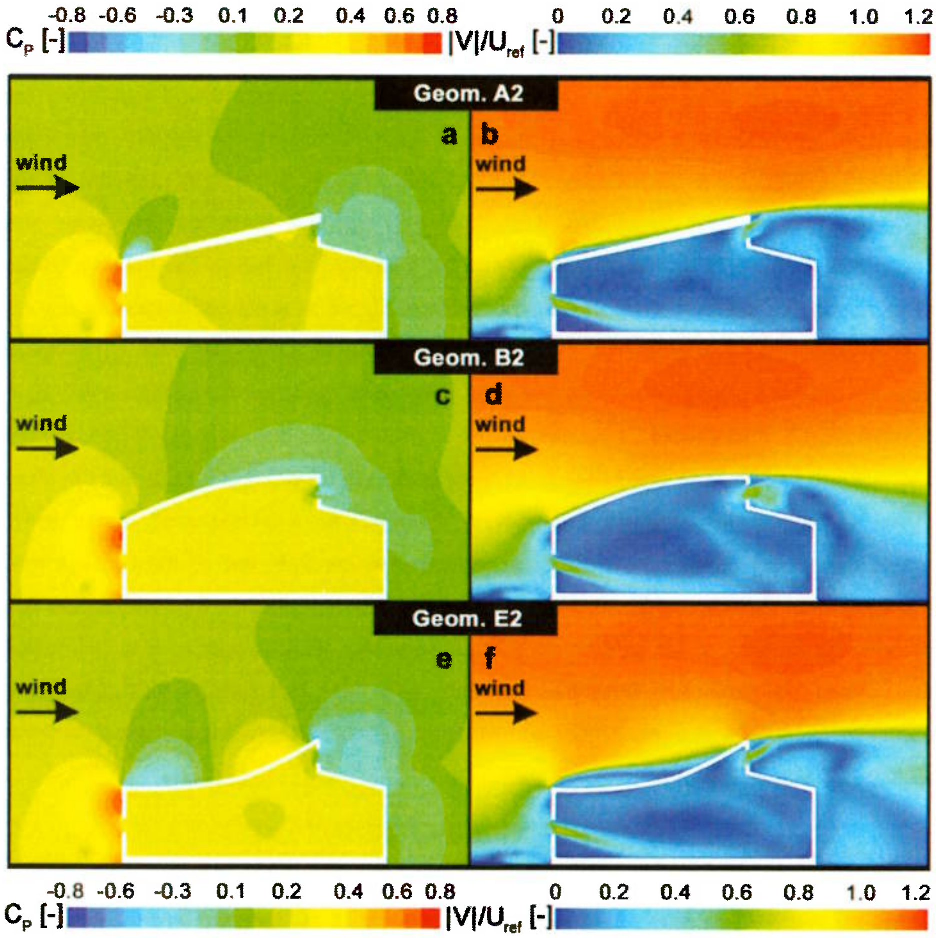

Figure 5.6: Contour plot of the pressure coefficient C_P (a,c,e) and the non-dimensional velocity magnitude ($|V|/U_{ref}$) (b,d,f) in the vertical center plane for the three single-span leeward sawtooth roof geometries. (a,b) Straight roof geometry A2. (c,d) Concave roof geometry B2. (e,f) Convex roof geometry E2.

5.5.2.1 Straight roof geometry

Figure 5.7a displays the volume flow rates for the straight roof geometry cases (A2 – reference case –, A2x2_OR1 and A2x2_OR0.5) and shows that the double-span leeward roof with an opening ratio of 1 (A2x2_OR1) reaches a slightly higher volume flow rate (increase of 1.4%) than the reference case (A2). The case A2x2_OR0.5 however reaches a 25.6% higher volume flow rate than reference case A2. This increase of volume flow rate with decreasing opening ratio (larger outlet openings) was already reported by Karava et al. [16], and can be attributed to the lower overall flow resistance as a result of the larger outlet opening leading to more pressure equalization between the indoor and outdoor environment near the outlet.

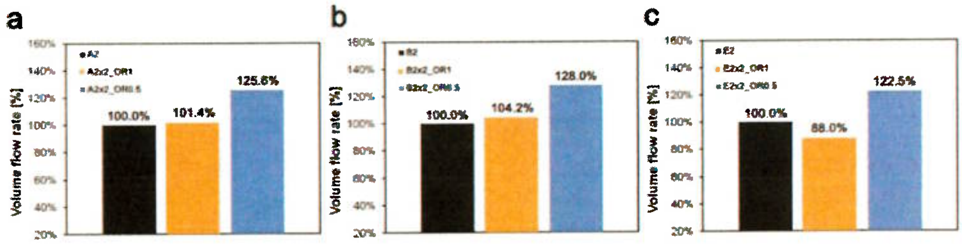

Figure 5.7: Impact of roof geometry and opening ratio on the volume flow rate under normal wind incidence angle for single-span and double-span leeward sawtooth roof geometries. (a) Case A2, A2x2_OR1 and A2x2_OR0.5. (b) Case B2, B2x2_OR1 and B2x2_OR0.5. (c) Case E2, E2x2_OR1 and E2x2_OR0.5.

The contours of the pressure coefficient (C_P) and the non-dimensional velocity magnitude ($|V|/U_{ref}$) are displayed in Figure 5.8.

This effect is more pronounced in Figure 5.8e than in Figure 5.8c. In addition, the underpressure behind the second span is quite similar to that behind the single span of the reference case A2. Figure 5.8 also clearly shows a lower internal positive pressure in Figure 5.8e for A2x2_OR0.5 ($-0.1 < C_P < 0.03$), compared to A2x2_OR1 ($0.12 < C_P < 0.22$), which can be attributed to the higher pressure equalization resulting from the larger outlet openings for case A2x2_OR0.5. This reduction in internal pressure reduces the internal resistance against the incoming airflow and increases the indoor velocities and the volume flow rate. Note that the average internal pressure for the double-span geometry A2x2_OR1 is about equal to the single-span geometry A2; i.e. $C_P \approx 0.17$. Figure 5.8f shows that the inlet jet velocity considerably increases in strength and shifts to a slightly more horizontal direction.

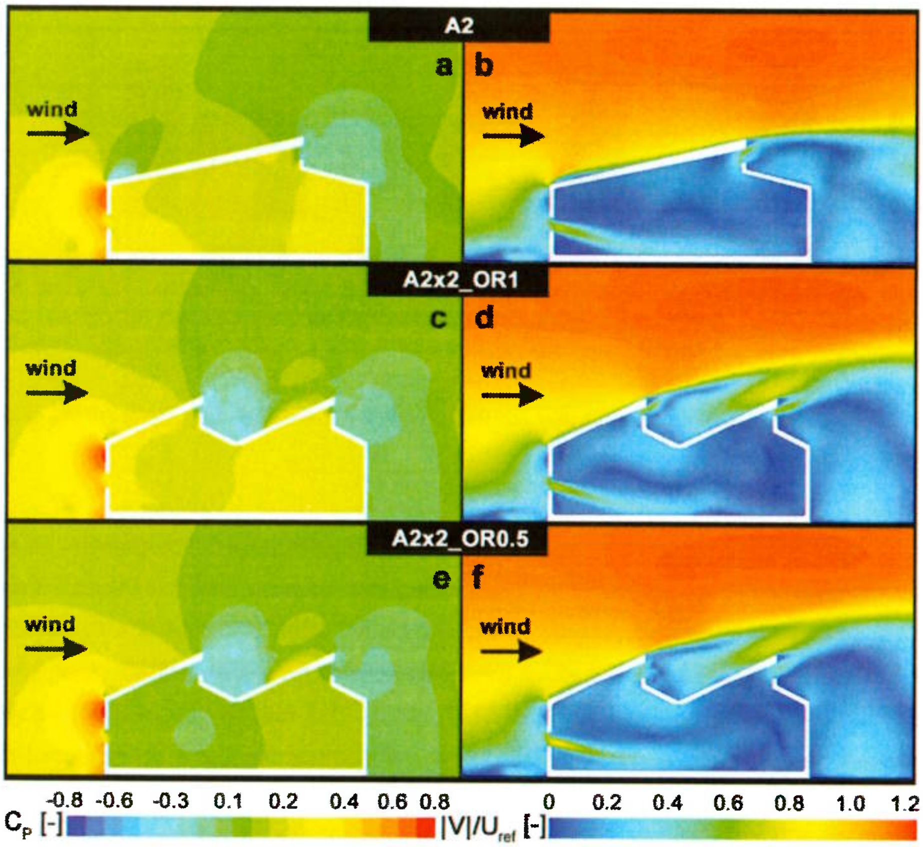

Figure 5.8: Contour plots of the pressure coefficient C_P (a,c,e) and the non-dimensional velocity magnitude ($|V|/U_{ref}$) (b,d,f) in the vertical center plane for the three cases with a straight roof geometry: (a,b) Single-span geometry A2. (c,d) Double-span geometry A2x2_OR1. (e,f) Double-span geometry A2x2_OR0.5.

5.5.2.2 Concave roof geometry

Figure 5.7b displays the volume flow rates for the concave roof geometries (B2 – reference case –, B2x2_OR1 and B2x2_OR0.5) and shows that the volume flow rates for the double-span cases B2x2_OR1 and B2x2_OR0.5 increase with 4.2% and 28.0% compared to the case B2, respectively. Contours of the pressure coefficient (C_P) and the non-dimensional velocity magnitude ($|V|/U_{ref}$) are depicted in Figure 5.9. It can be seen that the flow remains attached to the top of the first-span roof and that it also reattaches to the top of the second-span roof (Figure 5.9d and Figure 5.9f).

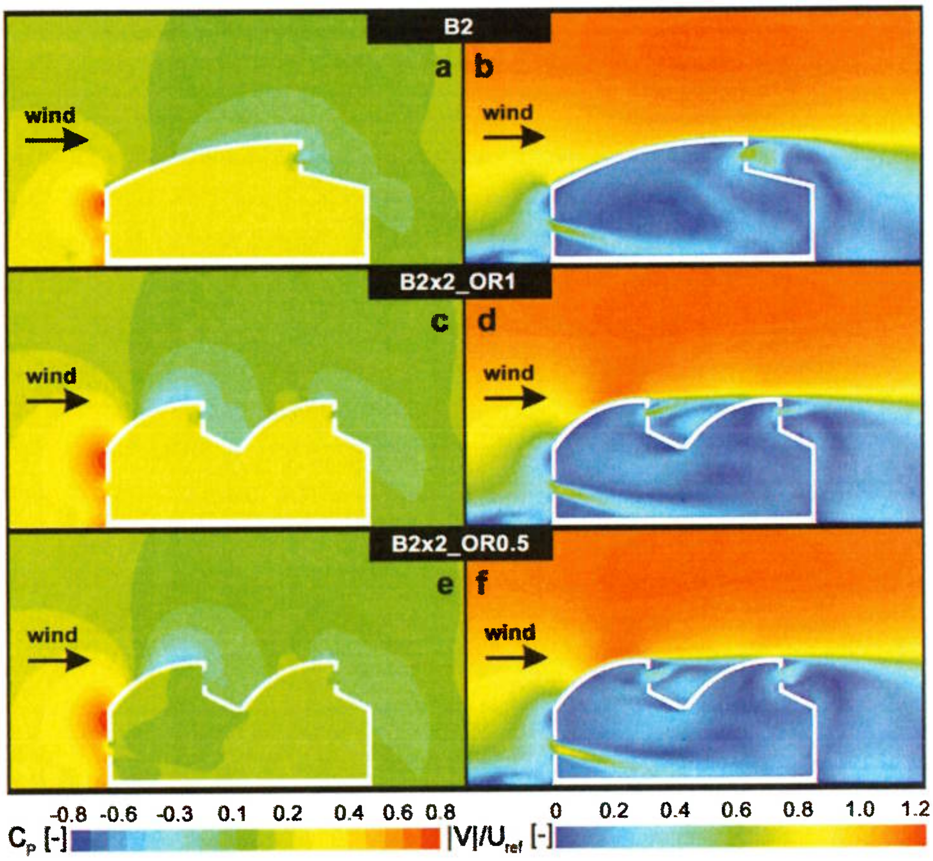

Figure 5.9: Contour plots of the pressure coefficient C_P (a,c,e) and the non-dimensional velocity magnitude ($|V|/U_{ref}$) (b,d,f) in the vertical center plane for the three cases with a concave roof geometry: (a,b) Single-span geometry B2. (c,d) Double-span geometry B2x2_OR1. (e,f) Double-span geometry B2x2_OR0.5.

The internal pressure in the building is lower in case B2x2_OR0.5 ($-0.02 < C_P < 0.08$), as shown in Figure 5.9e, than in case B2 ($0.17 < C_P < 0.25$) and B2x2_OR1 ($0.16 < C_P < 0.24$). The average internal pressure coefficient for B2x2_OR1 ($C_P = 0.20$) slightly deviates from the value for the single-span geometry B2 ($C_P = 0.215$). The inlet jet velocity considerably increases in case B2x2_OR0.5 (Figure 5.9f), as also observed for the straight roof geometry.

5.5.2.3 Convex roof geometry

The convex double-span roof geometry E2x2_OR1 results in the lowest volume flow rate, which reaches only 88.0% of the volume flow rate of the reference case E2, as depicted in Figure 5.7c. This is in contrast to the previous roof geometry types, where straight and concave double-span geometries reach slightly higher volume flow rates than the corresponding single-span geometry with the same opening ratio (i.e. 1.4% for A2x2_OR1 (Figure 5.8a) and 4.2% for B2x2_OR1 (Figure 5.8b)). The fact that case E2x2_OR1 reaches a lower volume flow rate than E2 is probably due to the relatively narrow internal area on the inside of the outlet openings (see dashed circles in Figure 5.10c) which appears to act as a resistance to the airflow near the outlet openings. As a result of this "blockage", the internal pressure coefficients (C_P) of case E2x2_OR1 reach slightly higher values than those of the other two double-span cases with identical opening ratios; the internal pressure coefficients (C_P) for case E2x2_OR1 range between 0.21

and 0.28 (Figure 5.10c), with an average C_P value of 0.245; for case A2x2_OR1 they range between 0.12 and 0.22 (Figure 5.8c), with an average C_P value of 0.170; and for case B2x2_OR1 they range between 0.16 and 0.24 (Figure 5.9c), with an average C_P value of 0.20. Note that only for the convex double-span roof geometry (E2x2_OR1) the average internal pressure coefficient increases compared to the single-span geometry (E2); the increase in average internal pressure coefficient amounts 32% (from $C_P = 0.185$ to $C_P = 0.245$).. The incoming airflow is reduced due to this higher internal pressure (higher internal resistance). However, E2x2_OR1 reaches an underpressure behind the first span which is 72% higher than that of case B2x2_OR1. But this higher underpressure cannot compensate for the higher internal resistance. A wider internal outlet-opening geometry or a larger outlet opening area (lower OR) could take advantage of the higher underpressure and could maybe result in a more efficient air exhaust. Note that the underpressure ($-C_P$) behind the outlet openings of case E2x2_OR1 is similar with the case E2x2_OR0.5 (see Figure 5.10c and Figure 5.10e), however, the volume flow rate of E2x2_OR1 is 34.5% lower than E2x2_OR0.5. This indicates again that the opening ratio is a very important parameter.

The convex roof geometry type is selected to compare the ventilation performance in terms of indoor mean air velocity. Figure 5.11b to Figure 5.11e show a comparison of the non-dimensional velocity magnitude ($|V|/U_{ref}$), along four horizontal lines located at a height of h = 0.1 m, 0.6 m, 1.1 m and 1.7 m from the internal floor (as shown in Figure 5.11a). Despite the fact that E2x2_OR1 has the worst performance, locally higher indoor mean velocities are reached than in case E2; e.g. at h = 0.6 m (between $0.28 < x/D < 0.41$) (Figure 5.11c), at h = 1.1 m (between $0.21 < x/D < 0.52$) (Figure 5.11d) and at h = 1.7 m (between $0.20 < x/D < 0.65$) (Figure 5.11e). Figure 5.11b shows that at h = 0.1 m the reference case (E2) has higher indoor mean velocities over the entire depth of the building compared to the cases E2x2_OR1 and E2x2_OR0.5. Figure 5.11c and Figure 5.11d show that a double-span roof with opening ratio = 0.5 can increase the indoor mean velocity at h = 0.6 m and h = 1.1 m at the first internal region; i.e, from $0.20 < x/D < 0.61$ at h = 0.6 m and from $0 < x/D < 0.73$ at h = 1.1 m.

These results illustrate that the ventilation performance cannot be evaluated based on the volume flow rates only [3]; local effects on the velocity field should be considered as well when assessing the ventilation performance of different building and roof geometries.

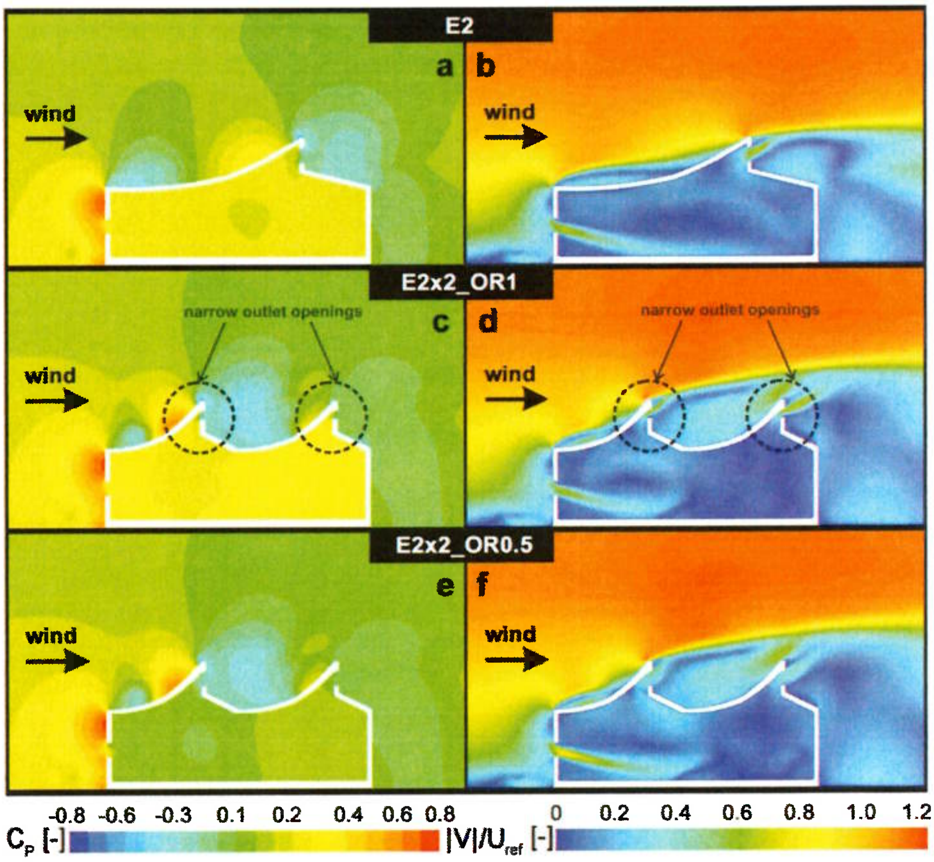

Figure 5.10: Contour plots of the pressure coefficient C_P (a,c,e) and the non-dimensional velocity magnitude ($|V|/U_{ref}$) (b,d,f) in the vertical center plane for the three cases with a convex roof geometry. (a,b) Single-span geometry E2. (c,d) Double-span geometry E2x2_OR1. (e,f) Double-span geometry E2x2_OR0.5. The dashed circles in (c,d) indicate the narrow outlet openings.

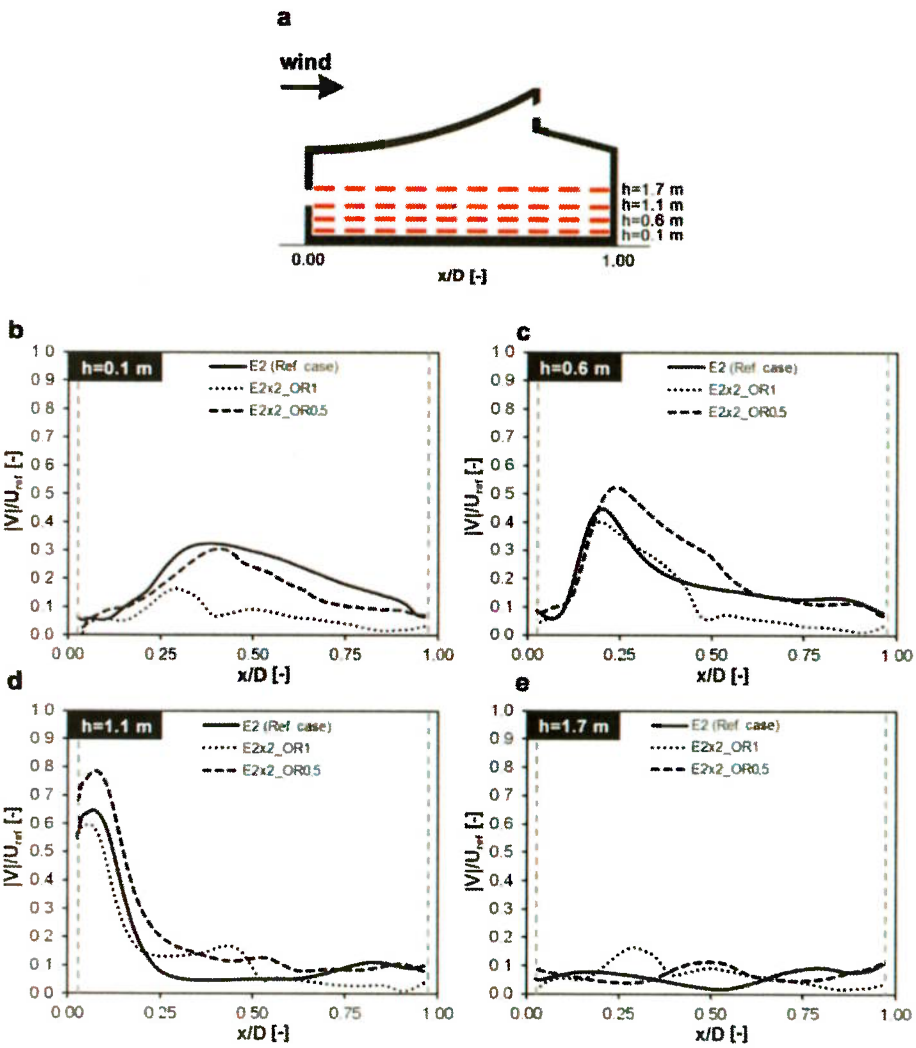

Figure 5.11: Impact of the roof geometry and opening ratio on the non-dimensional velocity magnitude ($|V|/U_{ref}$) under a normal wind incidence angle for cases E2, E2x2_OR1 and E2x2_OR0.5 along four horizontal lines at a height h above the floor. (a) Geometry E2 with indication of the four horizontal lines. (b-e) Results at (b) h = 0.1 m. (c) h = 0.6 m. (d) h = 1.1 m. (e) h = 1.7 m. The dashed vertical lines indicate the inner surfaces of the walls at the windward and leeward side of the building.

5.6 Comparison between all roof geometry types

Figure 5.12 shows the pressure coefficients at both outlet openings and the volume flow rate through both openings for double-span roof geometries with an opening ratio of 1 (OR = 1). It can be seen that for all three roof geometries the C_P values are larger at the upstream outlet opening (Out.Op.01) than at the downstream opening (Out.Op.02) (Figure 5.12a). The largest values at both openings are present for the case with a straight roof geometry (A2x2_OR1), closely followed by the convex roof geometry (E2x2_OR1). As a result of the larger pressure coefficients at the upstream opening, the fraction of volume flow rate through the upstream outlet opening is larger than that through the downstream outlet opening. For case A2x2_OR1 and E2x2_OR1, 55.0% of the total volume flow rate exits the building through the upstream outlet opening, and only 45.0% exists through the downstream opening. The differences are not so large for case B2x2_OR1, in which 51.4% of the air is exhausted through the upstream opening and 48.6% through the downstream opening.

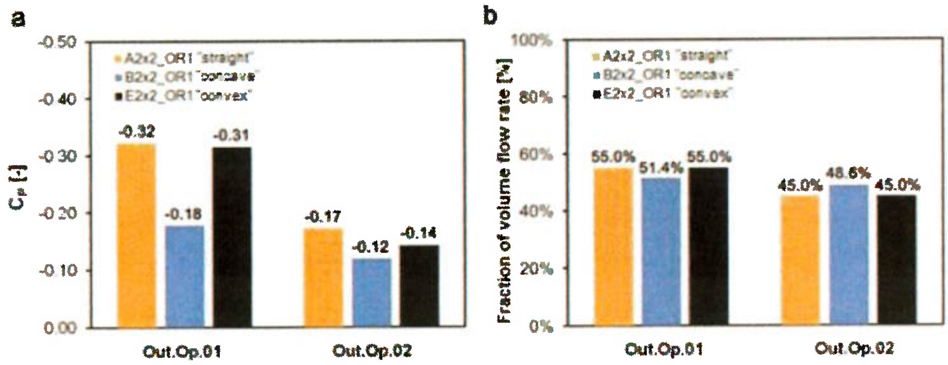

Figure 5.12: Impact of the roof geometry (straight, concave, convex) (opening ratio = 1). (a) External mean pressure coefficient (CP) at the surface of outlet opening 1 (Out.Op.01) and outlet opening 2 (Out.Op.02). (b) Fraction of volume flow rate through outlet openings 1 and 2.

To summarize the results regarding the volume flow rates, Figure 5.13 shows a comparison of all the single-span and double-span roof geometries analyzed in this study, based on the volume flow rate through the building. The convex single-span case E2 reaches the highest volume flow rate within the single-span cases. Therefore, the single-span convex roof geometry E2 is selected as a reference case (= 100%). The convex double-span E2x2_OR0.5 reaches the highest volume flow rate from all the cases with an opening ratio = 0.5 (i.e. straight type A2x2_OR0.5and concave type B2xOR0.5). For instance, the volume flow rate for E2x2_OR0.5 is 122.5% , for A2x2_OR0.5 it is 121.2% and for B2x2_OR0.5 it is 116.7%. The results show that the volume flow rate can be increased by opening ratios lower than 1, which is consistent with findings in previous studies on cross-ventilation (e.g. [16]). As indicated in Figure 7 already, it can again be seen that for straight and concave roof geometries (A2 and B2) the double-span geometries perform better than the single span geometries. From all the cases the case E2x2_OR0.5 results in the highest volume flow rate which is 22.5% higher than that of the reference case E2. Finally, the increase in volume flow rate when the opening ratio of a double-span roof is increased from 1 to 0.5 amounts 23% for the concave roof geometry, 24% for the straight roof geometry and 39% for the convex roof geometry.

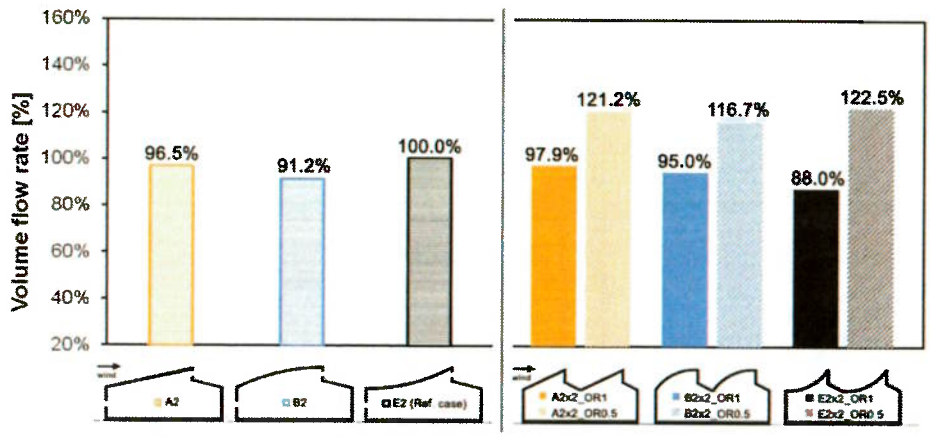

Figure 5.13: Impact of roof geometry and opening ratio for the three single-span roof geometries (A2, B2, E2) and six double-span leeward sawtooth roof geometries on the volume flow rate. The single-span geometry E2 is taken as reference case (= 100%).

5.7 Discussion

Based on the volume flow rate and the indoor air velocity in the occupied zone, the current study evaluates the ventilation performance of single and double-span roof configurations for a normal wind incidence angle ($\varphi = 0°$). First, three single-span leeward sawtooth roof geometry types are evaluated; a straight roof geometry (A2), a concave roof geometry (B2) and a convex roof geometry (E2). Then, three double-span leeward sawtooth roof cases with the same three roof geometry types and with the same opening ratio as the single-span (A2x2_OR1, B2x2_OR1 and E2x2_OR1) are studied. Finally, in order to better observe the potential of the double-span roof geometries, the same three double-span building geometries, but with larger outlet openings (A2x2_OR0.5, B2x2_OR0.5 and E2x2_OR0.5) are analyzed.
It is important to mention the limitations of the current study, which should be addressed in future research:

- All the single and double-span leeward sawtooth roof geometries have different internal volume as a consequence of the roof geometry; therefore, future research could focus on a building with the same internal volume in order to have similar parameter in the performance evaluation.
- The impact of the wind incidence angle could change the performance of each single and double span leeward sawtooth roof geometry. To study more oblique wind incidence angles it might be necessary to resort to unsteady simulations, such as Large Eddy Simulations (LES) or Detached Eddy Simulation (DES), to accurately predict the volume flow rates through the openings resulting from unsteady flow features.
- The impact of surrounding buildings must be assessed in future work, since they can strongly affect the urban flow field, and thus the natural ventilation flow through the building.

5.8 Conclusions

This paper presents numerical simulations to study the impact of single-span and double-span leeward sawtooth roof geometries on the wind-driven cross-ventilation flow in a generic isolated building. The ventilation performance is evaluated in terms of volume flow rate and indoor air velocities by performing CFD simulations with the 3D steady RANS approach and the SST k-ω turbulence model. Grid-sensitivity analysis and computational model validation using Particle Image Velocimetry (PIV) from literature are carried out. For a normal wind incidence angle a summary of the main conclusions is presented below:

- From all the single and double-span geometries with similar opening ratio (OR = 1), the convex single-span E2 reaches the highest volume flow rate.
- Within the single-span geometries, the convex single-span E2 results in a 8.8% higher volume flow rate than the concave single-span roof geometry B2, which shows the worst performance with respect to volume flow rate through the building.
- Straight and concave double-span roof geometries result in a slight increase of the volume flow rate compared to single-span roof geometries with similar geometry type. On the other hand, the convex double-span E2x2_OR1 reaches 12% lower volume flow rate than found for its reference case, the single-span E2.
- For convex double-span cases, such as E2x2_OR01, the building geometry near the outlet-opening plays an important role in the ventilation performance. The internal geometry contraction near the outlet openings results in higher internal pressure coefficients and reduces the volume flow rate.
- Reducing the opening ratio from 1 to 0.5 for the double-span roof geometries results in an increase of the volume flow rate with 23-39%, depending on the roof geometry.

5.9 Acknowledgments

This work was supported by The Coordination for the Improvement of Higher Level Personnel (CAPES), Brazil, The Civil Construction Engineering Department, Polytechnic School of the University of São Paulo (USP), Brazil and the unit Building Physics and Services of the Department of the Built Environment at Eindhoven University of Technology in the Netherlands. Twan van Hooff is currently a postdoctoral fellow of the Research Foundation – Flanders (FWO) and is very grateful for its financial support (project FWO 12R9715N).

5.10 Reference

[1] Chu C-R, Chiang B-F. Wind-driven cross ventilation in long buildings. Build Environ 2014;80:150–8. doi:10.1016/j.buildenv.2014.05.017.

[2] Montero JI, Hunt GR, Kamaruddin R, Antón A, Bailey BJ. SE—Structures and Environment: Effect of Ventilator Configuration on Wind-driven Ventilation in a Crop Protection Structure for the Tropics. J Agric Eng Res 2001;80:99–107. doi:10.1006/jaer.2000.0694.

[3] Bartzanas T, Boulard T, Kittas C. Effect of Vent Arrangement on Windward Ventilation of a Tunnel Greenhouse. Biosyst Eng 2004;88:479–90. doi:10.1016/j.biosystemseng.2003.10.006.

[4] Robbins CL. Daylighting: design and analysis. Van Nostrand Reinhold Company; 1986.

[5] Perén JI, van Hooff T, Leite BCC, Blocken B. CFD analysis of cross-ventilation of a generic isolated building with asymmetric opening positions: impact of roof angle and opening location. Build Environ 2014.

[6] Perén JI, Ramponi R, van Hooff T, Blocken B, Leite BCC. Impact of roof geometry of an isolated leeward sawtooth-roof building on cross-ventilation: Straight, concave, hybrid or convex? Submitted 2014.

[7] Perén JI, van Hooff T, Leite BCC, Blocken B. Effect of eave configuration in the upward cross-ventilation of a generic isolated leeward sawtooth building: upwind vs leeward eave. Submitted 2014.

[8] Stathopoulos T, Saathoff P. Codification of Wind pressure coefficients for sawtooth roofs. J Wind Eng Ind Aerodyn 1992;43:1727–38. doi:16/0167-6105(92)90584-W.

[9] Cui B. Wind Effects on Monosloped and Sawtooth Roof. Thesis. Clemson University, 2007.

[10] Mistriotis A, Bot GPA, Picuno P, Scarascia-Mugnozza G. Analysis of the efficiency of greenhouse ventilation using computational fluid dynamics. Agric For Meteorol 1997;85:217–28. doi:10.1016/S0168-1923(96)02400-8.

[11] Mistriotis A, Arcidiacono C, Picuno P, Bot GPA, Scarascia-Mugnozza G. Computational analysis of ventilation in greenhouses at zero- and low-wind-speeds. Agric For Meteorol 1997;88:121–35. doi:10.1016/S0168-1923(97)00045-2.

[12] Shklyar A, Arbel A. Numerical model of the three-dimensional isothermal flow patterns and mass fluxes in a pitched-roof greenhouse. J Wind Eng Ind Aerodyn 2004;92:1039–59. doi:10.1016/j.jweia.2004.05.008.

[13] Bournet P-E, Boulard T. Effect of ventilator configuration on the distributed climate of greenhouses: A review of experimental and CFD studies. Comput Electron Agric 2010;74:195–217. doi:10.1016/j.compag.2010.08.007.

[14] International Organization for Standardization. Ergonomics of the thermal environment - Analytical determination and interpretation of thermal comfort using calculation of the PMV and PPD indices and local thermal comfort criteria (ISO 7730:2005). European Committee for Standardization, Brussels, Belgium: 2005.

[15] Wolfram MathWorld. n.d. http://mathworld.wolfram.com/ConvexFunction.html (accessed December 1, 2014).

[16] Karava P, Stathopoulos T, Athienitis AK. Airflow assessment in cross-ventilated buildings with operable façade elements. Build Environ 2011;46:266–79. doi:10.1016/j.buildenv.2010.07.022.

[17] Franke J, Hellsten A, Schlunzen KH, Carissimo B. Best Practice Guideline for CFD simulation of flows in the urban environment. Bruss COST 2007. doi:10.1504/IJEP.2011.038443.

[18] Tominaga Y, Mochida A, Yoshie R, Kataoka H, Nozu T, Yoshikawa M, et al. AIJ guidelines for practical applications of CFD to pedestrian wind environment around buildings. J Wind Eng Ind Aerodyn 2008;96:1749–61. doi:16/j.jweia.2008.02.058.

[19] Blocken B. Computational Fluid Dynamics for urban physics: Importance, scales, possibilities, limitations and ten tips and tricks towards accurate and reliable simulations. Build Environ n.d. doi:10.1016/j.buildenv.2015.02.015.

[20] Karava P. Airflow prediction in buildings for natural ventilation design: wind tunnel measurements and simulation. Department of Building, Civil and Environmental Engineering, Concordia University, 2008.

[21] Blocken B, Stathopoulos T, Carmeliet J. CFD simulation of the atmospheric boundary layer: wall function problems. Atmos Environ 2007;41:238–52. doi:16/j.atmosenv.2006.08.019.

[22] Blocken B, Carmeliet J, Stathopoulos T. CFD evaluation of wind speed conditions in passages between parallel buildings—effect of wall-function roughness modifications for the atmospheric boundary layer flow. J Wind Eng Ind Aerodyn 2007;95:941–62. doi:10.1016/j.jweia.2007.01.013.

[23] Van Hooff T, Blocken B. Coupled urban wind flow and indoor natural ventilation modelling on a high-resolution grid: A case study for the Amsterdam Arena stadium. Environ Model Softw 2010;25:51–65. doi:10.1016/j.envsoft.2009.07.008.

[24] ANSYS. Fluent 12 user's guide. Lebanon: Fluent Inc. 2009.

[25] Menter FR. Two-equation eddy-viscosity turbulence models for engineering applications. AIAA J 1994;32:1598–605.

[26] Wieringa J. Updating the Davenport roughness classification. J Wind Eng Ind Aerodyn 1992;41:357–68. doi:10.1016/0167-6105(92)90434-C.

[27] Ramponi R, Blocken B. CFD simulation of cross-ventilation for a generic isolated building: Impact of computational parameters. Build Environ 2012;53:34–48. doi:10.1016/j.buildenv.2012.01.004.

[28] Launder BE, Spalding DB. The numerical computation of turbulent flows. Comput Methods Appl Mech Eng 1974;3:269–89. doi:10.1016/0045-7825(74)90029-2.

[29] Cebeci T, Bradshaw P. Momentum transfer in boundary layers. Hemisphere Publishing Corp. New York: 1977.
[30] ISO 2533. International Organization for Standardization. Standard Atmosphere. International Standards Organization; 1975.

Chapter 6

Discussion

6 Discussion

6.1 Limitations and recommendations for future research

In this thesis the potential of leeward sawtooth roof buildings to increase wind-driven upward cross-ventilation has been studied. The dependency of the volume flow rate and the indoor airflow pattern on the roof inclination angle (RIA), the roof geometry (RG), the eaves configuration (Eaves) and the inlet-outlet opening ratio (OR), has been shown. The former are considered as the most relevant geometric parameters of leeward sawtooth roofs to enhance upward cross-ventilation. In addition, a combination of roof spans, such as double-span roofs, is analyzed. Although, the impact of a wide range of roof parameters on wind driven cross-ventilation has been quantified, there are limitations of the work in this thesis and some questions still remain. A discussion has been presented in each of the Chapters 2 until 5, addressing the limitations of the study presented in that specific chapter as well as directions for future research. For brevity, the majority of this information will not be repeated here. Instead, a short overview will be given of the main limitations and the main directions for further research. Recommendations for future research are listed below:

- It would be very useful to perform Particle Image Velocimetry (PIV) wind tunnel experiments of a leeward sawtooth roof building considering the main roof parameters tested in this thesis (i.e. roof inclination angle, roof geometry, windward and leeward eaves) for an atmospheric boundary layers with an aerodynamic roughness length of z_0 = 0.1 m or $z_0 > 0.1$ m. These PIV measurements would provide data for the analysis of the flow pattern around buildings with a sawtooth roof, which is currently missing, and the data can thus be used for a direct validation of the CFD models.

- The accuracy of 3D Reynolds-Averaged Navier-Stokes (RANS) simulations to predict the volume flow rate and the airflow pattern of leeward sawtooth roof building geometries under oblique wind incidence angles should be assessed and extended for different wind directions. Since it is known from literature that steady RANS might show deviations for oblique angles [1,2], a comparison with experimental results and/or validated Large Eddy Simulations is highly recommended. In addition, LES simulations can also account for the effect of pressure fluctuations and other transient flow phenomena that affect the volume flow rate through the building, such as the collapse of separation and recirculation regions, vortex shedding, pulsating eddies and other transient flow features. These transient effects become even more important when the flow is parallel to the ventilation openings [1,2].

- Evaluation of the performance of sawtooth roof buildings working as wind catcher should be considered as well, since in many countries there is not one single dominant wind direction. It is important to mention that sawtooth roofs working as a windcatcher will not benefit from buoyancy forces assisting the wind forces. Therefore, application of sawtooth roof buildings as wind catcher is not recommended (not preferable) in naturally ventilated buildings under summer time conditions. In general, the ventilation flow in a building with a sawtooth roof depends – among others – on its orientation to the oncoming wind flow, and the presented research should be extended for both more oblique wind directions and for wind directions opposite from the one studied in this thesis (sawtooth roof as wind catcher) [3].

- An analysis of a combination of different roof and building parameters can be conducted to find the "optimal" configurations. For example, the study on the potential of eaves can be extended to other building and roof geometries, e.g. to double-span or multi-span leeward sawtooth roof buildings. It was shown that eaves can have a large effect for single-span sawtooth roof geometries, however, further analysis is needed to see whether this increased performance is also present when combined with other geometries.

- The studies presented in this thesis have been conducted for only one location of the windward ventilation opening (inlet opening). The performance of leeward sawtooth roof buildings with inlet openings at different positions can be conducted in an attempt to further optimize the cross-ventilation flow. Locations that can be studied are, for example: (a) below the floor, i.e. under-floor natural ventilation; (b) just above the floor level; (c) in the lateral sides of the wall, especially in elongated buildings.

- The main results of the current thesis can be used as a part of guidelines that can be written for building practice. These guidelines should provide information on the most efficient design of leeward sawtooth roofs with respect to the ventilation flow, but also with respect to building costs, daylight entrance, solar shading, etc. Therefore, additional research is needed on these other aspects of sawtooth roofs, to provide an integral guideline for building practice.

- Temperature effects (buoyancy) can alter the flow pattern in and around the building, especially when low wind velocities are present. Future studies can focus on the combined effects of wind and buoyancy on the ventilation flow in the building. For instance, heat sources can be located inside the building (e.g. in the occupeid zone (i.e. between 0.1 m and 1,7 m)) to evaluate the performance of the leeward sawtooth roof to exhaust this heat by the outlet openings in the upper part of the enclosure. Futhermore, the ability of the leeward sawtooth roof to release heat gained by transmission through the opaque building surfaces in general, and through the roof surface in particular, can be assessed and optimized.

- An evaluation of the convective heat transfer coefficient (CHTC) for different roof geometries of leeward sawtooth roof buildings would provide useful and important information. Both the internal and external convective heat transfer coefficients can be of interest. The internal CHTC determines the amount of heat that can be removed from the building's thermal mass by the cross-ventilation flow. The CHTC values over the building roof affect the heat exchange of the roof with the ambient environment. These values are important with respect to decreasing the surface temperatures of the roof cladding. Lower surface temperatures result in less heat transfer through the roof to the building interior, and can therefore reduce indoor overheating. Furthermore, information on the external CHTC value can be of importance when photovoltaics (PV) panels are installed on the roof construction to gain solar energy. Cooling of these PV panels by convection due to the wind flow is essential to limit the decrease in efficiency of the PV panels with increasing temperature.

6.2 References

[1] Jiang Y, Chen Q. Study of natural ventilation in buildings by large eddy simulation. J Wind Eng Ind Aerodyn 2001;89:1155-1178.

[2] Wright NG, Hargreaves DM. Unsteady CFD simulations for natural ventilation. Int J Vent 2006;5:13-20.

[3] Gandemer J, Barnaud G. Ventilation Naturelle des Habitations sous Climat TropicalHumide: Aproach Aerodynamique. Nantes: CSTB; 1989.

Chapter 7

Conclusions

7 Conclusions

This chapter is organized into two sections. The first section summarizes the main results and conclusions of this research as described in Chapters 2-5. The second section provides an indication of the main parameters of leeward sawtooth roofs to increase natural ventilation.

7.1 Conclusions by Chapter

7.1.1 Validation study

The CFD analyses of different sawtooth roof and building geometries are based on a grid-sensitivity analysis and on validation using Particle Image Velocimetry (PIV) wind-tunnel measurements of a building with asymmetric opening position and was presented in Chapter 2. The main conclusions are as follows:

- The validation study shows that the SST k-ω turbulence model provides the most accurate results, followed by the RNG k-ε turbulence model. The standard k-ε model, the realizable k-ε model, the standard k-ω model and the Reynolds Stress Model show larger deviations from the measured velocities.
- The strong influence of the upwind standing vortex on the accuracy of the indoor ventilation flow was confirmed. The influence of the parameter "a" for the calculation of the turbulent kinetic energy profiles at the inlet of the computational domain was tested, and the results shows that a value of 0.5 results in the best agreement. Relevant flow pattern characteristics, such as the standing vortex in the windward facade was accurately predicted using this value.

Once the numerical model was validated, several geometrical parameters of a single-span leeward sawtooth roof building including roof inclination angle (RIA), outlet opening position, roof geometry and eaves configuration have been studied. A summary of the most important results is provided below in Section 7.1.2.

7.1.2 Parametric studies

The most important findings are presented below, with a subdivision of these findings per chapter.

7.1.2.1 Chapter 2

Roof inclination angle (RIA):

- The volume flow rate depends on the roof inclination angle. The building with a 45° roof inclination angle (RIA_45) provides better results than all the other cases; the volume flow rate is 22% higher than for the reference case when the outlet opening is located at the same height as in the reference case; and the volume flow rate is 25% higher when the outlet opening is located near the roof.

- The indoor air flow pattern changes with changing roof inclination angle, which also influences the velocities at horizontal lines inside the building. It is shown that the angle under which the jet enters the building through the window changes (becomes more horizontal) with increasing the roof inclination angle due to a different pressure distribution on the windward facade of the building. However, the non-dimensional area-averaged velocity magnitude ($|V|/U_{ref}$) in the occupied zone for the vertical center plane only exhibits small changes up to 7%. Larger changes are found when splitting up the occupied zone in a lower and an upper part.
- To improve the volume flow rate in the studied low-rise building the roof inclination angle must be larger than 18°. For smaller roof inclination angles, such as 9°, the volume flow rate is lower than for the same building with a flat roof (reference case). It seems that the windward facade area (height) at lower roof inclination angles (9° and 18°) has a significant impact on the indoor airflow patterns and volume flow rates.

Outlet opening position:

- The vertical position of the outlet opening is less relevant than the roof inclination angle. It is shown that it can just increase the volume flow rate by 2% to 4% when located near the roof top. Furthermore, shifting the outlet opening to the top only provides small or no changes in non-dimensional ($|V|/U_{ref}$) average velocities in the occupied zone.

Building model without openings (sealed building):

- Simulations for a sealed building for RIA_00 and RIA_45 show that the sealed-building pressure difference (ΔC_P) between the windward and leeward facade cannot be clearly related to the actual volume flow rates with "open" ventilation openings. This is attributed to the differences in the flow resistance in the different cases but especially to the invalidity of the sealed-body assumption (in a building with large opening).

7.1.2.2 Chapter 3

Roof geometry:

- The internal airflow and the volume flow rate show a clear dependency on the roof geometry.
- The straight roof geometry (A) and the convex roof geometries (D and E) result in higher volume flow rates than concave (B) and hybrid convex-concave (C) roof geometry. The volume flow rates for geometry A, D and E are about 13% higher than that of geometry B, which shows the lowest performance.

- The roof geometry is an important design parameter to maximize the size and magnitude of the underpressure zone in the wake of the building, the pressure difference over the building and consequently the volume flow rate through the building. A roof that directs the external wind flow behind the building upwards will result in a larger underpressure zone and larger magnitude of the underpressure, and consequently in higher volume flow rates.
- The convex single-span E2 results in 8.8% higher volume flow rate than the concave single-span roof geometry B2, which shows the worst performance with respect to the volume flow rate through the building.

7.1.2.3 Chapter 4

Eaves configurations:

- Windward eaves with inclination angles lower than 0° increase the volume flow rate compared to the reference case. The largest increase is obtained when windward eaves with an inclination angle of -27° (A_WindEav-27) is applied: +15%. On the other hand, windward eaves with inclination angles higher than 0° decrease the volume flow rate with up to 16% for A_WindEav90. A horizontal eaves (0° inclination) result in a volume flow rate which is almost equal to the reference case.
- Application of leeward eaves with an inclination angle of 45° (A_LeeEav45) and 90° (A_LeeEav90) result in an increase of the volume flow rate with 5% and 6%, respectively. Leeward eaves with an inclination angle of 0° (A_LeeEav0) and -45° (A_LeeEav-45) result in a decrease of the volume flow rate with 8% and 9%, respectively. The leeward eaves with an inclination angle of 27° result in the same volume flow rate as in the reference case. The leeward eave should not block the outlet opening in the wake of the building.
- In general, to improve the volume flow rate in the studied low-rise leeward sawtooth roof building, the windward eaves inclination angle must be lower than 0°, such as -27° or -45°, and the inclination of the leeward eaves must be higher than 27°, for instance 45° or 90°. The coupled effect of the eaves (windward and leeward eaves working together) can be larger than the individual effects. Applying the best performing windward and leeward eaves simultaneously (i.e. A_WindEav-27_LeeEav90) can increase the volume flow rate with an additional 3% compared to the sum of the two individual effects.

7.1.2.4 Chapter 5

Double-span leeward sawtooth roof:

- Straight and concave double-span roof geometries result in a slight increase of the volume flow rate compared to single-span roof geometries with similar geometry type. On the other hand, the convex double-span E2x2_OR1 reaches 12% lower volume flow rate than found for its reference case, the single-span E2.

Inlet-outlet opening ratio and opening position:

- Reducing the opening ratio from 1 to 0.5 for the double-span roof geometries results in an increase of the volume flow rate with 23-39%, depending on the roof geometry.
- The ratio of the height between the inlet and outlet opening ($H_{in\text{-}out}$) and the depth between inlet and outlet opening ($D_{in\text{-}out}$) is also relevant. The results show that a single-span with 12 m depth reaches higher volume flow rate than the single-span with 6 m depth with the same roof geometry, despite the fact that a lower underpressure is present at outlet opening.

Internal geometry:

- For convex double-span cases the building geometry near the outlet-opening plays an important role in the ventilation performance. The internal geometry contraction near the outlet openings generates a resistance to the airflow and reduces the volume flow rate.

7.2 Contextualization

7.2.1 Implicit attributes of sawtooth roof building

As previously mentioned, a sawtooth roof is a multi-purpose building component as it:

a) allows daylight
b) protects the building from solar radiation and wind-driven rain
c) creates a wider spatial sensation
d) can increase the aesthetic value of the building as it generates a dynamic envelope design
e) promotes upward cross-ventilation by buoyancy and wind forces

Considering all the previously mentioned implicit attributes of a sawtooth roof building, the balance equation for the optimization of its design is:

$$S_{sawtooth\ roof\ design} = f(S_{program}, S_{layout}, S_{daylight}, S_{natural\ ventilation}, S_{environmental\ subjectivity}, S_{feasibility}, S_{material})$$

Where $S_{sawtooth\ roof\ design}$ is the leeward sawtooth roof design factor, $S_{program}$ the program (e.g. kitchen, bathroom, leaving room, open-office area, etc.) where the heat or pollutant source is located, S_{layout} is the layout organization factor (e.g. internal wall and furniture), $S_{daylight}$ is the daylight and solar shading factor, $S_{natural\ ventilation}$ is the natural ventilation factor (focus of current research), $S_{environ.\ subjectivity}$ is the environmental subjectivity factor which is difficult to quantify, $S_{feasibility}$ is the feasibility factor regarding constructability (cost and value), $S_{material}$ is the factor regarding the building material. All these factors must be considered in the design of a sawtooth roof and many factors influence each other. Since the current research has focused on the evaluation of the leeward sawtooth roof potential to address wind-driven upward cross-ventilation, the next section presents the most relevant parameters to maximize the volume flow rate and the airflow velocity inside the building.

7.2.2 Main parameters of leeward sawtooth roof

In order to discuss the design optimization of a leeward sawtooth roof design it is essential to firstly describe its main components or parameters. The building and roof parameters of a sawtooth roof building are described below and shown in Figure 7.1:

a) Building width
b) Building length
c) Span length
d) Main cord
e) Sawtooth roof height
f) Roof inclination angle (RIA)
g) External roof geometry of the main cord
h) Internal roof geometry of the main cord
i) Eaves (windward and leeward) configuration (inclination and length)
j) Wall porosity
k) Inlet-outlet opening ratio
l) Inlet-outlet opening inclination angle

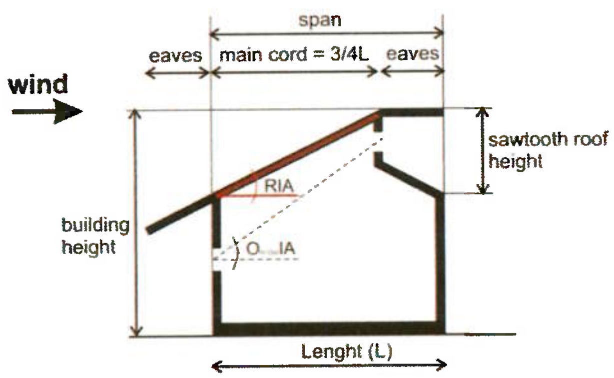

Figure 7.1: Schematic representation of the parameters (components) of a leeward sawtooth roof building.

A range of parameters has been described in this thesis, however, other parameters could be analyzed in the future. From the results obtained in this research, see Section 7.1.2, for the given set of boundary conditions (i.e. normal wind incidence and terrain roughness as mentioned in Chapters 2-5) the most important parameters to maximize the upward cross-ventilation flow in leeward sawtooth roof buildings are, in order of relevance:

1) Roof inclination angle (RIA)
2) Roof geometry type of the main cord
3) Eaves configuration (windward and leeward)
4) Inlet-outlet opening ratio (OR; must be lower than 1)
5) Inlet-outlet opening inclination angle

Appendix _ Chapter 8

Wind-tunnel measurements of internal and external mean pressure coefficients of single-zone isolated leeward sawtooth roof buildings: effect of upstream terrain roughness, roof shape and window openings

Published as:

Perén JI, van Hooff T, Nader G, Leite BCC, Blocken B. Wind-tunnel measurements of internal and external mean pressure coefficients of single-zone isolated leeward sawtooth roof buildings: effect of upstream terrain roughness, roof shape and window openings
Under preparation.

8 Wind-tunnel measurements of internal and external mean pressure coefficients of single-zone isolated leeward sawtooth roof buildings: effect of upstream terrain roughness, roof shape and window openings

ABSTRACT

Atmospheric boundary layer wind-tunnel measurements were performed for 1:15 scale models of single-zone isolated leeward sawtooth roof buildings focused on internal and external mean pressure coefficients (C_P). The effect of three parameters was investigated: upstream terrain roughness, roof shape and window openings (open versus closed). The two types of terrain roughness or boundary layers (BL) are "Open sea" (Case "BL1"), representing coastal conditions and "Roughly open country" terrain (Case "BL2"), representing suburban conditions. These two types were chosen as realistic extremes for the low-rise building type under study. The two roof shapes are a hybrid convex-concave roof (Geometry C) and a convex straight roof (Geometry D). The mean pressure coefficients (C_P) were obtained under normal wind incidence angle (0°). The experimental data for the resulting eight cases show that each of the investigated parameters has a considerable impact. For a higher upstream terrain roughness (Cases "BL2") the C_P values of a sealed building increase by 105.5% and decrease by 27.8% around the inlet openings of Geometry C and D, respectively, while they increase by 143.2% and 105.0% around the outlet opening of Geometry C and D, respectively. The internal pressure ($C_{P\ in}$) considerably decreases (around 36%) in the same proportion for both Geometries (C and D) from case BL1 to BL2. In addition, both geometries exhibits a clear non-uniform internal pressure and it was more pronounced in geometry D, with variations up to 144%. The results provide new insights in the aerodynamic performance of leeward sawtooth roof buildings and can be used to validate Computational Fluid Dynamics (CFD) simulations for this type of buildings.

Keywords: External pressure coefficient, Internal pressure coefficient, Leeward sawtooth roof, Upstream terrain roughness, Opening configuration, Roof shape, Building geometry.

8.1 Introduction

The design of the building envelope is important to enhance wind-driven cross-ventilation. Leeward sawtooth roof buildings, with inlet openings at the lower part of the windward facade and outlet openings at roof level, can be applied for improving cross-ventilation performance. These buildings can also achieve more uniform and higher daylight intensity levels due to the openings in the roof construction [1]. The relative inlet-outlet opening locations on a building facade are important parameters to be considered for evaluating the airflow in the building [2] as it must interact with the building envelope to lead the internal stream tube flow [3–6] from the inlet to the outlet opening. By evaluating the wind pressure distribution on a sealed and on a building with openings new insight can be obtained to better understand the wind-driven cross-ventilation on low-rise leeward sawtooth roof buildings. At the same time, upstream terrain roughness (Boundary layer - BL) and the size and location of opening [7] and also the roof shape [8] can significantly influence the pressure distribution around and inside a leeward sawtooth roof building.

Many research based on pressure coefficient have being carried out in reduced-scale wind tunnel measurement (e.g. [2–7,9–23]. Some of them have focused on: (1) simplified building geometries with flat roof (e.g. [2–6,9–12,7]); (2) building geometries with gabled roof or pitched roof (e.g. [13–16]; and a few on, (3) more complex roof geometries with opening on the roof level (e.g. [17–21]), such as sawtooth roof buildings (e.g. [19–21]). From the several research with focus on internal pressure reported in the state-of-the-art carried out by Oh et al (2007) just a few studied the impact of the upstream terrain roughness on the internal pressure (e.g. [16,22,23]) but in building geometries different than leeward sawtooth roof. More studies to evaluate the number of internal pressure taps required and theirs locations to obtain an accurate evaluation of the $C_{P\ in}$ in building are needed [7]. Furthermore, there is a lack of research evaluating the impact of the upstream terrain roughness (approaching flow) and the roof shape on the external and internal pressure of low-rise leeward sawtooth roof building.

The current research aims to verify the impact of (1) two upstream terrain roughness (BL) and of (2) two opening configurations (opened and closed windows openings) on the mean pressure coefficient (C_P) around and inside (3) two leeward sawtooth roof buildings: a hybrid convex-concave roof (Geometry C) and a convex straight roof with double inclination (Geometry D). Fig. 1 shows a cross section of the two leeward sawtooth roof geometries (with dimensions in full scale) selected for this study: Geometry C (Fig. 1a) and Geometry D (Fig. 1b). The wind tunnel experiment settings are presented in Section 2. The results are addressed in Section 3. Section 4 presents the Discussion and Section 5 the Conclusions, where the main findings are summarized.

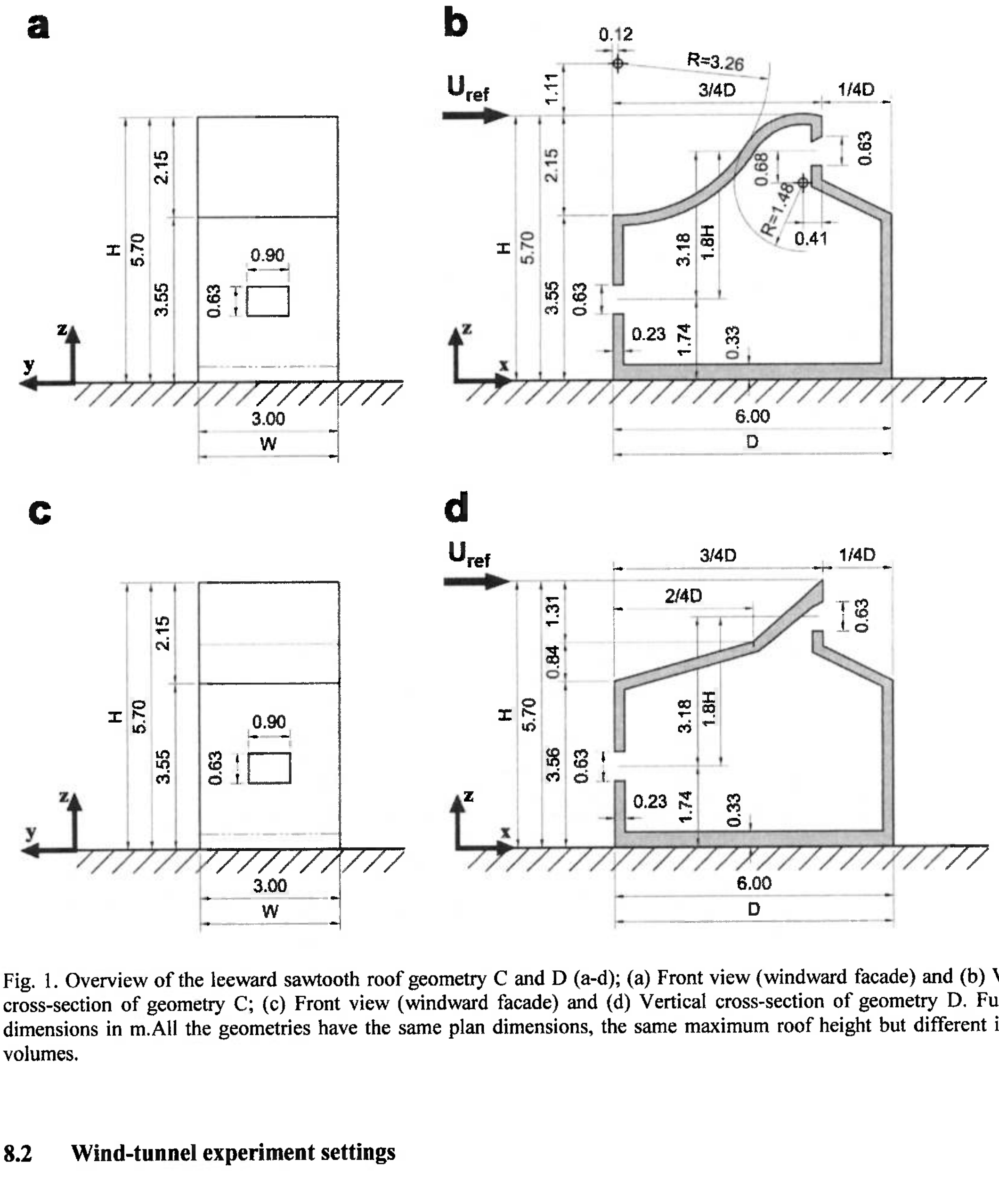

Fig. 1. Overview of the leeward sawtooth roof geometry C and D (a-d); (a) Front view (windward facade) and (b) Vertical cross-section of geometry C; (c) Front view (windward facade) and (d) Vertical cross-section of geometry D. Full-scale dimensions in m.All the geometries have the same plan dimensions, the same maximum roof height but different internal volumes.

8.2 Wind-tunnel experiment settings

Table 1 summarizes the nomenclature of the cases analyzed in the current paper. The cases are designated by a letter (i.e. "C" or "D") which represents roof geometry types analyzed by the authors in a previous study [8]. The hybrid convex-concave roof geometry C and the convex straight roof – Geometry D. The letters "BL" refers to the upstream terrain roughness or Boundary Layer case and the number following "BL" is related to the Boundary Layers case (i.e. 1 and 2), where BL1 is an upstream terrain roughness lower than BL2 (See more details about the upstream terrain roughness in the Section 2.1). The opening configuration are described by the letter "op" and "cl", which respectively indicate if the window openings of the reduced-scale building model are opened (op) or closed (cl). For all the eighth cases (i.e. C_BL1_cl, C_BL1_op, C_BL2_cl, C_BL2_op, D_BL1_cl, D_BL1_op, D_BL2_cl and D_BL2_op) the internal and the external mean pressure coefficients (C_P) were measured, discussed and are published in the end of this paper, in the Section Appendices.

Table 2 - Cases analyzed in the open-circuit BLWT

		Cases			
		Geometry C		Geometry D	
Terrain category		**op** (opened)	**cl** (closed)	**op** (opened)	**cl** (closed)
BL1	"Open sea" z_0* = 9^-5 m u* = 0.37 m/s	C_BL1_op	C_BL1_cl	D_BL1_op	D_BL1_cl
BL2	"Roughly open country" z_0 = 0.10 m u* = 1.23 m/s	C_BL2_op	C_BL2_cl	D_BL2_op	D_BL2_cl

The test was carried out in the low speed open-circuit BLWT facility of The Technological Research Institute of the State of São Paulo (IPT), Brazil. Figure 2 shows the BLWT which has an internal length of 28 m and a total length of 40 m, two testing sections (Fig. 2a); the first one, located just after the contraction cone (Fig. 2d), is employed for aerodynamic tests (laminar flow) and the second one, located at the end near the fan (exhaust) (Fig.2c,2e), is used for turbulent flow tests, as the present study. Both testing chambers have glass walls (for testing visualization) and 1.8 m-diameter turntable (which allows rotating the reduced-scale model 360 degrees and test various wind incidence directions). In this study the last wind tunnel test section with 3.0 m (wide) x 2.0 m (long) and 2.5 m (height) was employed. The air entrance of the wind tunnel has 5.0 m (long) per 4.0 m (height) and is composed by screens, honeycomb-shaped mesh and contraction cone (Fig. 2b).

8.2.1 Upstream terrain roughness: Boundary Layer (BL)

The vertical profiles of the mean wind speed (U) and the streamwise turbulence intensity (I_u) were measured at the middle of the wind tunnel turntable test section, without and at the same position where the reduced-scale building model were then located. Two Prandtl-Pitot tubes and one DANTEC hot-wire anemometer were employed. Two Scanivalve DSA3217 (16 channel), a Digital Barometer DHI RPM4 and two PT-100 were employed for the pressure tap measurement. The sampling frequency was 312.5 Hz and the duration was 30 s. Two upstream terrain roughness categories were analysed: (1) Case BL1; without roughness along the wind tunnel test section; and (2) Case BL2; with roughness element (with 60 mm and 80 mm height) positioned along the wind tunnel test section. The measured inlet wind-velocity profile U(z) is defined according to the logarithmic law (Eq. 1):

$$U(z) = \frac{u^*_{ABL}}{\kappa} \ln\left(\frac{z+z_0}{z_0}\right) \quad (1)$$

where the friction velocity (u^*) and the aerodynamic roughness length (z_0) for both Cases (BL1 and BL2) are described in Table 1, κ is the von Karman constant (0.42) and z the height coordinate. The value of u^*_{BL} is determined based on the values of the reference velocity (U_{ref}) at building height (H = 5.7 m).

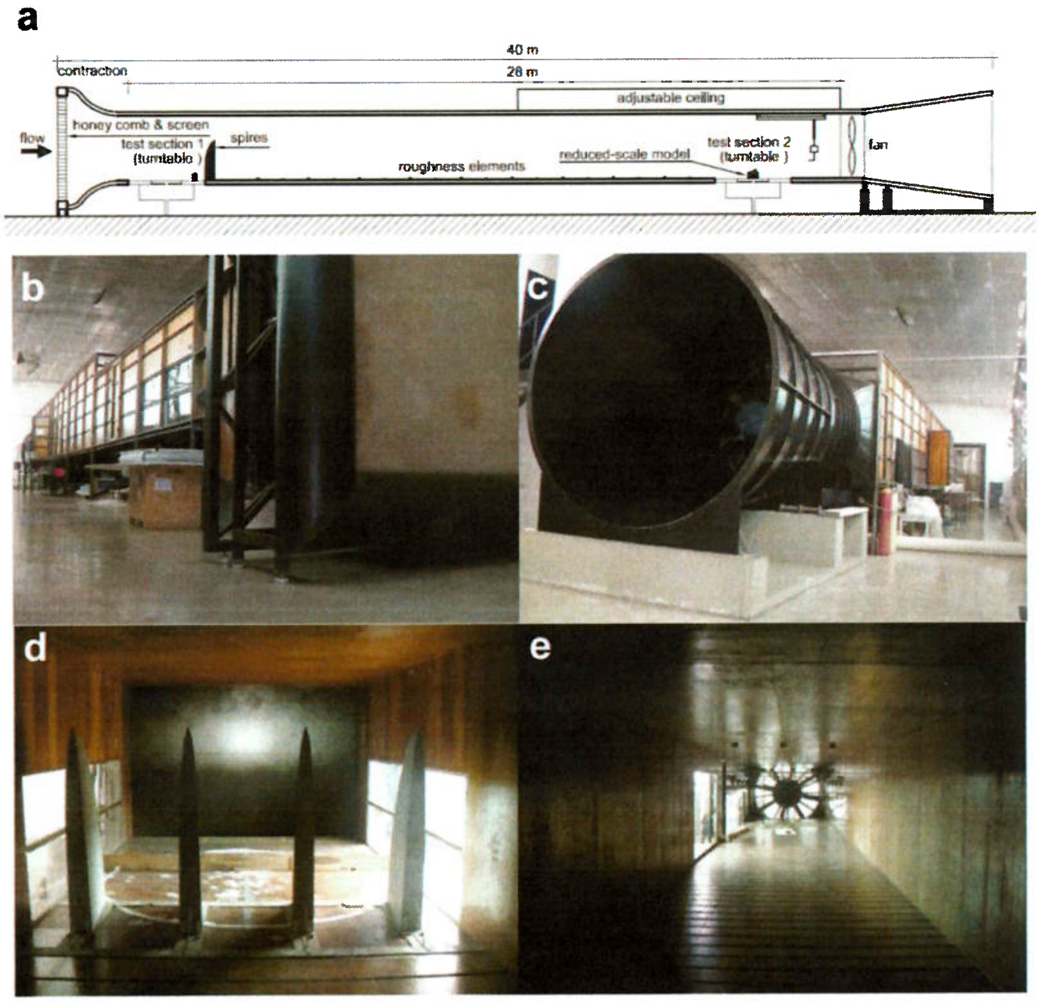

Fig. 2. (a) Vertical cross section of the ABL wind tunnel. (b-c) External view of the wind tunnel; (b) entrance, (c) fan. (d-e) Internal view of the wind tunnel; (d) View of the spires positioned after the testing section 1; (e) view of the 28 m-length platform used for placing the roughness elements to reproduce the terrain roughness.

The wind velocity (U) at the top of the leeward sawtooth roof scale-model was 10.26 m/s (for Case BL1) and 12.48 m/s (for Case BL2). The aerodynamic roughness length z_0 for Case BL1 and for Case BL2 corresponds respectively to an "Open sea" and a "Roughly open country", according to the updated Davenport roughness classification by [24]. The aerodynamic roughness length (z_0) for Case BL2 is higher than Case BL1 and represents a more realistic wind velocity profile. The streamwise turbulence intensity $I_u(z)$ varies for both cases. For case BL2, has a value of 15% at the top of the building model (at z_{ref}) and 45% at ground level. For case BL1, has a value of 10% at the top of the building model (at z_{ref}) and 15% at ground level. Five wind directions were measured: φ = 0°, 15°, 30°, 45° and 60°, but in the current study the wind direction perpendicular to the windward building facade (φ = 0°) is only considered. The wind velocity and turbulence intensity profiles for both Cases (BL1 and BL2) are shown in Fig. 3. It is noticed that the non-dimensional velocity (U/U_{ref}) at z/z_{ref} decreases from 0.88 in Case BL1 to 0.76 in Case BL2, which represents a decreases of 14% (See Fig.3a).

However, at the middle of the inlet opening (z/z_{ref} = 0.27 or 1.5 m height at full scale) the non-dimensional velocity (U/U_{ref}) decreases from 0.77 in Case BL1 to 0.52 in Case BL2, representing a decreases of 33%.

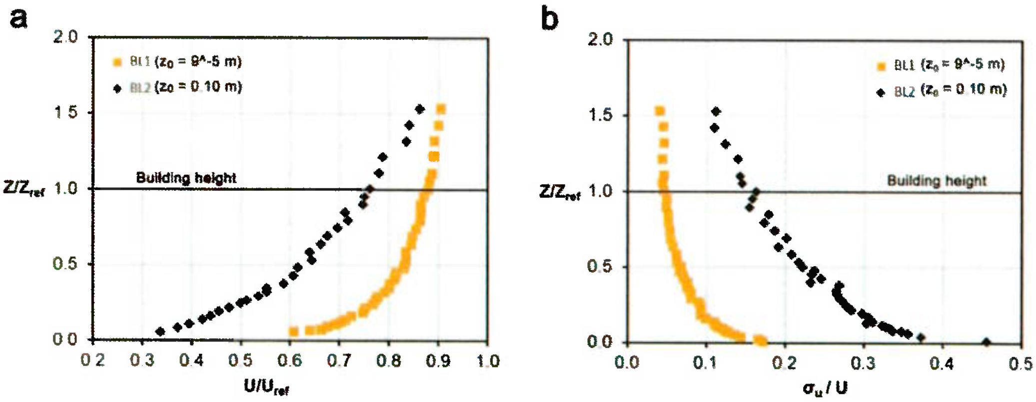

Fig. 3. (a-b) Vertical profiles of mean wind speed and longitudinal turbulence intensity for Case BL1, (c-d) Same for Case BL2.

8.2.2 Leeward sawtooth roof cases: geometry and reduced-scale model

Figure 1 previously shows a cross section of the leeward sawtooth roof geometry C (Fig. 1a and b) and the geometry D (Fig.1c and d) with the main dimensions. Since the two geometries (C and D) have a different roof geometry, as a consequence, each building has a different internal volume V: $V_C = 53.52\ m^3$ and $V_D = 50.78\ m^3$, in full scale). Both simplified geometries (without eaves) have the same porosity (5%), same plan and same roof height. The implicit roof inclination angle, which is the angle of a line from the upwind roof edge till the top roof edge, is 27° for both leeward sawtooth-roof geometries.

A 1:15 scale-model with rectangular plan and full-scale dimension of 3.0 m x 6.0 m and 5.7 m (W x D x H) roof height was constructed with double-face acrylic wall to embed the pressure taps. A double-face wall system for embedding the pressure taps was implemented to avoid blockage area of the plastic tubes, which connect the pressure tap with the Scanivalve Pressure Scanner, when located inside the reduced-scale model. This reduced-scale model could allow other tests such as smoke visualization and PIV measurement once the plastic tubes do not affect or interfere the airflow. Figure 4 shows an exploded view of the leeward sawtooth roof geometry C (Fig. 4a) and the geometry D (Fig.4b) with indication of the internal and external pressure taps location. A total of 60 pressure taps (aprox. 15 internal and 45 external) were located on each reduced-scale model (C and D) along three axes: edge axis 1 (E.A.1) and edge axis 2 (E.A.2) and central axis, as showed also in Figure 5. However, the pressure taps were mostly located on the central axis and around the openings, as indicated in Figure 4 and Figure 5. The pressure taps were connected to the Scanivalve Pressure Scanner. Figure 6 shows the reduced-scale model positioned in the BLWT test section.

The reduced-scale model represents a blockage ratio of about 4%, less than the limit of 5% indicated by [25]. The Reynolds number independence was confirmed by running four different flow regimes with wind tunnel setting speed of 15 m/s, 13 m/s, 10 m/s and 8 m/s. Finally, the velocity of 15 m/s (Building Reynolds number of 400,000) was selected for the whole pressure coefficient test.

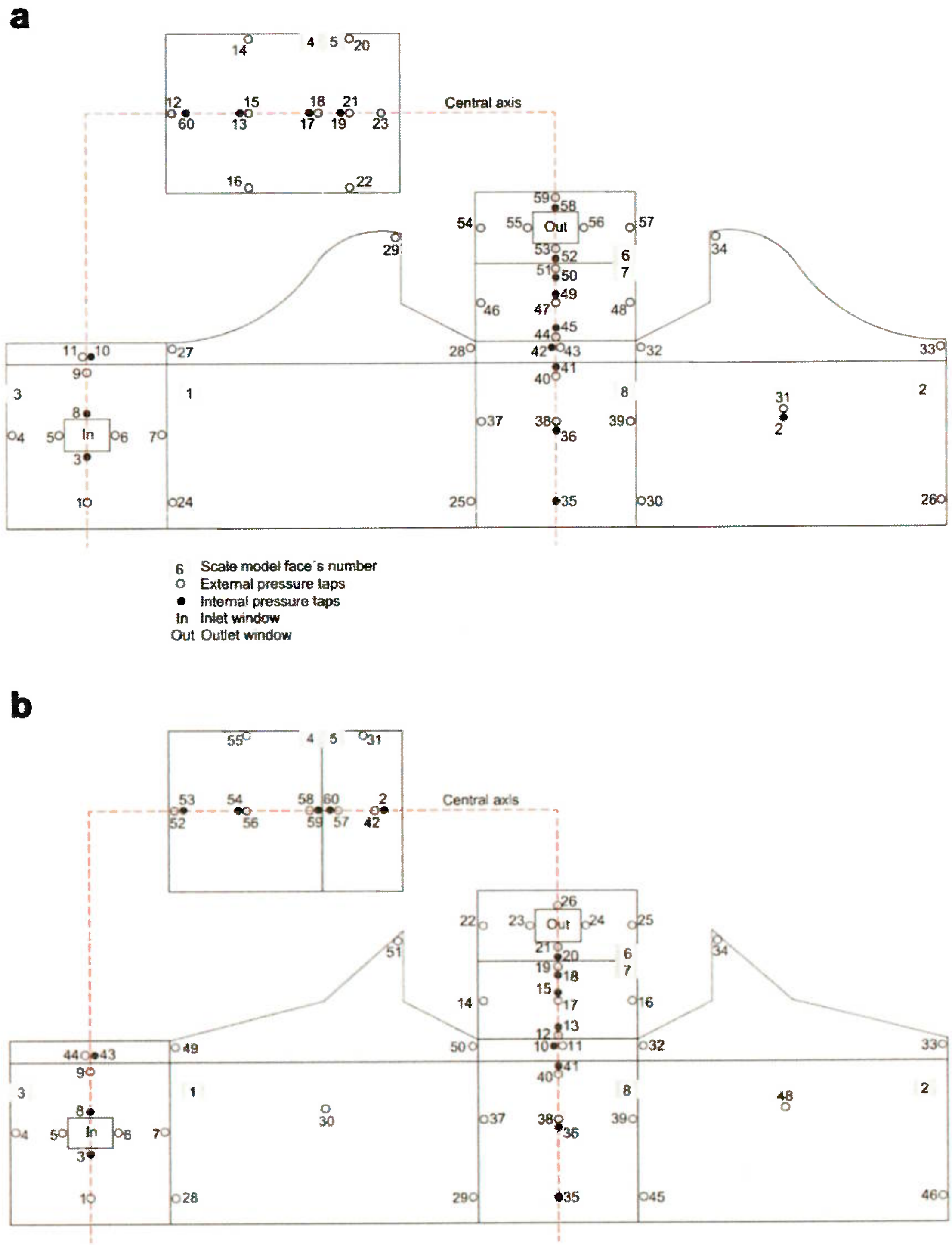

Fig. 4. Exploded view of the leeward sawtooth roof geometry C (a) and model D (b) with external and internal pressure taps locations used for pressure coefficient measurement in wind tunnel.

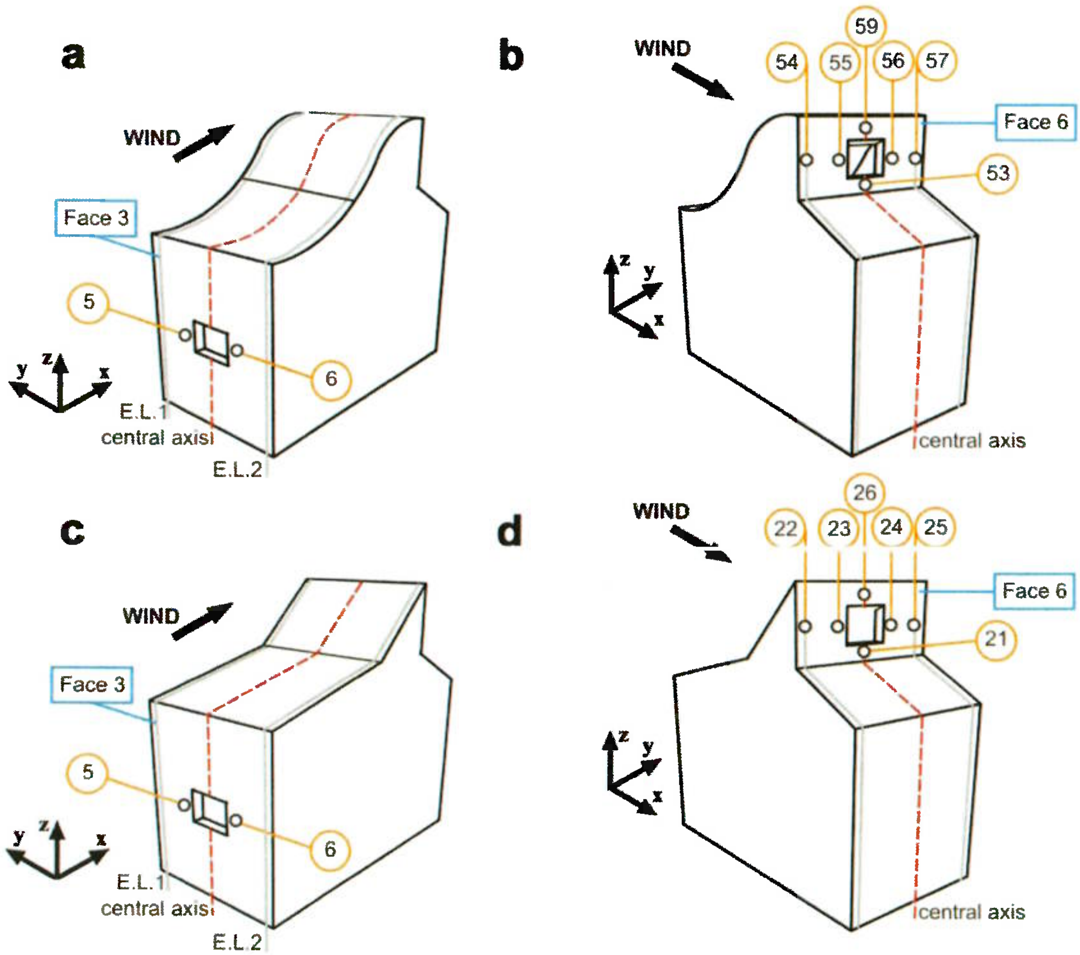

Fig. 5. (a,b,c and d) – Perspective view of the windward (a,c) and leeward facade (b,d) of Geometry C (a,b) and Geometry D (c,d) showing the vertical sections (edge axis in solid gray and central axis in dashed red line) along which the pressure taps were located. In addition, the pressure tap numbers near the inlet and the outlet opening are indicated.

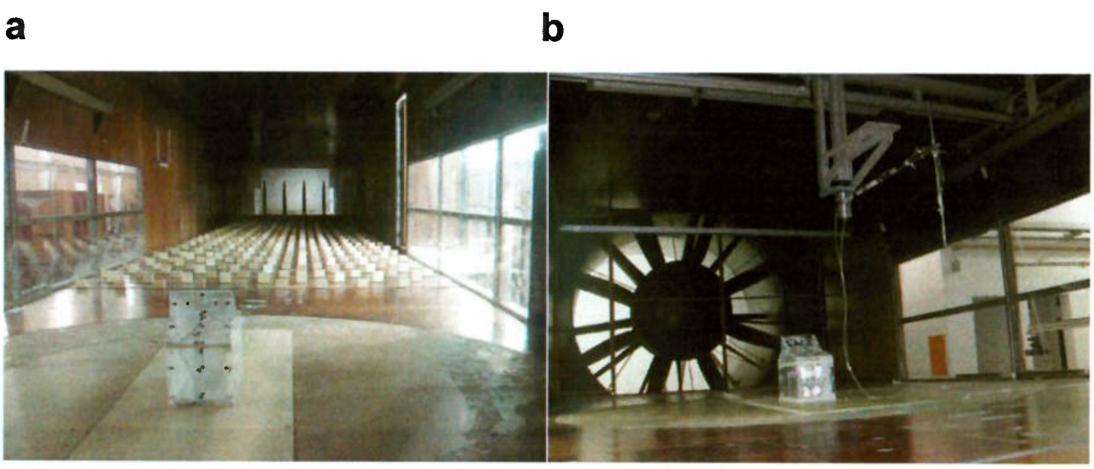

Fig. 6. View of the reduced-scale model: (a) Leeward sawtooth roof scale-model D downstream of fetch with spires and roughness elements(Case D_BL2_op); (b) Leeward sawtooth roof scale-model D downstream of fetch with only spires (Case D_BL1_op).

The impact of the BL and the opening configuration on the averaged external mean pressure coefficient (C_P) around the inlet and the outlet openings is analysed. The pressure coefficient is calculated as:

$$C_P = \frac{(P - P_0)}{(0.5 \rho U_{ref}^{\ 2})} \qquad (2)$$

where P is the static pressure, P_0 the reference static pressure (-6.94 Pa), ρ the density of air and U_{ref} is the approach-flow wind speed at building height (U_{ref} = 12.48 m/s at z_{ref} = 5.7 m). Two pressure taps were located around the inlet opening (Face 3) of Geometry C and D, as respectively showed by Figure 5a and 5c, and six pressure taps were located around the outlet opening, of both geometries, to obtain the external mean pressure coefficient, as showed in Figure 5b and 5d. The averaged external mean pressure coefficient ($C_{P\,avg} = (C_{P\,1} + C_{P\,2} + C_{P\,n\,...}) / n$) around the inlet opening at Face 3 is obtained from two pressure taps (5 and 6 for Geometry C and Geometry D) and the averaged external mean pressure coefficient around the outlet opening at Face 6 is obtained from six pressure taps (for Geometry C: 53, 54, 55, 56, 57 and 59 and, for Geometry D: 21, 22, 23, 24, 25 and 26, respectively).

8.3 Results

8.3.1 Impact of the upstream terrain roughness (BL) on a sealed building

8.3.1.1 External pressure coefficient ($C_{P\,ext}$)

Figure 7a and 7b display the averaged external mean pressure coefficient on Face 3 and Face 6 respectively, as a function of the upstream terrain roughness (BL) in a sealed building Geometry C and D. It is observed that the upstream terrain roughness (BL) affects differently and significantly each Geometry (C and D). For instance, when the upstream terrain roughness change from an "Open sea" to a "Roughly open country" (i.e. from BL1 to BL2), there is a small impact around the inlet opening surface of Geometry C but a much higher impact around the outlet opening surface of Geometry C. The other way around is observed for Geometry D. For Geometry C the pressure coefficient ($C_{P\,ext}$) around the inlet opening increases by 105.5% from Case C_BL1_cl to Case C_BL2_cl and for Geometry D it decreases down to 72.2% (Fig. 7a). On the outlet opening surface (Face 6), the C_P increases by 143.2% for Geometry C and by just 105.0% for Geometry D (Fig. 7b). The largest increase in pressure coefficient difference ($\Delta\ C_{P\,ext}$) between inlet opening and outlet opening surface take place on case C_BL2_cl (Geometry C under the highest Boundary Layer - BL2). Notice also that under the lowest upstream terrain roughness (i.e. the "Open sea" - BL1) the $C_{P\,ext}$ values at inlet and outlet opening surfaces are quite similar for both Geometry cases (C_BL1_cl and D_BL1_cl). In summary, in low-rise leeward sawtooth roof buildings the upstream terrain roughness (approaching wind vertical profile) has a considerable impact on the pressure coefficient ($C_{P\,ext}$) around the inlet and outlet openings.

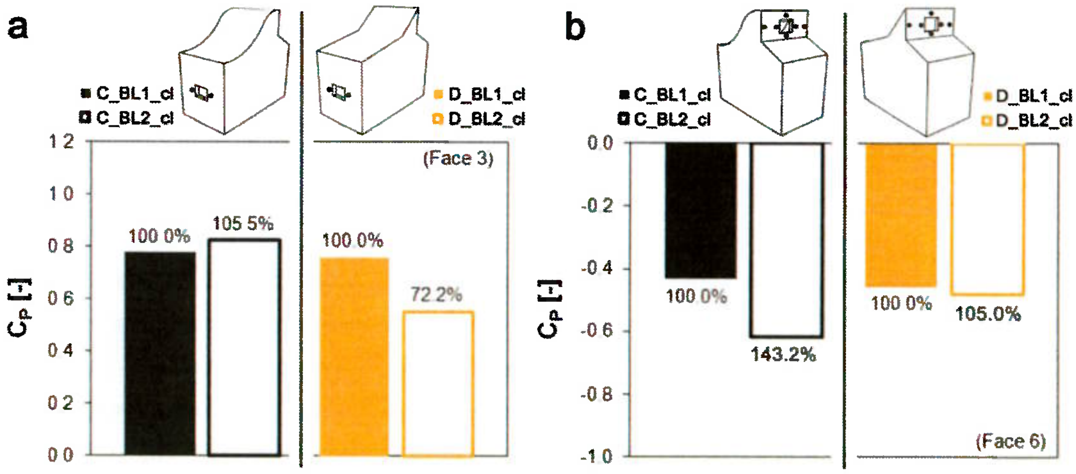

Fig. 7 – Impact of upstream terrain roughness (type of boundary layer) on surface pressure coefficients. (a) windward facade; (b) leeward facade of geometries C and D with closed openings (cl).

8.3.2 Impact of the upstream terrain roughness (BL) on a building with opened windows

8.3.2.1 Internal pressure coefficients ($C_{P\ in}$)

The internal pressure coefficient ($C_{P\ in}$) was measured at sixteen internal pressure taps located along a central axis of the internal faces (3, 4, 5, 6, 7 and 8), as previously showed in Figure 4. Figure 8 displays the averaged internal pressure coefficient ($C_{P\ in}$) of all the sixteen internal pressure taps and clearly shows the decreases of the internal pressure ($C_{P\ in}$) as a function of the upstream terrain. For instance, the $C_{P\ in}$ decreases down to 64.5% for Geometry C and down to 63.0% for Geometry D when increasing the upstream terrain roughness from "Open sea" to "Roughly open country" (i.e. from BL1 to BL2). It is also observed that the averaged internal pressure ($C_{P\ in}$) of Geometry D is higher than Geometry C under the Boundary Layer 1 and 2; by 151.8% (for Case BL1) and by 155.6% (for Case BL2). A reason for it appears to be a coupled-effect of the differences in the internal volume between both Geometries (C and D) and due the internal geometry of each geometry. For example, the Geometry D has an internal volume 5.5% lower than Geometry C and its internal geometry near the outlet opening is narrower than the one of Geometry C (See Fig. 1). Both parameters (internal volume and internal geometry) must be further evaluated. Figure 9 shows the $C_{P\ in}$ values of each pressure taps located along the central axis, as described in Figure 4. It was found that $C_{P\ in}$ is non-uniform and has a significant pressure decrease (by 144% with respect to the highest $C_{P\ in}$) near the outlet opening on the ceiling of the roof Geometry D. This non-uniform internal pressure is in line with a previous study carried out by [2]. However, the former author pointed out that the internal pressure is non-uniform in a flat roof building with large openings (wall porosity higher than 10%) and the current study has considered leeward sawtooth roof buildings with small asymmetric openings (wall porosity lower than 10%). In addition, the current results have shown that averaged $C_{P\ in}$ depends on the upstream terrain roughness and on roof shape (internal and external building Geometry).

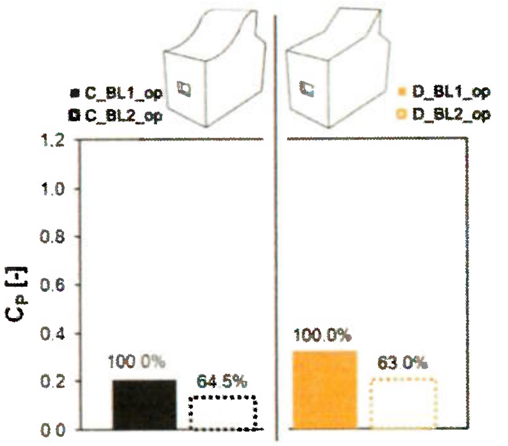

Fig. 8 – Averaged internal mean pressure coefficient ($C_{p\ in}$) under normal wind incidence angle for two BL on the two leeward sawtooth roof geometries (C and D) with opened windows openings.

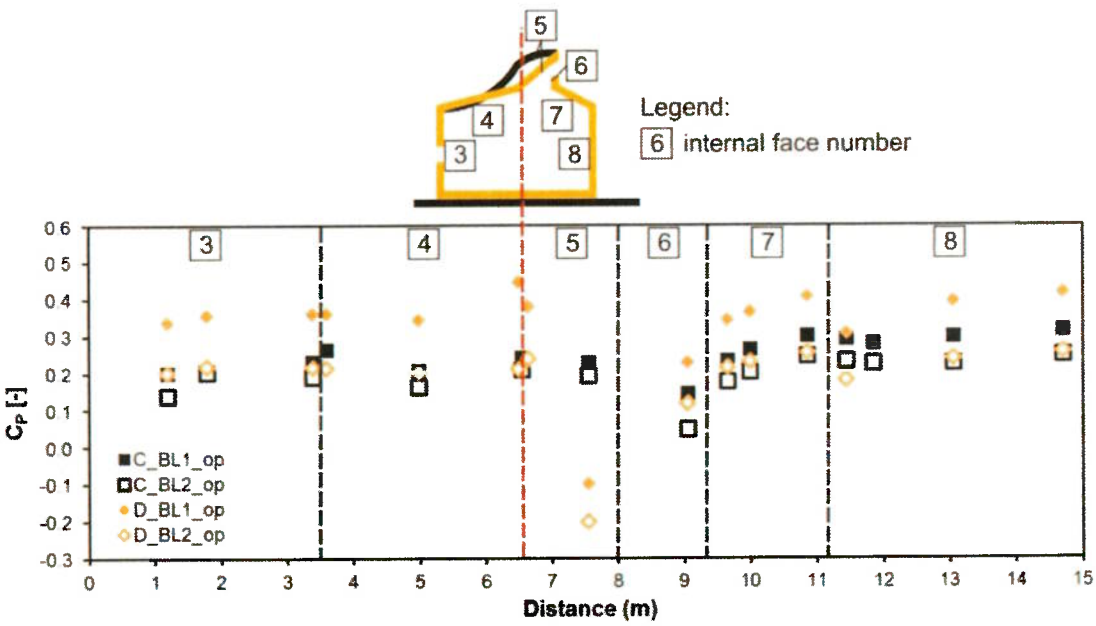

Fig. 9 – Internal mean pressure coefficient (C_P) of two leeward sawtooth roof geometries (C and D) with the windows opened under two Boundary Layer profiles (Cases: C_BL1_op, Cases C_BL2_op, Cases D_BL1_op and Cases D_BL2_op).

8.3.3 Impact around the outlet openings

Figure 10 (a,b,c and d) shows the averaged external mean pressure coefficients ($C_{P\ ext}$) around inlet opening (Face 3) and around outlet opening (Face 6) for Geometry C and D under two different BL (Case BL1 and Case BL2) when windows openings where closed (cl) and opened (op). There is a small increases of the pressure coefficient ($C_{P\ ext}$) around the inlet opening (Face 3) within a range of 101.7% and 107.3% for both Geometries (C and D); For instance, for Geometry C the pressure coefficient ($C_{P\ ext}$) increases from case C_BL1_cl to C_BL1_op by 101.7% and for case C_BL2_cl to C_BL2_op it increases by 107.3% (Fig. 10a); for Geometry D, the pressure coefficient ($C_{P\ ext}$) increases from D_BL1_cl to D_BL1_op by 105.1% and for D_BL2_cl to D_BL2_op it increases by 106.8% (Fig. 10c). Around the outlet opening (Face 6) of the Geometry C, a considerable increase takes place; from C_BL1_cl to C_BL1_op it increases by 114.2% and for cases C_BL2_cl to C_BL2_op it increase by 109.6% (Fig. 10b). Around the outlet opening (Face 6) of the Geometry D, the external pressure coefficient ($C_{P\ ext}$) increases by 104.5% from case D_BL1_cl to case D_BL1_op and by 112.0% from case D_BL2_cl to case D_BL2_op, as showed in Figure 10d. It is partially explained due the “suction effect” or “attractor effect” [26] induced by the stream tube flow going in at the inlet and out through the outlet opening. The internal geometry of both cases (C and D) force the air to increase the air velocity when leaving out the building by the narrow area of the outlet opening (this increase is showed at Figure 9).

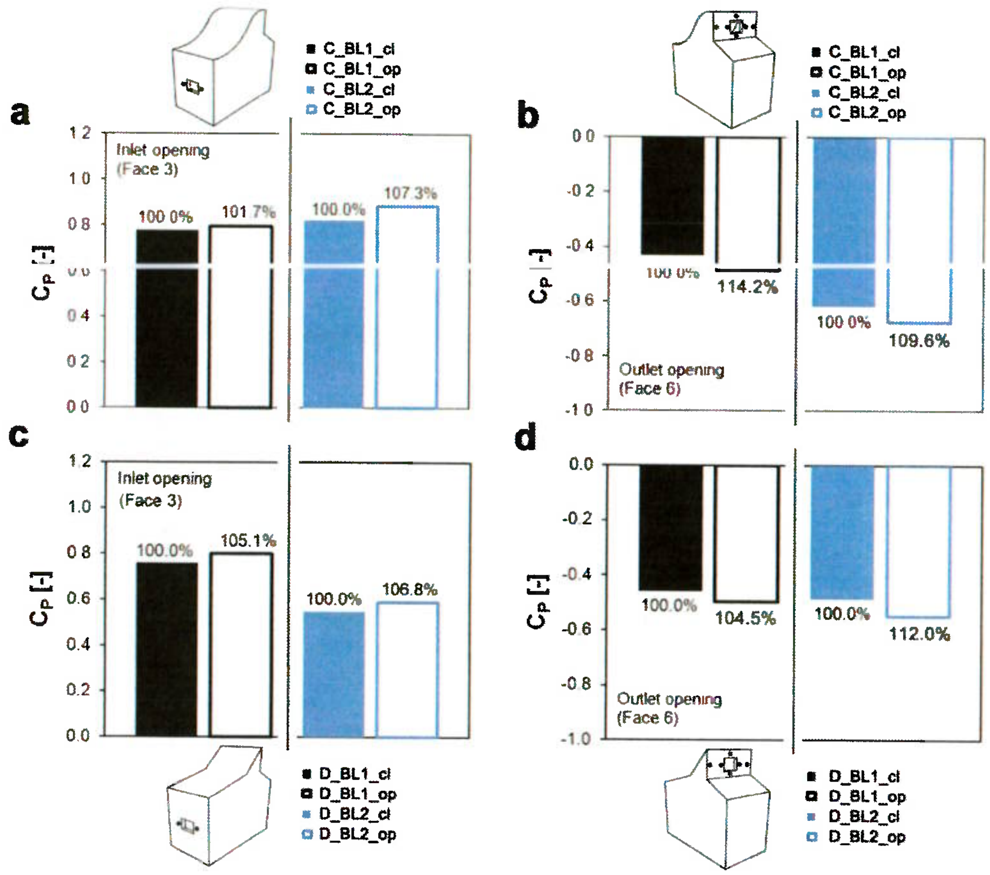

Fig. 10 – Impact of the openings (inlet and outlet) on the averaged external mean pressure coefficient under normal wind incidence angle for leeward sawtooth roof geometry (a,b) C and (c,d) D.

Figure 11 shows the mean pressure coefficient around inlet opening (on Face 3) and outlet opening (Face 6) of Geometries C and D under two different BL and when both windows opening were opened. For Geometry C, external mean pressure coefficient ($C_{P\ ext}$) around inlet opening increases by 111.2% from C_BL1_op to C_BL2_op. However, for Geometry D it decreases down to 73.5% (-26.5%) from D_BL1_op to D_BL2_op. Both Geometries cases (i.e. D_BL1_op and D_BL2_op and, in the other hand, C_BL1_op and C_BL2_op) have the same tendency than in a sealed building cases (i.e. D_BL1_cl and D_BL2_cl and, in the other hand, C_BL1_cl and C_BL2_cl, See Fig. 7). The average external pressure coefficient ($C_{P\ ext}$) around the outlet opening (Face 6) increases by 137.4% from case C_BL1_op to case C_BL2_op and on Geometry D it increases by 112.6% from case D_BL1_op to case D_BL2_op.

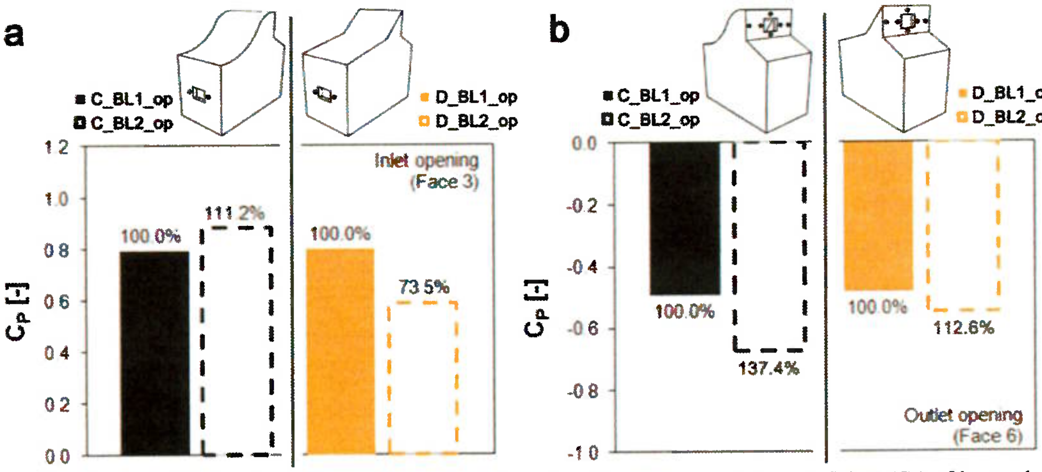

Fig. 11 – Impact of the Boundary Layer (BL) on the averaged external mean pressure coefficient (C_P) of leeward sawtooth roof geometry C and D with opened openings (inlet and outlet) around (a) inlet opening and (b) outlet opening (Face 6).

8.4 Discussion

The main goal of the current paper is to evaluate the impact of the approaching wind profile (upstream terrain roughness) and the openings configuration in two leeward sawtooth roof buildings under normal wind incidence angle. Eight cases are evaluated in an open-circuit Boundary Layer Wind Tunnel (BLWT) of the Institute for Technological Research (IPT), São Paulo, Brazil: two leeward sawtooth roof geometries (one convex straight roof – Geometry D, and one hybrid convex-concave roof – Geometry C); two opening configuration (when inlet and outlet windows opening were opened – Case "op", and when it where closed – Case "cl"); two upstream terrain roughness (an "Open sea" with z_0 = 9e^-5 m – Case "BL1", and a "Roughly open country" with z_0 = 0.1 m – Case "BL2". The internal and external mean pressure coefficient (C_P) is measured. External pressure coefficients over the Face 3 and Face 6, where inlet and outlet opening are respectively located, were compared. Finally, the wind tunnel pressure coefficient data of 60 pressure taps (15 internal and 45 external) of both Geometry C and D are presented at the last Section Appendix and can be used for validation.

The literature assumes that in buildings with small openings (porosity smaller than 10%) the external pressure coefficient on the facade surface is independent of the openings and thus can be replaced by those values measured on a sealed building. In the current study the external mean pressure coefficient ($C_{P\ ext}$) around the inlet openings increases between 101.7% and 107.3% when the windows were opened. Nevertheless, on the cases D_BL2_op and C_BL2_op there is a considerable increase of the external pressure ($C_{P\ ext}$) around the outlet opening (face 6), between 112.0% and 114.5% in Geometry D and C respectively. It is in line with [27] which reported that air pressure distribution around a solid model changes if it is provided with openings. Our findings also support a previous works that pointed out that the pressure coefficients from sealed buildings cannot always be used to predict the flow through an opening [26]. Nevertheless, it is important to mention the limitations of the current study, which should be addressed in future research:

- Regarding measurement uncertainty, some asymmetric values of pressure coefficient appear as a consequence of the difficulty in placing the wind tunnel test turntable in the right position (normal to the wind incidence). For instance, the external pressure taps around inlet openings T.5 and T.6 of Geometry

D and close to the outlet openings should have a similar value, as in both cases, the pressure taps are horizontally aligned.

- Some pressure taps failed to work during some cases (T.8 and T.12 on Geometry C and T.12, T.48 and T.51 on geometry D).
- The impact of wind incidence angles different than 0° on the pressure distribution are not presented but are going to be discussed in a future paper in combination with the Root Means Square (RMS) C_P.
- The ventilation flow rate should be analysed in both geometries once it depends of the pressure differences between the building surfaces where inlet and outlet opening are located and also on the discharge coefficient of each building geometry.

8.5 Conclusions

The following conclusions may be drawn from this research:

- The upstream terrain roughness of Boundary Layer (BL) has a considerable impact on the pressure coefficient distribution around and inside a low-rise leeward sawtooth roof building (with 5.7 m height) and it must be carefully considered in studies of wind cross-ventilation.
- The upstream terrain roughness or Boundary Layer (BL) considerably affects the pressure coefficient (C_P) around the inlet and the outlet openings of a sealed building and the magnitude of this impact depends also on the roof shape of the leeward sawtooth roof building. For instance, it strongly affects (by 27.8%) the C_P around the inlet opening of a convex leeward sawtooth roof, such as Geometry D and nearly not affects it (by 5.5%) in a concave leeward sawtooth roof, such as Geometry C. On the other hand, it strongly affects (by 143.2%) the C_P around the outlet opening of Geometry C, but a small impact is observed in Geometry D (by 5.0%).
- The averaged internal mean pressure coefficient ($C_{P\ int}$) of Geometry D is higher than Geometry C by 151.8% in Case BL1 and by 155.6% in Case BL2. The higher internal pressure seems to be related to the lower internal volume of the geometry D.
- The averaged internal mean pressure coefficient ($C_{P\ int}$) is higher at lower Boundary Layer (BL1). But it decreases around 36% under a higher Boundary Layer (BL2) in both Geometry cases (C_BL2_op and D_BL2_op).
- The internal pressure ($C_{P\ int}$) is non-uniform for both Geometry C and D. Geometry D has a considerable local decrease of the $C_{P\ in}$ on the ceiling surface near the outlet opening, having a difference of by 144% between the minimum and maximum $C_{P\ in}$.
- The external pressure coefficient ($C_{P\ ext}$) around the inlet and around the outlet opening is higher when the windows of the leeward sawtooth roof building are opened. For both Geometries (C and D) and when the openings were opened, the external mean pressure coefficient ($C_{P\ ext}$) around the inlet opening just increase between 101.7% and 107.3%. However, the C_P around the outlet opening considerably increases up to 112.0% and 114.2% in Geometry D and C respectively.

8.6 Acknowledgments

The first author was supported by The Secretary of Education, Science, Research and Technology of Panama (SENACYT). The wind tunnel experiment and measurements reported in this paper were supported by the Civil Construction Engineering Department of The Polytechnic School of The University of São Paulo (USP) and especially by the Laboratory of Electrical and Fluids Metrology of the Institute for Technological Research (IPT), São Paulo, Brazil. Special thanks go to Gabriel Borelli Martins and Paulo Jabardo, members of the wind tunnel research group, for their valuable contribution.

8.7 References

[1] Robbins CL. Daylighting: design and analysis. Van Nostrand Reinhold Company; 1986.

[2] Karava P, Stathopoulos T, Athienitis AK. Impact of internal pressure coefficients on wind-driven ventilation analysis. International Journal of Ventilation 2006;5:53–66.

[3] Murakami S, Akabayashi S, Kim Y-D, Kato S, Mizutani K. Wind tunnel test on velocity-pressure field of cross-ventilation with open windows. ASHRAE Transactions, 1991, p. 525–38.

[4] Kato S, Murakami S, Mochida A, Akabayashi S, Tominaga Y. Velocity-pressure field of cross ventilation with open windows analyzed by wind tunnel and numerical simulation. Journal of Wind Engineering and Industrial Aerodynamics 1992;44:2575–86. doi:10.1016/0167-6105(92)90049-G.

[5] Kobayashi T, Sagara K, Yamanaka T, Kotani H, Sandberg M. Wind driven flow through openings - Analysis of the stream tube. International Journal of Ventilation 2006;4:323–36.

[6] Kobayashi T, Sagara K, Yamanaka T, Kotani H, Takeda S, Sandberg M. Stream Tube based Analysis of Problems in Prediction of Cross-Ventilation Rate. International Journal of Ventilation 2009;7:321–34. doi:10.5555/ijov.2009.7.4.321.

[7] Karava P, Stathopoulos T. Wind-induced internal pressures in buildings with large façade openings. Journal of Engineering Mechanics 2012;138:358–70. doi:10.1061/(ASCE)EM.1943-7889.0000296.

[8] Perén JI, Ramponi R, van Hooff T, Blocken B, Leite BCC. Impact of roof geometry of an isolated leeward sawtooth-roof building on cross-ventilation: Straight, concave, hybrid or convex? Submitted 2015.

[9] Straw MP, Baker CJ, Robertson AP. Experimental measurements and computations of the wind-induced ventilation of a cubic structure. Journal of Wind Engineering and Industrial Aerodynamics 2000;88:213–30. doi:10.1016/S0167-6105(00)00050-7.

[10] Ohba M, Irie K, Kurabuchi T. Study on airflow characteristics inside and outside a cross-ventilation model, and ventilation flow rates using wind tunnel experiments. Journal of Wind Engineering and Industrial Aerodynamics 2001;89:1513–24. doi:10.1016/S0167-6105(01)00130-1.

[11] Jiang Y, Alexander D, Jenkins H, Arthur R, Chen Q. Natural ventilation in buildings: measurement in a wind tunnel and numerical simulation with large-eddy simulation. Journal of Wind Engineering and Industrial Aerodynamics 2003;91:331–53. doi:10.1016/S0167-6105(02)00380-X.

[12] Karava P, Stathopoulos T, Athienitis AK. Airflow assessment in cross-ventilated buildings with operable façade elements. Building and Environment 2011;46:266–79. doi:10.1016/j.buildenv.2010.07.022.

[13] Karava P, Stathopoulos T, Athienitis AK. Wind-induced natural ventilation analysis. In: Proc Fith Int Conf on Wind Engineering 2007;81:20–30. doi:10.1016/j.solener.2006.06.013.

[14] Holmes JD. Wind pressures on tropical housing. Journal of Wind Engineering and Industrial Aerodynamics 1994;53:105–23. doi:10.1016/0167-6105(94)90021-3.

[15] Prasad D, Uliate T, Ahmed MR. Wind loads on low-rise building models with different roof configurations. International Journal of Fluid Mechanics Research 2009;36:231–43. doi:10.1615/InterJFluidMechRes.v36.i3.30.

[16] Ho TCE, Surry D, Morrish D, Kopp GA. The UWO contribution to the NIST aerodynamic database for wind loads on low buildings: Part 1. Archiving format and basic aerodynamic data. Journal of Wind Engineering and Industrial Aerodynamics 2005;93:1–30. doi:10.1016/j.jweia.2004.07.006.

[17] Choinière Y, Tanaka H, Munroe JA, Suchorski-Tremblay A. Prediction of wind-induced ventilation for livestock housing. Journal of Wind Engineering and Industrial Aerodynamics 1992;44:2563–74. doi:10.1016/0167-6105(92)90048-F.

[18] Choinière Y, Tanaka H, Munroe JA, -Tremblay AS. A wind tunnel study of the pressure distribution around sealed versus open low-rise buildings for naturally ventilated livestock housing. Journal of Wind Engineering and Industrial Aerodynamics 1994;51:71–91. doi:10.1016/0167-6105(94)90078-7.

[19] Stathopoulos T, Saathoff P. Codification of Wind pressure coefficients for sawtooth roofs. Journal of Wind Engineering and Industrial Aerodynamics 1992;43:1727–38. doi:16/0167-6105(92)90584-W.

[20] Stathopoulos T, Mohammadian AR. Modelling of wind pressures on monoslope roofs. Engineering Structures 1991;13:281–92. doi:16/0141-0296(91)90039-F.

[21] Cui B. Wind Effects on Monosloped and Sawtooth Roof. Thesis. Clemson University, 2007.

[22] Stathopoulos, T., Surry D, Davenport, A.G. Internal pressure characteristics of low-rise buildings due to wind action. In: Proc Fifth Conf on Wind Engineering, (Fort Collins, USA: Jul 8-14, 1979) 1979.

[23] Liu H, Rhee KH. Helmholtz oscillation in building models. Journal of Wind Engineering and Industrial Aerodynamics 1986;24:95–115. doi:10.1016/0167-6105(86)90001-2.

[24] Wieringa J. Updating the Davenport roughness classification. Journal of Wind Engineering and Industrial Aerodynamics 1992;41:357–68. doi:10.1016/0167-6105(92)90434-C.

[25] Barlow JB. Low-speed wind tunnel testing /. 3rd ed. Wiley,; 1999.

[26] Sandberg M. An Alternative View on the Theory of Cross-Ventilation. International Journal of Ventilation 2004;2:409–18.

[27] Asfour OS, Gadi MB. A comparison between CFD and Network models for predicting wind-driven ventilation in buildings. Building and Environment 2007;42:4079–85. doi:10.1016/j.buildenv.2006.11.021.

8.8 Appendix

Table 2 – External and internal mean pressure coefficients (C_p) of Geometry C for two BL and two opening configuration.

Face		Pressure Tap N°		BL1		BL2	
		External	Internal	C_BL1_cl	C_BL1_op	C_BL2_cl	C_BL2_op
1	Right side wall	24		-0.78	-0.78	-0.99	-1.01
		25		-0.18	-0.19	-0.24	-0.27
		27		-0.94	-0.95	-1.29	-1.35
		28		-0.24	-0.24	-0.39	-0.40
		29		-0.59	-0.58	-0.80	-0.81
2	Left side wall		2	-	0.17	-	0.13
		26		-0.92	-0.88	-1.18	-1.12
		30		-0.17	-0.17	-0.29	-0.28
		31		-0.48	-0.46	-0.48	-0.45
		32		-0.25	-0.25	-0.37	-0.36
		33		-0.92	-0.94	-1.35	-1.36
		34		-0.57	-0.57	-0.81	-0.80
3	Windward	1		0.69	0.67	0.77	0.77
			3	-	0.20	-	0.14
		4		0.36	0.41	0.46	0.38
		5		0.78	0.80	0.83	0.88
		6		0.78	0.80	0.82	0.89
		7		0.31	0.34	0.26	0.30
			8	-	*	-	0.19
		9		0.85	0.85	0.90	0.97
			10	-	0.23	-	0.19
		11		0.73	0.73	0.93	0.86
4	Roof	12		-0.24	-0.24	*	-0.38
			13	-	0.21	-	0.16
		14		-0.22	-0.19	-0.10	-0.06
		15		-0.19	-0.17	0.21	0.27
		16		-0.23	-0.20	-0.06	-0.03
			17	-	0.24	-	0.21
		18		0.26	0.25	0.26	0.27
			60	-	0.26	-	0.24
5	Roof		19	-	0.23	-	0.19
		20		-0.79	-0.78	-0.92	-0.97
		21		-1.11	-1.11	0.39	-1.43
		22		-0.76	-0.75	-0.90	-0.94
		23		-0.99	-0.62	-1.18	-1.30
6	Outlet opening face		52	-	0.14	-	0.05
		53		-0.40	-0.37	-0.59	-0.40
		54		-0.46	-0.46	-0.67	-0.67
		55		-0.41	-0.58	-0.59	-0.82
		56		-0.43	-0.60	-0.58	-0.64
		57		-0.45	-0.46	-0.66	-0.67
			58	-	-0.56	-	-0.80
		59		-0.43	-0.49	-0.61	-0.72
7	Leeward face	44		-0.58	-0.51	-0.82	-0.74
			45	-	0.30	-	0.25
		46		-0.49	-0.47	-0.71	-0.68
		47		-0.45	-0.42	-0.67	-0.63
		48		-0.48	-0.46	-0.69	-0.63
			49	-	0.26	-	0.20
			50	-	0.24	-	0.18
		51		-0.41	-0.38	-0.62	-0.58
8	Leeward face		35	-	0.31	-	0.25
			36	-	0.30	-	0.23
		37		-0.29	-0.28	-0.43	-0.42
		38		-0.28	-0.27	-0.43	-0.42
		39		-0.28	-0.27	-0.40	-0.41
		40		-0.30	-0.29	-0.44	-0.44
			41	-	0.28	-	0.23
			42	-	0.29	-	0.23
		43		-0.35	-0.33	-0.56	-0.51

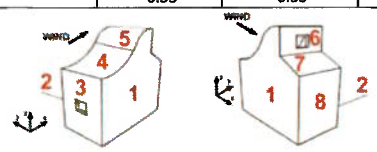

*pressure tap with problem

Table 3– External and internal mean pressure coefficients (C_P) of Geometry D for two BL and two opening configuration.

Face		Pressure Tap N°		BL1		BL2	
		External	Internal	C_BL1_cl	C_BL1_op	C_BL2_cl	C_BL2_op
1	Right side wall	28		-0.76	-0.76	-0.66	-0.68
		29		-0.32	-0.31	-0.29	-0.29
		30		-0.42	-0.44	-0.28	
		49		-0.91	-0.85	-0.89	-0.89
		50		-0.11	-0.32	-0.38	-0.36
		51		*	-0.51	*	-0.54
2	Left side wall	32		-0.39	-0.35	-0.40	-0.39
		33		-0.93	-0.90	-0.90	-0.90
		34		-0.58	-0.51	-0.54	-0.54
		45		-0.36	-0.31	-0.33	-0.34
		46		-0.77	-0.79	-0.68	-0.69
		48		-0.01	-0.38	*	-0.28
3	Upward face	1		0.70	0.69	0.52	0.52
			3	-	0.34	-	0.20
		4		0.33	0.44	0.23	0.24
		5		0.78	0.81	0.57	0.59
		6		0.75	0.79	0.53	0.58
		7		0.31	0.30	0.17	0.20
			8	-	0.36	-	0.22
		9		0.82	0.85	0.60	0.63
			43	-	0.36	-	0.21
		44		0.74	0.74	0.57	0.56
4	Roof	52		-0.63	-0.60	-0.60	-0.59
			53	-	0.36	-	0.21
			54	-	0.34	-	0.20
		55		-0.21	-0.18	-0.16	-0.15
		56		-0.03	-0.01	0.12	0.12
		58		0.45	0.45	0.36	0.35
			59	-	0.45	-	0.21
5	Roof		2	-	-0.10	-	-0.20
		31		0.12	0.13	0.07	0.06
		42		0.82	0.30	0.25	0.23
		57		0.53	0.52	0.43	0.42
			60	-	0.38	-	0.24
6	outled opening face		20	-	0.23	-	0.11
		21		-0.47	-0.44	-0.48	-0.46
		22		-0.49	-0.47	-0.51	-0.51
		23		-0.46	-0.46	-0.48	-0.55
		24		-0.46	-0.51	-0.48	-0.54
		25		-0.48	-0.46	-0.51	-0.51
		26		-0.44	-0.57	-0.47	-0.62
7	Leeward face	12		-0.32	0.09	-0.15	*
			13	-	0.41	-	0.25
		14		-0.46	-0.30	-0.43	-0.38
		17		-0.39	-0.10	-0.05	0.23
		16		-0.47	-0.33	-0.44	-0.40
			15	-	0.36	-	-0.18
			18	-	0.34	-	0.21
		19		-0.46	-0.45	-0.48	-0.49
8	Leeward face		10	-	0.31	-	0.18
		11		-0.46	-0.45	-0.46	-0.40
			35	-	0.41	-	0.26
			36	-	0.39	-	0.24
		37		-0.44	-0.40	-0.42	-0.42
		38		-0.46	-0.42	-0.43	-0.43
		39		-0.23	-0.40	-0.41	-0.42
		40		-0.46	-0.42	-0.44	-0.44
			41	-	-	-	0.46

*pressure tap with problem

Biography

Jorge Isaac Perén Montero was born on 27-10-1978 in David, Chiriqui, Republic of Panama. He obtained his high school diploma in Sciences and Arts in 1996 at the Marista San Vicente de Paul, catholic high school in his home town (David, Chiriqui). During his high-school period, he was President of the Government of Student body by general election during two periods (1996 and 1997). Furthermore, he was involved in the organization of several sport and social activities. He was director of his high school Marching Band from 1994 until 1996.

In order to start his university studies, he moved to Panama city, where he studied in the Architecture Department of the University of Panama (UP) for two and a half year. In 1999, he won a half scholarship in a competition initiated by the Brazilian Embassy in Panama, which allowed him to start the five-years Architecture and Urban Planning course at the University of São Paulo (USP), Brazil. During one year of his Architecture and Urban Planning course he held an "*Iniciação Científica*" scholarship (in English: Scientific Initiation grant for undergraduate students) of the São Paulo Research Foundation (FAPESP) within the group Architecture, Technologies and Materials (in Portuguese: ArqTeMas) under the supervision of prof.dr. Rosana Caram. In 2002 he earned his diploma in just four years. In 2003 he submitted an application to University of São Paulo for the national selection (in Brazil) to obtain a place to study for a master degree at the same institution and won one of the four scholarships available. During his master degree period he also worked in the international architecture and engineering office TSyA. He obtained his Master degree in Architecture and Technology in 2006.

From 1998 (first as practitioner and then as a certified professional) until 2010 he worked in different architecture and engineering offices in Panama and Brazil. During his period in Brazil he was involved with the Panamanian Association of São Paulo (APSP) and he was the President of this association between 2007 and 2009. Since 2010 he was active as consultant in urban and building physics. After a professional experience in the design of several healthcare buildings designed by the Brazilian Architect João Filgueiras Lima (Lelé), he decided to start developing his PhD research project on natural ventilation. In 2010 he classified in the National selection of the Architecture and Urban Planning Department of the University of São Paulo, Brazil, to start his PhD project. He started as a PhD student at the Polytechnic School of the University of São Paulo (USP) under supervision of dr. Brenda Leite in 2011 and since June 2013 he is also a guest PhD student at Eindhoven University of Technology (TU/e) in the Netherlands under supervision of prof.dr.ir. Bert Blocken and dr.ir. Twan van Hooff (co-supervisor), as part of a double-degree PhD agreement between both universities (USP and TU/e). So far, he has published one ISI journal article and has submitted three papers to different ISI journals. In addition, other journal paper is under preparation, all of them as a first author. He has also published nine conference papers and two articles in professional journals.

Publications

ISI journal papers

Published

1. PERÉN, J.I., van HOOFF, T., LEITE, B.C.C., BLOCKEN, B. (2015); "CFD analysis of cross-ventilation of a generic isolated building with asymmetric opening positions: impact of roof angle and opening location". Building and Environment, vol.85, pp. 263-276. doi:10.1016/j.buildenv.2014.12.007.

2. PERÉN, J.I., van HOOFF, T., LEITE, B.C.C., BLOCKEN, B.; "Impact of eaves on cross-ventilation of a generic isolated leeward sawtooth-roof building: windward eaves, leeward eaves and eaves inclination angle". Building and Environment, in Press.

Submitted

3. PERÉN, J.I, van HOOFF, T., RAMPONI, R., BLOCKEN, B., LEITE, B.C.C.; "Impact of roof geometry of an isolated leeward sawtooth roof building on cross-ventilation: Straight, concave, hybrid or convex?".

4. PERÉN, J.I., van HOOFF, T., BLOCKEN, B., LEITE, B.C.C.; "CFD simulations of wind-driven upward cross ventilation and its enhancement in long buildings: Impact of single-span versus double-span leeward sawtooth roof and opening ratio".

Under preparation

5. PERÉN, J.I, van HOOFF, T., NADER, G., LEITE, B.C.C., BLOCKEN, B.; "Wind-tunnel measurements of internal and external mean pressure coefficients of single-zone isolated leeward sawtooth roof buildings: effect of upstream terrain roughness, roof shape and window openings".

Conference proceedings

1. PERÉN, J.I., van HOOFF, T., LEITE, B.C.C., BLOCKEN, B (2015, accepted). "Wind-Driven Upward Cross-Ventilation in a 12 m Long Building: Single-Span versus Double-Span Leeward Sawtooth-Roof". The 9th International Symposium on Heating, Ventilation and Air Conditioning (ISHVAC) and The 3rd

International Conference on Building Energy and Environment (COBEE 2015), Tianjin, China, July 12 - 15, 2015.

2. PERÉN, J.I., van HOOFF, T., LEITE, B.C.C., BLOCKEN, B. (2015; Abstract Submitted). "Effect of upwind and leeward eave configuration in the upward cross-ventilation of leeward sawtooth-roof buildings". Abstract submitted to Building Simulation Conference (BS2015), Hyderabad, India, December 7-9, 2015.

3. PERÉN, J.I., RAMPONI, R., van HOOFF, T., BLOCKEN, B., LEITE, B.C.C. (2014); "Natural upward cross-ventilation potential of a leeward sawtooth-roof for a single zone building model". In: Proceedings of the 6th International Symposium on Computational Wind Engineering (CWE 2014), 8-12 June 2014, Hamburg, Germany, (pp. 1-8).

4. PERÉN, J.I., SANTOS, E.T., LEITE, B.C.C. (2012); "Upward-airflow ventilation system: an architectural proposal for tropical weather". In: Proceedings of Zero Energy/CO_2 emission Mass-Customisable Homes 2012 (ZEMCH 2012), Glasgow, UK, (pp. 726–741).

5. PERÉN, J.I., SANTOS, E.T., LEITE, B.C.C. (2011); "The influence of the sawtooth roof geometry in building ventilation". In: Proceedings of URBENVIRON 2011 (URBENVIRON 2011), Cairo, Egito, (pp. 1–14).

6. PERÉN, J.I., CARAM, R.M. (2007); "Interação da ventilação natural, mecânica e climatização: Estudo do hospital Sarah Kubitschek – Fortaleza, do arquiteto João Filgueiras Lima, Lelé", In: Encontro Nacional e Latino Americano de Conforto no Ambiente Construído, Anais 2007. (ENCAC/ELACAC 2007), Ouro Preto, MG - Brazil.

7. PERÉN, J.I., CARAM, R.M.; GRECO, P. (2007); "Análise computacional dos sheds da Rede de hospitais Sarah Kubitschek utilizando o Software Ansys CFX", In: Encontro Nacional e Latino Americano de Conforto no Ambiente Construído, Anais 2007. (ENCAC/ELACAC 2007), Ouro Preto, MG - Brazil.

8. PERÉN, J.I., CARAM, R.M. (2001); "Reflexão da radiação solar em vidros e películas refletivas", In: Encontro Nacional e Latino Americano sobre Conforto no Ambiente Construído, Anais 2001 (ENCAC/ELACAC 2001), São Pedro, SP - Brazil.

9. PERÉN, J.I., CARAM, R.M. (2001); "Reflexão da radiação solar em vidros e películas refletivas" (Poster), In: SIICUSP 2001, São Paulo, SP - Brazil.

Professional journals

1. PERÉN, J.I. (2014); "Iluminação e ventilação naturais na arquitetura de Lelé". AU Educação No 244, July 2014 (http://au.pini.com.br/arquitetura-urbanismo/244/iluminacao-e-ventilacao-naturais-na-arquitetura-de-lele-318112-1.aspx).

2. PERÉN, J.I. (2007); "Estudo sobre a obra de João Filgueiras Lima (Lelé): Hospital Sarah Kubitschek - Fortaleza,CE". Finestra No 50, July-September, 2007 (http://arcoweb.com.br/finestra/tecnologia/jorge-isaac-peren-estudo-sobre-a-obra-de-joao-filgueiras-lima-01-09-2007).